

Manufacturing of Oxide Dispersion Strengthened Steels for Nuclear Applications



Sarah Connolly
Wolfson College
University of Oxford

A thesis presented for the degree of Doctor of Philosophy

Supervised by Professor Patrick Grant and Professor James Marrow

Trinity Term 2018

Preface

The research described in this thesis was carried out by the author in the Department of Materials at the University of Oxford between October 2014 and April 2018, under the supervision of Professor Patrick Grant, Professor James Marrow and Daniel Shepherd (NNL). All the work is original and where work from others has been included it has been clearly referenced and acknowledged. No part of this thesis has been submitted or accepted for any other degree at this university or elsewhere.

Parts of this work have been published in peer reviewed journals or presented at conferences and workshops as follows:

Journal Publications

F.Bergner, I.Hilger, J.Virta, J.Lagerbom, G.Gerbeth, S.Connolly, Z.Hong, P.S.Grant, T.Weissgarber "Alternative Fabrication Routes toward Oxide-Dispersion-Strengthened Steels and Model Alloys", Metallurgical and Materials Transactions A, Nov. 2016, vol. 47A, pp. 5313-5324.

Reports

S.Connolly, P.S.Grant "Spray Casting of ODS Steel", Report to NNL, Sept. 2018.

S.Connolly, P.S.Grant "Attritor Milling as a Comparison to Planetary Ball Milling", Report to NNL, Sept. 2018.

U.Ehrnsten, F.Bergner, M.Hernandez-Mayoral, E.Onorbe-Esparraguera, K.F.Nilsson, A.Hobt, Z.Spirit, Y.de Carlan, F.Delabrouille, B.Radiguet, M.Blat, M.Walter, S.Holmstrom, N.Mozzani, J.Rantala, S.Connolly, V.Radu, J.Chen, M.Serrano "Assessment of the effect of anisotropy on the mechanical properties of ODS steel tube", MatISSE – Deliverable D4.22, Nov. 2017.

Oral and Poster Presentations

S.Connolly, R.G.Abernethy, D.Shepherd, P.S.Grant "Field Assisted Sintering of ODS Steels for Advanced Fission Applications", Oral presentation at MAPP 1^{st}

International Conference, Sheffield, 30-31 January, 2018.

S.Connolly, P.S.Grant "Thermal Stability of Cladding Tubes", Oral presentation at MatISSE WP4 Meeting, VTT Helsinki, 6-7 June, 2016.

S.Connolly, D.Shepherd, P.S.Grant "ODS Steels for Fuel Cladding Applications produced via Novel Processing Routes", Oral presentation at 3^{rd} International ODS Workshop, HZDR Dresden, 20-21 April, 2016.

S.Connolly, D.Shepherd, T.J.Marrow, P.S.Grant "ODS Steels for Fuel Cladding Applications in Nuclear Reactors", Oral presentation at University Nuclear Technology Forum, UNTF, University of Sheffield, 5-7 April, 2016. 2^{nd} place for best presentation award.

S.Connolly, P.S.Grant, D.E.J.Armstrong "ODS Steels for Fuel Cladding Applications in GenIV Reactors", Oral presentation at 2^{nd} Oxide Dispersion Strengthened Steels group of young European Scientists workshop, ODISSEUS, University of Oxford, Oxford, 23-24 March, 2015.

S.Connolly, P.S.Grant "Manufacturing of Oxide Dispersion Strengthened (ODS) Steels for Nuclear Energy Applications", Poster presentation at NE Signature Research Seminar, Birchwood Park, Warrington, UK, 8 December, 2014.

Manufacturing of Oxide Dispersion Strengthened Steels for Nuclear Applications

Sarah Connolly
Wolfson College
University of Oxford

A thesis submitted for the degree of Doctor of Philosophy

Trinity Term 2018

Abstract

This work concerns developing understanding of powder processing of oxide dispersion strengthened (ODS) ferritic steels for fuel cladding tubes in fission nuclear reactors. Ferritic ODS steels are candidate materials for these applications due to their good creep resistance that arises from the pinning of grain boundaries by a distribution of inert nanoparticles, as well as the pinning of radiation-induced defects such as vacancies, interstitials and He bubbles. Industrial uptake of ODS steels has been limited by their expensive and labour intensive production that typically includes a 60 h mechanical alloying (MA) step to dissolve the oxide particles into the heavily worked ferrite matrix.

The key parameters of the MA process have been explored and re-optimised using a Fe-14Cr-3W-0.3Ti+0.25Y_2O_3 powder resulting in a 33% reduction in the time-consuming MA stage while maintaining all key microstructural features such as the acceptable dispersion of Y and O, and induced levels of mechanical work.

An alternative ODS powder production method was also investigated in which a supersaturated Fe-Y solid solution was formed during the gas atomisation of Fe-14Cr-3W-0.3Ti-0.4Y. The resulting powder was mixed with Fe_3O_4 nanoparticles in a short milling step to disperse but not dissolve the Fe_3O_4 and to introduce some mechanical work considered important for the subsequent fine-scale nucleation of Y-rich oxides by 'internal oxidation' of Y reacting with sacrificial Fe_3O_4 at elevated temperature.

MA and atomised powders were sintered by hot isostatic pressing (HIP) and the field assisted sintering technique (FAST), which offered further savings in process time, from 4 h to only 5 min. Four ODS materials were studied in detail, from the two types of powder and the two sintering methods, revealing differences in both the nano-scale oxides micro-scale ferritic grains. Fine particles in the gas atomised alloy were primarily TiO_x and not the Y-Ti rich oxides usually seen in MA material due to the lower oxygen affinity of Ti compared to Y.

Long term thermal annealing at reactor relevant temperatures (650°C) showed the ferritic grain structures to be stable. Following long exposure (675 h), Y-Ti rich oxides were identified. Electro-thermal mechanical testing (ETMT) was used to investigate tensile properties. MA Fe-14Cr-3W-0.3Ti+0.25Y_2O_3 consolidated by HIP and FAST had similar strengths to the literature, but brittle failure when tested at 350°C or below because of the limited plasticity deformation mechanisms active in this temperature range; ductility at 650°C was more typical. Fe-14Cr-3W-0.3Ti-0.4Y+Fe_3O_4 showed good strength, out-performing the literature across the testing temperature range, but suffered from brittle failure with little elongation due to dislocation pinning mechanisms remaining active even at elevated temperatures. Small punch test simulations of creep testing gave comparative creep resistance between MA Fe-14Cr-3W-0.3Ti+0.25Y_2O_3 consolidated by HIP and FAST and Fe-14Cr-3W-0.3Ti-0.4Y+Fe_3O_4 consolidated by FAST.

Fe-14Cr-3W-0.3Ti+0.25Y_2O_3 FAST resisted high loads for short amounts of time, but long term creep tests were unsuccessful, indicating crack opening resistance was being tested rather than creep resistance. The other samples

behaved more as expected from literature, with Fe-14Cr-3W-0.3Ti-0.4Y+Fe_3O_4 FAST showing better creep resistance, but limitations of the technique mean absolute properties could not be identified. All samples failed rapidly in a brittle manner, similar to in ETMT.

Overall, the alternative ODS production approach led to good strength across the temperature range of interest but ductility was limited, meaning fracture was rapid and unpredictable. Further work should reduce the density of oxide particles, or the oxygen contamination through processing, to generate a more ductile material, that is competitive with current reference austenitic stainless steels (15:15Ti).

Acknowledgements

Firstly, I would like to thank my supervisors, Professor Patrick Grant and Professor James Marrow for all of their support, guidance and direction throughout my studies for which I am incredibly grateful. Special thanks also go to Professor David Armstrong, for always being a sounding board for results and providing fruitful discussions.

Thanks go to the Engineering and Physical Science Research Council for providing the sponsorship funding for this project, and to The National Nuclear Laboratory for providing an industrial case award. Appreciation is owed to Daniel Shepherd and Jonathan Hyde of the National Nuclear Laboratory for providing an industrial perspective and technical advice on various topics during this work.

I would also like to thank my collaborators within the MatISSE project, and those at UKAEA for use of their small punch tester. Special thanks go to Dr Mike Gorley and Dr Mark Richardson of UKAEA for their support with this testing and with the wider mechanical properties work.

Thanks go to the Oxford Materials TSG team for all of their training and support, particularly Mrs G. Chapman, Mrs J. Holter, Dr G. Hughes and Dr N. Young. Extra special thanks go to Jack Haley, Robbie Abernethy and especially Dr I. Griffiths for their (almost) endless patience in the search for yttrium.

I would like to thank all my past and present colleagues within the Processing of Advanced Materials group, especially Dr Alasdair Morrison for his endless discussions in processing and microstructural understanding, which I hope will continue to flow, Dr Zuliang Hong and Dr Atsushi Sato for their training and Jack, Lukas and Kylee for making the days more enjoyable and Begbroke a happier place.

I am incredibly grateful to my wonderful friends at Wolfson College, for keeping me sane and helping me enjoy the last four years. Special mentions go to Robbie for his balance of microscopy aide and sports enthusiast, Edd for always listening and being ready for a G&T and Steve for making the writing process the most enjoyable I could ask for, and without which the last year especially would not have been the same.

Mum, Dad and J, for all your love, support, encouragement and competitive drive, and for always knowing when I just need a Sunday roast.

Lastly to Matt, who this would not have been possible without. Your love and patience, especially when MATLAB ‘breaks’ yet again, have been unwavering and will always be cherished.

Contents

List of Figures **xi**

List of Tables **xxi**

1 Introduction **1**
1.1 Motivation for the Thesis 1
1.2 Content and Structure of the Thesis 3

2 Literature Review **5**
2.1 Introduction 5
2.2 Nuclear Fission Energy 5
2.2.1 Sodium-cooled Fast Reactors 7
2.3 ODS Steels 12
2.3.1 Strengthening Mechanisms 13
2.3.2 Boundaries, Zener Pinning and Abnormal Grain Growth . . 15
2.3.3 Typical Microstructure 17
2.3.4 Alloying Additions 18
2.4 Fabrication of ODS Steels 23
2.4.1 Mechanical Alloying of Powder 24
2.4.2 Consolidation Methods 26
2.4.3 Novel Processing Methods 35
2.5 ODS Steel Microstructure 44
2.5.1 Thermal Stability 45
2.6 Mechanical Properties 46
2.6.1 15:15Ti Austenitic Steel Properties 52
2.6.2 Small Punch Test 53
2.6.3 Important Considerations for Future Research 55
2.6.4 Mechanical Properties Summary 56
2.7 Literature Review Summary 57

3 Experimental Methods **59**
3.1 Introduction . . . 59
3.2 Processing . . . 60
3.2.1 Raw Materials . . . 60
3.2.2 Mechanical Alloying . . . 61
3.2.3 Sintering . . . 62
3.2.4 Heat Treatment . . . 65
3.3 Sample Preparation . . . 65
3.3.1 Powder . . . 65
3.3.2 Consolidated Material . . . 65
3.4 Powder Analysis . . . 67
3.4.1 Powder Size Distribution . . . 67
3.4.2 Powder Density Analysis . . . 70
3.4.3 Powder Hardness . . . 70
3.4.4 BET Surface Area Analysis . . . 70
3.5 Characterisation of Consolidated Material . . . 71
3.5.1 Scanning Electron Microscopy . . . 71
3.5.2 Transmission Electron Microscopy . . . 72
3.5.3 Atom Probe Tomography . . . 73
3.5.4 X-ray Diffraction . . . 74
3.6 Chemical Analysis . . . 77
3.7 Mechanical Properties . . . 77
3.7.1 Microhardness . . . 77
3.7.2 ETMT . . . 78
3.7.3 Small Punch Testing . . . 78

4 "Industry Standard" Material **81**
4.1 Introduction . . . 81
4.2 Microstructural Analysis . . . 83
4.3 Thermal Stability . . . 83

5 Fabrication of ODS Steels: Powder Production **89**
5.1 Introduction . . . 89
5.2 Milling parameter study . . . 91
5.2.1 Milling cycle length . . . 92
5.2.2 Final milling parameters . . . 101
5.2.3 Strengthening mechanisms in Fe-14Cr-3W-0.3Ti+0.25Y_2O_3 . . . 103
5.3 Y-containing pre-alloyed powder . . . 105
5.4 Comparison Between Powders . . . 113
5.4.1 Powder Size and Morphology . . . 113

5.4.2 Powder Hardening Mechanisms . . . 113
5.4.3 Powder Packing Properties . . . 114
5.4.4 Powder Chemistry . . . 114
5.5 Summary . . . 115

6 Fabrication of ODS Steels: Powder Consolidation 117
6.1 Introduction . . . 117
6.2 Experimental Parameters . . . 118
6.2.1 Hot Isostatic Pressing . . . 118
6.2.2 Field Assisted Sintering . . . 120
6.3 Chemical Composition . . . 125
6.4 Microstructure . . . 128
6.4.1 HIP Consolidated Fe-14Cr-3W-0.3Ti+0.25Y_2O_3 . . . 128
6.4.2 HIP Consolidated Fe-14Cr-3W-0.3Ti-0.4Y+Fe_3O_4 . . . 131
6.4.3 FAST Consolidated Fe-14Cr-3W-0.3Ti+0.25Y_2O_3 . . . 135
6.4.4 FAST Consolidated Fe-14Cr-3W-0.3Ti-0.4Y+Fe_3O_4 . . . 142
6.4.5 Microstructural differences and similarities between HIP and FAST . . . 153
6.5 Thermal Stability . . . 157
6.5.1 Fe-14Cr-3W-0.3Ti+0.25Y_2O_3 HIP . . . 157
6.5.2 Fe-14Cr-3W-0.3Ti-0.4Y+Fe_3O_4 HIP . . . 157
6.5.3 Fe-14Cr-3W-0.3Ti+0.25Y_2O_3 FAST . . . 162
6.5.4 Fe-14Cr-3W-0.3Ti-0.4Y+Fe_3O_4 FAST . . . 165
6.5.5 Thermal Stability Summary . . . 167
6.6 Microstructural Summary . . . 169

7 Mechanical Properties 171
7.1 Introduction . . . 171
7.2 Microhardness . . . 173
7.2.1 Hot Microhardness . . . 174
7.2.2 Thermal Stability . . . 174
7.3 Electrothermal Mechanical Testing . . . 175
7.3.1 Fe-14Cr-3W-0.3Ti+0.25Y_2O_3 Alloys . . . 175
7.3.2 Fe-14Cr-3W-0.3Ti-0.4Y+Fe_3O_4 Alloys . . . 177
7.3.3 Validation of Experimental Results Against Estimations . . . 185
7.3.4 ETMT Summary . . . 202
7.4 Small Punch Testing . . . 203
7.4.1 Constant Displacement Rate Tests . . . 204
7.4.2 Creep Tests . . . 206
7.4.3 SPT Summary . . . 212
7.5 Summary of Mechanical Behaviour . . . 215

8 Conclusions and Further Work **217**
8.1 Conclusions 217
8.2 Further Work 222

List of Figures

2.1 Worldwide uranium resource predictions based on the uptake of fast reactor technologies (redrawn from [2]). 6
2.2 Schematic representation of a SFR (redrawn from [2].) 8
2.3 Cladding candidate materials showing their maximum operating temperature and technology readiness level with 3 being proof of concept, 7 successful prototype, 8 commission, 9 successful operation and 10 long term operation [5]. 10
2.4 Schematic of the oxide dispersion strengthened (ODS) strengthening mechanisms showing a high density of nanooxides pinning He in fine bubbles and providing a high density of sink points for irradiation-induced defects (redrawn from [12]). 12
2.5 Comparative sketch of a normal and an abnormal grain growth distribution after annealing [30]. 16
2.6 FEG SEM micrographs of Fe-14Cr-1W-0.3Ti-0.3T_2O_3 powder after in-situ annealing at 1100°C showing abnormal grain growth [30]. . . 17
2.7 Bright field (bright field (BF)) transmission electron microscope (transmission electron microscopy (TEM)) images of bimodal microstructure seen in Fe-14Cr ODS alloys [38]. 17
2.8 TEM micrographs of (a) (i) bright field (BF) image of Cr-rich particle (ii) high angle annular dark field (HAADF) image of Ti-rich precipitate (b) (i) HAADF of Y-rich particles (ii) HAADF of nm scale particles [8]. 19
2.9 Ellingham diagram showing the free energy of formation of 1 mole of oxide (reproduced from [44]). 20
2.10 Comparison between the size and composition of Y_2O_3 oxides with (a) Ti additions (b) Al additions (c) Nb additions in Fe-13Cr-3W-0.46Y_2O_3 [40]. 21
2.11 Dependence of the oxide particle size, density and material grain size on the Ti alloy concentration in Fe-14Cr-2W-0.3Y_2O_3 (redrawn from [28]). 22
2.12 Schematic representation of a HIP. 27

2.13 Microstructure of 14Cr-2W-0.3Ti-0.3Y_2O_3 following hot isostatic pressing (HIP)ing at 1150°C for 2.5 h (a) secondary electron (SE) micrograph showing the ferritic grain structure [76] and (b) high angle annular DF micrograph showing particles [75]. 28
2.14 Schematic of the direct extrusion process. 29
2.15 EBSD maps of the microstructure in extruded rods in the (a) longitudinal direction (b) transverse direction (c) colour key for crystallographic orientation [84]. 29
2.16 Difference between tensile properties in transverse and longitudinal extrusion directions for Fe-14Cr-1W-0.4Ti-0.3Y_2O_3 (redrawn from [85]). 30
2.17 Schematic representation of a field assisted sintering machine. . . . 31
2.18 Effect of sintering temperature on relative density of spark plasma sintering (SPS)ed 14YT alloy (redrawn from [97]). 32
2.19 SEM micrographs from 14YT FAST samples at different sintering temperatures (a) 900°, (b) 1000°C, (c) 1100°C, (d) 1150°C. Arrows indicate the direction of applied pressure [97]. 33
2.20 SEM micrograph of the bimodal grain structure in Fe-14Cr-1W-0.3Ti-0.3Y_2O_3 alloy consolidated by FAST [97]. 34
2.21 BF TEM micrograph of 14YT alloy consolidated by FAST [101]. . . 34
2.22 (a) scanning transmission electron microscopy (STEM) high-angle anular dark field (HAADF) micrograph with inset energy dispersive x-ray spectroscopy (EDX) maps for Fe, Y and O (b) high-resolution transmission electron microscopy (HRTEM) image of small in-grain particle (c) fast Fourier transform (FFT) image and crystallographic analysis of particle in (b) [107]. 38
2.23 Schematic of the spray casting process. 39
2.24 (a) TEM BF image of laser melted ODS steel with oxide particles highlighted by arrows (b) HAADF STEM image of aggregated nanoparticle [112]. 40
2.25 TEM micrographs of nanoparticles in HIPed GARS ODS Fe-16Cr-1W-0.5Ti-0.65Y_2O_3 powder [120]. 41
2.26 BSE field emission gun (FEG)-SEM micrographs in HIPed STARS ODS powder of (a) nanoparticles and (b) grain structure [121]. . . . 42
2.27 Strength of commercial and experimental alloys (a) ultimate tensile strength (UTS) and yield strength (σ_y) of Fe-14Cr-3W-0.3Ti-0.25Y_2O_3 (14YWT), Fe-12Cr-3W-0.3Ti-0.25Y_2O_3 (12YWT), Fe-9Cr-2W-1V-1Ta non-ODS steel and Fe-14Cr-0.3Mo-1Ti-0.25Y_2O_3 (MA957) as a function of testing temperature and (b) creep strength of 9Cr-1W-1Mo-1V-1Nb a non-ODS tempered martensitic steel, MA957, 12YWT and 14YWT. 47

2.28 SEM fracture surface images of Fe-12Cr-2W-0.2Ti-0.25Y_2O_3 tested at 500°C (a) macro view showing elliptical necking with microcracks (b) magnified view of microcracks from selected area with an arrow in (a), (c) magnified view of dimples with particles and micropores from the selected area in (a), and (d) magnified area showing the shallow dimples with micropores at the shear-lip region from the selected area in (a) [126]. 48
2.29 Ultimate tensile strength from literature data for material produced using current and novel processing methods for HIP He 2012 [75], HIP Oksiuta 2014 [128], FAST Auger 2013 [100], and Extruded Serrano 2012 [84]. 50
2.30 YS from literature data for material produced using current and novel processing methods for HIP Oksiuta 2014 [128], FAST Boulnat [101], Extruded Fournier 2012 [79] and Extruded Serrano 2012 [84]. 51
2.31 Total elongation values from literature data for material produced using current and novel processing methods for HIP Oksiuta 2014 [128], FAST Auger 2013 [100], FAST Boulnat [101], FAST Sun 2012 [130], Extruded Fournier 2012 [79], Extruded Garcia 2012 [131] and Extruded Serrano 2012 [84]. 52
2.32 Stress-rupture data for small punch creep tests at 650°C [134]. . . . 54
2.33 Small punch test failed specimens (a) transverse direction (b) longitudinal direction [134]. 55

3.1 SEM images of the powder size and morphology of four as-received powders. 61
3.2 Photo of the Fritsch Pulverisette model 5 used for milling. 62
3.3 Schematic representation of HIP set-up. 63
3.4 Schematic representation of FAST set-up. 64
3.5 Series of stages of fib-liftout process. 67
3.6 Schematic representation of laser scattering. 68
3.7 Example of particle counting using thresholding within the Matlab image analysis script (a) original optical image, and (b) threshold overlay to analyse particle area and thus equivalent spherical diameter. 69
3.8 BET adsorption isotherm plot showing calculation for the SSA of the as-received base powder and Y_2O_3 milled powder. 72
3.9 Schematic representation of XRD rig. 75
3.10 Separation of microstrain and crystallite size contributions to peak broadening 76

3.11 Schematic drawing of SPT set-up 1. WC punchhead 2. Top of die set 3. Sample 4. Bottom of die set 5. Displacement extensometer Inset. e.g. sample [133]. 79
3.12 Photograph of SPT apparatus at 650°C. 80

4.1 false-coloured EBSD orientation maps of the Fe-14Cr-1W-0.3Ti-$0.25Y_2O_3$ as-received tubes in the (a) longitudinal and (b) transverse directions with (c) corresponding pole figures for the longitudinal direction. 84
4.2 false-coloured EBSD orientation maps of Fe-14Cr-1W-0.3Ti-$0.25Y_2O_3$ extruded tubes following thermal ageing for (a) 0 h, (b) 7.5 h, (c) 25 h, (d) 75 h, (e) 125 h, (f) 675 h at 750°C. 86
4.3 Pole figures for the as-received and 675 h aged microstructures. . . 87
4.4 Grain size and hardness of Fe-14Cr-1W-0.3Ti-$0.25Y_2O_3$ extruded tubes as a function of ageing time. 88

5.1 Fe-Y phase diagram [150]. 91
5.2 Schematic of the mill:pause ratios explored in this study. 93
5.3 (a) hardness and (b) powder diameter as a function of milling time for each mill:pause ratio. 94
5.4 (a) Number average particle diameter (d(50)) and tap density of Fe-14Cr-3W-0.3Ti+$0.25Y_2O_3$ powder milled for 60 h as a function of mill:pause ratio and (b) sintered density and hardness of 20 mm diameter 10 mm thick compacts using the Fe-14Cr-3W-0.3Ti+$0.25Y_2O_3$ powder after 60 h of milling as a function of the mill:pause. 95
5.5 SEM images showing powder size and morphology of Fe-14Cr-3W-0.3Ti-$0.25Y_2O_3$ powder milled for (a) 5h (b) 20h (c) 30h (d) 40h (e) 50h (f) 60h. 97
5.6 XRD spectra from the Fe-14Cr-3W-0.3Ti+$0.25Y_2O_3$ milled at a ratio of 20:40 and shown as a function of total milling time, with inset detail of the ferrite (211) peak showing broadening with time. . . . 98
5.7 Microstrain and crystallite size contributions to peak broadening in Fe-14Cr-3W-0.3Ti+$0.25Y_2O_3$ powder as a function of total milling time. 99
5.8 Hardness and dislocation density of Fe-14Cr-3W-0.3Ti+$0.25Y_2O_3$ powder as a function of milling time. 100
5.9 (a) Particle diameter and tap density of Fe-14Cr-3W-0.3Ti+$0.25Y_2O_3$ milled using a pause ratio of 20:40 as a function of total milling time and (b) sintered density and hardness of 20 mm diameter 10 mm thick FAST consolidated compacts using the Fe-14Cr-3W-0.3Ti+$0.25Y_2O_3$ powder as a function of total milling time. 101

5.10 Typical EPMA maps showing the distribution of Y in Fe-14Cr-3W-0.3Ti+0.25Y_2O_3 after milling for a total time of (a) 5 h (b) 20 h (c) 30 h (d) 40 h (e) 50 h and (f) 60 h. 102
5.11 SEM images of the powder size and morphology of Fe-14Cr-3W-0.3Ti-0.4Y+Fe_3O_4 powder (a) A-R (b) S (c) Mx (d) M0.5 (e) M10 and (f) M-O as defined in Table 5.3. 107
5.12 Microstrain and domain size contributions to peak broadening for the powders listed in Table 5.3. 108
5.13 Powder hardness and estimated dislocation densities for the powders listed in Table 5.3. 108
5.14 (a) powder diameter and tap density for all powders listed in Table 5.3 and (b) sintered density and hardness for 20 mm diameter, 10 mm height sintered compacts from all powders listed in Table 5.3 109
5.15 Sintered hardness and following a 750°C 1 hr heat treatment, for 20 mm diameter, 10 mm height, sintered compacts from all powders listed in Table 5.3 with FeCrWTi+Y_2O_3 sintered in the same way shown for reference. 110
5.16 EPMA maps showing the distribution of (a) Y in AR, (b) O in AR, (c) Y in M10 and (d) O in M10. 112

6.1 Temperature and pressure profiles during consolidation by HIP. . . 119
6.2 Photographs of the HIP can and sealing process. 120
6.3 Photograph of the [1] graphite punch, [2] graphite die set and [3] sintered 40 mm disc. 121
6.4 Density of Fe-14Cr-3W-0.3Ti and Fe-14Cr-3W-0.3Ti-0.25Y_2O_3 after 60 h of milling as a function of FAST temperature, with results for Fe-14Cr-0.4Ti-0.25Y_2O_3 from Zhang *et al.* [97] for comparison. . . . 122
6.5 Macro-scale porosity in ⌀ 20 mm Fe-14Cr-3W-0.3Ti-0.25Y_2O_3 milled powder sintered at 1150°C and pressure of 50 MPa. 122
6.6 Sintered density of ⌀ 20 mm, 10 mm height Fe-14Cr-3W-0.3Ti-0.25Y_2O_3 milled powder compacts as a function of applied pressure during FAST. 123
6.7 Sintered density of ⌀ 20 mm Fe-14Cr-3W-0.3Ti-0.25Y_2O_3 milled powder compacts as a function of isothermal hold time during FAST. 124
6.8 FAST and HIP profiles as a function of time for temperature and pressure, used for the consolidation of Fe-14Cr-3W-0.3Ti-0.25Y_2O_3 and Fe-14Cr-3W-0.3Ti-0.47Y_2O_3 powders. 125
6.9 SEM back-scattered electron (BSE) image of milled Fe-14Cr-3W-0.3Ti+0.25Y_2O_3 powder consolidated by HIP. 129

6.10 EBSD false coloured orientation maps of milled Fe-14Cr-3W-0.3Ti+0.25Y_2O_3 powder consolidated by HIP (a) low magnification, (b) high magnification (c) histogram of grain size distribution and (d) histogram of grain area distribution. 130
6.11 SE micrographs and EDS maps of (a) and (b) W- and C-rich particles and (c) and (d) Ti- and O-rich particles in HIP consolidated Fe-14Cr-3W-0.3Ti+0.25Y_2O_3 milled powder. 131
6.12 BF TEM micrograph of particles seen in Fe-14Cr-3W-0.3Ti+Y_2O_3 milled powder consolidated by HIP. 132
6.13 SEM micrograph of Fe-14Cr-3W-0.3Ti-0.4Y+Fe_3O_4 milled powder consolidated by HIP. 132
6.14 EBSD maps of Fe-14Cr-3W-0.3Ti-0.4Y+Fe_3O_4 milled powder consolidated by HIP (a) low magnification, (b) high magnification (c) histogram of grain size distribution and (d) histogram of grain area distribution. 133
6.15 SE micrographs and EDS maps of larger particles in HIP consolidated Fe-14Cr-3W-0.3Ti-0.4Y+Fe_3O_4 milled powder. 134
6.16 TEM bright field micrographs of the microstructure and particles seen in Fe-14Cr-3W-0.3Ti-0.4Y+Fe_3O_4 milled powder consolidated by HIP. 135
6.17 EBSD maps of the microstructure of Fe-14Cr-3W-0.3Ti+0.25Y_2O_3 milled powder consolidated by FAST (a) low magnification (b) high magnification (c) histogram of grain size distribution. 137
6.18 SEM micrograph of Fe-14Cr-3W-0.3Ti+0.25Y_2O_3 milled powder consolidated by FAST then heat treated at 750°C for 1 h. 138
6.19 False coloured EBSD orientation maps of Fe-14Cr-3W-0.3Ti+0.25Y_2O_3 milled powder consolidated by FAST then heat treated at 750°C for 1 h (a) low magnification (b) high magnification (c) histogram of grain size distribution and (d) histogram of grain area distribution. 139
6.20 SE micrographs and EDS maps of larger particles in FAST consolidated Fe-14Cr-3W-0.3Ti+0.25Y_2O_3 milled powder following heat treatment at 750°C for 1 h. 140
6.21 Bright field TEM micrographs of (a) the microstructure and (b) the particles seen in Fe-14Cr-3W-0.3Ti+0.25Y_2O_3 milled powder consolidated by FAST and heat treated at 750°C for 1 h. 140
6.22 An ADF image of Fe-14Cr-3W-0.3Ti+0.25Y_2O_3 consolidated by FAST and corresponding EELS spectra (from the area highlighed in the ADF image) suggesting Ti-rich oxides with a Cr-rich shell. . . . 141

6.23 An ADF image of Fe-14Cr-3W-0.3Ti+0.25Y_2O_3 consolidated by FAST and corresponding EELS spectra (from the area highlighed in the ADF image) suggesting a Ti-Cr-rich shell, and local matrix enrichment of Y. 142
6.24 APT reconstructions from a Fe-14Cr-3W-0.3Ti-0.25Y_2O_3 FAST needle approximate dimensions 40 × 40 × 270 nm showing the main alloying elements. 143
6.25 APT reconstructions from (a) Ti, Y, TiO and YO (b) isolated clusters (c) enlarged image of cluster from region of interest in (b). 144
6.26 Proxigram concentration profile over the cluster seen in Figure 6.25 (c) showing decomposed atomic concentrations of Fe, Cr, W, Ti, Y, O and Mn and inset enlarged view of Ti, Y and O concentrations. . 144
6.27 SEM micrograph of the bimodal grain size distribution in Fe-14Cr-3W-0.3Ti-0.4Y+Fe_3O_4 milled powder consolidated by FAST. 145
6.28 False coloured EBSD orientation maps of the microstructure of Fe-14Cr-3W-0.3Ti-0.4Y+Fe_3O_4 milled powder consolidated by FAST (a) low magnification (b) high magnification (c) histogram of grain size distribution and (d) histogram of grain area distribution. 146
6.29 SEM micrograph of the microstructure of Fe-14Cr-3W-0.3Ti-0.4Y+Fe_3O_4 milled powder consolidated by FAST and heat treated for 1 h at 750°C. 147
6.30 False coloured EBSD orientation maps of the microstructure of Fe-14Cr-3W-0.3Ti-0.4Y+Fe_3O_4 milled powder consolidated by FAST then heat treated at 750°C for 1 h (a) low magnification (b) high magnification (c) histogram of grain size distribution and (d) grain area distribution. 148
6.31 SE micrographs and EDS maps of larger particles in FAST consolidated Fe-14Cr-3W-0.3Ti-0.4Y+Fe_3O_4 milled powder. 149
6.32 Bright field TEM micrographs of the microstructure and particles seen in Fe-14Cr-3W-0.3Ti-0.4Y+Fe_3O_4 milled powder consolidated by FAST. 149
6.33 APT reconstructions from a Fe-14Cr-3W-0.3Ti-0.4Y+0.27Fe_3O_4 FAST needle approximate dimensions 40 × 40 × 180 nm showing the main alloying elements. 150
6.34 APT reconstructions from (a) Ti, Y, TiO and YO (b) isolated clusters (c) enlarged image of cluster from region of interest in (b). 151
6.35 Proxigram concentration profile over the cluster seen in Figure 6.34 (c) showing decomposed atomic concentrations of Fe, Cr, W, Ti, Y, O and Mn and inset enlarged view of Cr, Ti, Y and O concentrations. 152

6.36 Microstrain and crystallite size estimations from XRD data for Fe-14Cr-3W-0.3Ti+0.25Y_2O_3 consolidated by HIP and FAST and Fe-14Cr-3W-0.3Ti-0.4Y+Fe_3O_4. 155
6.37 EBSD maps of Fe-14Cr-3W-0.3Ti+0.25Y_2O_3 HIP following a heat treatment at 650°C for (a), (b) 0 h (c), (d) 24 h (e), (f) 675 h under vacuum. 158
6.38 Histogram of grain size distributions and grain area distributions from EBSD orientation maps of Fe-14Cr-3W-0.3Ti+0.25Y_2O_3 milled powder consolidated by HIP following a heat treatment at 650°C for (a) and (c) 24 h and (b) and (d) 675 h. 159
6.39 EBSD maps of Fe-14Cr-3W-0.3Ti-0.4Y+Fe_3O_4 HIP following an isothermal hold at 650°C for (a), (b) 0 h (c), (d) 24 h (e), (f) 675 h. 160
6.40 Histogram of grain size distributions and area distributions from EBSD orientation maps of Fe-14Cr-3W-0.3Ti-0.4Y+Fe_3O_4 milled powder consolidated by HIP following a heat treatment at 650°C for (a) and (c) 24 h and (b) and (d) 675 h. 161
6.41 BSE micrograph of the Fe-14Cr-3W-0.3Ti+0.25Y_2O_3 HIP microstructure following 675 h at 650°C with Y- and Ti-rich regions higlighted in blue, Ti-, Cr- and Ti-rich regions highlighted in purple and W rich regions in green. 162
6.42 EBSD maps of Fe-14Cr-3W-0.3Ti+0.25Y_2O_3 FAST following heat treatment at 650°C for (a), (b) 0 h (c), (d) 24 h (e), (f) 675 h under vacuum. 163
6.43 Histogram of grain size distributions from EBSD orientation maps of Fe-14Cr-3W-0.3Ti+0.25Y_2O_3 milled powder consolidated by FAST following a heat treatment at 650°C for (a) 24 h and (b) 675 h. . . 164
6.44 BSE micrograph of the Fe-14Cr-3W-0.3Ti+0.25Y_2O_3 FAST microstructure following a 675 h hold at 650°C with Y and Ti rich regions higlighted in blue, Ti- Cr- and Y- rich regions highlighted in purple, Ti- and Cr- rich regions highlighted in orange, W- rich regions in green and CrN in red. 165
6.45 EBSD maps of Fe-14Cr-3W-0.3Ti-0.4Y+Fe_3O_4 FAST following an heat treatment at 650°C for (a), (b) 0 h (c), (d) 24 h (e), (f) 675 h under vacuum. 166
6.46 Histogram of grain size distributions from EBSD orientation maps of Fe-14Cr-3W-0.3Ti-0.4Y+Fe_3O_4 milled powder consolidated by HIP following a heat treatment at 650°C for (a) 24 h and (b) 675 h. . . 167

6.47 BSE micrograph of the Fe-14Cr-3W-0.3Ti+0.25Y_2O_3 microstructure following 675 h at 650°C with Y- and Ti-rich regions higlighted in blue, Ti- Cr- and Y-rich regions highlighted in purple, Ti- and Cr-rich regions highlighted in orange, W-rich regions in green and Cr-rich areas in red. 168

7.1 Microhardness of MA Fe-14Cr-3W-0.3Ti+0.25Y_2O_3 HIP and FAST, Fe-14Cr-3W-0.3Ti-0.4Y+Fe_3O_4 HIP and FAST, with FAST data both pre- and post- heat treatment. 174
7.2 Microhardness as a function of testing temperature for Fe-14Cr-3W-0.3Ti+0.25Y_2O_3 HIP. 175
7.3 Microhardness of MA Fe-14Cr-3W-0.3Ti+0.25Y_2O_3 HIP and FAST and Fe-14Cr-3W-0.3Ti-0.4Y+Fe_3O_4 HIP and FAST following an isothermal hold at 650°C for 24 and 675 h. 176
7.4 Stress-strain curves for Fe-14Cr-3W-0.3Ti+0.25Y_2O_3 HIP and FAST ETMT samples. 178
7.5 SEM images of the fracture surface of a Fe-14Cr-3W-0.3Ti+0.25Y_2O_3 HIP ETMT specimen tested at (a) room temperature and a cleavage plane (enlarged from the red box) highlighted in (b), (c) 350°C and surface dimpling (enlarged from the red box) highlighted in (d), and (e) 650°C and dimpling with possible particle pull out (from the red box) highlighted in (f). 179
7.6 SEM images of the fracture surface of a Fe-14Cr-3W-0.3Ti+0.25Y_2O_3 FAST ETMT specimen tested at (a) room temperature and cleavage planes (enlarged from the red box) highlighted in (b), (c) 350°C and surface dimpling (enlarged from the red box) highlighted in (d), and (e) 650°C and dimpling with possible particle pull out (from the red box) highlighted in (f). 180
7.7 Stress-strain ETMT curves for Fe-14Cr-3W-0.3Ti-0.4Y+Fe_3O_4 consolidated by HIP and FAST. 181
7.8 SEM images of the fracture surface of a Fe-14Cr-3W-0.3Ti-0.4Y+Fe_3O_4 HIP ETMT specimen tested at (a) room temperature and a cleavage plane (enlarged from the red box) highlighted in (b), (c) 350°C and surface dimpling (enlarged from the red box) highlighted in (d), and (e) 650°C and dimpling (from the red box) highlighted in (f). 182
7.9 SEM images of the fracture surface of a Fe-14Cr-3W-0.3Ti-0.4Y+Fe_3O_4 FAST ETMT specimen tested at (a) room temperature and a cleavage plane (enlarged from the red box) highlighted in (b), (c) 350°C and surface dimpling (enlarged from the red box) highlighted in (d), and (e) 650°C and dimpling (from the red box) highlighted in (f). 183

7.10 Stacked bar chart of the contributions of the summation model to yield stress for each of the four Fe-14Cr-3W-0.3Ti-based alloys at room temperature. 191
7.11 Shear modulus, G, of Fe-14Cr-1W-0.4Ti-0.3Y_2O_3 as a function of temperature [25]. 193
7.12 Comparison between the strengthening model and experimental yield strength values for (a) Fe-14Cr-3W-0.3Ti-0.25Y_2O_3 HIP showing both experiment and hardness predictions and (b) Fe-14Cr-3W-0.3Ti-0.25Y_2O_3 FAST. 198
7.13 Comparison between the strengthening model and experiment yield strength for (a) Fe-14Cr-3W-0.3Ti-0.4Y+Fe_3O_4 HIP and (b) Fe-14Cr-3W-0.3Ti-0.4Y+Fe_3O_4 FAST. 200
7.14 Yield strength as a function of temperature for Fe-14Cr-3W-0.3Ti+0.25Y_2O_3 HIP (Y_2O_3 HIP), Fe-14Cr-3W-0.3Ti+0.25Y_2O_3 FAST (Y_2O_3 FAST) and Fe-14Cr-3W-0.3Ti-0.4Y+Fe_3O_4 FAST (Fe_3O_4 FAST) compared with similar alloys. 201
7.15 Ultimate tensile strength as a function of temperature for Fe-14Cr-3W-0.3Ti+0.25Y_2O_3 HIP (Y_2O_3 HIP), Fe-14Cr-3W-0.3Ti+0.25Y_2O_3 FAST (Y_2O_3 FAST) and Fe-14Cr-3W-0.3Ti-0.4Y+Fe_3O_4 FAST (Fe_3O_4 FAST) compared with similar allloys. 202
7.16 Total elongation as a function of temperature for Fe-14Cr-3W-0.3Ti+0.25Y_2O_3 HIP (Y_2O_3 HIP), Fe-14Cr-3W-0.3Ti+0.25Y_2O_3 FAST (Y_2O_3 FAST) and Fe-14Cr-3W-0.3Ti-0.4Y+Fe_3O_4 FAST (Fe_3O_4 FAST) compared with similar allloys. 203
7.17 Load-displacement curves for constant displacement tests at 0.2 mm/min tested at (a) room temperature and (b) 650°C using small punch testing for Fe-14Cr-3W-0.3Ti+0.25Y_2O_3 HIP (Y_2O_3 HIP), Fe-14Cr-3W-0.3Ti+0.25Y_2O_3 FAST (Y_2O_3 FAST) and Fe-14Cr-3W-0.3Ti-0.4Y+Fe_3O_4 FAST (Fe_3O_4 FAST). 205
7.18 SEM micrographs of the fracture surface of (a) Fe-14Cr-3W-0.3Ti+0.25Y_2O_3 HIP at room temperature (b) at 650°C (c) Fe-14Cr-3W-0.3Ti+0.25Y_2O_3 FAST at room temperature (d) at 650°C (e) Fe-14Cr-3W-0.3Ti-0.4Y+Fe_3O_4 FAST at room temperature and (f) at 650°C. 207
7.19 SPT calibration tests. 208
7.20 Stress-rupture plots for all SPT samples and literature values. . . . 210
7.21 SEM images of the fracture surface of 10 h SPT creep tests (a) Fe-14Cr-3W-0.3Ti+0.25Y_2O_3 HIP (b) edge of deformed region (c) Fe-14Cr-3W-0.3Ti+0.25Y_2O_3 FAST (d) edge of deformed region (e) Fe-14Cr-3W-0.3Ti-0.4Y+Fe_3O_4 FAST (f) edge of deformed region. . 213

List of Tables

2.1 Summary of strengthening mechanisms [26]. 14
2.2 Reference values for common powder properties for Fe-14Cr ODS steels. 25
2.3 Microstructural features as generated by common processing methods. 44
2.4 Hardness of ODS steels produced by a variety of processing methods. 49
2.5 Tensile mechanical properties (YS - yield strength, UTS - ultimate tensile strength and Str % - strain at failure) of 15:15Ti austenitic steel [132]. 53

3.1 Chemical composition of pre-alloyed base powders from chemical analysis supplied by Sandvik-Osprey Ltd., UK. 60
3.2 Chemical composition of milling pots and balls. 62
3.3 Optimum PID constants used in FAST experiments. 64
3.4 Major electron energy loss edges for elements of interest [143]. . . . 74

5.1 Final milling parameters for production of Fe-14Cr-3W-0.3Ti+0.25Y_2O_3 powder. 103
5.2 Estimation of strengthening mechanism contributions in Fe-14Cr-3W-0.3Ti+0.25Y_2O_3 powder milled for 40 h at a pause ratio of 20:40, H(Fe-14Cr-3W-0.3Ti+0.25Y_2O_3) = 14 GPa, H(FeCrWTi) = 1060 MPa, k = 0.22 MPam$^{1/2}$ [158], d = 7 nm, M = 2.9 [159], α = 0.24 [159], G = 81.5 [25] b = 0.25 nm*, $\rho = 75\times10^{13}$. *assuming all dislocations have a Burgers vector of type $\frac{1}{2}(111)$ 104
5.3 Powders prepared without / with various additions to the pre-alloyed Fe-14Cr-3W-0.3Ti-0.4Y powder. 105
5.4 Estimation of strengthening mechanism contributions in M10 and M-O powders, values used in calculations: H(M10) = 11.8 GPa, H(M-0) = 10.7 GPa, H(Fe-14Cr-3W-0.3Ti) = 1060 MPa, k = 0.22 MPam$^{1/2}$ [158], d = 7 nm, M = 2.9 [159], α = 0.24 [159], G = 81.5 [25] b = 0.25 nm*, $\rho = 75\times10^{13}$. *assuming all dislocations have a Burgers vector of type $\frac{1}{2}111$ 111
5.5 Comparison between final powder properties. 113

5.6 Chemical composition of prealloyed Fe-14Cr-3W-0.3Ti base powder as measured by Sandvik-Osprey (SO), as measured in chemical analysis by AMG Superalloys, and following 40 h of milling with Y_2O_3 (wt%). 115
5.7 Chemical composition of prealloyed Fe-14Cr-3W-0.3Ti-0.4Y base powders as measured by Sandvik-Osprey (SO), as measured in chemical analysis by AMG Superalloys, and following 10 h of milling with Fe_3O_4 (wt%). 115

6.1 Sintering parameters for HIP consolidation of Fe-14Cr-3W-0.3Ti+0.25Y_2O_3 and Fe-14Cr-3W-0.3Ti-0.4Y+Fe_3O_4 powders. 119
6.2 Sintering parameters for HIP and FAST consolidation of Fe-14Cr-3W-0.3Ti-0.25Y_2O_3 and Fe-14Cr-3W-0.3Ti-0.47Y_2O_3 powders. . . . 124
6.3 Sample designations. 126
6.4 Chemical composition of base powder (measured by Sandvik-Osprey (SO), Fe-14Cr-3W-0.4Ti+0.25Y_2O_3 milled powder, FeCrWTi+Y_2O_3 milled powder consolidated by HIP, and by FAST (wt%), measured by AMG Superalloys with compositions of concern highlighted in red. 127
6.5 Chemical composition of base powder (measured by Sandvik-Osprey (SO), Fe-14Cr-3W-0.3Ti-0.4Y+Fe_3O_4 milled powder, Fe-14Cr-3W-0.3Ti-0.4Y+Fe_3O_4 milled powder consolidated by HIP, and by FAST (wt%) with compositions of concern highlighted in red. 128
6.6 Microstructural comparison between final material. 153
6.7 Mean grain size and crystallite size pre- and post- HT for all materials. 154
6.8 Dislocation density of Fe-14Cr-3W-0.3Ti+0.25Y_2O_3 consolidated by HIP and FAST+HT and Fe-14Cr-3W-0.3Ti-0.4Y+Fe_3O_4 consolidated by HIP and FAST+HT estimated from XRD data. 155
6.9 Grain size as a function of ageing time for Fe-14Cr-3W-0.3Ti+0.25Y_2O_3 HIP material. 157
6.10 Grain size as a function of ageing time for Fe-14Cr-3W-0.3Ti-0.4+Fe_3O_4 HIP material. 159
6.11 Approximate chemical composition of particles highlighted in Figure 6.41 measured by EDS. 162
6.12 Grain size as a function of ageing time for Fe-14Cr-3W-0.3Ti+0.25Y_2O_3 FAST material. 164
6.13 Chemical composition of particles highlighted in Figure 6.44 measured by EDS. 165
6.14 Grain size as a function of ageing time for Fe-14Cr-3W-0.3Ti-0.4Y+Fe_3O_4 material. 167
6.15 Chemical composition of particles highlighted in Figure 6.47 measured by EDS. 168

7.1 Tensile properties for all four alloys tested by ETMT. 184
7.2 Strain hardening coefficient n and bulk modulus K estimated from a best fit to the ETMT stress-strain plots. 186
7.3 Strain hardening coefficients n for the four alloys, the corresponding yield strength estimated and measured by ETMT at room temperature. 186
7.4 Solid solution strengthening contributions for the four Fe-14Cr-3W-0.3Ti-based alloys. 187
7.5 Bailey Hirsch contributions for the four Fe-14Cr-3W-0.3Ti-based alloys at room temperature. 188
7.6 Hall-Petch strengthening for the four Fe-14Cr-3W-0.3Ti-based alloys at room temperature. 189
7.7 Orowan strengthening for the four Fe-14Cr-3W-0.3Ti-based alloys at room temperature. 190
7.8 Comparison between output from the summation model for yield stress and experimental values. 191
7.9 Estimated Bailey-Hirsch contributions for the four Fe-14Cr-3W-0.3Ti-based alloys at room temperature, 350°C and 650°C. 193
7.10 Estimated Hall-Petch strengthening for the four Fe-14Cr-3W-0.3Ti-based alloys at room temperature and 350°C. 194
7.11 Orowan strengthening for the four Fe-14Cr-3W-0.3Ti-based alloys at room temperature and 350°C. 194
7.12 Estimated Coble-creep contributions for the four Fe-14Cr-3W-0.3Ti-based alloys at room temperature, 350°C and 650°C. 195
7.13 Estimated Arzt-Rösler-Wilkinson contributions for the samples at each of the testing temperatures. 196
7.14 Estimated stress during the secondary creep regime during SPT creep tests (maximum, mean and standard deviation of applied stress) compared with the yield strength from ETMT (σ_{UAY}) at room temperature. 211
7.15 Average extension before failure for the three alloys. 212

Glossary

Acronym Definition

ADF annular dark field
APT atom probe tomography
AR as-received
BCC body-centred cubic
BF bright field
BSE back scattered electron
CVD chemical vapour deposition
DF dark field
dpa displacements per atom
EBSD electron back scattered diffraction
EDS energy dispersive spectroscopy
EDX energy dispersive X-ray spectroscopy
EELS electron energy loss spectroscopy
EPMA electron probe micro-analysis
ETMT electro-thermal mechanical testing
FAST field assisted sintering technique
FR fast breeder reactor
FCC face-centred cubic
FFT fast Fourier transform
FIB focussed ion beam
F/M ferritic / martensitic
FWHM full-width half maximum
GARS gas atomised reaction synthesis
GenIV generation IV
HAADF high angle annular dark field
HE hot extruded
HIP hot isostatically pressed
HP hot pressed
HSHE high speed hydrostatic extrusion
HT heat treated
IHR initial hardening rate
LWR light water reactor
MA mechanical alloying
MBE molecular beam epitaxy
ODS oxide dispersion strengthened
PM powder metallurgy

PVD physical vapour deposition
SE secondary electron
SEM scanning electron microscope
SFR sodium-cooled FAST reactor
SLM selective laser melting
SPS spark plasma sintering
SPT small punch testing
STARS surface treatment of atomised reaction synthesis
STEM scanning tunelling electron microscopy
TEM transmission electron microscopy
TRL technology readiness level
UTS ultimate tensile strength
XRD X-ray diffraction
YS yield strength

1 Introduction

Contents

1.1 Motivation for the Thesis 1
1.2 Content and Structure of the Thesis 3

1.1 Motivation for the Thesis

With the anticipation of a greater international reliance upon nuclear power, and the associated demand this will put upon uranium availability and the storage of spent fuel, there is a growing drive within the nuclear industry to pursue successful fast reactor development. These reactors permit nuclear fuel to be bred from almost all the actinides, including depleted uranium or thorium (waste from current light water reactors), and produce spent fuel with significantly reduced radioactivity lifetimes.

To allow use of the fast neutrons (integral to the reactor design), most designs utilise a different coolant, so as to prevent slowing of the neutrons and allowing operation at higher temperatures than pressurised water (a strong neutron moderator) would allow. The most prominant design uses sodium as the coolant due to its low neutron moderation and high heat capacity. Due to the change in coolant

and neutron spectrum, a new fuel cladding material and alternatives to Zr based alloys are required for this reactor design.

Stainless steels have been identified as potential candidates for the role of cladding material that contains the fuel pellets, but conventional austenitic stainless steels suffer from embrittlement and dimensional swelling after prolonged irradiation and ferritic/martensitic (F/M) steels have relatively low strength at higher temperature. This has led to consideration of oxide dispersion strengthened (ODS) F/M steels for which the dispersion can improve both high temperature strength and irradiation resistance.

The current 'state-of-the-art' ODS steel is powder processed through a time-consuming milling stage, followed by canning and direct extrusion. The literature review included in this thesis summarises the large quantity of published information on the mechanical properties and irradiation resistance of powder processed ODS alloys. However, the processing route is expensive, manually intensive, and time-consuming, ultimately reducing the likelihood that ODS steels will be utilised as a cladding material. In terms of processing, there is a much more limited literature in alternative, novel ODS processing methods that might advance industrial uptake, and this is the principal focus of the current work. Justification of a new processing method may derive from reduced processing time whilst maintaining useful thermal stability of the microstructure at reactor relevant temperatures. Principally this stability derives from a high number density of nano-scale oxide based particles or clusters. Mechanical properties are assessed with respect to any trade-off between process scale / convenience / cost and properties.

The objectives of the work in this thesis are:

1. To assess the thermal stability at reactor relevant temperatures of a current 'state-of-the-art' ODS steel developed as part of the Euratom Framework 7 project MatISSE, to act as a baseline for comparisons with similar materials produced by alternative novel processing methods.

2. To investigate possible reductions in powder production time that can be achieved using tailored parameters through a comparison of powder microstructures.

3. To investigate the effect of novel sintering techniques on the consolidation of these powders and the resulting microstructure and mechanical properties.

4. To assess the success of novel processing methods on creating stable microstructures and useful mechanical properties, as preliminary indication of in-reactor performance, and thus the potential for any further development.

1.2 Content and Structure of the Thesis

A more thorough description of the motivation behind this work is given in Chapter 2. Experiments investigating novel processing methods for ODS steel production are outlined in Chapter 3. An assessment of the thermal stability of a current 'state-of-the-art' ODS steel at reactor relevant temperatures is presented in Chapter 4, acting as a baseline for comparison with material produced later. An exploration of powder production and how novel methods might lead to a reduction in production time is described in Chapter 5. The consolidation of resulting powders through both conventional and more novel sintering routes is presented in Chapter 6, along with their microstructural characterisation. Chapter 7 reports the mechanical properties of consolidated materials, both at room temperature and at reactor relevant temperatures. Throughout Chapter 6 and Chapter 7 thermal stability is investigated using the stability of the microstructure and high temperature mechanical properties respectively, comparing with that of the 'state-of-the-art' material. Finally, the results are summarised in Chapter 8, where suggestions for further work are also given.

All alloy compositions are presented in the form E_1-nE_2-mE_3 where E represents any element and n and m are the weight percentage (wt%) of the element unless otherwise stated.

2
Literature Review

Contents

2.1 Introduction **5**
2.2 Nuclear Fission Energy **5**
2.3 ODS Steels **12**
2.4 Fabrication of ODS Steels **23**
2.5 ODS Steel Microstructure **44**
2.6 Mechanical Properties **46**
2.7 Literature Review Summary **57**

2.1 Introduction

This review outlines the plans for advanced fission reactors, with a particular focus on operating requirements and materials currently being investigated for these applications. The development of ODS steels constitutes the bulk of the review, with an emphasis on their processing and their possible application as fuel rod cladding material.

2.2 Nuclear Fission Energy

Nuclear fission reactors currently provide ∼11% of the world's total electricity generation [1], but with an increasing population, and a rapidly increasing global

demand for energy and electricity, it is predicted that nuclear generation may be increased by over 50% by 2030 to meet new demands [1]. This expansion of nuclear is key, as unlike most renewable sources, it can produce a baseline power load regardless of weather conditions, and without high carbon and greenhouse gas emissions.

The increase in nuclear power generation capacity will only be maintained with advanced reactor technology. Figure 2.1 shows the predicted uranium resource utilisation based on the current 'Generation II/III' light water reactor (LWR) technology, and the uptake of 'Generation IV' fast breeder reactor (FR) technologies, as calculated by the Generation IV International Forum (GIF). By 2050, the limiting factor facing the nuclear industry using the current 'once-through cycle' will be the availability of uranium resources, unless breakthroughs occur in mining or extraction technologies [2]. This, combined with limited available geological repository space for the waste created, means once-through cycles are unsustainable.

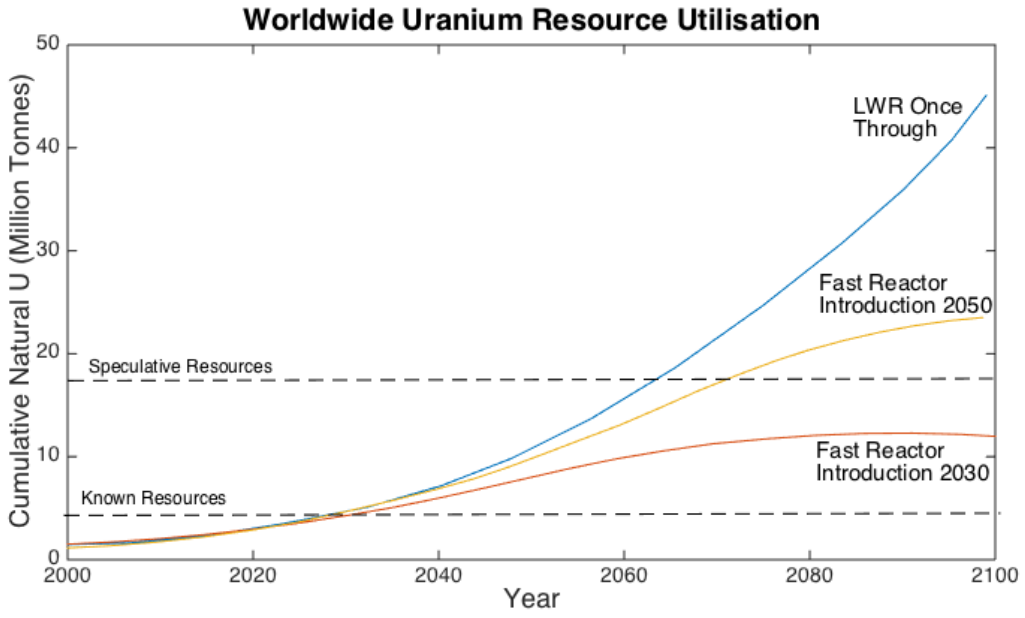


Figure 2.1: Worldwide uranium resource predictions based on the uptake of fast reactor technologies (redrawn from [2]).

In comparison with LWRs, fast reactors allow much more effective burning of recycled spent fuel, producing more power from the available resources and reducing the need for uranium mining and enrichment. If deployed by 2030, Figure 2.1 shows

uranium usage to stay within predicted resources. Fast reactors utilise the fast neutron spectrum (∼1 MeV) as opposed to the lower energy thermal spectrum (10-11 keV), the latter resulting from neutrons being slowed by a moderating substance e.g. water or graphite. At high fluence, a fast spectrum, combined with a high irradiation temperature, puts much higher demands on materials in the reactor environment than is the case for previous generation reactor types. This creates the need for reactor and fuel materials that have excellent resistance to irradiation-induced swelling and damage, as well as minimal deterioration in mechanical properties in a fast neutron, hot environment. A number of potential designs have been proposed, but one of the most promising advanced reactor types, which will be explored further, is the sodium-cooled fast reactor (SFR).

2.2.1 Sodium-cooled Fast Reactors

As a design, the SFR is the only fast reactor type with a sufficient knowledge base and industrial experience to be deployed in the short term [3]. Approximately 20 prototype reactors have been built worldwide, with 100 reactor-years of operating experience at commercial power generation levels.

Figure 2.2 shows a schematic of the primary system of an SFR, which is usually arranged in a pool layout. In comparison to currently operating LWRs, SFRs use liquid sodium as a coolant, rather than water, leading to different corrosion challenges. The liquid metal coolant gives superior cooling efficiency without moderating neutrons, keeping them in a higher energy state [4].

2.2.1.1 SFR Cladding Tube Requirements

In addition to high temperatures (300-700°C), intense irradiation damage, and sometimes high and varying stresses, the components of the sub-assembly will experience corrosive attack from contact with the liquid metal coolant and the fuel.

One of primary limitations of a fuel rod is the radiation-induced swelling and growth that eventually impedes coolant flow around the fuel elements, which could lead to the failure of the fuel containment (the cladding), and consequent

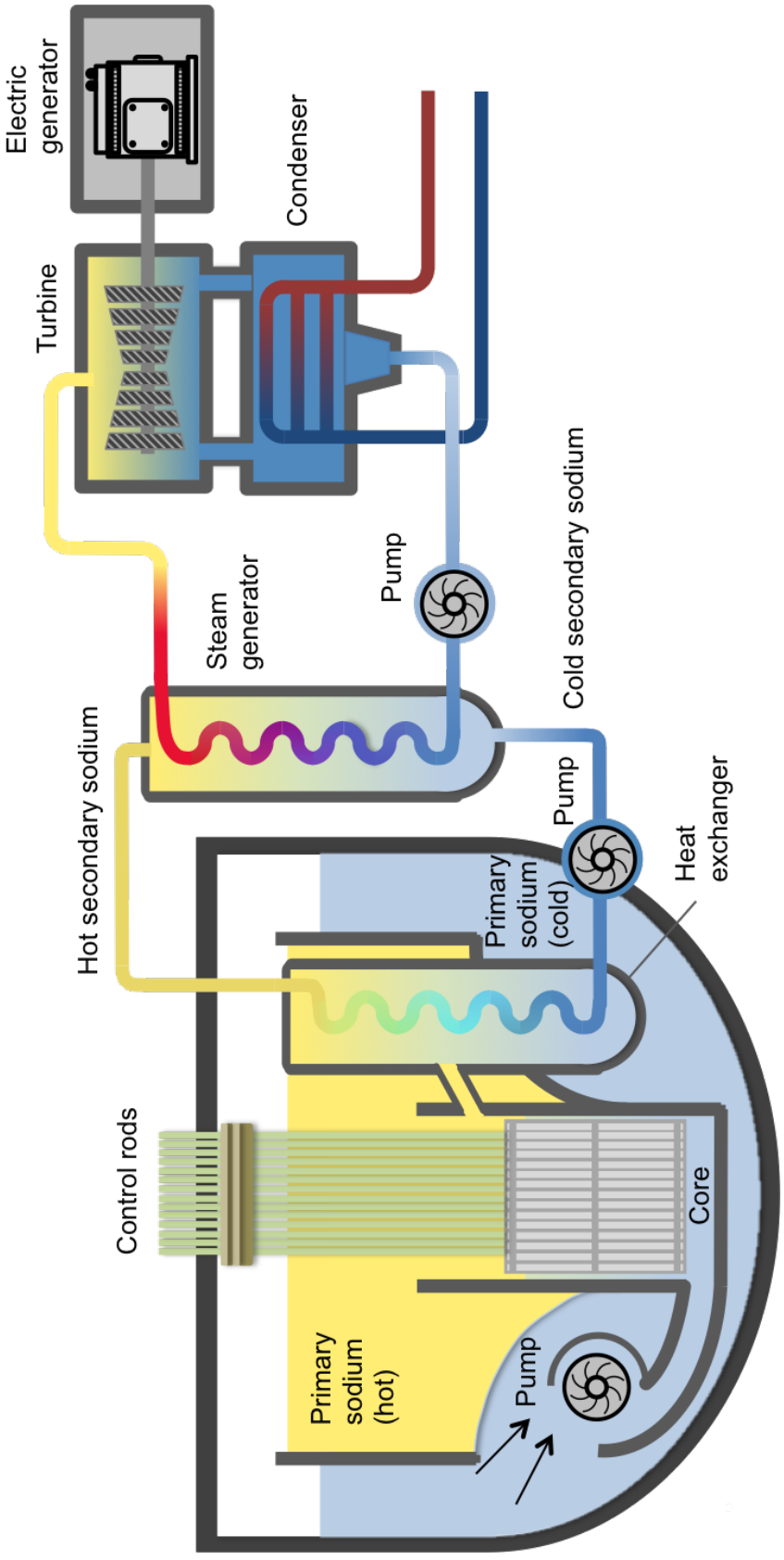


Figure 2.2: Schematic representation of a SFR (redrawn from [2].)

release of actinides and/or fission products from the fuel into the coolant [4]. Such failure could also arise from coolant (or fuel) induced corrosion (hence the need for high compatibility of the cladding material with the sodium coolant) and/or from the high operating temperature (hence a material stable both structurally and mechanically at these temperatures is needed). In order to reduce parasitic neutron absorption, the tubes must be very thin (∼0.5 mm), making the risk of deformation and corrosion-induced failure even higher.

Property requirements for candidate SFR fuel cladding materials therefore include:

- High temperature stability
  - low coefficient of expansion
  - good high temperature strength
  - high creep resistance
- Mechanical properties
  - high strength
  - ductility
  - stiffness
  - toughness under start-up, elevated temperatures and accident conditions
- Irradiation resistance
  - creep
  - swelling
  - embrittlement
  - resistance to neutron-induced residual radioactivity (activation)
  - resistance to mechanical property degradation
- Chemical resistance to fuel and coolant

- Manufacturing considerations
  - material availability and cost
  - joinability
  - formability

2.2.1.2 Candidate Materials for SFR Cladding

A number of potential cladding materials are shown in Figure 2.3, with their approximate maximum operating temperature shown as a function of their technology readiness level (TRL) [5].

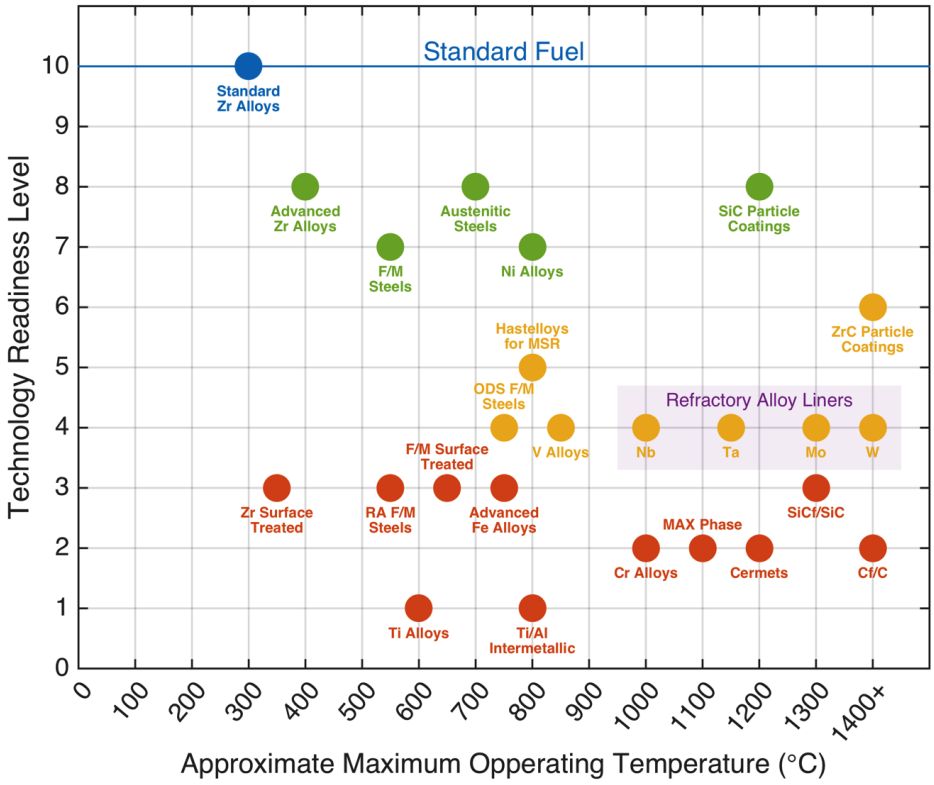


Figure 2.3: Cladding candidate materials showing their maximum operating temperature and technology readiness level with 3 being proof of concept, 7 successful prototype, 8 commission, 9 successful operation and 10 long term operation [5].

Initially, austenitic steels were utilised in SFRs, but limitations due to swelling and potential embrittlement led to the development of ferritic / martensitic (F/M) steels as an alternative [6]. The body centred cubic (BCC) crystal structure of

F/M steels exhibited better swelling resistance than the face centred cubic (FCC) of austenitic steels due to the longer incubation periods prior to the onset of steady-state swelling [7], but operating temperatures were limited to 550-650°C, due to insufficient tensile and creep strength at elevated temperatures [8]. To enable an increased operation temperature range, second phase precipitates were introduced to harden the alloy, and stabilise grain structures at high temperatures [9].

Significant research effort has been devoted to combining the desirable properties of F/M steels with the introduction of inert, fine-scale second phase particles, creating ODS steels. Figure 2.3 shows this introduction can increase operating temperatures by ∼200°C but are at a lower developmental stage. ODS steels have been trialled in reactors for the first time in a Japanese SFR design [10], which is expected to reach commercialisation by around 2050 [11].

The main competitor material for use in SFRs is 15:15Ti austenitic steel, the clad used in Super-Phenix, the SFR in France (decomissioned in 1997 following 10 years of grid operation). This will be the main comparison for an alternative material in terms of mechanical properties required for operation within an SFR.

2.3 ODS Steels

As high displacement damage is expected in SFRs (due to the high energy of incident neutrons) any cladding material must be damage resistant. Radiation damage resistant materials must be developed to encourage recovery of defects and prevent He from forming large bubbles. The effects of irradiation damage upon materials are well documented [12] and so will not be covered in the current work. A focus will instead be placed upon how ODS materials can resist such irradiation damage.

Two important features of ODS steel alloys are: (a) high density of stable dislocation pinning points and especially large numbers of stable, nanometre-scale precipitates that trap He in preference to grain boundaries in fine-scale bubbles to avoid swelling and (b) sufficient creep strength, permitting operation at elevated temperatures [12]. These phenomena can be seen schematically in Figure 2.4.

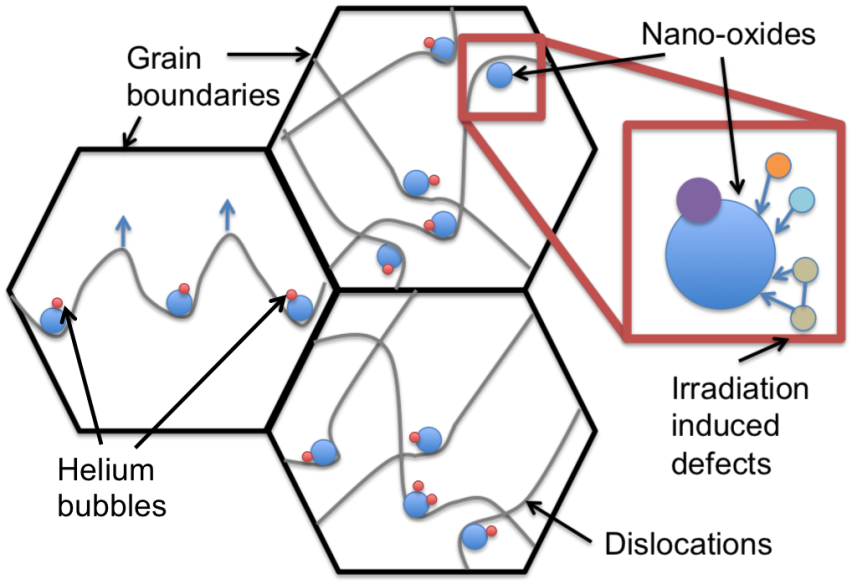


Figure 2.4: Schematic of the ODS strengthening mechanisms showing a high density of nanooxides pinning He in fine bubbles and providing a high density of sink points for irradiation-induced defects (redrawn from [12]).

Swelling and irradiation creep resistance has been seen in numerous studies of ODS steels [13, 14], as has the formation of embrittling α' and χ precipitates [15, 16]. Cavity formation around oxide particles, indicative of these sites acting as point defect sinks and nucleation sites for defect clusters is also commonly seen [17, 16, 18].

He trapping at particle interfaces also prevents large bubble formation and swelling. This has been shown from first principles in [19] and experimentally in [20].

Many studies have necessarily used a range of very high magnification imaging techniques, such as atom probe tomography and TEM, to show Y-O and Y-Ti-O nanoclusters to be comparatively and encouragingly stable under both neutron and ion irradiation [17, 21, 22, 23, 24] at irradiation temperatures between 300-700°C and doses ∼15 to 150 dpa.

The most evident conclusion from literature is that a homogeneous dispersion of oxides is required at all scales, with no oxide-free zones, in order to facilitate good irradiation stability [15]. However, a definition of 'homogeneous' or 'uniform' in relation to nano-oxide dispersion has not been suggested or quantified.

2.3.1 Strengthening Mechanisms

A number of strengthening mechanisms contribute to the yield strength of ODS steel and it has become relatively common in the field (e.g. [25]) to express strengthening effects as a simple sum:

$$\sigma_y = \sigma_{SS} + \sigma_{BH} + \sigma_0 + \sigma_D + \sigma_K \tag{2.1}$$

where σ_y is yield strength, σ_{SS} is solid solution strengthening, σ_{BH} is Bailey-Hirsch strengthening due to dislocations (work hardening), σ_{HP} is Hall-Petch strengthening from grain size contributions and is made up of σ_0 from lattice friction and σ_D from grain strengthening and σ_K is Orowan strengthening from particles blocking dislocation paths.

Some of the strengthening mechanisms can be utilised at high temperature only with care due to the possible onset of recovery (the rearrangement of dislocations into a low energy state forming cell walls or subgrains to separate regions of small changes in orientation with low angle boundaries) and acceleration of diffusion based mechanisms for microstructural change such as grain growth. As shown in Table 2.1, at reactor operating temperatures of 0.5-0.7 T_m [26], only precipitation

strengthening and dispersion strengthening are considered sufficiently effective and stable contributions to yield strength.

Work hardening effects and dislocation tangling anneal out, grain boundaries enable fast paths for diffusion and thermal creep, and dislocations have the ability to overcome obstacles due to their thermal energy [26]. Two more terms are used in the summation equation to describe the breakdown of strengthening behaviour at high temperature, σ_{ARW}, Arzt-Rösler-Wilkinson stress from interfacial pinning and dislocation climb at elevated temperatures and σ_{CC} is the resistance to Coble creep[27]. It has been shown that σ_D undergoes a progressive breakdown in the temperature range 500-600°C, and is replaced by σ_{CC} as grain boundaries provide fast paths for diffusion, and the Orowan stress (σ_K) loses its efficiency above 500°C and is substituted by σ_{ARW} when dislocations are able to overcome obstacles.

The effectiveness of each strengthening mechanism over prolonged thermal exposure can be related to the absolute melting point T_m of the material.

Strengthening Mechanism	Effective Temperature	Details
Work Hardening	$\sim 0.3T_m$	Dislocation/Dislocation Interaction
Grain Size Refinement	$\sim 0.3T_m$	Grain Boundary Area/Dislocation Interaction
Solid Solution Strengthening	$\sim 0.4T_m$	Lattice Strain Fields: Modulus Change, Dislocation Interaction
Precipitation Strengthening	$\sim 0.6T_m$	Metastable 2^{nd} Phase Particles, Impede Dislocation Motion
Dispersion Strengthening	$\sim 0.9T_m$	Insoluble 2^{nd} Phase, Stabilise Grains, Subgrains and Prevent Creep

Table 2.1: Summary of strengthening mechanisms [26].

Precipitation strengthening, usually a thermomechanical approach, involves trapping of relatively high concentrations of alloying elements at low temperatures, via fast cooling or quenching to create a metastable supersaturated solid solution. On

heating to an intermediate temperature, solute atoms are precipitated from solution and interact with solvent atoms or other solute atoms to form distinct, second phases in the form of disperse precipitates. Depending on their size, strength and coherency, the precipitates can impede dislocation motion, and enhance yield strength. However, if a temperature is too high, the particles become soluble and strengthening lost. Therefore for very high temperature, long term applications, *insoluble* second phase particles are required. While stability is improved, precipitation processing is no longer possible for the same reason. Oxides usually possess excellent thermal stability, and if small enough the nano-oxides in ODS steels can act as dislocation pinning points as well as point defect sinks, up to 1300°C [28].

The strengthening contributions will be revisited in Section 7.1, where this approach is used to estimate different contributions for the ODS materials used within this work.

2.3.2 Boundaries, Zener Pinning and Abnormal Grain Growth

Boundaries in materials, denoting a change in crystallographic orientation, have high energy costs associated with them. Because of this, there is a driving force to reduce the interfacial lengths, or eliminate grain boundaries by grain coarsening. Generally, this only occurs at elevated temperatures where thermally activated diffusion processes allow migration of the grain boundaries.

This process often occurs alongside others, such as recovery and recrystallisation. Recovery is the rearrangement of dislocations into lower energy configurations, often forming cell walls or subgrains, forming low angle boundaries. Recrystallisation is the nucleation and growth of new perfect crystals within existing grains forming clean grains free of work. In a highly worked, nano-grained material such as ODS steels, these processes are common to relieve stored work, but due to the presence of pinning particles, a further mechanism is also seen.

Zener pinning is the pinning of grain boundaries by an array of insoluble, incoherent particles [29], such as those within ODS steels. The drag on the boundary is caused by a reduction of grain boundary area upon intersection of the particle,

meaning breaking away from the particle requires creation of a new surface costing further energy. If particles are fully coherent with the matrix then the boundary can wet the particle surface completely, causing particles to lose their coherency,and the boundary to continue moving [30]. A degree of coherency, however, will cause an increased Zener pinning force [31]. A cubic particle is nearly twice as efficient at pinning than a spherical particle of the same volume, and pinning strength is heavily dependent upon the orientation of the cube relative to the boundary [30]. Zener pinning occurs on all boundaries that interact with particles, and affects both recovery and recrytallisation.

As a grain boundary breaks away from the Zener pinning, for any of the above reasons, the Gibbs-Thompson curvature effect means that the smaller nearby grains appear relatively soluble due to their higher curvature and are consumed by the larger, comparatively stable grain which grows rapidly absorbing neighbouring grains. This process of abnormal grain growth leads to the bimodal grain size distribution seen commonly in ODS steels [32, 33, 34, 35, 36, 37]. A comparative sketch of the distributions seen following normal and abnormal grain growth can be seen in Figure 2.5 and illustrative SEM micrographs seen in Figure 2.6.

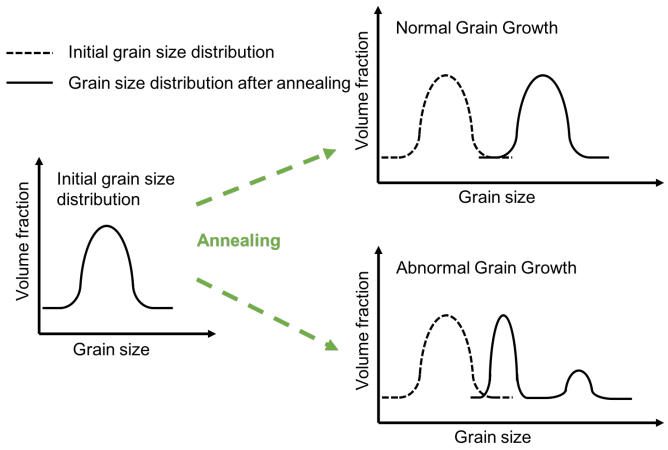


Figure 2.5: Comparative sketch of a normal and an abnormal grain growth distribution after annealing [30].

Abnormal grain growth and Zener pinning are both well documented for fine scale Y_2O_3 dispersions in steels[12], and are not usually of particular concern as it is the

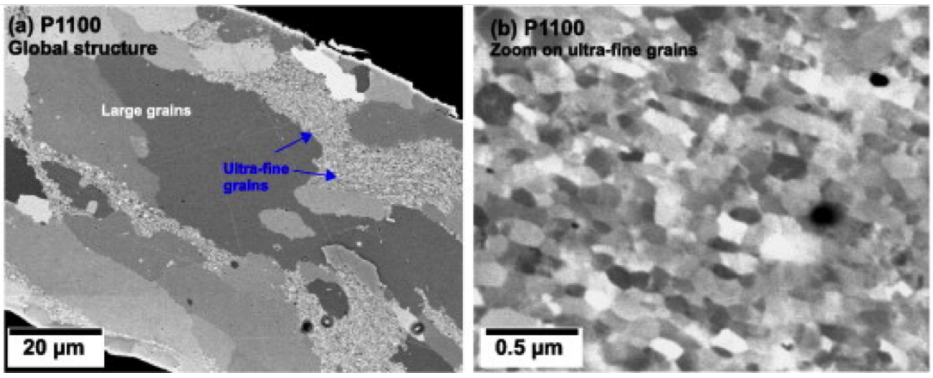


Figure 2.6: FEG SEM micrographs of Fe-14Cr-1W-0.3Ti-0.3T_2O_3 powder after in-situ annealing at 1100°C showing abnormal grain growth [30].

'natural' condition of all heavily pinned and heat treated microstructures. However in the case of thin walled cladding applications, a small number of abnormally coarsened grains could span the millimetre scale wall thickness, decreasing transverse strength in unpredictable ways. Thus, being able to predict abnormal grain growth is imperative for tube cladding applications. It is likely that a homogeneous dispersion of nano-oxides is important that, in turn, can only be developed from an acceptably uniform dispersion of dissolved Y.

2.3.3 Typical Microstructure

Figure 2.7 shows the typical microstructure of ferritic ODS steels, containing a mixture of large (3-10μm) and submicron or nano-sized (<400nm) ferrite grains.

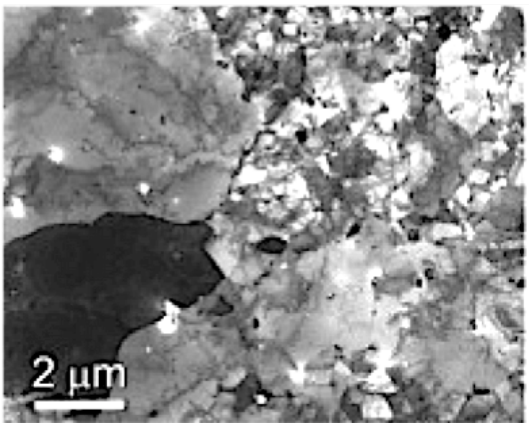


Figure 2.7: Bright field (BF) transmission electron microscope (TEM) images of bimodal microstructure seen in Fe-14Cr ODS alloys [38].

Figure 2.8 shows the four types of precipitates suggested to be seen in ODS steels [17]:

• Large precipitates with average diameter of 200 nm and relatively low number density of $2\times10^{19}/m^3$, often Cr carbides (Figure 2.8(a) (i)) or Cr oxides (Figure 2.8(a) (ii))

• Globular Ti-rich precipitates of average diameter 50 nm (Figure 2.8(b) (i))

• Y-rich particles around 20 nm in diameter with intermediate number density $4\times10^{20}m^{-3}$ (Figure 2.8(b) (ii))

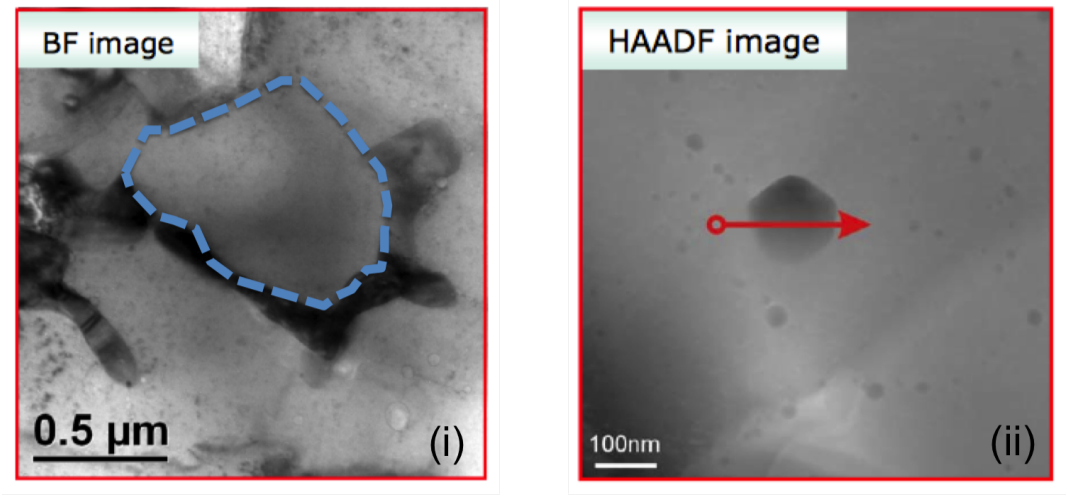
• Small faceted precipitates uniformly dispersed with relatively high number density ($5\times10^{23}m^{-3}$) and small size (1.4 nm)

2.3.4 Alloying Additions

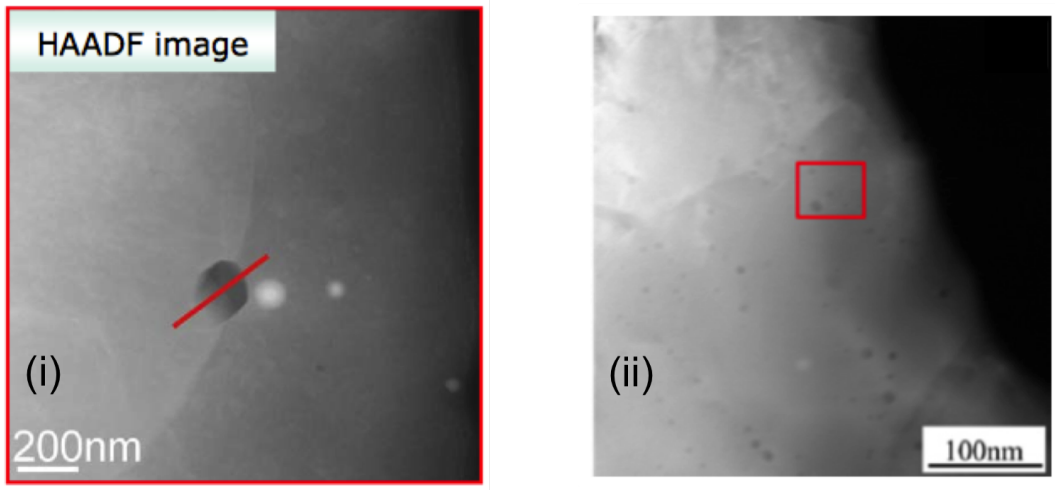
To generate a microstructure of fine scale ferritic grains, carbides and insoluble oxides, ODS steels contain three main components: the ferritic steel base (for swelling resistance), solid solution strengthening elements (for strengthening the matrix and giving low temperature strength) and complex oxide formers (for stability, creep resistance and high temperature strength). A brief description of, and justification for, the alloying elements typically added is given below, but has been widely covered elsewhere (e.g. [12] and [39]) and will not be covered in detail here.

2.3.4.1 Solid Solution Strengthening

The widely studied Fe-Cr-W matrix composition gives a fully ferritic (BCC) microstructure, with Cr concentrations controlling the phase fractions (100% ferrite) [7]. The most promising alloy has been suggested to contain approximately 14 wt% Cr, to give sufficient oxidation resistance at the high operating temperatures, remain ferrite without reversion to austenite, high strength and sufficient corrosion resistance. W contributes to solution hardening of the matrix [7, 40], with 2-3 wt% additions increasing high temperature tensile strength, but further concentrations risking the formation of Laves phases which can cause embrittlement.



(a) (i) Cr carbides (ii) Cr oxides



(b) (i) Ti oxides (ii) Y-Ti oxides

Figure 2.8: TEM micrographs of (a) (i) bright field (BF) image of Cr-rich particle (ii) high angle annular dark field (HAADF) image of Ti-rich precipitate (b) (i) HAADF of Y-rich particles (ii) HAADF of nm scale particles [8].

2.3.4.2 Oxides

Many oxides have been considered for ODS steel such as Al_2O_3, ThO_2, ZrO_2 and La_2O_3, but Y_2O_3 is the most widely adopted due to its superior dimensional, structural and thermodynamic stability even up to 1300°C [41, 42] based on its high affinity for oxygen (Gibbs free energy of oxidation) [43].

The Gibbs formation energy indicates the oxide stability shown in Figure 2.9. Y oxides are amongst the most stable (highest negative free energy change on

formation), inhibiting dissociation at elevated temperatures, even in contact with most other elements.

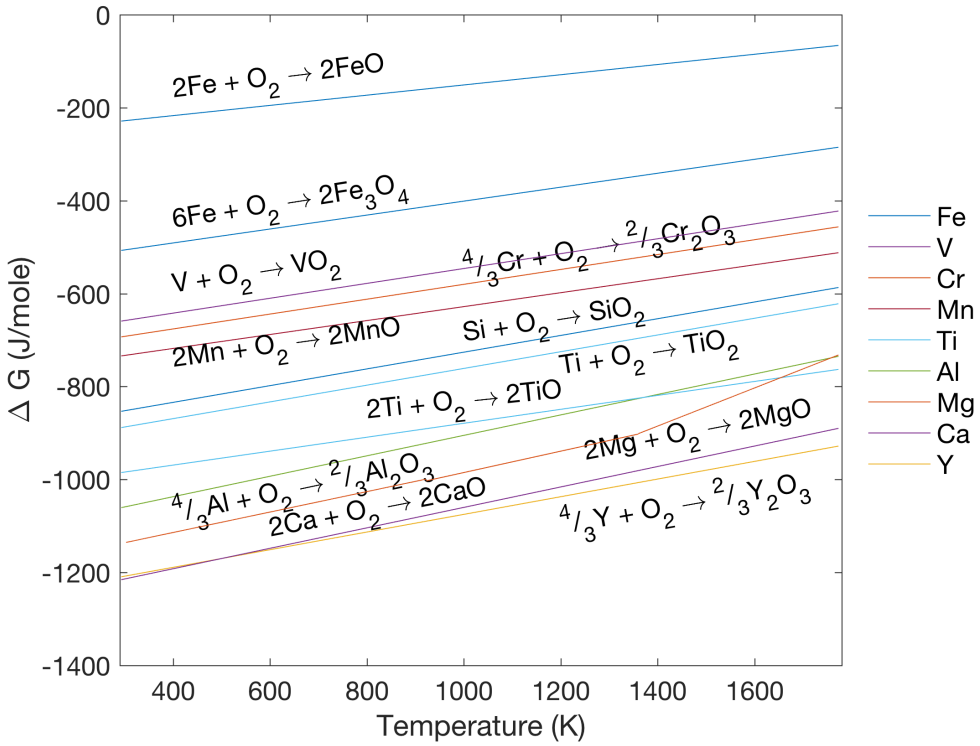


Figure 2.9: Ellingham diagram showing the free energy of formation of 1 mole of oxide (reproduced from [44]).

Several elements (such as Ti, Nb, V and Cr) have been investigated for their ability to impart improved refinement and stability of nano-oxides, with both Ti and Nb additions leading to finer, more complex oxides [7, 28, 40, 42, 45, 46], with Ti most effective in creating a higher number density of smaller particles [47]. Nb led to increased strength but reduced ductility [40], and Zr was effective for creep resistance but not strength [8]. The relative effects of Ti, Nb and Al additions can be seen in Figure 2.10 with Ti leading to the smallest and most evenly distributed particles.

Rogozhkin *et al.* [28] investigated the effects of Ti in Fe-13.5Cr-2W-0.3Y_2O_3 and showed that 0.3 wt% Ti was optimal in achieving the maximum density and minimum size of oxides in Figure 2.11(a). Figure 2.11(b) shows the potency of Ti in promoting fine ferritic grains in an ODS steel. Despite additions >0.3 wt%Ti

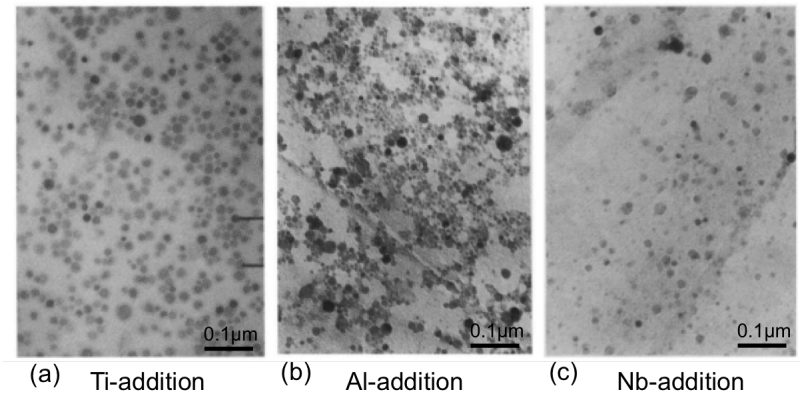
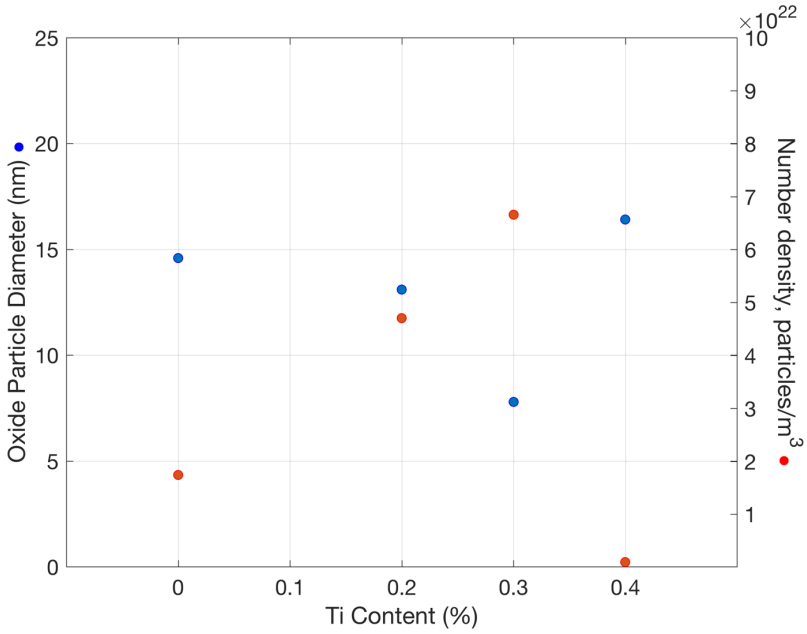


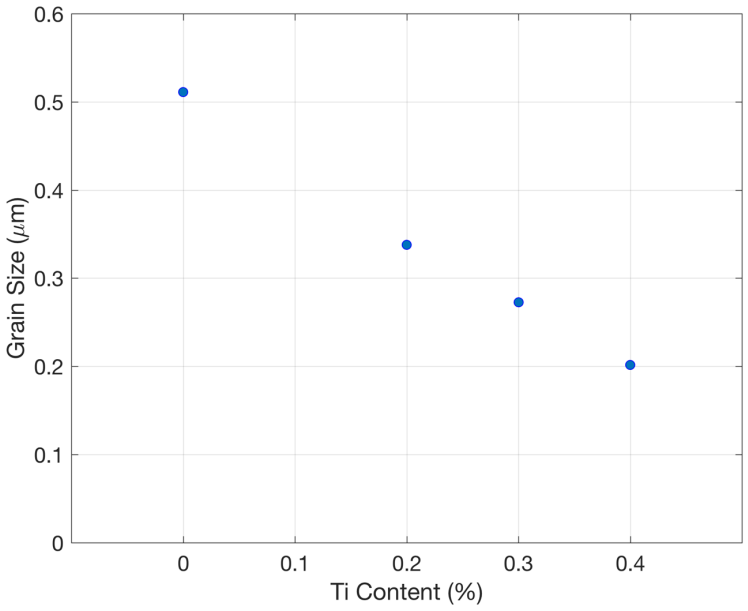
Figure 2.10: Comparison between the size and composition of Y_2O_3 oxides with (a) Ti additions (b) Al additions (c) Nb additions in Fe-13Cr-3W-0.46Y_2O_3 [40].

leading to a further reduction in grain size, oxide particles become larger and of lower number density [48]. Additions of 0.3wt% were therefore chosen for this work.

Based on these findings and to provide comparatively with prior work, the initial composition chosen for this work was Fe-14Cr-3W-0.3Ti-0.25Y_2O_3 (wt%). Note that C is rarely an alloying addition due to its undesirable austenite-stabilising effect; thus ODS steel is something of a misnomer and this material is more correctly referred to as an ODS Fe alloy.



(a) Dependence of the average particle size and density on the titanium content (redrawn from [28])



(b) Dependence of the average size of grains on the titanium content (redrawn from [28])

Figure 2.11: Dependence of the oxide particle size, density and material grain size on the Ti alloy concentration in Fe-14Cr-2W-0.3Y_2O_3 (redrawn from [28]).

2.4 Fabrication of ODS Steels

The most challenging issues that must be addressed within the ODS steel community for nuclear applications are the fabrication of fuel cladding tubes at a scale for engineering deployment, quality (microstructural) assurance and the joining of cladding to end plugs [49].

ODS steels are inherently difficult to process because precipitation from a supersaturated solution quenched from elevated temperatures is not feasible. Melt processing, in which the oxides are simply stirred in as a fine powder, is difficult to apply as the oxides do not wet molten steel, and it is practically impossible to work with powders at the nano-scale in the foundry environment. The oxides, which must be insoluble in liquid Fe alloy ($T_m^{Fe} = 1538°C$, $T_m^{Yttria} = 2400°C$) have very different densities to the melt ($\rho^{Fe} = 7.87 g/cm^3$, $\rho^{Yttria} = 5 g/cm^3$) and so even where wetting can be overcome, buoyancy and flotation is a significant problem [26].

Excess O (i.e. O not intentionally present in the nano-oxides) often incorporated into the steel from reactions with other alloying elements, or from ingress during the various stages of production and transfer, may have a detrimental effect on the oxides intentionally within the alloys. Excess O dramatically reduces the distribution density and uniformity of oxide particles, degrading high temperature strength [50, 51]. Excess oxygen may also combine with elements such as Ti to form relatively coarse (>50 nm) TiO_2 particles that are considered less effective in dispersion strengthening. Tight control over excess O during processing is therefore critical.

The most widely explored conventional method for the production of ODS steels relies on non-equilibrium processing using mechanical alloying (MA) to disperse / dissolve added oxide powder, followed by sintering. Although widely practised in R&D and semi-commercial production, the extended processing time, small batch size, high cost of powders and tendency for contamination all hinder process uptake at an industrial scale.

Bergner *et al.* [52] reviewed the latest fabrication routes employed for production of ODS steels and alongside the conventional method, novel methods were categorised into four groups:

- Modifications to a standard powder metallurgy (PM) route: gas atomisation reaction synthesis (GARS) and surface treatment of gas atomised reaction synthesis (STARS)
- Physicochemical routes: chemical vapour deposition (CVD), physical vapour deposition (PVD), molecular beam epitaxy (MBE)
- Hybrid routes: selective laser melting (SLM), melt spinning, spray forming
- Liquid metal routes

These are described in more detail later. There are several other lesser techniques, some under equilibrium and some in non-equilibrium conditions, described by Alinger [26].

The main problems preventing uptake of ODS steels are the anisotropy associated with the processing methods, batch-to-batch variations, the limitations of scale-up and, above all, cost [4, 47]. These factors were used to assess the feasibility of the main methods and compared to more conventional means.

2.4.1 Mechanical Alloying of Powder

MA is a solid state powder processing technique that involves repeated welding, fracturing and re-welding of powder particles in a high energy ball mill [53]. MA is commonly used for the production of a fine dispersion of second phase particles, as well as extending solid solubility, and thus the creation of metastable solutions. Many MA powders and materials have crystal sizes <100 nm [53].

The milling container and mill ball material, milling speed, time, ball-to-powder weight ratio and milling atmosphere and temperature must all be optimised for the desired phase or microstructure [53].

Milling time has been investigated intensively [26, 39, 54, 55, 56] and is usually optimised to be the shortest time required to achieve a steady state defined as the point when the rate of fracture and cold welding of the powder particles is equal. This point may also signify when no further microstructural change is taking place

i.e. dislocation density is at a maximum and crystallite size is at a minimum. In general, the higher the energy of the mill, the less time is required to reach this steady state [39]: longer times increase the risk of unnecessary contamination e.g. by O, and the formation of undesirable phases. Industrially, shorter milling times are economically and environmentally desirable.

Initially during milling, the particle size increases, with particles being pressed and cold welded together to form bigger flakes, but as work hardening increases, fracture begins to dominate and particle size decreases [54]. MA powders have been investigated by laser diffraction [39, 55], scanning electron microscopy (SEM) [39, 55, 57] and transmission electron microscopy (TEM) [54, 57] to analyse the change in size and shape of the powders; X-ray diffraction (XRD) is also used widely to analyse the crystallite size and lattice strain [58, 55, 59, 60, 61] along with indentation for microhardness [39, 53, 62].

A summary of final powder properties from a number of studies is given in Table 2.2, showing large variations within the supposedly optimised properties, for powders as close in chemistry to Fe-14Cr-3W-0.3Ti-0.25Y_2O_3 as possible.

Property								
d(50) μm	80	[39]	60	[54]	35	[25]	10	[63]
Hardness (GPa)	10	[39]	5	[25]	7	[64]		
Crystallite Size (nm)	32	[63]	20	[64]				
Lattice Strain (%)	0.7	[63]	0.89	[64]				

Table 2.2: Reference values for common powder properties for Fe-14Cr ODS steels.

Some uncertainty remains as to exactly what happens to Y_2O_3 during mechanical alloying, with contrasting opinions. Several sources show diffraction peaks for both α-ferrite Fe and Y_2O_3 to decrease in intensity and broaden with milling time, and after sufficient milling time, the Y_2O_3 peak can no longer be detected [41, 42, 58, 65]. Some sources suggest that the Y_2O_3 decomposes (dissociates) into yttrium and oxygen atoms that then dissolve into the matrix [12, 42, 48, 66, 67]. This is supported by atom probe tomography (APT) [68] and TEM studies [38] that were unable to resolve any remnants of distinct Y_2O_3 in powder particles ball milled for

40h, and showing a significantly higher O concentration in the matrix than before Y_2O_3 was added. The presence of other elements, such as Ti, within the oxides, i.e. Y-Ti-O complex oxides, is at least consistent with the concept that Y and O dissociate, dissolve and then re-precipitate [67, 69, 70].

However, other sources report no peak shift (lattice strain) or broadening of α-Fe peaks according to XRD and neutron diffraction; instead Y_2O_3 disappearance was suggested to be due to progressive amorphisation due to damage and the high defect density induced by milling [41, 58, 59, 71].

It is possible that both processes may occur. While at equilibrium the solubility of Y in Fe is very small, this solubility may be enhanced in Fe with enormous lattice strain associated shift in the free energy—composition curves. Similarly, the stability of Y_2O_3 itself may be undermined once intimately mixed into the Fe lattice with its high concentration of defects. The detection of such small amounts of Y within the matrix by techniques such as XRD is also difficult, contributing to the ongoing uncertainty [12]. The highly defective, metastable solution created by mechanical alloying may also mask any shifts in XRD peak positions [39].

Some sources also maintain Y-O association, simply on an unresolvable scale [72].

Regardless of the method of Y_2O_3 refinement, a uniform (however defined) distribution of Y following milling is of paramount importance for subsequent uniformity in precipitation response.

2.4.2 Consolidation Methods

Once a fine powder with an acceptable dispersion of Y/Y_2O_3 has been achieved, it is consolidated to form a dense solid product. Powder particles bond together when heated during sintering, a process that can involve atomic diffusion, creep, viscous flow, plastic flow and/or evaporation depending upon conditions [73].

Pressureless sintering gives insufficient densification and *pressure-assisted sintering* is required to increase powder contact points and decrease porosity. Hot isostatic pressing (HIP) or direct extrusion are commonly used for ODS alloys and are described in detail along with the newer field assisted sintering technique (FAST).

2.4.2.1 Hot Isostatic Pressing

The addition of pressure enhances the densification rate during sintering and is utilised in techniques such as hot uniaxial pressing (HP), or hot isostatic pressing (HIP), which have been widely used in the consolidation of ODS steels [15, 67, 70, 74]. Figure 2.12 shows a schematic of the setup, where MA powders, contained within evacuated mild steel cans, are subject to high temperatures and pressures (either uniaxially in HP or isostatically) to drive densification.

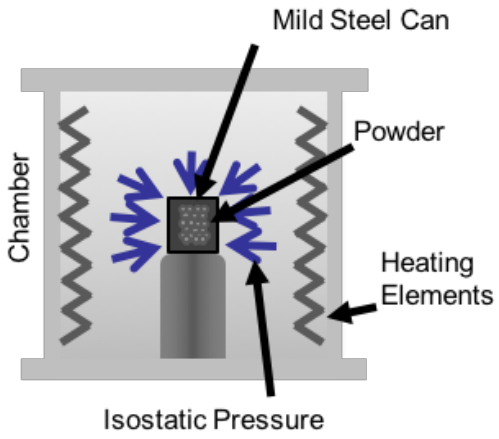


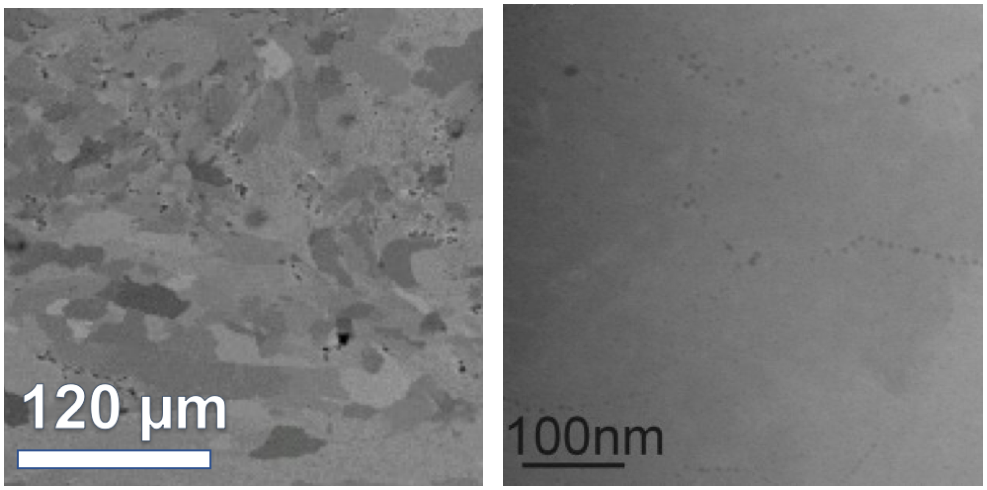
Figure 2.12: Schematic representation of a HIP.

Compared to HIP, HP often gives a lower overall density and thus poorer mechanical properties, and is not examined in this work [39].

Figure 2.13(a) shows the typical microstructure of ODS steel produced using HIPing at a temperature of 1150°C where abnormal grain growth had occurred, as described previously, giving the bimodal grain structure. Figure 2.13(b) shows a high density of fine Y-Ti-O nanoclusters (4 nm average size [75]).

Atom probe analysis [45, 77] showed 3-5 nm particles, enriched in Y, Ti and O. The high Ti concentration indicated that the particles were distinctly different to the initial Y_2O_3 particles, suggesting that the particles were not simply fragments of the initial Y_2O_3 powder. This addition of solutes to the oxide particles was also seen by Klueh *et al.* [47] in a Ti-containing alloy and Zhang *et al.* [78] in a Al-containing alloy.

HIP has been shown to give good microstructural and mechanical isotropy (as long as the effects of abnormal grain growth are understood) and batch-to-batch



(a) SEM micrograph showing grain structure (b) HAADF TEM micrograph

Figure 2.13: Microstructure of 14Cr-2W-0.3Ti-0.3Y_2O_3 following HIPing at 1150°C for 2.5 h (a) secondary electron (SE) micrograph showing the ferritic grain structure [76] and (b) high angle annular DF micrograph showing particles [75].

variations have been well studied. Scale-up is a restriction of the technique with costs being acceptable for developmental work but too high for industry uptake, justifying the development of more rapid processes.

2.4.2.2 Direct Extrusion

It is becoming more common to produce ODS steels by direct extrusion of MA powder [40, 47, 79, 80, 81, 82]. Figure 2.14 shows a schematic of the process whereby canned MA powders are degassed, sealed and then directly hot extruded. Hot extrusion normally occurs in a similar temperature range to HIPing - approximately 1100°C, producing a long billet, or hollow tube (mother tube) ready for further extrusion and thinning, in the case of cladding tube applications. The high shear stresses inherent to the process rupture surface oxides within the powder and leads to an excellent worked microstructure which is very stable compared with the HIP material, with low intergranular misorientation, strong texture and an unfavourable shape for grain boundary mobility [47].

Figure 2.15 shows false coloured EBSD maps of the microstructure in (a) longitudinal and (b) transverse directions. The microstructure is directionally orientated along the extrusion direction, with grain aspect ratio of ∼3 [82], leading

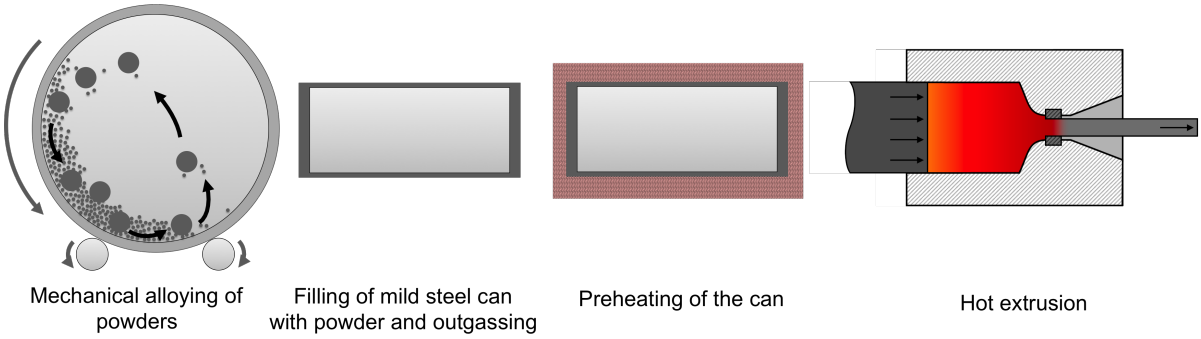
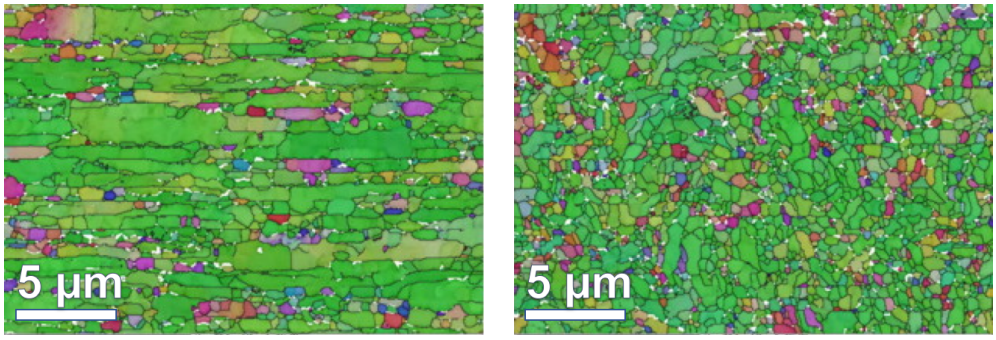
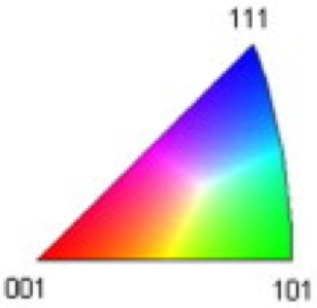


Figure 2.14: Schematic of the direct extrusion process.

to anisotropy in strength (both yield and ultimate tensile) [80], with a ∼20% difference in the ultimate tensile strength (UTS) between the two directions [83]. Figure 2.16 also shows a similar difference in elongation results.



(a) Longitudinal (b) Transverse



(c) Colour Key

Figure 2.15: EBSD maps of the microstructure in extruded rods in the (a) longitudinal direction (b) transverse direction (c) colour key for crystallographic orientation [84].

A detailed comparison of mechanical properties between direct extrusion processed material and other routes will be given in Section 2.6.

Direct extrusion gives good scale-up potential, especially as a mother tube can

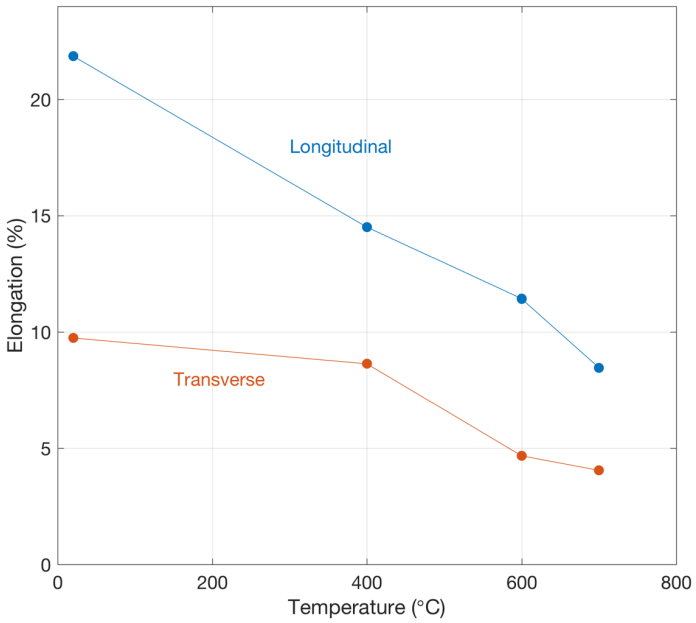


Figure 2.16: Difference between tensile properties in transverse and longitudinal extrusion directions for Fe-14Cr-1W-0.4Ti-0.3Y_2O_3 (redrawn from [85]).

be created directly from the extrusion process, which simply needs drawn further to create the thin walled tube. Inherent isotropy is still a factor to consider, as are any batch-to-batch variations. These are beginning to be characterised through large scale projects such as EU FP7 MatISSE, but due to a lack of smaller scale extrusion facilities, research costs are high and the collection of large amounts of data is slow and requires greater industry involvement in collaborative projects such as this one.

2.4.2.3 Field Assisted Sintering Technique

Field assisted sintering technique (FAST), also known as spark plasma sintering (SPS), utilises both uniaxial force and a pulsed or constant current to shorten sintering times from hours to minutes and often reduce the required sintering temperature [73]. The application of very high heating and cooling rates (as high as 1000°C/min [86] compared to 1-10°C/min in a hot press [73]) allows densification to dominate over grain growth, so a finer consolidated microstructure can be achieved.

Figure 2.17 shows a schematic of the FAST setup, whereby the powder is placed in a conductive die and pressed with conductive punches under pressure

whilst electric current is applied [87].

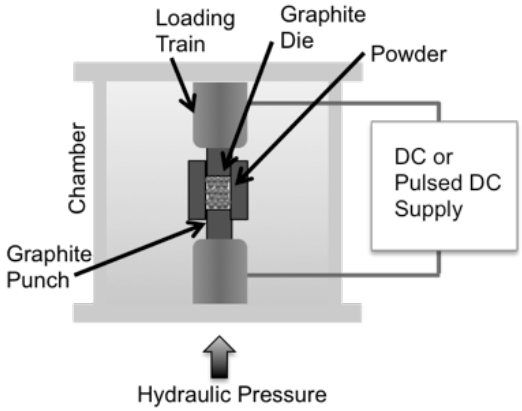


Figure 2.17: Schematic representation of a field assisted sintering machine.

Rapid consolidation times are in part due to the localised heating from the current application. Heating occurs at the contact points between powder particles but other effects of the applied current include plasma generation [86, 88, 89], a surface cleaning effect [73, 88, 89, 90, 91] and an electroplastic effect [73, 92, 93, 94]. The most widely accepted idea is that Joule heating contributes to consolidation, which occurs due to the passage of electric current through particle-particle contacts in a conducting powder [86]. As green compacts are not usually completely homogeneous and dense, current paths and heating zones are complex. The concept of sintering temperature in FAST is also not straightforward as significant temperature gradients exist, and change with time as densification occurs.

An important issue in field assisted sintering (FAST) is the uniformity of electrical current. In the early stages, when the relative density is low, the size of interparticle contact varies significantly and the concentration of current along certain paths can be favourable [73]. If the resultant localised heating cannot be effectively transferred away, then accelerated densification or even localised melting can occur [73, 93]. The application of pressure (as with pressure-assisted sintering methods) can alleviate this effect as powder particles can be rearranged and agglomerates broken down, and pore shapes changed [73].

It is widely accepted that temperature is strongly influenced by electrical and thermal diffusivity, and the dimension of the tool setup, as well as the powder

that is consolidated [95]. It is commonly reported that there are strong variations between the temperature at the edge and the centre of the sample, especially for larger die sizes [96].

Despite rapid heating and cooling, grain growth may still occur especially in regions of very high, transitioning temperature [73], and in late sintering stages, current application may accelerate diffusion kinetics and coarsening [73].

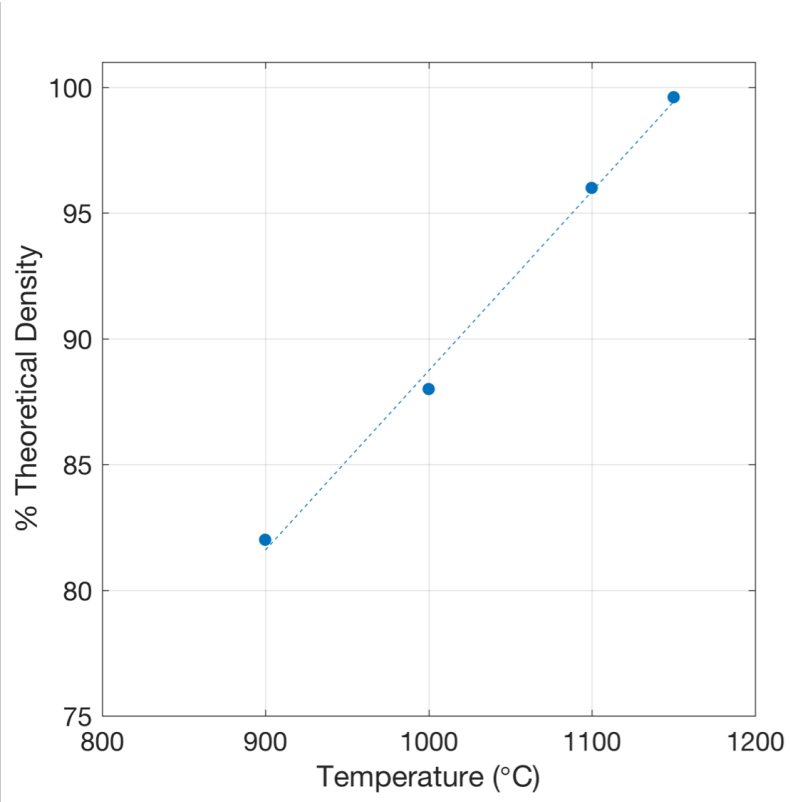


Figure 2.18: Effect of sintering temperature on relative density of SPSed 14YT alloy (redrawn from [97]).

FAST is becoming increasingly popular for ODS materials including Cu [98], W [99] and steels [100]. A study on the effects of FAST on the consolidation of ODS steels [97] used a Fe-14Cr-0.4Ti-0.25Y_2O_3 (14YT) alloy. Figure 2.18 shows the relative density of the compacts as a function of sintering temperature, where almost theoretical density is achieved at a sintering temperature of 1150°C. The micrographs shown in Figure 2.21 demonstrate the effects of temperature upon the ease of realignment of the powders under applied pressure, with higher temperatures reducing porosity. Due to milled powders often being plate-like, as

seen in Figure 2.21, this is a very important effect in minimising porosity. Depending upon the milling and storage gases used for the powders, residual porosity and trapped gas may lead to detrimental mechanical properties or high temperature swelling. Under optimised FAST conditions of 1150°C for FAST pressure of 50 MPa, held for 5 minutes, a density of 99.6% was seen, similar to that for a 4h hold in HIP, confirming the potential advantage of FAST in requiring shorter dwell times and lower pressures for consolidation.

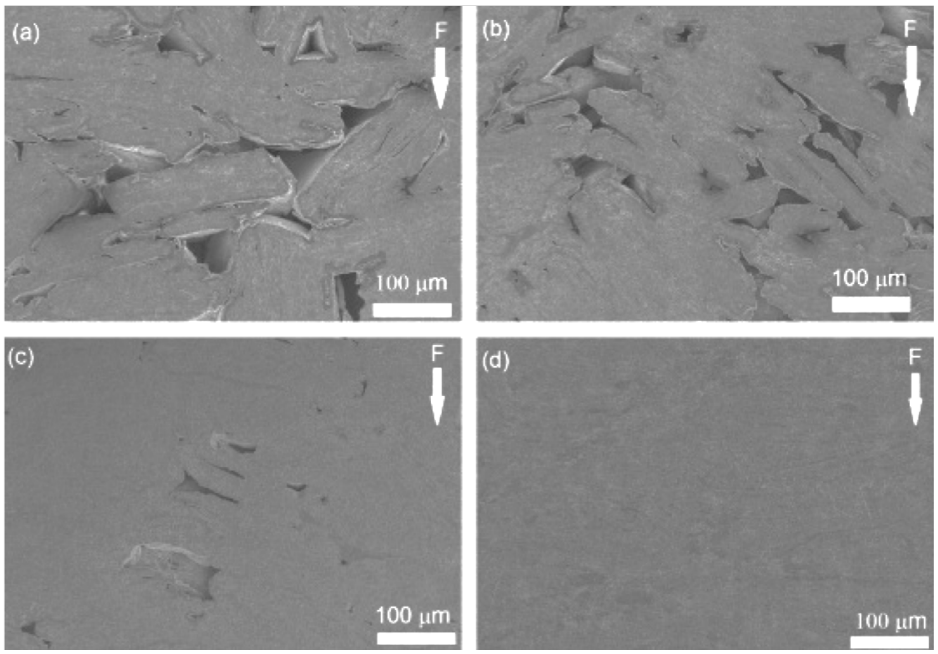


Figure 2.19: SEM micrographs from 14YT FAST samples at different sintering temperatures (a) 900°, (b) 1000°C, (c) 1100°C, (d) 1150°C. Arrows indicate the direction of applied pressure [97].

Figure 2.20 (a) shows a SE micrograph from Boulnat *et al.* [101] of a Fe-14Cr-1W-0.3Ti-0.3Y_2O_3 alloy consolidated by FAST demonstrating a bimodal microstructure. This means that despite the rapid sintering, particle stabilised fine-scale ferritic microstructure is unstable and breakaway, or abnormal grain growth (to be discussed further in Section 2.3.2) can occur. The resulting nanoparticles in a 14YT alloy can be seen in Figure 2.21, with average size <5 nm and number density of 1.4 $\times$ 10^{23} m^{-3}, within the expected range for ODS steels.

In contrast to extrusion, FAST material shows no mechanical anisotropy however volumes are severely restricted to ensure even current distribution, with the largest

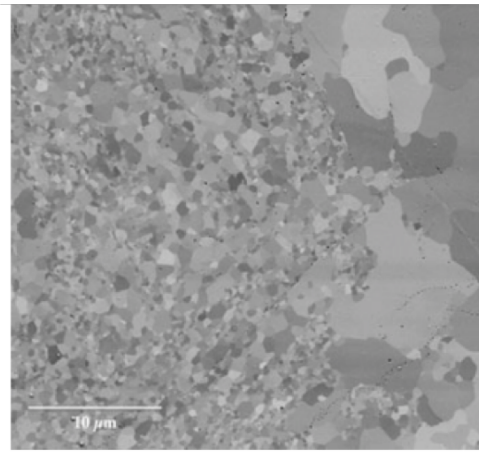


Figure 2.20: SEM micrograph of the bimodal grain structure in Fe-14Cr-1W-0.3Ti-$0.3Y_2O_3$ alloy consolidated by FAST [97].

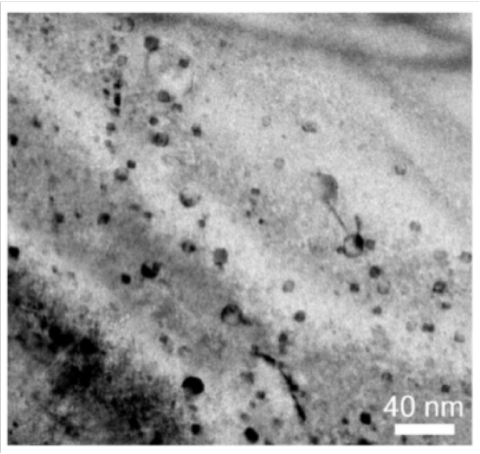


Figure 2.21: BF TEM micrograph of 14YT alloy consolidated by FAST [101].

successful FAST volume ∼300 mm diameter of 40 mm height, with simple near net shape components being insufficiently densified and prohibitively expensive.

Ultimately neither FAST nor HIP create a mother tube, something that is achieved during direct extrusion, but leads to a much more less directional microstructure and therefore isotropic mechanical properties. Could this increase in microstructural control be worth the trade-off for an extra processing step?

This will be evaluated alongside more novel processing methods.

2.4.3 Novel Processing Methods

The primary aims for alternative manufacture methods for ODS alloys are to either:

- Shorten processing time
- Improve microstructure and consequently material performance

when compared with MA + HIP or MA + powder extrusion.

As described by Bergner *et al.* [52], these novel processing routes can be split into:

- Liquid metal routes
- Hybrid routes
- Physicochemical routes
- Modifications to the standard PM MA route

2.4.3.1 Liquid Metal Routes

Liquid processing routes, e.g. casting, allow for complex alloying and are technologically mature, hence the focus on developing a liquid metal processing route for ODS steel. The associated difficulties include limited wettability of the oxide particles, their tendency to agglomerate before introduction into the melt, when in the melt their buoyancy and difficulties in penetrating the surface oxide skin, as well as the inherent difficulties of working with loose nanoparticles in a foundry environment [52].

If the oxide particles are to be less than 20 nm (shown to be the most important for strengthening mechanisms) then milling is required to reduce oxide powder diameter prior to addition. To prevent agglomeration, a low concentration and low viscosity Y_2O_3 colloidal powder suspension has been developed [52]. The wetting angle of Fe-Cr droplets on Y_2O_3 substrates was investigated, and the addition of Y to the melt shown to improve wettability [102, 103].

In terms of particle insertion, several methods have been investigated, such as filling cavities in the feedstock ingot, full or partial MA to pre-coat the particles with the matrix alloy, and various types of intense stirring including magnetically-induced [52].

To minimise agglomeration once within the melt, powerful agitation is considered critical, such as using ultrasound to produce shocks and micro-jets that can overcome the agglomeration forces [52]. However designing a sonotrode (that applies the ultrasound) that can withstand the temperatures, corrosion and reducing atmosphere of the melt is often problematic.

Once successfully introduced and separated, the nanoparticles must then be incorporated into the microstructure during solidification. If the particle has poor wettability with the solid-liquid interface, it will be pushed ahead of the advancing solidification front, increasing the local concentration in the shrinking liquid fraction and being forced together into large agglomerates.

Verhiest *et al.* [103] had some success in using a Y-containing alloy followed by internal oxidation, with many micron-sized and some sub-micron Y-rich particles. However, the size and distribution of the particles was not sufficiently uniform and further understanding of the formation mechanisms and processing is required.

Miran *et al.* [104] successfully cast a Fe-16Cr-0.2Al-0.05Y alloy and through a series a different oxidising atmospheres and temperatures, formed micron size oxides at a penetration depth of 2 mm using a V_2O_5 oxygen source at 1450°C for 20 h, with negligible excess O contamination.

Key to this success was the lower affinity for oxygen of V than Y, and a heat treatment temperature at which the O diffuses into the sample quicker than the Y diffuses out to the O-rich surface.

In summary, there are inherent difficulties in a liquid processing route to an ODS alloy, but the potential savings in terms of cost and scalability continue to attract research efforts and progress is being made. As of yet, no mechanical property or irradiation resistance data has shown any competition to powder processing.

2.4.3.2 Hybrid Routes

Hybrid routes combine the understanding of powder processing routes with the scale potential of liquid metal routes. Many researchers focus upon the 'entrapment' of Y into a super saturated solid solution and later controlled 'internal oxidation' to form the oxide particles.

The principle of controlled internal oxidation has been demonstrated in the gas atomisation reaction synthesis (GARS) of Fe-16Cr alloy powders by Rieken *et al.* [105]. As Y_2O_3 is more stable (lower free energy of formation) than Cr_2O_3, as illustrated by the Ellingham diagram (seen previously in Figure 2.9), the post-solidification heat treatment allows solid-state O exchange from Cr-rich oxides to Y-rich oxides to form a distribution of nanometre-sized mixed oxides [52]. The GARS method is described further in Section 2.4.3.4.

In MA, the high defect densities (such as vacancies and dislocations) likely play a critical role in promoting fine scale nucleation of the oxides. As hybrid routes generally avoid the MA step, oxides tend to be >10 nm or even micron scale rather than 2-5 nm considered to be optimum in the MA route [52].

Methods such as melt spinning and spray forming avoid powder processing and aim to use rapid solidification to prevent Y precipitation and trap the Y into flakes or small ingots respectively, ready for internal oxidation.

Melt spinning comprises a crucible, in which the alloy is melted. A stream of molten alloy is ejected by a protective gas overpressure onto a cool fast rotating substrate where it is rapidly solidified as a thin metallic ribbon promoting a Fe-Y supersaturated solution [106].

Hong *et al.* [107] demonstrated the principle of internal oxidation of Fe-Y based ribbons using the Rhines pack method [108] to produce O-rich nanoparticles within grains and at grain boundaries rich in Y. Figure 2.22 (a) shows a scanning tunnelling electron microscope (STEM) HAADF micrograph of the particles with inset EDX maps for Fe, Y and O. Figure 2.22 (b) shows a high resolution TEM micrograph of a < 20 nm in-grain particle and Figure 2.22 (c) is a fast fourier transform (FFT)

image with crystalligraphic analysis of the particle showed Y_2O_3. Ribbons can be densified to bulk, for example using FAST [107].

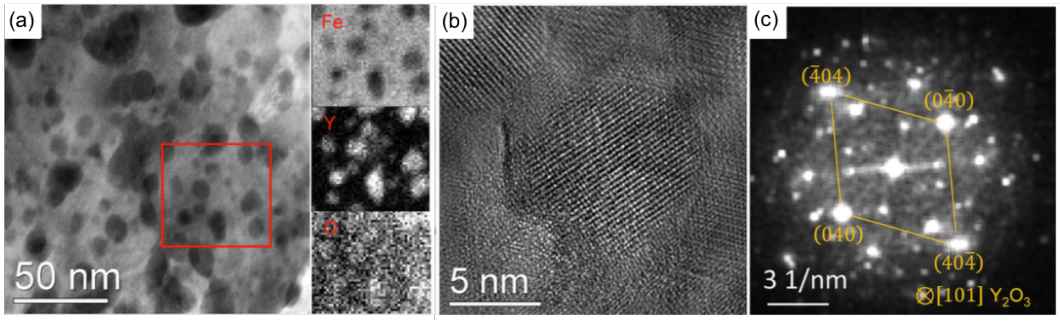


Figure 2.22: (a) STEM HAADF micrograph with inset EDX maps for Fe, Y and O (b) HRTEM image of small in-grain particle (c) FFT image and crystallographic analysis of particle in (b) [107].

The addition of Ti to refine oxides was also explored. Hardness values for the final compact was only half those of the powder processed equivalents (1.5 GPa compared to 3-4) suggesting that the particles generated were coarser, or the ribbons had not fully bonded during FAST due to non-optimised conditions or excessive O or C contamination. There was, however, sufficient encouragement to suggest further work on melt spinning / internal oxidation using optimised heat treatments.

Spray forming is another potential hybrid method, which involves the inert gas atomisation of a liquid metal stream into droplets that deposit on a substrate before solid, forming incrementally a coherent, near fully dense preform. The substrate can be a rotating disc, tube or moving strip, allowing billets, tubes and strips to be formed. The characteristic microstructure consists of refined equiaxed grains (10-100 μm) and can frequently exhibit extended solid solubility or metastable phases [109]. A schematic of the process is shown in Figure 2.23.

The attraction of the route arises from the reduction in processing steps (compared to powder processing methods) and the large volume capacity. Stainless steel tubes have been successfully manufactured by Sandvik using spray forming since 1986, giving properties comparable to conventionally manufactured tubes without any subsequent work [109].

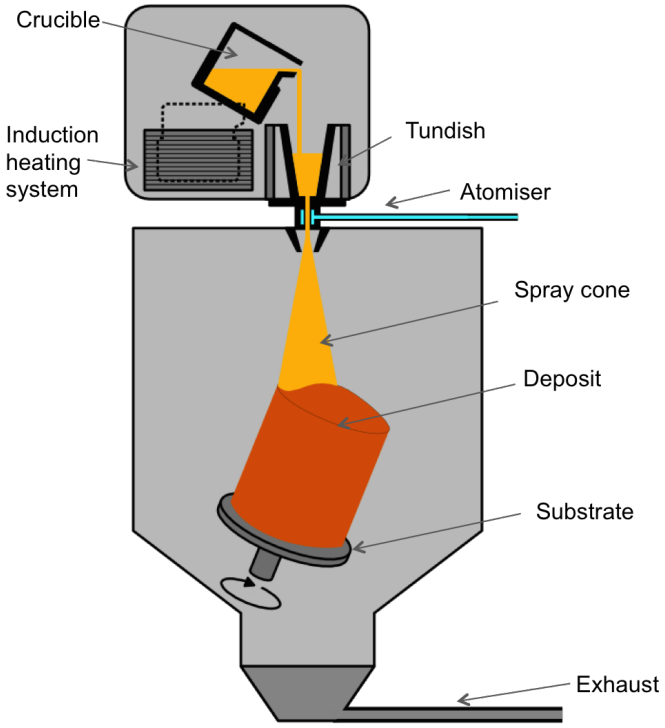


Figure 2.23: Schematic of the spray casting process.

The technique has also been used to produce ODS materials, in combination with internal oxidation. Successful production of Ni ODS materials has been reported by Hasegawa *et al.* [110], with an even dispersion of 72 nm ZrO_2 particles, and Cu ODS alloys by Li *et al.* [111], with a dispersion of 20 nm Y_2O_3 particles.

Despite the high potential of the technique, no published evidence of ODS steels being produced by spray casting was found. Initial studies completed by the author were documented by Bergner *et al.* and can be seen in further detail in [52].

Other potential hybrid routes include additive manufacturing (AM) technologies such as selective laser melting SLM or selective laser sintering [112, 113, 114, 115], that produce densified, sometimes complex, shapes from metal powders. A full review of the technique is given in [116]. AM requires MA ODS powders with opportunities for net-shape production, which can be restrictive as no forging or similar process is available to recrystallize the material, and even simple heat treatments can be problematic, leading to distortion.

Most of the studies using SLM have focussed on the FeCrAl range of ODS alloys where nanoparticles are less refined (at 30 - 50 nm [113]), so target particle size and density may be more achievable. Chang *et al.* [112] studied SLM of Fe-14Cr-2W-0.3Ti + $0.5Y_2O_3$ powder and showed that the high diffusivity of Y_2O_3 within the melt means that particles often agglomerate. Figure 2.24 shows that this led to average particle diameters of between 30 nm and 150 nm after the SLM process and a number density of only 4×10^{18} m^{-3}.

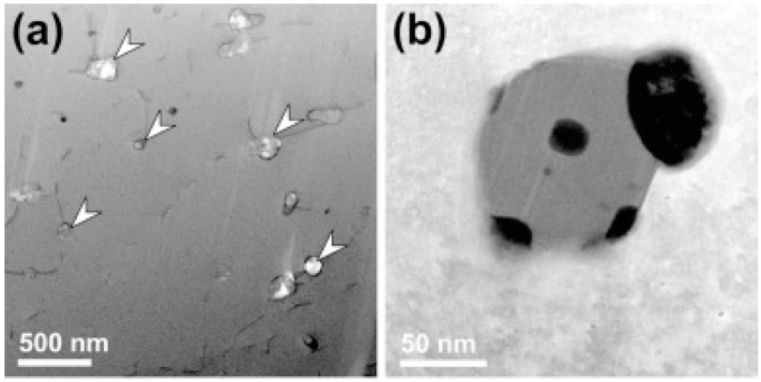


Figure 2.24: (a) TEM BF image of laser melted ODS steel with oxide particles highlighted by arrows (b) HAADF STEM image of aggregated nanoparticle [112].

Generally hybrid routes are not aimed at recreating or improving the MA microstructure, or the resulting performance, but rather to offer a compromise between the necessary properties of the end product and a more suitable scalable fabrication method. So far, no route has offered a credible alternative to MA / consolidation and further work is required to demonstrate reproduceable predictable microstructures, particle distributions and mechanical properties.

2.4.3.3 Physicochemical Routes

Physicochemical methods include chemical vapour deposition (CVD) & physical vapour deposition (PVD) [52, 117] and molecular beam epitaxy (MBE) [52, 118]. Although capable of producing tiny amounts of model alloys for investigation of key properties (such as matrix / oxide interfaces and irradiation behaviour), the products are essentially films of coatings of only a few microns in thickness.

2.4.3.4 Modifications to the PM Route

Modifications to the standard PM route include use of powders made by gas atomisation reaction synthesis (GARS), surface treatment of gas atomised reaction synthesis (STARS), and controlled oxidation.

GARS involves the addition of O to the Ar gas used in gas atomisation to form a surface oxide on the droplets. Several institutions have used a Fe-Cr-W-Ti-Y melt to form a Cr-rich oxide shell on solidified powders (with yttrium segregation to the grain boundaries) [52, 105, 119]. During consolidation, such as sintering, the surface-oxide shell decomposed with O preferentially forming Y-rich oxide clusters. A further heat treatment then completed dispersoid formation and stabilised the matrix grain structure. The resulting nanoparticle distribution was then compared to that developed by applying HIP to the same powder. Figure 2.25 shows a Fe-16Cr-1W-0.5Ti-0.65Y_2O_3 alloy produced using GARS by Rieken *et al.* demonstrating a uniform distribution of particles with diameters 3-12 nm and number density $\sim 3{\times}10^{22}m^{-3}$. When analysing batch-to-batch variations, sufficient O concentration was available at larger particle sizes but further work was required to improve oxidation of fine powders.

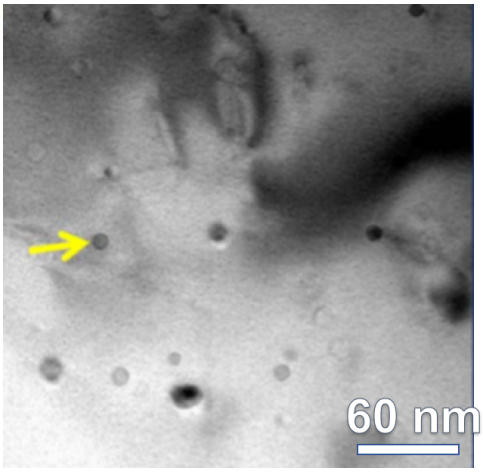


Figure 2.25: TEM micrographs of nanoparticles in HIPed GARS ODS Fe-16Cr-1W-0.5Ti-0.65Y_2O_3 powder [120].

In comparison, STARS is the surface oxidation of a conventionally inert gas atomised Y containing alloy in a furnace under air. This approach has been

developed at VTT in Finland [52] using gas atomised Y containing Fe-9Cr powder. HIP, heat treatment and hot and cold work led to a fine grain structure <2 μm, and the development of nanoparticles that were ~0.4 μm and less refined than through the powder production route. Other work using STARS [121] on Fe-14Cr-2W-0.3Ti-0.24Y powders can be seen in Figure 2.26 with (a) showing a distribution of < 50 nm Y and Ti rich particles along grain boundaries and within grains and (b) showing a bimodal grain structure. Hardness of this compact was ~ 1.8 GPa, half that of a HIPed compact (3-4 GPa), likely due to the removal of matrix work that is induced by MA.

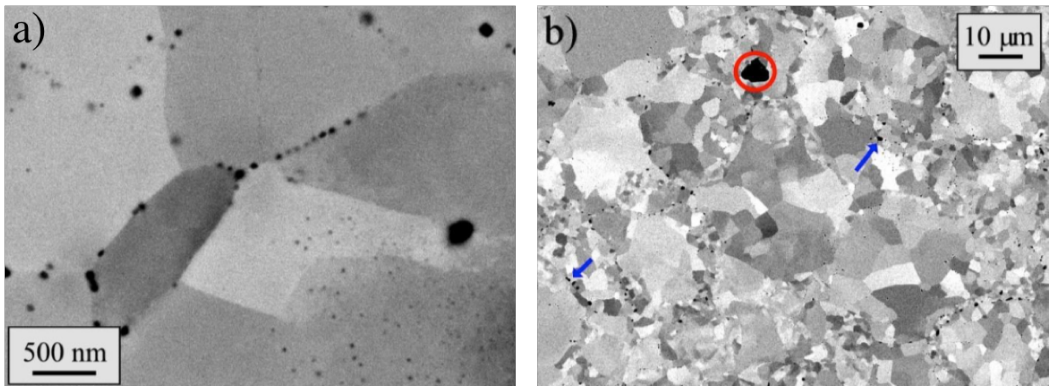


Figure 2.26: BSE field emission gun (FEG)-SEM micrographs in HIPed STARS ODS powder of (a) nanoparticles and (b) grain structure [121].

All melt routes have an additional challenge in that Y is so reactive (tendency to form Y_2O_3) that controlling the alloy Y concentration is difficult. Y is frequently lost during melting and dispatching and thus the remaining Y concentration can be variable, leading to batch-to-batch variations. The standard approach is to 'overalloy' Y concentration but even with significant foundry experience, Y concentrations could fluctuate severely.

In summary, these alternative processes aim to remove the MA stage offering potential savings in processing time, but most retain the need for a consolidation step and thermomechanical processing. Practically all studies show that a distribution of particles on a similar scale to that of MA / consolidation is yet to be achieved, and as will be seen in Section 2.6, this leads to a dearth of convincing mechanical

property data. Nonetheless, MA imposes such severe limitations, and the patchy but encouraging process in the immature alternatives, ensures further research into alternatives to MA will continue.

2.5 ODS Steel Microstructure

Each processing method will generate a slightly different microstructure and thus slightly different mechanical properties. The novel, immature methods of production aim to enable shorter, more feasible production times, but almost always is at the expense of microstructural control or mechanical properties compared with the mature MA route.

The microstructure generated by each of the processing methods is now briefly discussed, and "target" microstructural parameters are summarised in Table 2.3.

Processing route	Composition	Grain structure (μm)	Particle size (nm) & distribution (m^{-3})
MA + HE [84]	Fe-14Cr-1W-0.4Ti-0.3Y_2O_3	Elongated 0.9×0.5 (longitudinal), Equiaxed 0.4 (transverse)	4, 1.4×10^{24}
MA + HE [47]	Fe-12Cr-3W-0.4Ti-0.25Y_2O_3		3-5, $1\text{-}2\times10^{23}$
MA + HIP [28]	Fe-14Cr-2W-0.3Ti-0.3Y_2O_3	0.25 ± 0.15	8, 2×10^{21}
MA + HIP [75]	Fe-14Cr-2W-0.3Ti-0.3Y_2O_3	Bimodal few microns and 0.2-0.5	4 nm
MA + FAST [97]	Fe-14Cr-0.4Ti-0.25Y_2O_3	Bimodal peaks at 0.5 and 15	2, 1.4×10^{23}
MA + FAST [122]	Fe-14Cr-2W-0.4Ti-0.25Y_2O_3	~ Homogeneous 0.5	5, 2×10^{24}
Melt Spun [107]	Fe-1Ti-1Y+Fe_3O_4	Unimodal 0.6	< 20 nm
STARS [121]	Fe-14Cr-2W-0.3Ti-0.3Y_2O_3	Bimodal (> 25 μm and <5 μm)	< 50 nm
SLM [112]	Fe-14Cr-2W-0.3Ti-0.5Y_2O_3		30-150, 4×10^{18}

Table 2.3: Microstructural features as generated by common processing methods.

Table 2.3 shows the average MA + HE microstructure to be elongated grains of ~ 0.5 μm width, and 1 μm length with a distribution of 4-5 nm ODS particles at a density of 10^{23}-10^{24} m^{-3}. In comparison, MA + HIP showed a bimodal grain size distribution with peaks at a few 100s of nm and on the micron scale, but slightly larger particles (5-10 nm) at a lower distribution (10^{21}). MA + FAST also led to a bimodal grain size distribution on a similar scale to HIP, but led to a finer distribution (2-5 nm) of particles at a higher density (10^{23}-10^{24}). More novel, immature methods have shown promise in terms of particle sizes (< 20 nm in melt spinning and < 50 nm in STARS), but these are not the 2-5 nm particles achieved using MA. Grain size distributions were also generally less fine for methods without the MA stage, on the micron scale.

From Table 2.3 and associated mechanical property data, an idealised ODS steel microstructure would comprise a grain structure on the micron scale or finer, and insoluble oxide based particles between 2-5 nm with a number density of 10^{23}-10^{24} m^{-3} to provide grain pinning and trapping sites for radiation-induced defects.

2.5.1 Thermal Stability

ODS steels microstructures should be stable at reactor relevant temperatures. Several important strengthening mechanisms depend upon grain size and particle strengthening and so coarsening of either must be understood.

Several sources confirm stability of the grain structure and nano-oxides up to elevated temperatures (> 1000°C) [123, 124, 125] due to the successful pinning of grain boundaries by the nano-oxides.

Most studies have focussed upon short term, accelerated thermal exposure to temperatures above reactor operating temperatures (> 800°C) and examining the temperature at which control is lost, but different mechanisms were active in these regimes compared to reactor operating temperatures. Obviously, few studies have focussed upon long term reactor relevant temperatures due to the drawn out timescales.

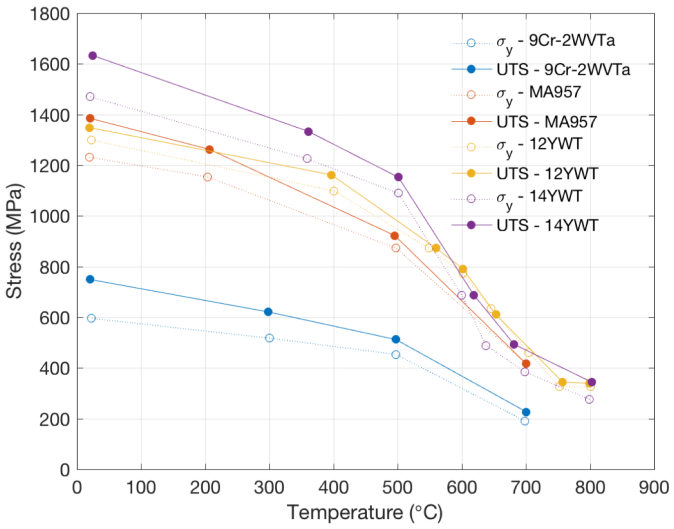
2.6 Mechanical Properties

The mechanical characteristics of an ODS steel depend largely on the size and spatial distribution of the dispersed particles with the best creep resistance and tensile strength being achieved by a high density (10^{23}-10^{24}) of uniformly distributed nano-particles [28, 46, 47].

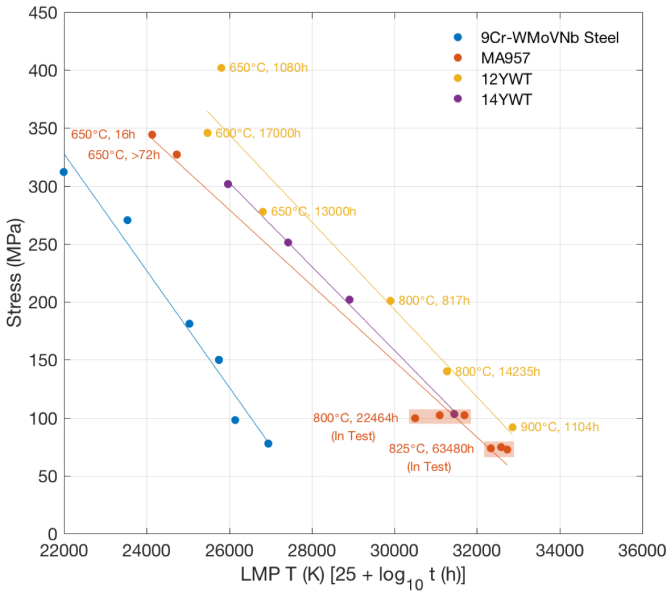
Figure 2.27(a) shows the strength of ODS alloys from literature, in terms of ultimate tensile strength (ultimate tensile strength (UTS)) and yield strength (YS, σ_y). From the alloys examined, Fe-14Cr-3W-0.3Ti-0.25Y_2O_3 (14YWT) shows the highest strength up to 600°C. There was a trade-off between high temperature strength and the improved corrosion resistance that is provided by the higher Cr levels when compared to Fe-12Cr-3W-0.3Ti-0.25Y_2O_3 (12YWT) but both of the experimental alloys (14YWT and 12YWT) outperformed the then commercially available MA957 (Fe-14Cr-0.3Mo-1Ti-0.25Y_2O_3). Figure 2.27 (b), with 12YWT showing the highest creep strength, however 14YWT still out performed the commercial ODS alloy, MA957.

An in-depth study by Chauhan *et al.* [126] shows the change in deformation mode with temperature for ODS steels. At room temperature, fracture occurs in a mixed mode, with limited cleavage steps and facets connected by ductile ridges covered in dimples. A ragged fracture surface can be indicative of a mismatch in properties between smaller and larger grains. Smaller grains allow lower dislocation activity, therefore tend to fracture first showing lower ductility. In comparison, the large grains undergo localised deformation of protrusion and steps with dimples and cleavage facets. Dimples represent the coalesced voids that nucleate surrounding oxide particles, often the sites for initiation of cracks. Cleavage steps form because of the changes in cleavage surface directions at grain boundaries and the need to follow the new planes of the adjacent crystal.

Grain boundaries can act as weak points, especially if they retain residual cold work or coarse Ti-rich oxide particles. If grain boundaries are aligned parallel to each other (such as in extruded materials) then they act as a weak point during testing in the opposite direction leading to a loss of ductility.



(a) Ultimate tensile strength (UTS) and yield strength (YS) of commercial and experimental alloys at high temperatures (redrawn from [68])



(b) Creep strength of commercial and experimental alloys at high temperatures (redrawn from [68])

Figure 2.27: Strength of commercial and experimental alloys (a) ultimate tensile strength (UTS) and yield strength (σ_y) of Fe-14Cr-3W-0.3Ti-0.25Y_2O_3 (14YWT), Fe-12Cr-3W-0.3Ti-0.25Y_2O_3 (12YWT), Fe-9Cr-2W-1V-1Ta non-ODS steel and Fe-14Cr-0.3Mo-1Ti-0.25Y_2O_3 (MA957) as a function of testing temperature and (b) creep strength of 9Cr-1W-1Mo-1V-1Nb a non-ODS tempered martensitic steel, MA957, 12YWT and 14YWT.

At temperatures approaching 500°C an increase in ductility is seen as a result of high temperature mobility. The crack tip can now proceed by plastic deformation mechanisms, characterised by dense arrays of dimples without cleavage steps or facets. Ductile deformation is normally seen most clearly in the centre of fracture surfaces with a shear lip seen as the termination of this behaviour. Micropores are key indicators of crack initiation and linking sites as can be seen in Figure 2.28.

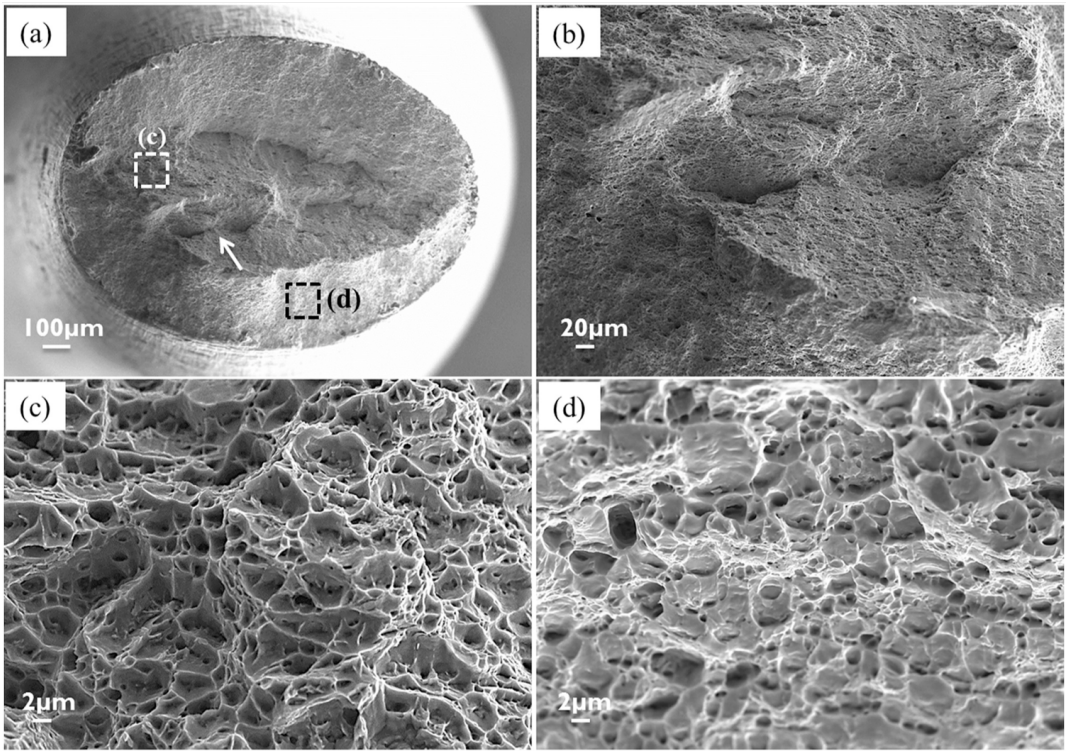


Figure 2.28: SEM fracture surface images of Fe-12Cr-2W-0.2Ti-0.25Y_2O_3 tested at 500°C (a) macro view showing elliptical necking with microcracks (b) magnified view of microcracks from selected area with an arrow in (a), (c) magnified view of dimples with particles and micropores from the selected area in (a), and (d) magnified area showing the shallow dimples with micropores at the shear-lip region from the selected area in (a) [126].

At 600°C, more necking is observed, with the fracture surface full of deep dimples without cracks, showing the point of maximum ductility. In this range it is usually intragranular fracture that leads to failure.

At 700°C the change in fracture mechanism from intragranular to inter-granular leads to the formation of decohesion zones that may form after grain boundary sliding or migration. These are likely the result of the weakening of grain boundary strength at high temperatures due to void formation, grain boundary diffusion,

or thermal misfit between the matrix and grain boundaries, due to segregation. All of these mechanisms lead to a loss of ductility.

These general trends must be adapted to specifics of processing methods, such as inherent porosity, directionality or segregation and will be discussed further separated by processing method. This further discussion of mechanical properties is based solely on Fe-14Cr-3W-0.3Ti-0.25Y_2O_3 or as similar as possible.

Microhardness values for the main processing routes of ODS steels alongside more novel approaches are shown in Table 2.4. MA + HE leads to an average hardness of 4 GPa, slightly harder than HIP (3 GPa) due to the high shear forces applied during the extrusion process generating higher dislocation densities. Early FAST values were highly variable and fall in the range 3-5 GPa, due to the use of model alloys rather than the alloys containing W and Ti. More novel techniques were much softer (1-2 GPa) due to the lack of dislocation build up that MA provides. GARS + cold rolling was harder due to the presence of cold work.

Consolidation Method	Composition	Hardness (GPa)
Hot extrusion	Fe-14Cr-3W-0.4Ti-0.3Y_2O_3	4.5 [124]
Hot extrusion	Fe-14Vr-2Al-1Si-0.3Ta-1Y_2O_3	4.2 [127]
HIP	Fe-14Cr-2W-0.3Ti-0.3Y_2O_3	3 [75]
HIP	Fe-14Cr-2W-0.3Ti-0.3Y_2O_3	3.6 [128]
FAST	Fe-16Cr-3Al-1Ti-0.5Y_2O_3	4.7 [129]
FAST	Fe-14Cr-0.3Y_2O_3	2.8 [100]
Melt Spinning	Fe-1Ti-1Y+Fe_3O_4	1.47 [107]
GARS	Fe-16Cr-0.1Hf-1Y_2O_3	1.8 [105]
GARS + 80% reduction cold rolling	Fe-16Cr-0.1Hf-1Y_2O_3	3 [105]
STARS	Fe-14Cr-2W-0.3Ti-0.23Y+O	1.8 [121]

Table 2.4: Hardness of ODS steels produced by a variety of processing methods.

Data for tensile properties has been published for the more mature techniques. Figure 2.29 shows UTS and Figure 2.30 shows YS data from a range of sources on a range of processing methods. The characteristic drop-off of UTS and YS with temperature is seen for all data sets. In terms of UTS, extruded and some HIPed material showed room temperature strength of 1100-1200 MPa. Other HIPed data and data for FAST alloys showed much lower results (950 and 800 MPa respectively).

UTS remains constant for most processing methods until 400°C where it starts to drop, with most processing methods showing a 200-400 MPa UTS by 700°C. Most processing methods showed a yield point of 1000-1100 MPa at room temperature, with the HIPed material (which had a lower UTS), also showing a lower YS. The same drop off in strength was seen with temperature with an average YS of 200-350 MPa by 700°C. Extruded material showed the highest YS across the temperature range, outperforming both FAST and HIP.

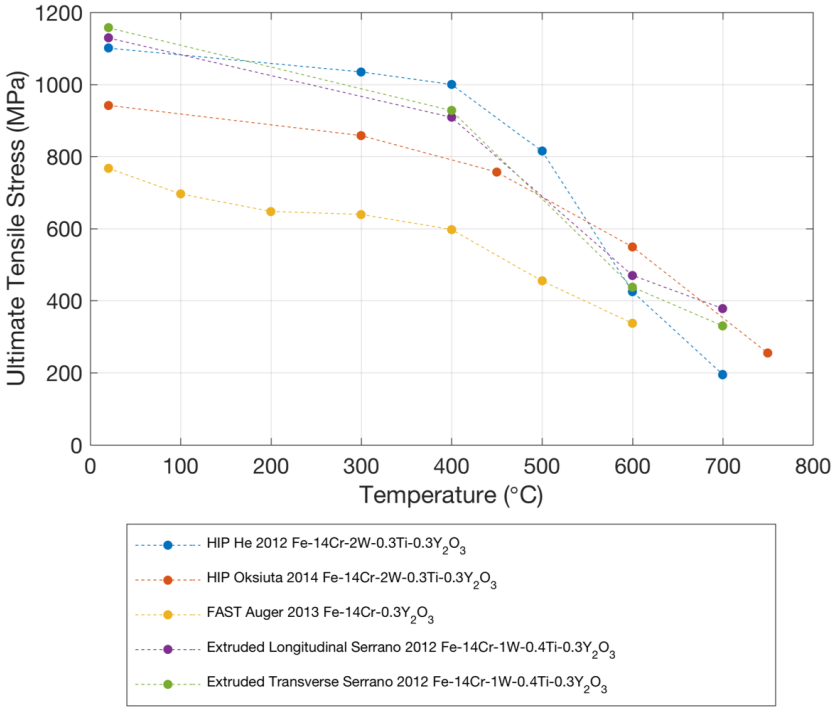


Figure 2.29: Ultimate tensile strength from literature data for material produced using current and novel processing methods for HIP He 2012 [75], HIP Oksiuta 2014 [128], FAST Auger 2013 [100], and Extruded Serrano 2012 [84].

Figure 2.31 shows the total elongation data for a range of materials. Three different trends can be seen within the data. Early FAST data on a model (Fe-14Cr-1Y+O) alloy, and the transverse direction of extruded material showed low elongation ($< 10\%$) over the whole temperature range, suggesting an easy crack path was followed (common in extruded materials with aligned grain boundaries and pores in the longitudinal direction weakening the transverse direction, and

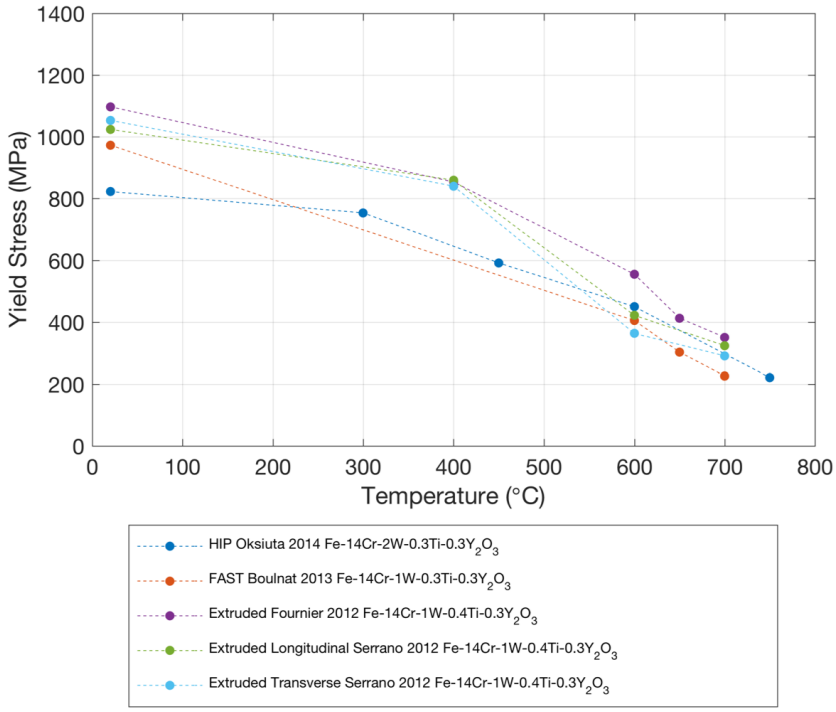


Figure 2.30: YS from literature data for material produced using current and novel processing methods for HIP Oksiuta 2014 [128], FAST Boulnat [101], Extruded Fournier 2012 [79] and Extruded Serrano 2012 [84].

indicating insufficient sintering to gain good powder bonds in the FAST combined with the low YS and UTS). HIP data showed the same independence of temperature up to 600°C but was slightly more ductile at $\sim$ 12% deformation. Some of the extruded material tested in the longitudinal direction saw a drop off in elongation with temperature, whereas FAST and other extruded material saw an increase.

Boulnat *et al.* [101] attributed the good levels of ductility seen in their work to low porosity and the presence of both large grains and nano-sized ultrafine grains, which is likely to be a good compromise between strength and ductility. Through a combination of methods, the microstructure of fracture surfaces was investigated. It was found that large grains kept their isotropy all through the test, proving that they effectively accumulated the plastic strain through organised sub-grains or rotation. In the ultra-fine-grained regions, it is most likely that the predominant mechanisms were super-plasticity and grain boundary sliding.

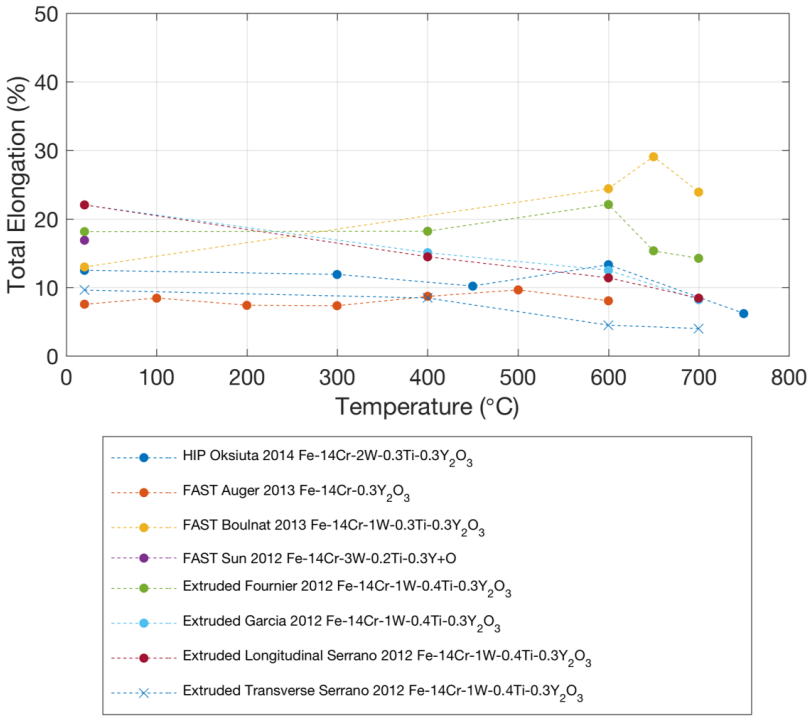


Figure 2.31: Total elongation values from literature data for material produced using current and novel processing methods for HIP Oksiuta 2014 [128], FAST Auger 2013 [100], FAST Boulnat [101], FAST Sun 2012 [130], Extruded Fournier 2012 [79], Extruded Garcia 2012 [131] and Extruded Serrano 2012 [84].

Whilst grain boundary sliding can contribute significantly to strain hardening, these mechanisms are much weaker in isolation and only allowed such large levels of ductility when combined with the larger grains.

What is clear is that a lack of standards exists for the minimum level of ductility, so data generated in this work will be compared to that seen in literature to gauge whether new processing methods meet levels gained by current time consuming processes or see a trade-off in their performance which will have to be assessed.

2.6.1 15:15Ti Austenitic Steel Properties

As mentioned previously, the main competitor material being considered for cladding applications in SFRs is 15:15Ti austenitic steel. With a lack of requirements from industry as to the required properties for operation, properties of a material utilised previously in an SFR could give a target for potential properties.

Results from another EERA JPNM pilot project (TASTE) [132] are shown in Table 2.5.

Testing Temperature	YS (MPa)	UTS (MPa)	Str (%)
RT	723	813	13
300(°C)	677	793	5
500(°C)	729	806	7

Table 2.5: Tensile mechanical properties (YS - yield strength, UTS - ultimate tensile strength and Str % - strain at failure) of 15:15Ti austenitic steel [132].

Yield strength and ultimate tensile strength were maintained up to 500°C at $\sim$ 700 MPa and 800 MPa respectively, but ductility reduced from a total strain of 13% down to 7%. These values will be compared to those for ODS steels from literature and produced within the current work.

2.6.2 Small Punch Test

Of key consideration in the field of ODS steels for fuel cladding applications is creep resistance. Conventional creep tests occur over thousands of hours to simulate in-reactor behaviour.

Due to time constraints within the duration of the project, accelerated creep tests must be used to simulate long term creep resistance. In the nuclear field, it has become more common to use small punch testing to complete such tests, as it allows the use of small volumes of material and accelerates the creep behaviour.

Details of this procedure will be given in Section 3.7.3. In the present section, only a brief introduction to the technique and the results from small punch creep testing on 14YWT ODS materials are given.

The small punch test (SPT) involves clamping a thin (0.5 mm) disc circumferentially and pushing in a spherical indenter to allow deformation under a constant load or displacement [133]. Further details of the technique can be seen in Section 3.7.3.

SPT was completed on Fe-14Cr-1W-1Ti-0.3Y_2O_3 extruded material by Bruchhausen *et al.* [134] in both the longitudinal and transverse directions. The stress-rupture plot for all tests can be seen in Figure 2.32.

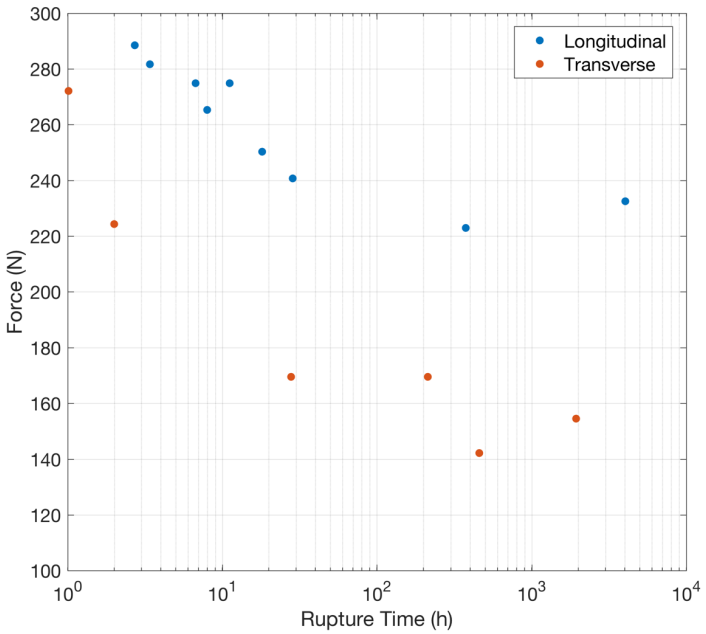


Figure 2.32: Stress-rupture data for small punch creep tests at 650°C [134].

The results of these tests showed anisotropy in creep strength, with the transverse direction being weaker than the longitudinal direction, but this difference is less strong than in conventional tests. This is due to the complex 3D deformation that takes place within small punch tests, meaning that the longitudinal tests were also being strained in the transverse direction, and delamination of grain boundaries parallel to the extrusion axis will also occur. Figure 2.33 shows the fracture surfaces resulting from small punch tests on samples (a) transverse to and (b) longitudinal to the extrusion direction. The transverse fracture surface shows the radial cracks also seen in the work by Hernandez-Mayoral *et al.* [122], but the longitudinal direction shows elongated cracks corresponding to delamination along grain boundaries of grains elongated in the extrusion direction. Whilst still being the stronger direction, this is the reason for the smaller levels of anisotropy between longitudinal and transverse directions than in conventional tests.

SPT has been shown to accurately represent trends in creep resistance, especially when comparing between different processing methods, but cannot necessarily be used as a quantitative tool due to the difficulties in quantifying the stress state

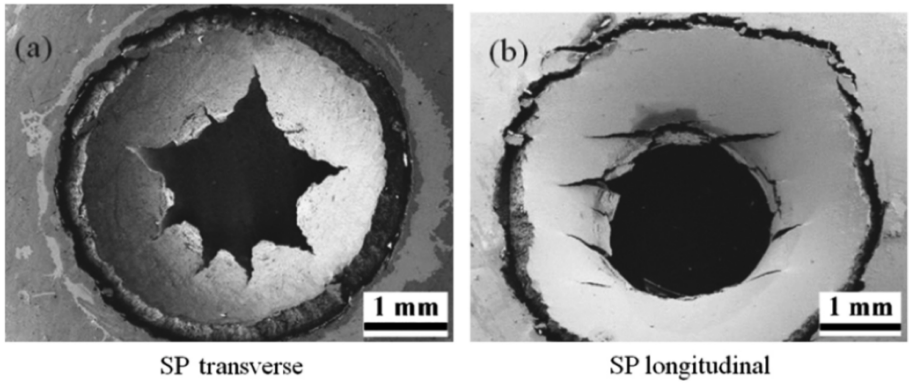


Figure 2.33: Small punch test failed specimens (a) transverse direction (b) longitudinal direction [134].

in the material. It will be used in this work as a validation of creep resistance comparatively between the different processing methods explored and give further clarification of the failure modes.

2.6.3 Important Considerations for Future Research

Throughout completion of this literature review, conflicting information has been found regarding the desired microstructure in a final tube cladding material. As demonstrated, Boulnat *et al.* [101] relate their high levels of ductility to the bimodal microstructure, with large grains allowing dislocation motion and work hardening, and nanograins relying upon superplasticity and grain boundary sliding at high temperatures to grant such ductility.

Other studies indicate equiaxed grains are considered key to making a good fuel cladding [46] and should be achieved by post deformation heat treatments. Work by Miao *et al.* [74] has shown that the bimodal grain structure may cause fracture, with the boundaries between hard small grains (high dislocation density) and coarser grains (almost dislocation-free) acting as fracture initiation sites. Their results suggest that producing alloys with a more uniform, finer distribution of grain sizes, lead to higher fracture toughness and a lower transition temperature. Similar effects, with the bimodal grain size distribution affecting the nature of the nucleation and propagation of cracks, reducing the creep rupture strength, was seen in work by Rogozhkin *et al.* [28] and Oksiuta *et al.* [135].

An investigation into the trade-off between low temperature strength (high dislocation and grain boundary density), high temperature strength (dislocation motion impedance and no weak interfaces) and high temperature ductility (strain hardening mechanisms) must be considered, especially for these high temperature, high pressure applications.

It should be borne in mind that ultimately what are suitable mechanical properties for an ODS steel will be determined through multi-physics fuel performance modelling considering all the relevant parameters of reactor operation and appropriate steel property relationships with respect to these, which is then qualified against actual irradiation testing. However, at present such models for ODS steels require greater information on the property relationship tests, which in turn would like greater clarity from the modelliing. It is a slight 'Catch 22' situation which can only really be progressed through gradual iteration between testing and modelling.

2.6.4 Mechanical Properties Summary

This literature search has confirmed the high variability in the mechanical properties generated in the production of ODS steel. As the material class is still in development, standards do not yet exist as to the required properties for these materials, so novel methods will be compared to current processing methods in order to ascertain success levels. Some new processing methods show potential in terms of microstructures being developed, but a lack of published mechanical properties to accompany them indicate a lack of success thus far within the field. This review gives a thorough description of the current state of the art within the field and acts as a good baseline for comparison of further novel work.

2.7 Literature Review Summary

As previously mentioned, the initial composition chosen for this work was selected to be Fe-14Cr-3W-0.3Ti-0.25Y_2O_3. This is similar to the already established 14YWT, which optimises corrosion resistance and fracture properties, but with increased W content and Ti content for increased low and high temperature strength with a higher density of complex oxides. Targets for achievable strengths and ductilities have been collated, and common problems resulting from processing defects identified. Several novel processing methods have been identified as areas for potential research, and the lack of mechanical property data, especially, has been identified.

Although irradiation performance is important, this thesis focuses on developing a method for economical production of appropriately microstructured ODS steel. Given the large amounts of information that exist in the literature on the irradiation performance of other ODS microstructures, these will be used as benchmarks to guide the present study. This saves the costs associated with performing extensive irradiation studies, as only limited irradiation studies need to be performed in the future on an optimised microstructure that can be produced through an up-scalable economical processing route that is relevant to industrial production.

3
Experimental Methods

Contents

3.1 Introduction 59
3.2 Processing 60
3.3 Sample Preparation 65
3.4 Powder Analysis 67
3.5 Characterisation of Consolidated Material 71
3.6 Chemical Analysis 77
3.7 Mechanical Properties 77

3.1 Introduction

Characterisation and mechanical testing of ODS steels can be complex, involving a number of techniques applied over varying length scales. For standard processing, the powder and the subsequent bulk material is usually viewed from the macro-scale down to the nano-scale, to analyse coarse pores down to fine-scale oxides. These oxides are at the resolution limit of conventional techniques and so advanced high resolution characterisation techniques are frequently also applied.

All work was completed by the author using equipment within the Department of Materials at the University of Oxford unless otherwise stated.

3.2 Processing

3.2.1 Raw Materials

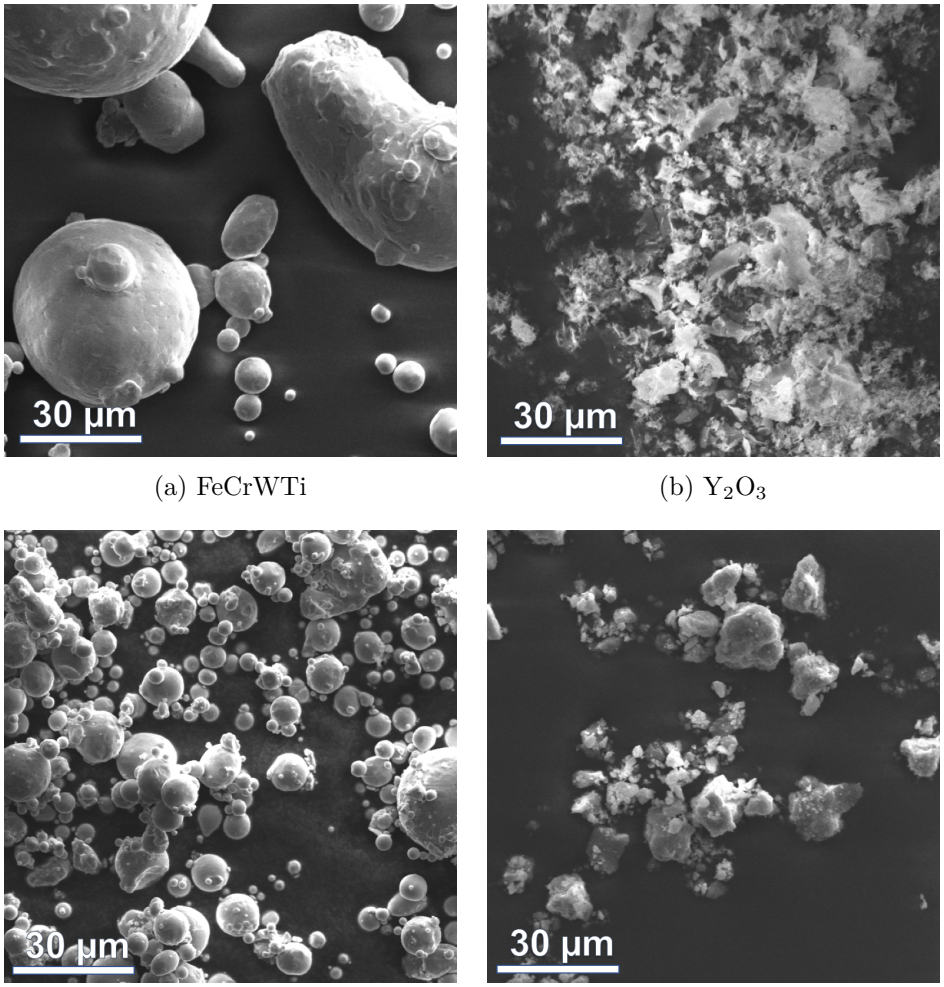
The four primary powders used were based on a pre-alloyed base powder of composition Fe-14Cr-3W-0.3Ti (wt%) with Y_2O_3, and on a pre-alloyed powder of composition Fe-14Cr-3W-0.3Ti-0.4Y (wt%) with a sacrificial oxide source of Fe_3O_4.

Fe-14Cr-3W-0.3Ti with mean powder particle size 40 μm, was supplied by Sandvik-Osprey Ltd., UK and paid for by NNL; Y_2O_3 99.999% purity with nominal particle size 20-40 nm, was supplied by PI-KEM Ltd., UK; Fe-14Cr-3W-0.3Ti-0.4Y with mean powder particle size 20 μm, (Sandvik-Osprey Ltd., UK); and Fe_3O_4 powder 99.5% purity with particle size 15-20 nm (US Research Nanomaterials Inc.), and the alloys are summarised in Table 5.6.

Element	FeCrWTi	FeCrWTiY
Fe	81.73	81.48
Cr	14.5	14.0
W	3.1	3.1
Ti	0.3	0.5
Mn	0.26	0.3
Si	0.1	0.2
C	0.01	0.027
Y		0.4
All other elements	<0.05	

Table 3.1: Chemical composition of pre-alloyed base powders from chemical analysis supplied by Sandvik-Osprey Ltd., UK.

The four powders can be seen in Figure 3.1. The pre-alloyed powders produced by gas atomisation were spherical as expected. The oxide particles had a strong tendency to agglomerate due to their high surface to volume ratio and resulting large electrostatic forces [136]. The average particle size of Y_2O_3 for example, as measured by laser scattering was $\sim$25 μm due to agglomeration.



(a) FeCrWTi (b) Y_2O_3

(c) FeCrWTiY (d) Fe_3O_4

Figure 3.1: SEM images of the powder size and morphology of four as-received powders.

3.2.2 Mechanical Alloying

Mechanical alloying was completed using a planetary ball, Fritsch Pulverisette model 5. This is a four station mill, capable of milling four pots holding 80 g of powder at once. A photo of the mill with two pots in can be seen in Figure 3.2.

The milling pots were made in house from X210CrW12 steel, while the milling balls were AISI 52-100 steel balls, 10 mm in diameter and 8 g in weight; their compositions are given in Table 3.2, chosen to avoid Ni which is a potent austenite stabiliser. Each pot was loaded with 80 g of powder and 800 g of milling balls to maintain a 10:1 ball:powder ratio. Loading and unloading were completed under an argon atmosphere within a glovebox.



Figure 3.2: Photo of the Fritsch Pulverisette model 5 used for milling.

Element	X210CrW12 pot	AISI 52-100 balls
Fe	Bal	Bal
C	2-2.3	0.98-1.1
Cr	11-13	1.3-1.6
Si	0.1-0.4	0.15-0.3
Mn	0.3-0.6	0.25-0.45
P	< 0.03	< 0.03
W	< 0.6-0.8	< 0.03
All other elements	$<$0.05	

Table 3.2: Chemical composition of milling pots and balls.

To reduce contamination between runs, after every milling cycle, pots were cleaned using the pre-alloyed powder on a short cycle to remove any embedded powder from the container walls or balls.

3.2.3 Sintering

3.2.3.1 Hot Isostatic Pressing

Hot isostatic pressing (HIP) was completed at the University of Birmingham at the Advanced Manufacturing and Processing Laboratory using an EPSI lab scale HIP.

Powders were canned in a mild steel can and degassed at 500 °C for 4 hours prior to crimp sealing and sintering. A schematic of the HIP set-up is shown in Figure 3.3.

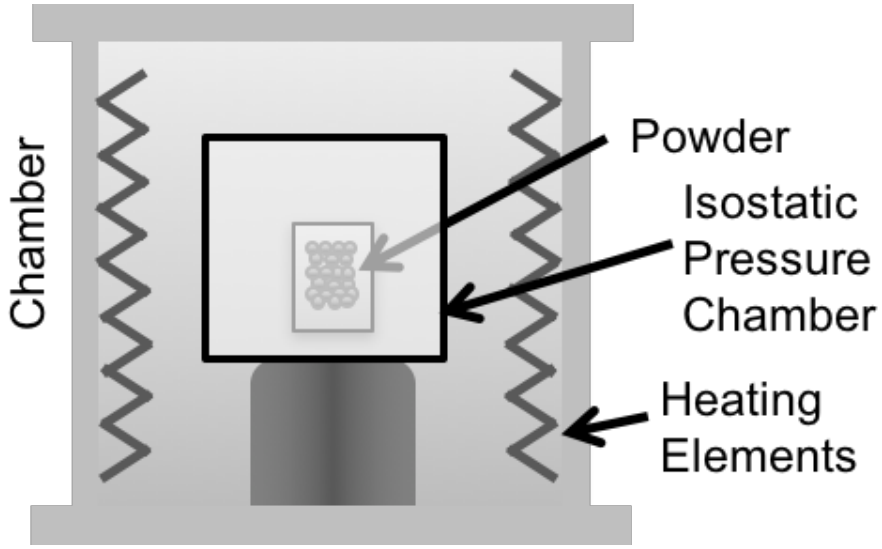


Figure 3.3: Schematic representation of HIP set-up.

The HIP allowed a maximum heating rate of 10°Cmin^{-1}, maximum dwell temperature of 1450°C and maximum pressure of 200 MPa.

3.2.3.2 Field Assisted Sintering

Field assisted sintering technique (FAST) was performed in-house using a Dr Fritsch GmbH DSP-507. The vacuum chamber was capable of achieving $< 5 \times 10^{-2}$ mbar using a rotary pump. The heating was provided by a DC current up to 4.2 V and 13 kA that passed through graphite electrodes above and below the cold pressed powder compact. The electrode position was controlled by a hydraulic press that also applied a uniaxial pressure. A schematic of the set-up can be seen in Figure 3.4.

The machine recorded parameters relating to sintering behaviour such as vacuum pressure, temperature from up to 6 thermocouples or pyrometer, electrode displacement, applied voltage and current.

Powder was placed within a cylindrical graphite die, with graphite punches at each open end. Sacrificial graphite paper protected the dies from bonding to the powder. This bonded to the compact during sintering and was removed using grit blasting but the outer 500 μm was discarded due to C-diffusion.

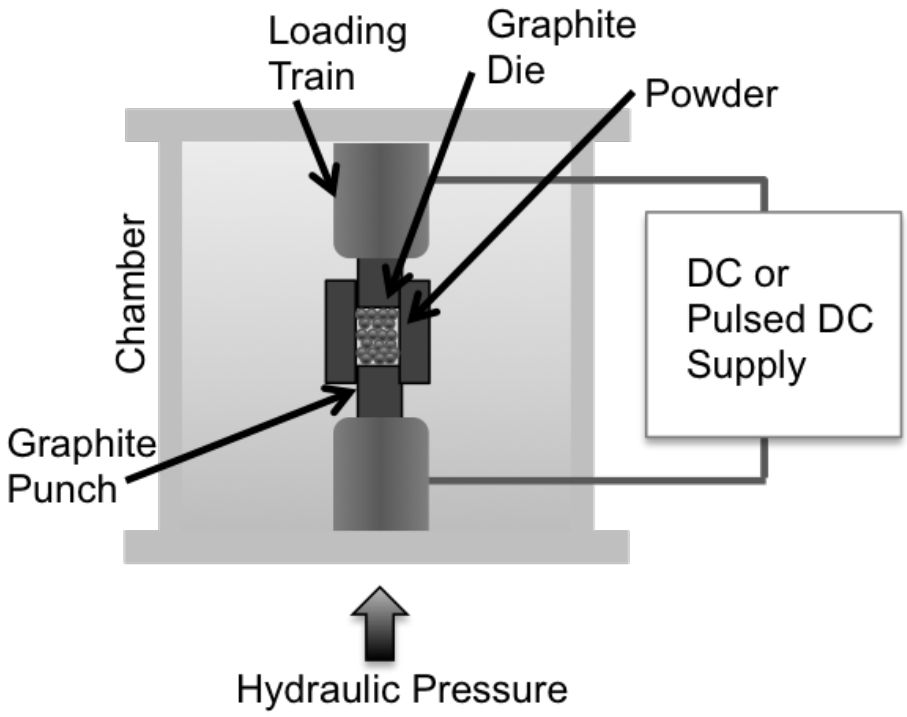


Figure 3.4: Schematic representation of FAST set-up.

Heating was controlled by varying the current and voltage to achieve the desired temperature using a proportional integral derivative (PID) controller. The PID constants for each material were obtained from a series of calibration experiments to ensure minimal overshoot as the hold temperature was approached. The PID constants are given in Table 3.3. Specific conditions for each set of experiments are given later.

PID	FeCrWTi	FeCrWTi + Y_2O_3	FeCrWTiY
P	0.842	1.316	2.306
I	33.9	32.8	35.4
D	8.5	8.2	8.8

Table 3.3: Optimum PID constants used in FAST experiments.

Initial sintering parameters, for 20 mm diameter and 10 mm thick samples, were a temperature of 1150°C and applied pressure of 50 MPa for 30 minutes.

3.2.4 Heat Treatment

A 'relaxation' heat treatment (annealing) of 750°C for 1 h was applied to all FAST samples to reduce hardness and increase toughness (restore some ductility) while also encouraging full development of any oxide particles if precipitation was incomplete [137]. Samples produced via HIP did not require this stage as they were exposed to high temperatures for much longer.

3.3 Sample Preparation

3.3.1 Powder

For SEM characterisation of particle size and shape, powder was distributed onto a carbon sticky pad attached to a microscope stub. For XRD analysis, powder was randomly distributed onto a Si substrate. For microhardness measurements and optical analysis, powders were mounted in cold resin and polished using the procedure below.

3.3.2 Consolidated Material

3.3.2.1 Sectioning

Samples were cut to the required size using waterjet cutting for rough cuts (Globel Jet Model 1212, jet width <10 mm and position accuracy of 0.05 mm) and final cuts using a gravity fed slow saw (Buehler Isomet low speed saw with a cubic boron nitride blade) for reduced damage on the faces to be polished.

3.3.2.2 Polishing

Oxide particles were easily plucked from the microstructure during polishing, and this was minimised by the method:

Grinding:

- 30s on 1200, 2500 and 4000 grit SiC paper with water lubrication

Polishing:

- 3 minutes semi-automated polishing with Struers DP-Suspension 3 μm polycrystalline diamond suspension on MetPrep Trounoire cloth
- 3 minutes semi-automated polishing with Struers DP-Suspension 1 μm polycrystalline diamond suspension on MetPrep Trounoire cloth
- 3 minutes semi-automated polishing with Struers DP-Suspension 0.25 μm polycrystalline diamond suspension on MetPrep Nap cloth
- 1.5 minutes semi-automated polishing with Struers OP-S 0.04 μm colloidal silica on a MetPrep Nap cloth with 1.5 minutes manual polishing on the same cloth using de-ionised water

The samples were rinsed with de-ionised water between stages and cleaned for 3 minutes in de-ionised water in an ultrasonic bath after the polishing process.

3.3.2.3 Focussed Ion Beam Liftout

Samples for TEM and APT analysis were prepared by focussed ion beam (FIB) liftout using both a Zeiss Auriga (operated by Robert Abernethy) and a Zeiss Crossbeam (operated by Gareth Hughes), with the guidance of conditions and area selection by the author. A typical series of lift out stages can be seen in Figure 3.5.

Figure 3.5 (i) shows the initial trenching stage with a layer of platinum (20 μm$\times$2 μm$\times$1.5 μm) protecting the region of interest, and trenches cut to a depth of $\sim$ 15 μm using a probe current of 3000 pA 2 μm either side of the platinum. The trench was polished back towards the platinum using 1000 pA Ga ions until the foil was thin enough to lift out. The foils were lifted out in-situ using a micromanipulator and bonded to a Cu grid using Pt deposition (Figure 3.5 (ii)). After adhesion to the surface of the grid, the needle was cut free and thinning was undertaken by progressive reductions in the beam current from 30 keV (Figure 3.5 (iii)) to 3 keV when the sample was partially transparent (Figure 3.5 (iv)).

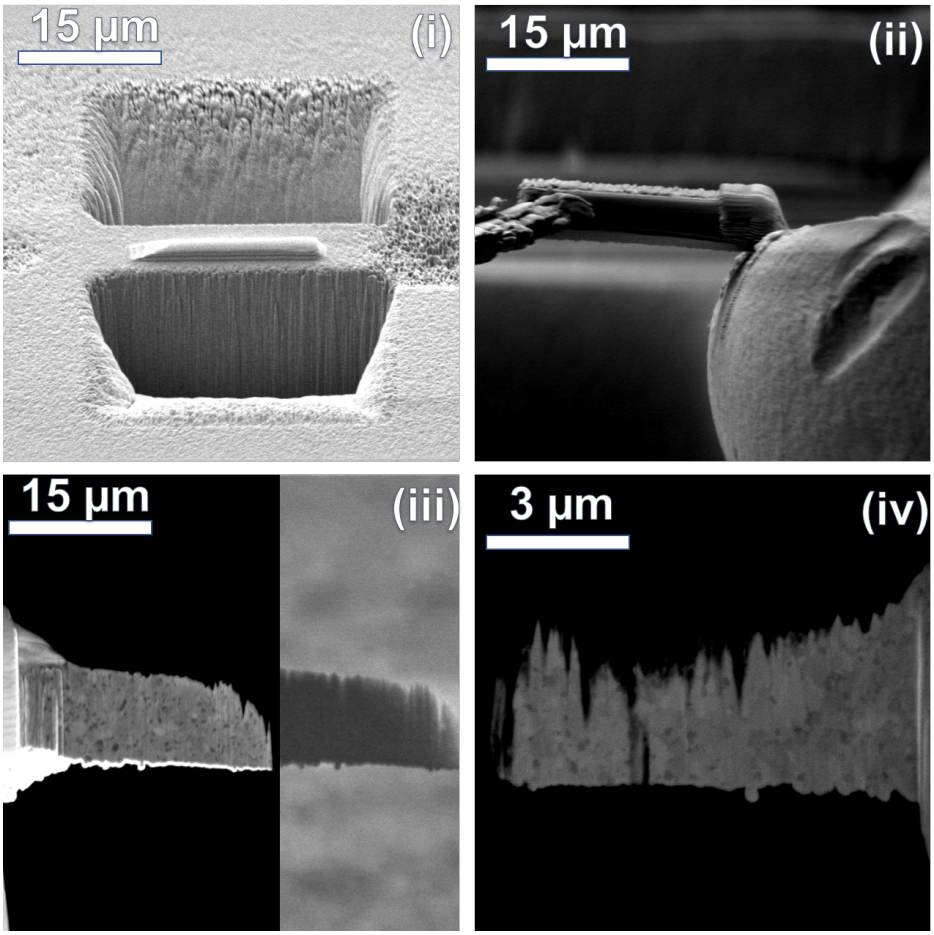


Figure 3.5: Series of stages of fib-liftout process.

3.4 Powder Analysis

3.4.1 Powder Size Distribution

The size and shape of powder, prior to, and post milling, was assessed using laser scattering and SEM, as described below.

3.4.1.1 Laser Scattering

Laser Scattering (LS) of the pre-alloyed and MA powder was completed using a Malvern Instruments Mastersizer 2000 [138]. The technique uses laser scattering from a dispersion of the powder suspended in de-ionised water, as shown schematically in Figure 3.6. This suspension passes through the focal point of two laser beams, and the angular variation in the intensity of scattered light is measured and

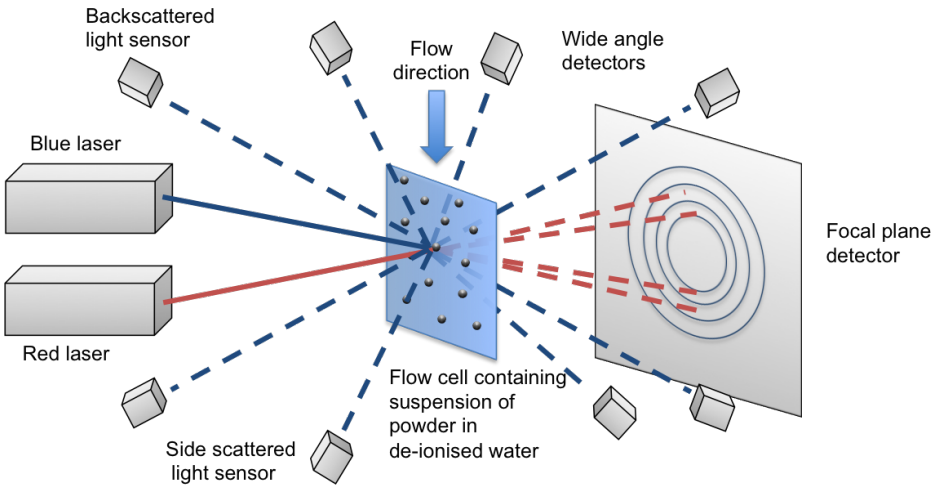


Figure 3.6: Schematic representation of laser scattering.

used to calculate the diameter of the particles: larger particles scatter the light at small angles relative to the laser beam, smaller particles scatter at larger angles.

The angular scattering intensity is analysed using the Mie theory of light scattering [139], assuming a volume equivalent sphere model. This series of algorithms uses the optical properties of both the suspension liquid and the powder (refractive index and absorption coefficient) as well as the powder density to infer particle sizes. The Mastersizer software uses irregular shape analysis to perform an iterative fitting of the powder size distributions until a best-fit is met in order to account for the non-spherical particles during milling.

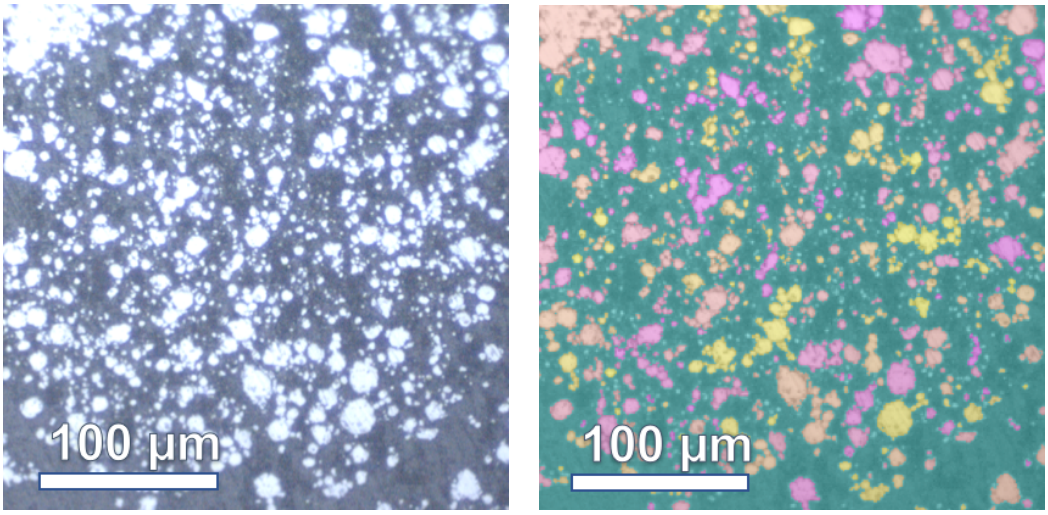
3-5 g of the powder was dispersed in de-ionised water until the efficiency of transmitted to detected light settled at between 10-20%. For each sample, 10 experiments were completed and the mean found. Mastersizer software analysed the distributions (using a refractive index for Fe of (2.81 [138])), and produced an average with a calculated standard error. Due to some non-spherical particles, either the major or minor axis of the particles was calculated depending upon the orientation of the particles relative to the lasers. This method therefore only gives approximate average diameters and visual analysis using scanning optical microscopy was also required to confirm that the morphology was spherical enough (i.e. not platelets or needle-shaped) and that powder agglomeration was sufficiently minimal for such analysis to be appropriate.

3.4.1.2 Scanning Electron Microscope Imaging

A Zeiss EVO Scanning Electron Microscope (SEM) was used for the image analysis of powders. This microscope uses a LaB_6 tip and was operated at 20 keV accelerating voltage, 200 pA probe current and a working distance of 10 mm.

3.4.1.3 Optical Microscopy

For analysis of small volumes of powders, optical microscopy and particle counting techniques were used. Resin mounted and polished powders were analysed at 10x magnification. Micrographs were analysed using Matlab Image Measurement tools for mean particle diameter. An optimum density of powder gave a sufficient number of powder particles (around 100 per image) to be representative, but without excessive overlap. Thresholding was manual to ensure distinction of particle boundaries. A typical optical image is shown in Figure 3.7 (a) and an example analysis overlaid image can be seen in Figure 3.7 (b). A multiplication factor of 1.4 to the mean of the data accounts for the probability of the powder not being sectioned across a diameter [140].



(a) Optical Micrograph of FeCrWTi+Y_2O_3 Milled Powder

(b) Corresponding Matlab Overlay and Thresholding

Figure 3.7: Example of particle counting using thresholding within the Matlab image analysis script (a) original optical image, and (b) threshold overlay to analyse particle area and thus equivalent spherical diameter.

3.4.2 Powder Density Analysis

Powder pour and tap density were measured using the method described in [141]. A 10 ml measuring cylinder, readable to the nearest 0.2ml, was filled with 25.0g of each powder. This technique is useful in terms of its simplicity and speed to apply in large industrial plants with the Hausner ratio (that of tap to pour density) for which values of less than 1.25 indicate good powder flowability and pressability i.e. suitability for consolidation.

3.4.2.1 Pour Density

The 25g of powder was poured into the cylinder using a fine funnel in the centre of the cylinder. The resulting height of the settled powder was measured and accurate weight of the powder within the cylinder measured to the nearest 0.001g. Errors may arise due to the uneven level of as-poured powder ($\pm$ 0.2 ml).

3.4.2.2 Tap Density

The powder within the cylinder was then subjected to a series of taps, each from approximately 3cm above the bench. As suggested in [141], T_5 (5 taps), T_{10} (10 taps), T_{20} (20 taps) and T_{50} (50 taps) were all recorded until no measurable change could be seen.

3.4.3 Powder Hardness

Resin mounted and polished powders were hardness tested using a weight of 10g to ensure powder was not pressed into the resin and small particles could also be tested, as necessary for the milled powders. 10 particles were selected at random for testing, and the mean and standard deviation obtained.

3.4.4 BET Surface Area Analysis

BET (Beunauer, Emmett and Teller) analysis was used to investigate the specific surface area (SSA) of each powder in a Micromeritics Gemini V. 1 g of powder was inserted into a test tube and dried using N_2 purging at 150°C, allowing any

outgassing for at least 2 h. Following evacuation of the gas within the container of known volume and cooling using liquid N_2, an adsorbate gas (N_2) was admitted in sufficient volume to give a relative pressure of $P/P_0 = 0.05$. The amount of gas adsorbed (V_a) was then calculated from the change in pressure. This process was repeated at successively higher P/P_0 values, up to 0.3.

Using the BET adsorption isotherm equation:

$$\frac{1}{\left[V_a\left(\frac{P_0}{P}-1\right)\right]} = \frac{C-1}{V_m C} \times \frac{P}{P_0} + \frac{1}{V_m C} \tag{3.1}$$

where V_m is the volume of gas adsorbed to produce a monolayer on the sample surface in ml and C is a dimensionless constant related to the enthalpy of adsorption of the adsorbate gas on the powder sample, and the term on the left hand side of the equation is called the BET value.

Figure 3.8 shows a plot of a series of BET values against their corresponding relative pressures, allowing calculation of the gradient and intercept. Using Equation 3.1,V_m and C were obtained.

The specific surface area S (m^2g^{-1}) can then be calculated:

$$S = \frac{V_m \times N \times a}{m \times 22400} \tag{3.2}$$

where N is Avogadro's constant, a is the effective cross-sectional area of one adsorbate molecule (m^2) and m is the mass of the powder (g).

3.5 Characterisation of Consolidated Material

3.5.1 Scanning Electron Microscopy

Scanning electron microscopy used a Zeiss Merlin unless otherwise stated.

3.5.1.1 Imaging and Energy Dispersive X-ray Spectroscopy

For high resolution imaging and energy dispersive x-ray spectroscopy (EDS), also known as EDX, an accelerative voltage of 5 keV was used, at a working distance of 8.5mm and probe current of 500pA. Secondary electron (SE) imaging used

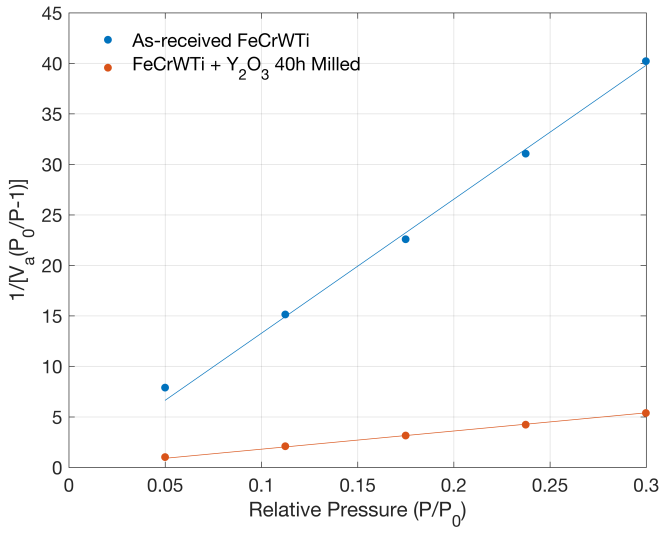


Figure 3.8: BET adsorption isotherm plot showing calculation for the SSA of the as-received base powder and Y_2O_3 milled powder.

an Everhart-Thornley detector, alongside an In-Lens SE detector and In-Lens backscattered (BSE) detector. When completing EDS, an Oxford Instruments X-Max^n 150 mm^2 Si drift detector with a Be window was used, at 10keV, required to capture the full range of elements, and a probe current of 500pA. Analysis of EDS data used Oxford Instruments Aztec software.

3.5.1.2 Electron Backscattered Diffraction

Electron backscattered diffraction (EBSD) used an accelerating voltage of 15 keV, and probe current of 10nA at a working distance of 17 mm. Maps were taken over two different sized regions per sample: 12 μm square region with point spacing of 100 nm, and 2 μm square with a point spacing of 20 nm. Samples were tilted to 70° and analysed using a Bruker Quantax EBSD system. Analysis used the MTEX package within MatLab and individual grains were identified by a misorientation angle >12° with at least 5 points per grain and a confidence index >0.1.

3.5.2 Transmission Electron Microscopy

TEM was employed to characterise fine-scale microstructural features.

3.5.2.1 JEOL JEM-2100

Using a LaB_6 source, this TEM (operated by Robert Abernethy of the Department of Materials) was used for imaging grain structures and particles. The accelerating voltage was 200 kV and particles were identified from under-focussed images [142].

3.5.2.2 JEOL ARM 200F

This instrument (operated by Dr Ian Griffiths of the Department of Materials) comprised a spherical aberration corrected cold-FEG TEM/STEM system equipped with a JEOL 100 mm^2 Centurio EDS detector and Gatan GIF Quantum 965 ER, the latter enabling dual electron energy loss spectroscopy (EELS) and energy filtered transmission electron microscopy (EFTEM).

STEM imaging was completed using dark field (DF) and HAADF detectors.

EELS spectra were obtained at a camera length of 2 cm using probe size 4C to maximise the output intensity, with a convergence angle of 30 mrad and collection angle of 40 mrad, and an entrance aperture of 5 mm.

Low-loss and core-loss regions were collected at a dispersion of 0.25 eV/channel from 10 to 500 eV and 400 to 900 eV respectively.

Major ionisation edges for elements of interest are listed in Table 3.4.

Analysis of EELS data was completed by Dr Matthew Blackmur, NNL, using Digital Micrograph 3 software.

3.5.3 Atom Probe Tomography

Atom probe tomography (APT) in an Imago local electrode atom probe 3000X HR system was used for 2 ODS samples. FIB liftout, polishing and APT experiments were completed by Thomas Davis, with analysis of the data collaboratively with the author. The AP was run using a pulse frequency of 200 kHz, cooled to 50 K, using a pulsed voltage. A 0.2% detection rate gave 12 million ions captured.

All data analysis included thresholding the elemental energy peaks to identify the respective elements then performing cluster analysis to identify oxides using the maximum separation method described in [69]. A maximum separation distance

Element	Edge	Electron-loss (eV)
Fe	$M_{2,3}$	54
	L_3	708
	L_2	721
Cr	$M_{2,3}$	42
	L_3	575
	L_2	584
W	$O_{2,3}$	36
Ti	$M_{2,3}$	35
	L_3	456
	L_2	462
Y	$N_{2,3}$	26
	$M_{4,5}$	157
O	K	532
C	K	284

Table 3.4: Major electron energy loss edges for elements of interest [143].

of 0.8 nm was chosen and the minimum number of core atoms to define an oxide cluster set at 17. The remaining atoms were included in a cluster within a distance of 0.6 nm and atoms on the interface eroded (removed) if within 0.6 nm from a matrix atom. 281 clusters were identified in the sample and a 3D reconstruction was completed. The Guinier radius (R_g) is commonly used to determine cluster size:

$$R_G = \sqrt{\frac{5}{3}} R_g \tag{3.3}$$

where R_g is the radius of gyration, defined as the average distance between each cluster atom and the centre of mass of the cluster.

3.5.4 X-ray Diffraction

X-Ray Diffraction (XRD) used a Bruker D5000 with Dr Philip Holdway as the primary operator. XRD was used for phase identification and for estimating the lattice parameters and crystallite size. The latter parameter describes the size of areas of order, separated by stacking faults, and so either describes grains or subgrains, dependent on plastic work and the accumulation of defects. For example, any broadening of Bragg reflections following MA is generally interpreted as a

result of crystallite size reduction. It is to be noted that measured crystallite size is typically significantly smaller than grain size measured by other microscopy methods.

The sample (either powder or bulk) was mounted onto a goniometer and placed within the X-ray beam. The goniometer rotated the sample so X-rays were incident between 10° and 120° (seen schematically in Figure 3.9). The resulting X-ray intensity spectrum over the range of angles was plotted and the Bragg reflection peaks identified.

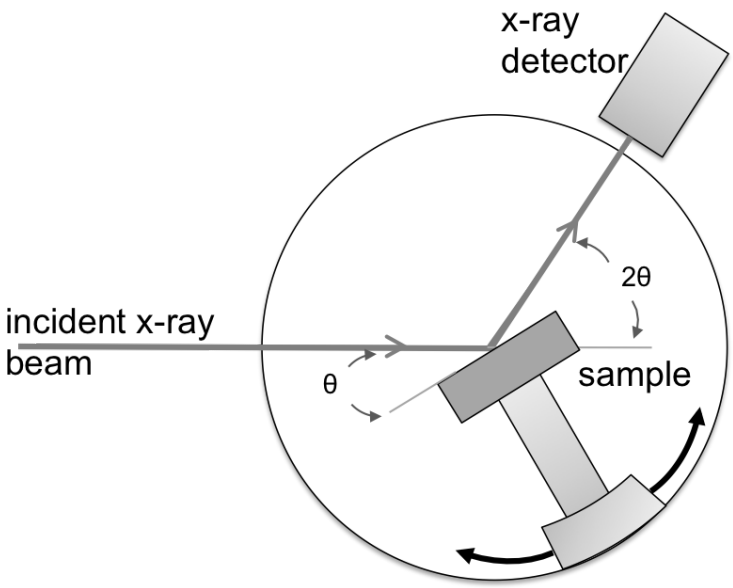


Figure 3.9: Schematic representation of XRD rig.

Broadening of peaks in the X-ray spectrum can arise from crystal imperfections and distortion, and a comparatively fine crystallite size, and these can be approximated using the following equations:

$$\epsilon \approx \beta_s / tan\theta \tag{3.4}$$

for microstrain (ϵ) contributions and:

$$D = \frac{k\lambda}{\beta_D cos\theta} \tag{3.5}$$

for crystallite size contributions, where β is the peak broadening, θ is the angle of maximum peak intensity, D is the crystallite size, k is a constant of value 0.94, and λ is the wavelength of the radiation (1.54056 angstrom for CuK_α radiation).

Combining:

$$\beta_{HKL} = \beta_s + \beta_D \tag{3.6}$$

$$\beta_{HKL} = \left(\frac{k\lambda}{Dcos\theta}\right) + \left(4\epsilon \tan\theta\right) \tag{3.7}$$

$$\beta_{HKL} \cos\theta = \left(\frac{k\lambda}{D}\right) + \left(4\epsilon \sin\theta\right) \tag{3.8}$$

Using the peak position and width to obtain the full-width-half-maximum (FWHM or β_{HKL}), the best-fit Williamson-Hall linear plot allows the separation of microstrain and crystallite contributions, with the gradient relating to microstrain and the intercept relating to crystallite size. An example from the milled powder completed in this work is given in Figure 3.10.

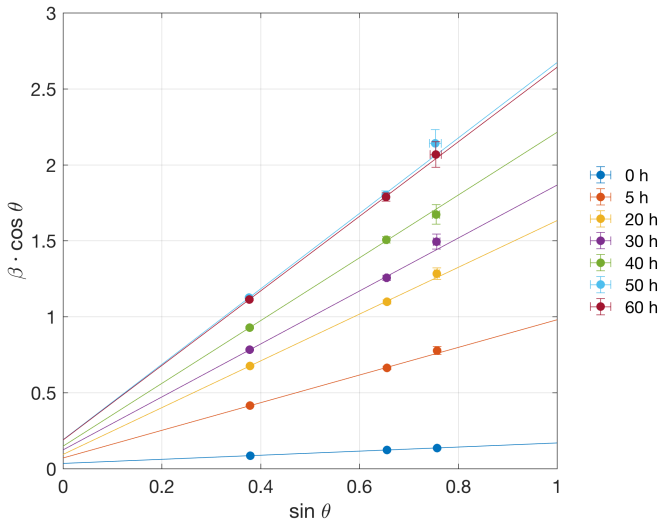


Figure 3.10: Separation of microstrain and crystallite size contributions to peak broadening

3.6 Chemical Analysis

3.6.0.1 Electron Probe Microanalysis

Electron Probe Microanalysis (EPMA) used a JXA-8800 microprobe, operated by Dr Chris Salter, and 20kV and current of 30nA. The technique is a microscopy based method of quantifying sample chemistry to more than 100ppm accuracy. A focussed electron beam (probe), is used to excite characteristic X-rays, dependent upon the atomic number of the contained elements. Wavelength dispersive X-ray spectrometers (WDS or WDX) detect and measure these X-rays allowing quantitative analysis based on known standards. Samples can then be characterised using a combination of SE and BSE imaging and elemental mapping. Exact detection limits are dependent on the particular element and on the combination of elements. The technique is capable of analysing samples between 5µm and 50mm in size, and contained particles down to ∼100 nm.

EPMA was used to investigate the distribution of elements across powder particles and bulk samples, in particular the spatial distribution of Y.

3.7 Mechanical Properties

3.7.1 Microhardness

Microhardness testing at room temperature used a Wolfson Instruments 402MVD Microindenter with a Vickers indenter diamond tip, loaded to 100 g and held for 10 s. Indentations used polished surfaces and average hardness and standard deviation taken from 10 indents placed randomly. Microhardness measurements were converted from H_v to MPa throughout.

Hot microhardness was performed on an in-house instrument using a sapphire indenter up to 700°C on polished samples mounted on alumina stubs using Ag dag. Tests were carried out using a 200 g load for 20 s under a $<1\times10^{-4}$ vacuum. Unfortunately the machine failed between the first material produced and the next and so only one sample was investigated.

3.7.2 ETMT

Tensile testing was conducted between room temperature and 650°C on a 5 kN Instron electro-thermal mechanical testing (ETMT) machine. Miniature specimens had a cross section $1 \times 1mm^2$ and a gauge length of 14 mm and overall length of 36 mm. Samples were obtained using wire-based electrical discharge machining (EDM) for 1 mm slices, then water jet cutting to a dogbone shape; samples were polished with 1200 grit SiC paper.

Temperature measurement during testing was achieved by spot-welding a K-type thermocouple to the centre of the specimen gauge. Specimens were heated in air using electrical resistance. A constant strain rate of $1 \times 10^{-4} s^{-1}$ was used for all tests.

Engineering strain was used as a measure of ductility, defined as $\epsilon = [(L_f - L_0)/L_0]$ where the gauge length, $L_0 - L_f$ was monitored using digital image correlation following a thermal paint pattern on the central 5 mm of the specimen, where temperature and therefore deformation is uniform [144]. Rapid heating and cooling rates achieved by the electrical resistance combined with short testing cycles meant oxidation was minimised. All testing was undertaken by Sabin Sulzer.

3.7.3 Small Punch Testing

Small punch testing (SPT) simulated accelerated creep testing in a MeT1 system (Pheonix Calibration and Service Ltd). The equipment was based in the Materials Testing Team at UKAEA Culham, jointly owned by UKAEA and NNL, and testing followed ASTM E 643-15.

A schematic of the set-up can be seen in Figure 3.11. A 8 mm wide, 0.5 mm disc (tolerance ±0.5 microns) was clamped into a die set circumferentially, to a pre-set torque. Samples were cut to 0.6 mm thickness using a Buehler Isomet low speed saw then hand polished using 600 and 1200 grit SiC paper. A 1 mm radius spherical WC indenter was pushed down vertically onto the sample disc centre, either under constant displacement rate (for breakthrough tests) or constant load (for creep tests). As the material deformed under the indenter and 'bulged' into the cavity below, a low friction alumina probe connected to a positional transducer free

to move in the vertical plane (sensitive to ±1 nm) measured the deflection of the distorting (creeping) surface. A photo taken during a test at 650°C (Figure 3.12) shows the infra-red heaters used to achieve the temperature. Thermocouples were inserted into holes within the die set, as close to the sample location as possible, and a PID controller maintained a constant temperature. To prevent oxidation, the chamber was firstly flushed with Ar at 10 L/min and then 0.5 L/min during testing. To allow stabilisation of temperature, a hold period of 30 minutes prior to beginning testing was used. During the tests, data was taken at a sampling rate of 1 Hz.

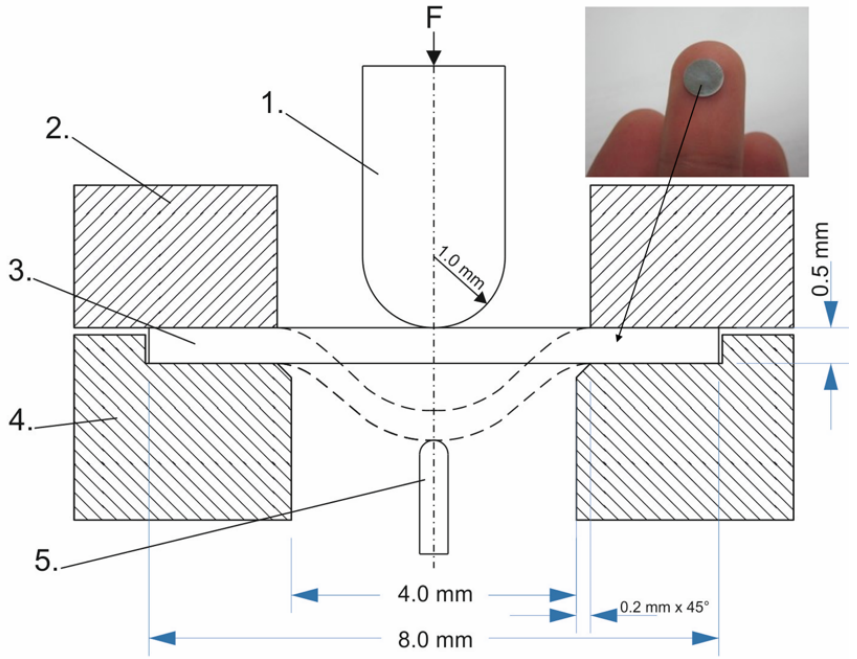


Figure 3.11: Schematic drawing of SPT set-up 1. WC punchhead 2. Top of die set 3. Sample 4. Bottom of die set 5. Displacement extensometer Inset. e.g. sample [133].

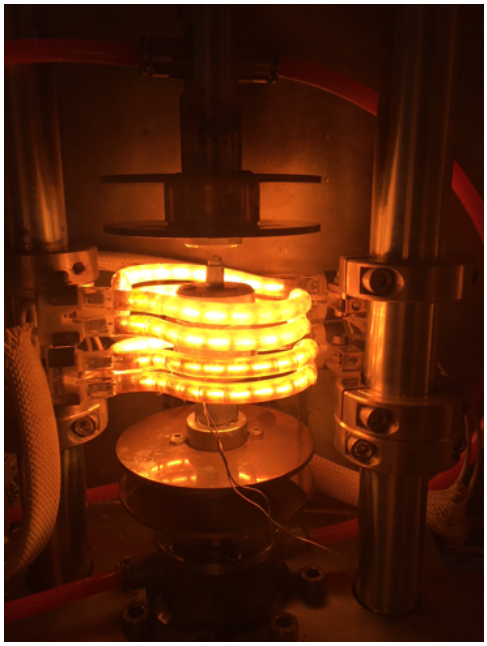


Figure 3.12: Photograph of SPT apparatus at 650°C.

4

"Industry Standard" Material

Contents

4.1 Introduction 81
4.2 Microstructural Analysis 83
4.3 Thermal Stability 83

4.1 Introduction

This Chapter describes investigations as part of the EU FP7 MatISSE project, administered by the European Energy Research Alliance (EERA) Joint Program for Nuclear Material (JPNM). EERA JPNM is a voluntary combination of thematic projects from 27 partners related to materials used in fuel and structural elements for safe and sustainable advanced nuclear systems.

Key priorities of the JPNM are: pre-normative research in support of ESNII (European Sustainable Nuclear Industrial Initiative) systems, ODS steels, refractory composites for the high temperature fuel applications, and development of predictive capability. Within the sub-programme of ODS steels, the primary objectives were to produce, characterise and test ODS in their progression to near reactor ready, thin-walled tube format. Critically for this thesis, liaison with the MatISSE group

allowed access to state-of-the-art ODS steels for nuclear applications. This material helped to provide a validated comparison for material developed in the thesis in terms of microstructure, mechanical properties and high temperature stability.



Within the University of Oxford / NNL contribution to MatISSE and JPNM, specific responsibility was assigned to the thermal stability of thin wall ODS steels, which had not been previously investigated. Analysis of the thermal stability under reactor suitable conditions was critical in the wider assessing of suitability for industrial use. Particularly important was the potential for grain growth to sizes comparable to the wall thickness and any associated degradation of mechanical properties.

As part of the MatISSE project, a 30 mm length of Fe-14Cr-1W-0.3Ti-0.25Y_2O_3, 12 mm diameter 0.5 mm wall thickness tube was donated by CEA for the purpose of this research. The tube was manufactured by de Carlan *et al.* at CEA from pre-alloyed Fe-14Cr-1W-0.3Ti powder combined with Y_2O_3 in an attritor mill for 12 hours [145]. The milled powder was sealed into mild steel cans where it was preheated, degassed and evacuated. The powder containing can was then directly extruded at 1100°C to a rod. A series of cold pilgering and intermediate heat treatment stages allowed progressive reduction of the inner radius and wall thickness before a final heat treatment (750°C/ 1 h) was applied to allow relaxation of the microstructure. Full details of the tube processing history is given in Loge *et al.* [146].

The resulting material is termed the 'Industry Standard' and provides a benchmark for comparison of the material described in this thesis. All property data for the alloy was-received through Oxford University's participation in the MatISSE collaboration, with credit given to the relevant authors and institutions.

4.2 Microstructural Analysis

The microstructure analysis was investigated first using SEM and EBSD to ensure the material was consistent with previous reports and with that received by others in the MatISSE project.

Figures 4.1(a) and (b) show false-coloured EBSD orientation maps of the as-received tube with misorientation of more than 15° shown by the black grain boundaries, in the longitudinal (extrusion) direction and transverse (perpendicular to extrusion) directions respectively. There was highly defined extrusion texture with grains elongated in the extrusion direction i.e. despite a final heat treatment, the strong extrusion texture of highly elongated grains was retained.

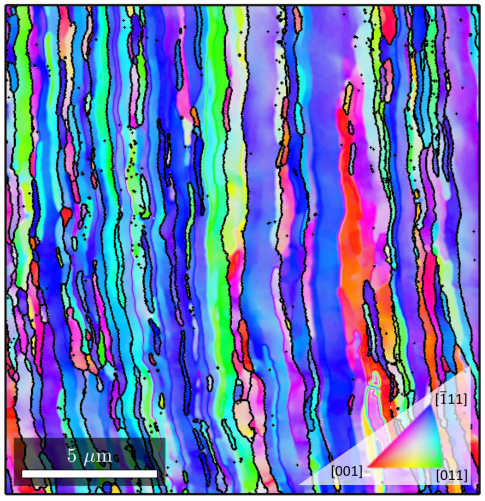
The three primary pole figures for the longitudinal direction in Figure 4.1(c) show the 'α-fibre' texture that typically develops during extrusion of bcc materials, characterised by the alignment of $\{001\} < 110 >$ and $\{112\} < 110 >$, alongside the 'γ-fibre' $\{111\} < 110 >$ [147].

Figures 4.1(a) and (b) show retained misorientation within many grains, suggesting the presence of sub-grains (indicated by variations in colour within each grain) and that some residual work from the extrusion / pilgering deformation was retained within grains, and that recovery has not yet been fully completed. There was no compelling evidence for widespread recrystallisation.

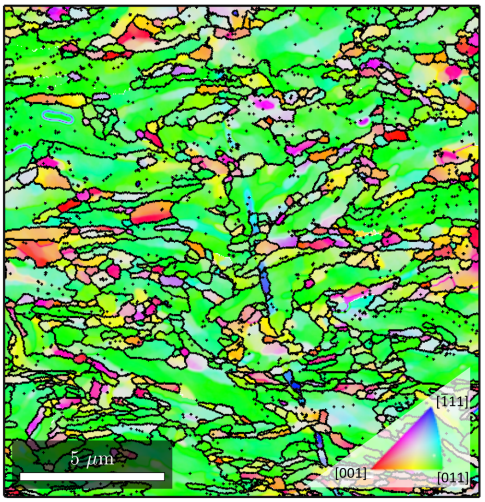
4.3 Thermal Stability

Given the identification of residual work within the as-received microstructure, the effect of a more prolonged thermal age treatment at 750°C (reactor relevant temperature) was investigated. The motives were to identify any further initial microstructural relaxation and then any longer term microstructural degradation caused by excessive grain or particle growth.

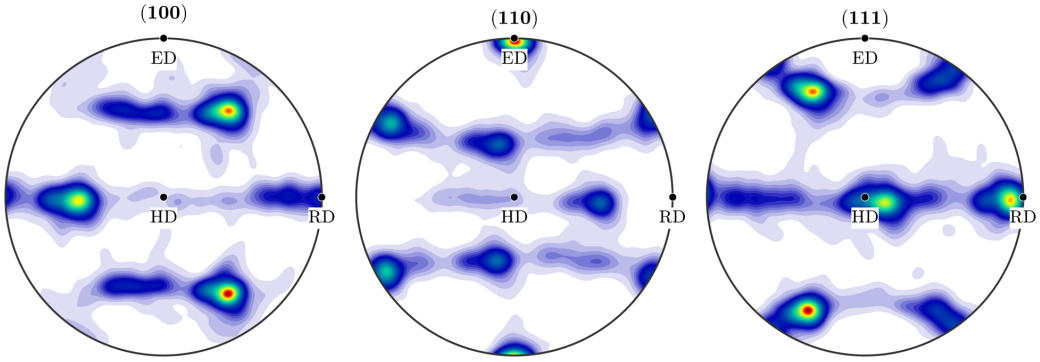
The ageing conditions are given in Table 4.3. Note that for each set of conditions, a separate sample was used, so microstructural features would not be tracked explicitly although samples were large enough to ensure that the area analysed was



(a) Longitudinal direction



(b) Transverse direction



(c) Pole figures for the longitudinal direction

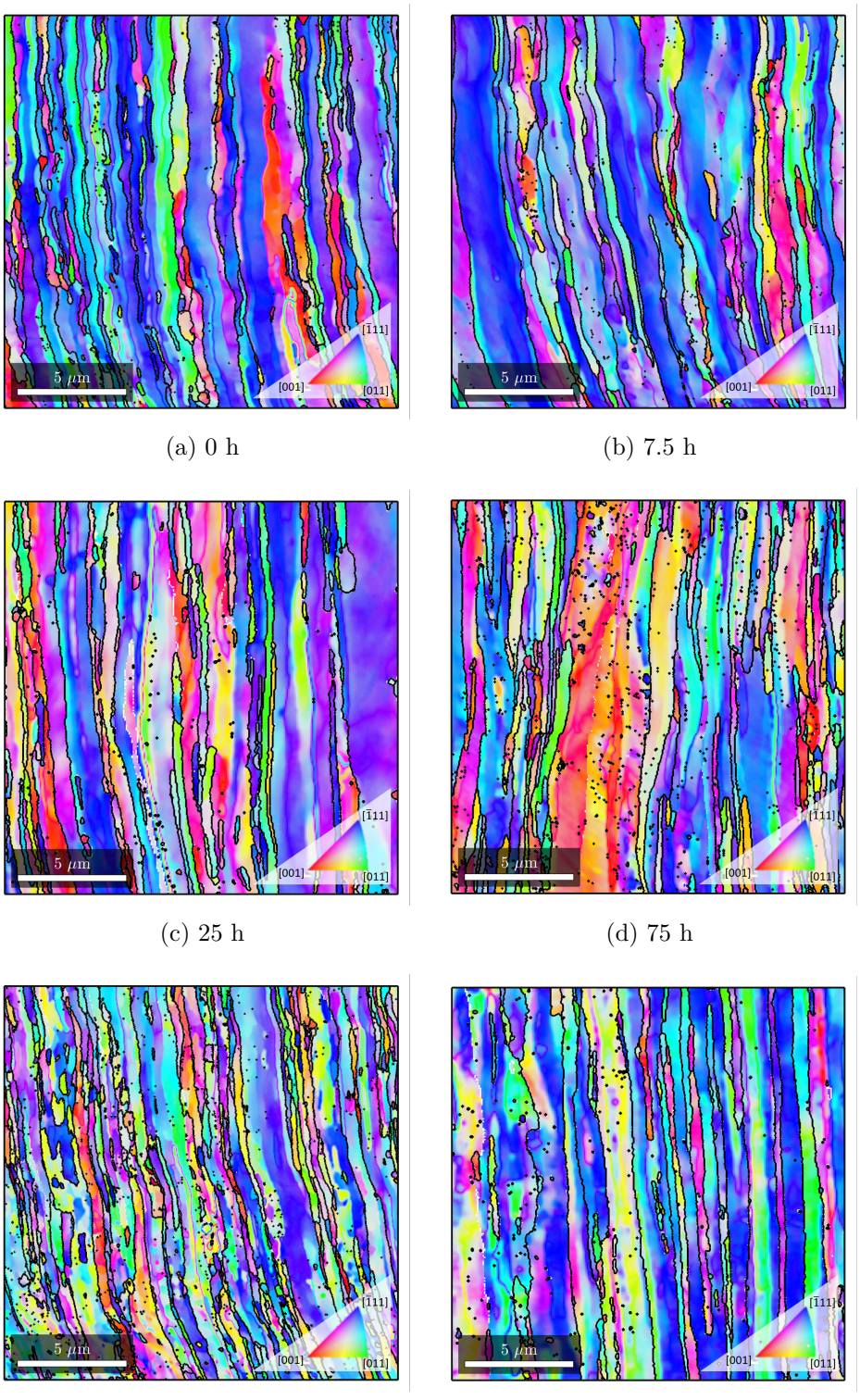
Figure 4.1: false-coloured EBSD orientation maps of the Fe-14Cr-1W-0.3Ti-0.25Y_2O_3 as-received tubes in the (a) longitudinal and (b) transverse directions with (c) corresponding pole figures for the longitudinal direction.

representative. The first four samples (0-10 h) were chosen to analyse microstructural relaxation under short term ageing, and the second four (25-675 h) to analyse the longer term effects of this temperature.

Sample	Ageing Time
1	0h
2	5h
3	7.5h
4	10h
5	25h
6	75h
7	150h
8	675h

Figures 4.2 (a) to (f) show a series of false-coloured EBSD orientation maps at various stages of thermal ageing. Surprisingly, the residual extrusion texture was preserved throughout, with elongated grains continuing to be orientated parallel to the extrusion direction. The slight curvature towards the bottom of each image was an artifact due to drift within the microscope over long EBSD scans.

Post-processing of the EBSD data from the three primary (100), (110) and (111) pole figures also confirmed the stability of the deformation texture. Figure 4.3 shows the pole figures for as-received and following 675 h of ageing at 750°C, demonstrating equivalent textures (albeit different sub-sets of the same family of planes).

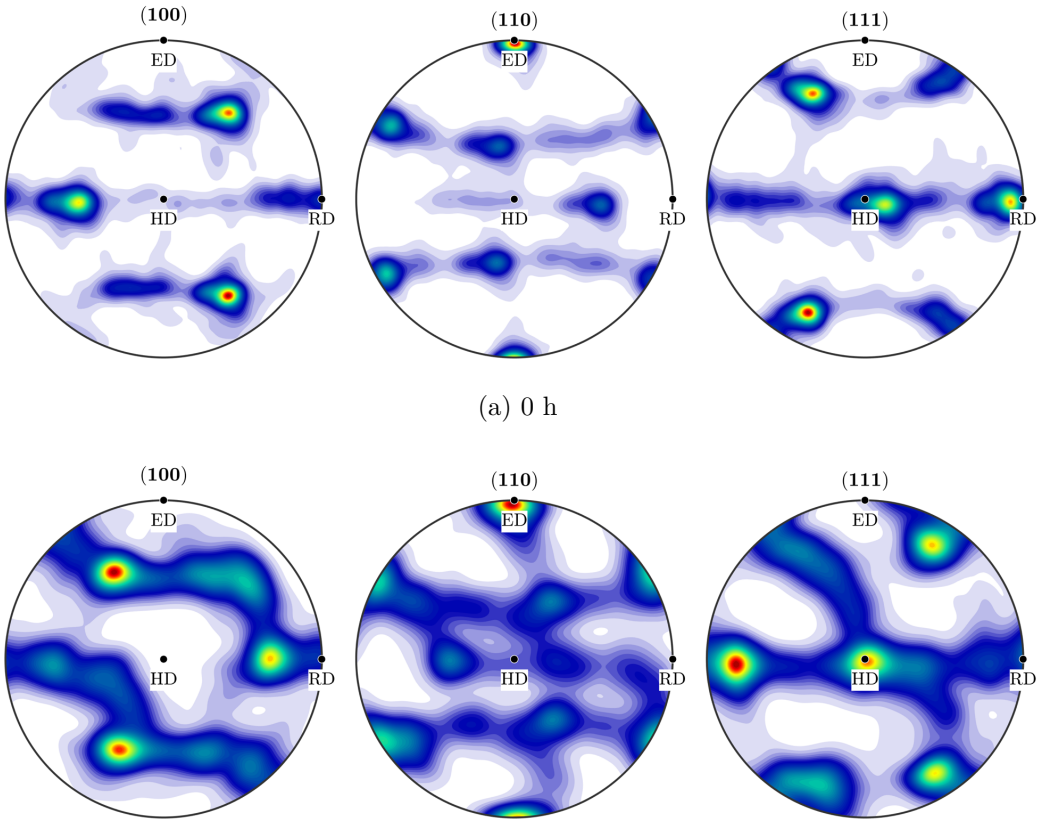


(a) 0 h (b) 7.5 h

(c) 25 h (d) 75 h

(e) 125 h (f) 675 h

Figure 4.2: false-coloured EBSD orientation maps of Fe-14Cr-1W-0.3Ti-0.25Y_2O_3 extruded tubes following thermal ageing for (a) 0 h, (b) 7.5 h, (c) 25 h, (d) 75 h, (e) 125 h, (f) 675 h at 750°C.



(a) 0 h

(b) 675 h

Figure 4.3: Pole figures for the as-received and 675 h aged microstructures.

Figure 4.4 shows the stability of the hardness and the ferrite grain size over the ageing period. Due to the elongated nature of the grains, grain size was a measure of grain width rather than length as length was unquantifiable over the scan region. Grain width was stable over the ageing time, and even hinted at a slight decrease rather than the expected increase. This may be due to the highly worked microstructure relaxing into sub-grains, developing into grain boundaries (15° misorientation). Microhardness was also stable, although after 7.5 h and 10 h there was a slight drop in hardness from ∼4 GPa to ∼3.9 GPa. Again, this could be indicative of a restricted extent of recovery. Samples aged for 25 h were perhaps slightly harder (4 GPa), perhaps due to residual precipitation, but overall, hardness remained stable across all samples. As 750°C is the tempering temperature for high Cr steels, other thermal stability studies of ODS steels have shown that carbides may form, which might also contribute to the slight hardening at ∼10 h [148].

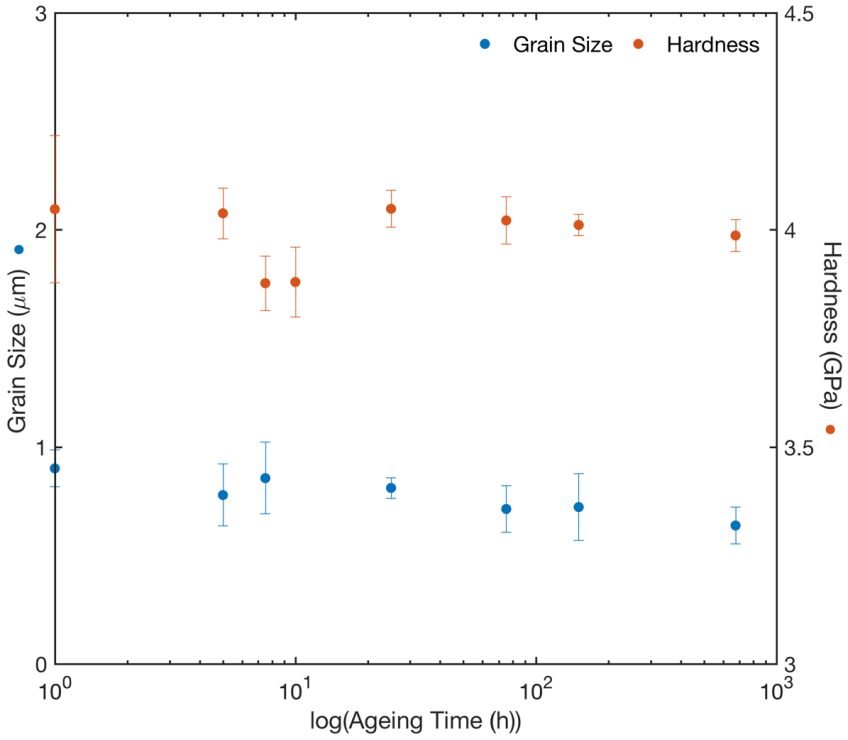


Figure 4.4: Grain size and hardness of Fe-14Cr-1W-0.3Ti-0.25Y_2O_3 extruded tubes as a function of ageing time.

The average ferrite grain size of just under 1 μm was slightly larger than expected from literature [84]. A hardness of ~4 GPa was consistent with previous work. The key finding was that the fine-scale ferritic microstructure was strongly stabilised, even after prolonged thermal exposure. The MA / extrusion route was effective at creating a high number density of grain boundary stabilising Y-based nano-oxides.

The full results of the collaborative project are given in the final MatISSE report [149].

5

Fabrication of ODS Steels: Powder Production

Contents

5.1 Introduction 89
5.2 Milling parameter study 91
5.3 Y-containing pre-alloyed powder 105
5.4 Comparison Between Powders 113
5.5 Summary 115

5.1 Introduction

The main limiting factor for scaled up production of ODS steels by the most popular powder processing route is the time-consuming milling process. Alternatives such as melt processing are difficult to apply despite many years of research. The milling process relies upon mechanical alloying (MA) - which leads to non-equilibrium microstructures - followed by sintering during which consolidation and microstructural relaxation towards equilibrium phases occurs, along with the possibility of grain and cluster coarsening. Although practised at the R&D scale and in semi-commercial production, extended processing time, small batch

size, high cost of powders and tendency for contamination all hinder a MA-based process at an industrial scale.

To explore more efficient variants of the conventional MA route, two approaches were explored.

First, to minimise the milling time required to produce a suitable ODS powder (in terms of size and shape, levels of mechanical work and Y distribution) using a high energy planetary ball mill. The evolution of the key characteristics of the powder, microstructural evolution and Y distribution at different stages of milling were explored, with the aim of identifying the fastest route to powder that was acceptable for further downstream processing.

Initial milling parameters were taken from previous work on similar materials within the Processing of Advanced Materials Group [39]. In these works, reaching a microstructural steady-state was prioritised, in terms of Y-breakdown and its distribution. With the focus here on industrial scale up posibilities and alternatives, it was hypothesised that these conditions were overly conservative and a shorter milling time could be developed.

Second, it was hypothesised that inert gas atomisation of a Y-containing ferritic steel melt into powders could be used to form a supersaturated solution of Y in Fe(Cr). Then, in the presence of a suitable O source, as the Y is rejected from solution on subsequent heat treatment (due to the very low equilibrium solubility of Y in Fe, see the Fe-Y phase diagram in Figure 5.1) it simultaneously forms a fine Y-O based dispersion. Milling may still be required but only comparatively briefly to distribute a sacrificial source (Fe_3O_4) around each Fe(Cr,Y) based powder particle i.e. there was no requirement to dissolve Y_2O_3 particles. This approach is termed "internal oxidation" and has similarities to GARS / STARS routes, described in the literature review. It was a more speculative route to ODS-type microstructures, but may offer potential for time reduction, scale-up and reduced cost. This Chapter addresses the findings of these investigations.

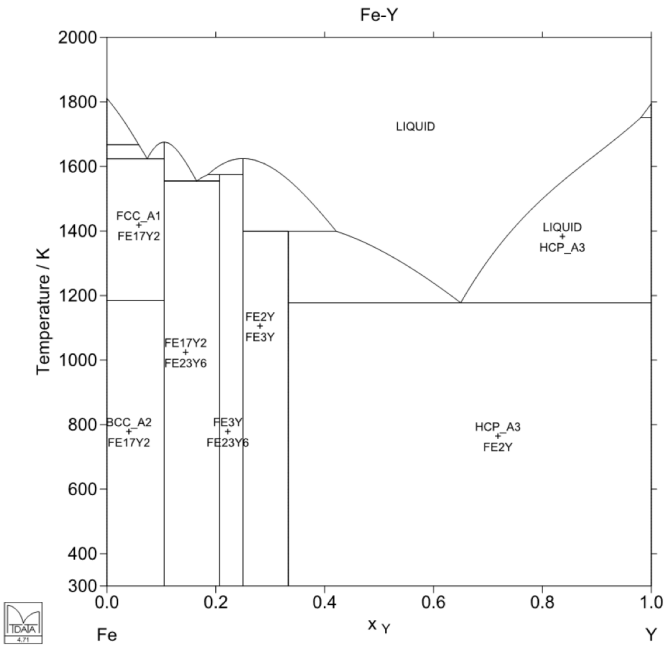


Figure 5.1: Fe-Y phase diagram [150].

5.2 Milling parameter study

Planetary milling is a high energy milling process that causes the physical mixing of powders through continuous particle work hardening and cold welding, and fracture during interactions between the grinding medium (milling balls) and the powder. Centrifugal forces cause the milling balls to press against the wall of the milling vial (frictional effects cause grinding of the material) while the off-axis planetary orbit motion flings the balls across the vial periodically to collide with the opposite wall, causing impact with the powder.

Due to the high energy of this process, the mill heats up and a pause in milling must be applied to let the container and powder cool back down to continue effective milling. The pause is generally twice the length of the milling time, i.e. a ratio of 1:2.

Some sources have suggested that the milling process is only effective at the beginning of a milling cycle when the balls and powder are in contact with the container walls, and that after prolonged time in this condition, the powder and balls settle to the bottom of the containers, making milling much more ineffective

and leading to unnecessarily prolonged milling times [151, 152][1].

Thus, with the aim of making milling more efficient, stopping and restarting milling more frequently within the same total milling time might promote greater overall milling efficiency, and a number of different mill:pause ratios were investigated. Then, the most successful mill:pause ratio was examined in more detail to establish the minimum necessary total milling time required for powders with suitable characteristics for consolidation processing.

5.2.1 Milling cycle length

The milling ratios of 5:10, 10:20, 20:40 and 30:60 minutes (shown schematically in Figure 5.2) were chosen and all other parameters, including total milling time, unchanged and as given in Section 3.2.2.

Initially, the effects of milling parameter changes were investigated through changes in hardness and powder diameter. Due to the large number of samples taken (10-15 per set of parameters) throughout the milling experiment, and the need to maintain as close to 10:1 ball to powder weight ratio (BPWR), 0.6g of powder was taken from the milling vial at each sampling point. Powder size distributions were analysed using optical microscopy followed by MATLAB-based image analysis as described in Section 3.4.1.3.

Figure 5.3 (a) and (b) show the effect mill:pause ratio on hardness and powder diameter respectively, both as a function of total milling time. For all cycle lengths, hardness increased with milling time due to work hardening, an increase in dislocation density and the accumulation of strain energy within the powder, to a final hardness of $\sim$ 14 GPa. From these data, the initial hardening rate (IHR) and the plateau hardness were studied. Both the IHR and plateau hardness were lowest in the 5 min cycles. Overall, the 20 min cycle had the highest IHR but plateau hardness and the time taken to reach the plateau hardness was essentially insensitive to mill:pause ratio when measurement error was taken into account.

[1]Report read and cited with permission of Sellafield Ltd

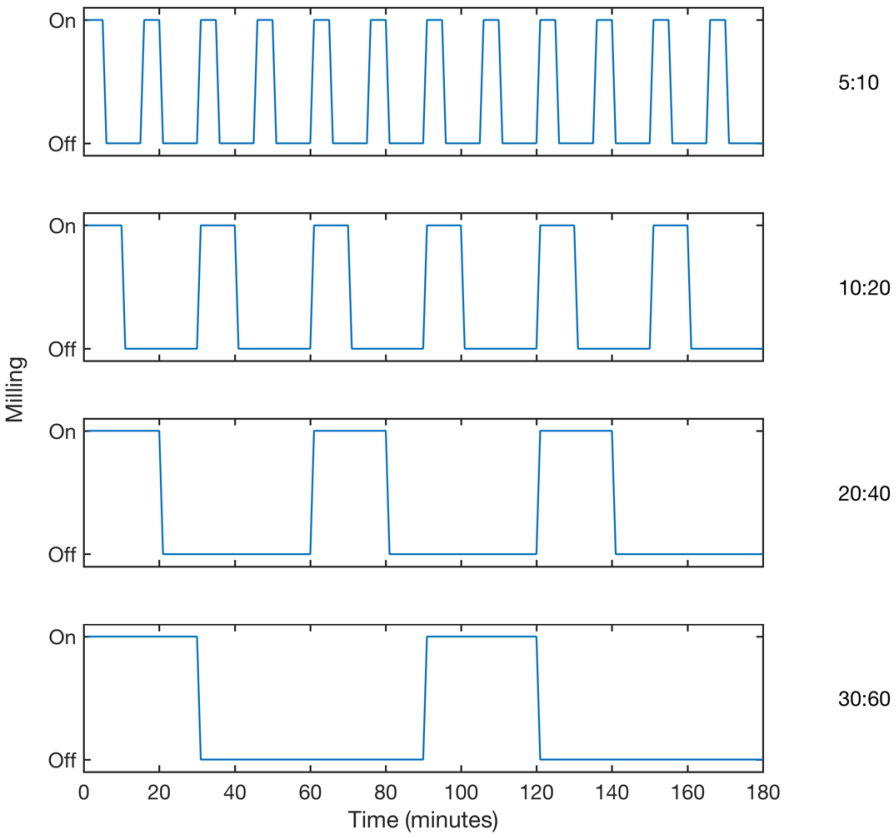


Figure 5.2: Schematic of the mill:pause ratios explored in this study.

Initially, cold welding of powder particles dominated, leading to an overall increase in powder particle size. The continued work hardening and dislocation build up eventually exhausted plasticity, leading to fracture of particles and a reduction in mean particle diameter to a plateau of < 30 μm.

The similarity in hardness and powder size suggested that milling efficiency was independent of the number of milling stops and starts. This was interpreted as suggesting that the rotation speed was sufficient that the balls and the powders remained in contact with the milling container for the duration of milling, rather than settling to the bottom. This is called the impact and friction regime, where balls collide, skirt the vial wall and leave at another point to collide on the opposite wall.

After 60 h milling, powder diameter was more accurately assessed using laser scattering and the powder packing density measured using the tap density method

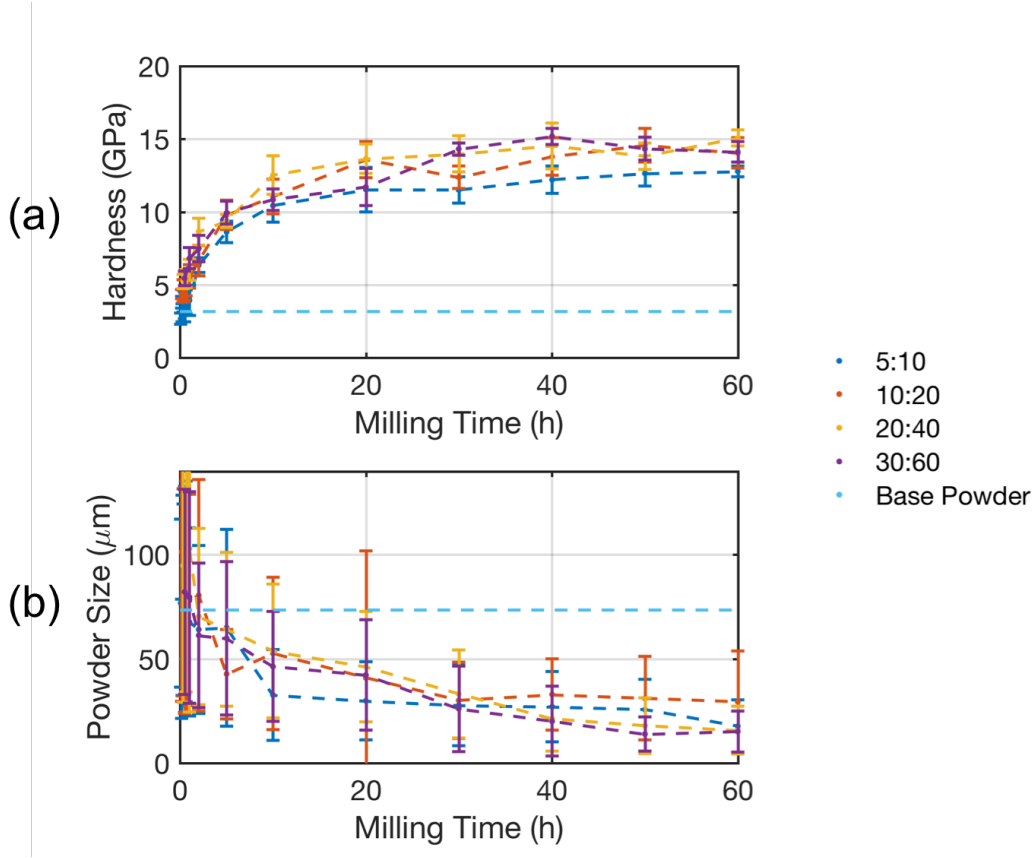


Figure 5.3: (a) hardness and (b) powder diameter as a function of milling time for each mill:pause ratio.

described in Section 3.4.2. Laser scattering measures the diameter of a large number of powder particles, giving much more representative results than optical analysis. The powder was then sintered using the procedures and parameters described in Section 3.2.3.2 and the resulting sintered density calculated. Figure 5.4 (a) shows the tap density of the powders alongside their (number) average diameter, both as a function of the chosen mill:pause ratios for a total milling time of 60 h. Figure 5.4 (b) shows the sintered density and hardness of 20 mm diameter 10 mm thick compacts using the Fe-14Cr-3W-0.3Ti+Y_2O_3 powder after 60 h of milling again as a function of the mill:pause.

Powder diameter was approximately constant at 15 μm and essentially independent of milling ratio. Similarly, the powder tap density showed little systematic variation with mill:pause at $\sim$ 3.75 g/cm^3. After sintering, the sintered hardness was constant at $\sim$ 7.5 GPa and density constant at $\sim$ 7.6 g/cm^3, except at the

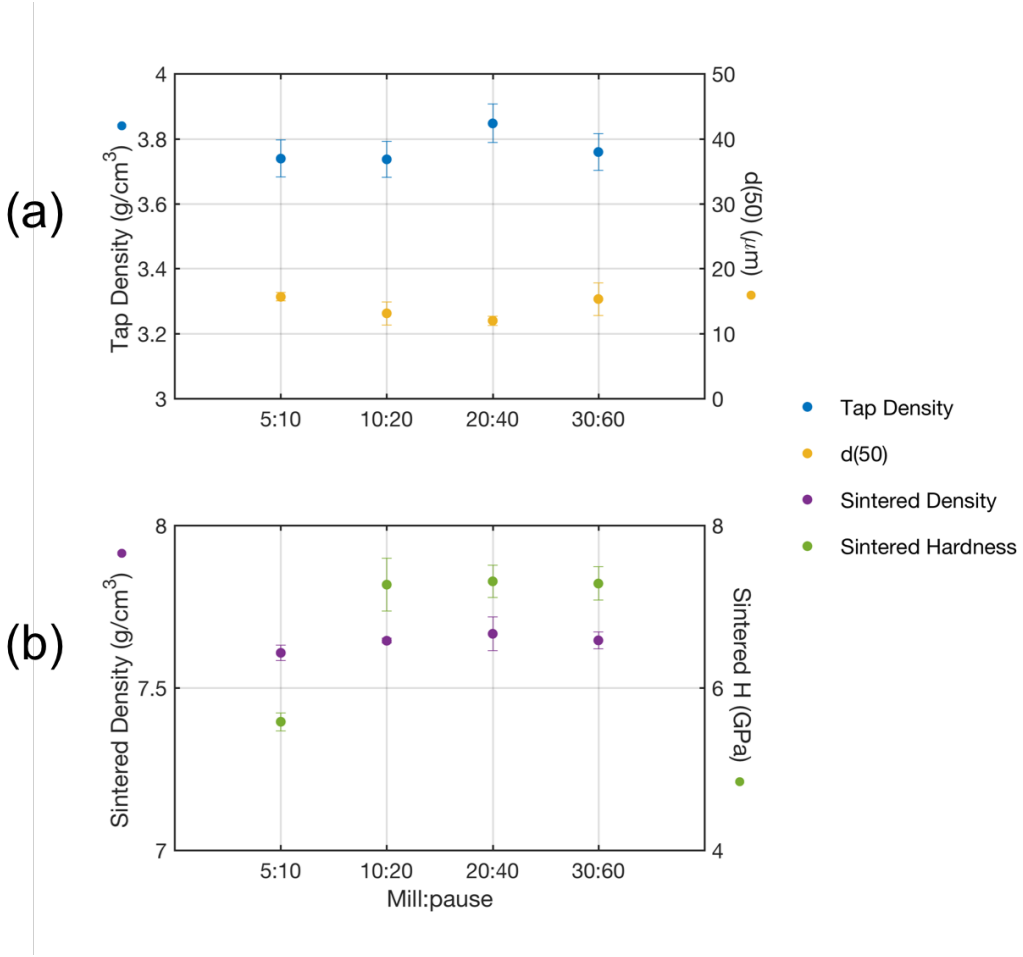


Figure 5.4: (a) Number average particle diameter (d(50)) and tap density of Fe-14Cr-3W-0.3Ti+0.25Y_2O_3 powder milled for 60 h as a function of mill:pause ratio and (b) sintered density and hardness of 20 mm diameter 10 mm thick compacts using the Fe-14Cr-3W-0.3Ti+0.25Y_2O_3 powder after 60 h of milling as a function of the mill:pause.

shortest milling time ratio of 5:10, which may be associated with its slightly larger mean diameter or narrow size distribution.

Although differences were slight, 20:40 was chosen as the mill:pause ratio for subsequent work, with the slightly longer ratio chosen to ensure low tap densities were avoided.

Figure 5.3 (a) indicated that a plateau in hardening and particle size was reached after a total milling time ∼30 h, representing the point where fracture and cold-welding effects on powder diameter were roughly equal. Further investigations were required in order to judge the distribution of added Y_2O_3.

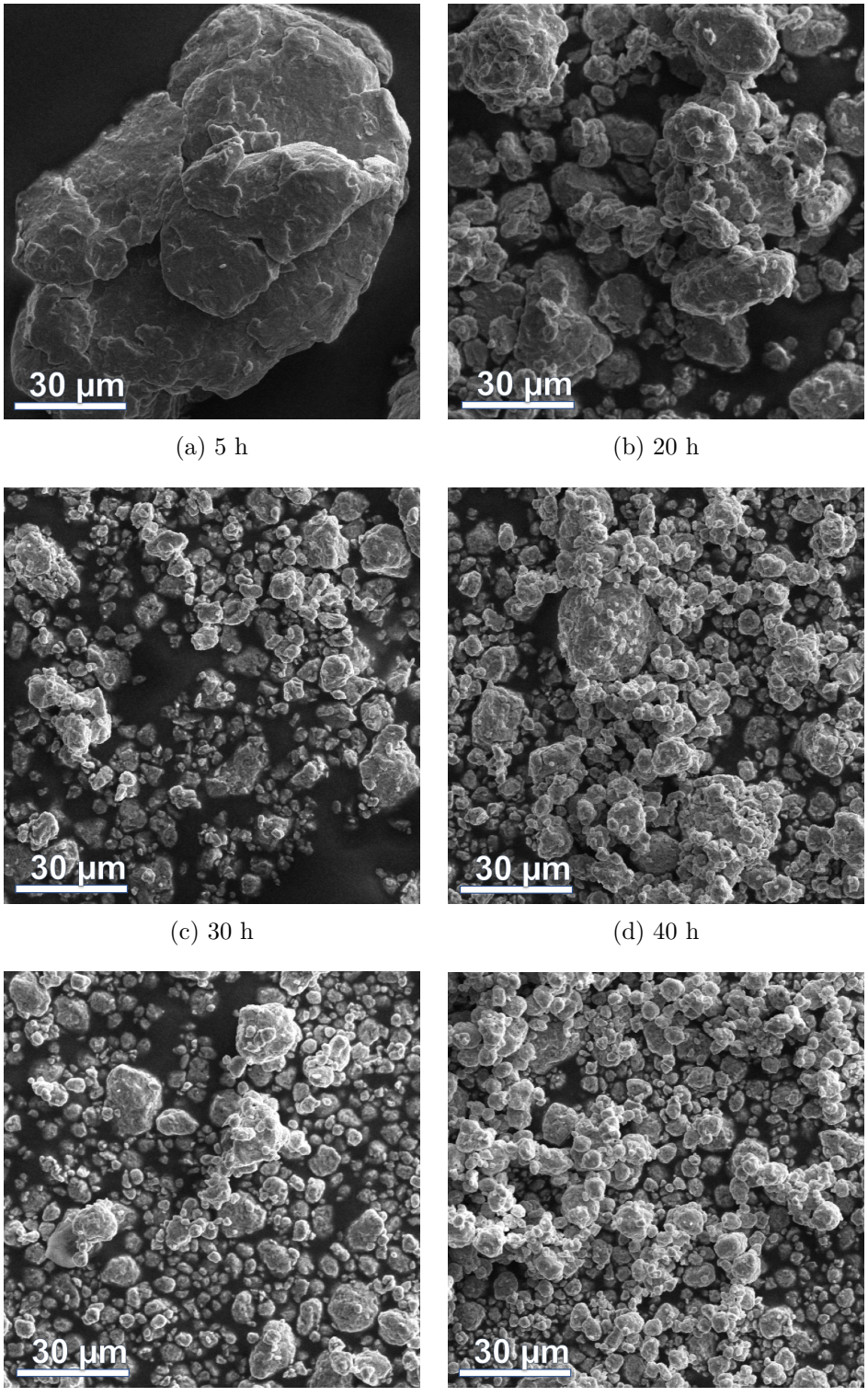
5.2.1.1 Total milling time

Milling time is an important parameter in MA of ODS alloys: short milling times do not promote acceptable distribution and possible dissolution of Y_2O_3, whereas long milling times, aside from costing more, increase the risk of contamination from the milling media, milling atmosphere and milling pot material (particularly from O and Fe, leading to dilution of alloying elements). Franke *et al.* [153] showed increased milling times correlated closely to increased porosity, and a decrease in final modulus due to residual interconnected pores.

Fe-14Cr-3W-0.3Ti+0.25Y_2O_3 powder was manufactured using a 20:40 ratio for 5 to 60 h total milling time followed by chemical and morphological analysis, as well as analysis of packing and sintered density at each stage.

Figure 5.5 shows SEM images of the powder after various total milling times. In (a) after 5 h, milling was judged incomplete and a steady state not yet achieved, with cold-welding dominating leading to a relatively large particle diameter. After 20 h in (b) work hardening and fracture was more evident. Between 30 to 60 h there was little change in powder shape and size, with the powder remaining approximately spherical, a plateau in particle diameter from 30h onwards was suggested, consistent with Figure 5.3 (b).

To investigate if significant microstructural changes were occurring during further milling, XRD was used to estimate the effective crystallite size and any internal lattice strain, using the procedure described in Section 3.5.4. Figure 5.6 shows the XRD spectra as a function of 2θ for each powder. As the Y_2O_3 additions (at 0.25 wt%) were was so small, no Y_2O_3 peak was resolvable. There was no evidence of any retained austenite and the spectra were interpreted as indicating a microstructure comprising a solid solution based on bcc ferrite only. However, there was ferrite peak broadening as milling progressed, highlighted for example in the inset of the (211) peak. The second peak on the base dataset arose from the polychromatic Cu source used. Peak broadening was due to combination of a decrease in crystallite size, and increase in lattice strain. These two factors can



(a) 5 h (b) 20 h

(c) 30 h (d) 40 h

(e) 50 h (f) 60 h

Figure 5.5: SEM images showing powder size and morphology of Fe-14Cr-3W-0.3Ti-$0.25Y_2O_3$ powder milled for (a) 5h (b) 20h (c) 30h (d) 40h (e) 50h (f) 60h.

be approximately separated (as discussed in Section 3.5.4) into microstrain and crystallite size contributions, and are plotted in Figure 5.7.

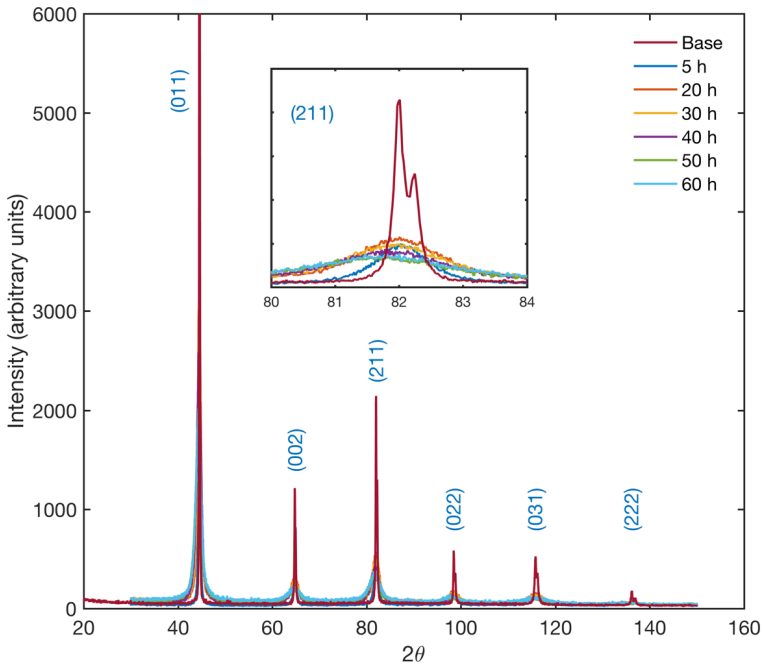


Figure 5.6: XRD spectra from the Fe-14Cr-3W-0.3Ti+0.25Y_2O_3 milled at a ratio of 20:40 and shown as a function of total milling time, with inset detail of the ferrite (211) peak showing broadening with time.

Figure 5.7 shows a significant initial decrease in the crystallite size and increase in microstrain over the first 5 hours and approached a steady state of 0.6 and 7 nm respectively after 60 h, consistent with the literature [63, 154]. Error was calculated from the errors in fitting the Williamson-Hall plot shown in Section 3.5.4 resulting from propogation of errors in the measured θ and FWHM values.

Using the estimated microstrain and crystallite size, the mean dislocation density (ρ) can be estimated [155]:

$$\rho = 2\sqrt{3}\frac{\langle\sigma^2\rangle^{1/2}}{\langle L\rangle\beta} \tag{5.1}$$

where $\langle\sigma^2\rangle^{1/2}$ is the root mean square microstrain from the XRD spectra, $\langle L\rangle$ is the mean crystallite size from the spectra and β is the magnitude of the Burgers vector on the closest-packed plane which is (110) for bcc ferrite:

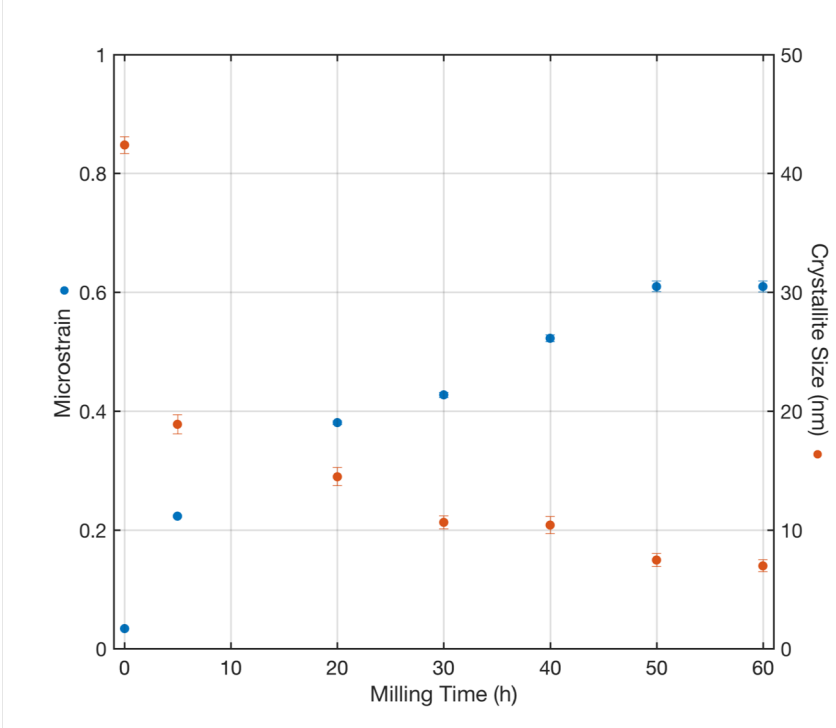


Figure 5.7: Microstrain and crystallite size contributions to peak broadening in Fe-14Cr-3W-0.3Ti+0.25Y_2O_3 powder as a function of total milling time.

$$\beta = \frac{a}{2}\sqrt{h^2 + k^2 + l^2} \tag{5.2}$$

where a is the unit cell length of the crystal, estimated from XRD data, and h, k, and l are the Miller indices.

Figure 5.8 shows the evolution of dislocation density calculated using Equation 5.1 and Equation 5.2, shown alongside the hardness, as a function of milling time. Milled hardness was high (plateau ∼14 GPa) when compared to sintered hardness, due to the large amounts of retained work. As expected, hardness and dislocation density increase more or less in proportion. Hardness reached a plateau after ∼ 30 h but reduces in spread as milling time continued. Dislocation density reached a plateau slightly later, after ∼50 h.

Figure 5.9 (a) shows the powder diameter and tap density of Fe-14Cr-3W-0.3Ti+0.25Y_2O_3 powder as a function of total milling time and Figure 5.9 (b) shows the sintered density and hardness of 20 mm diameter 10 mm thick FAST consolidated compacts using the Fe-14Cr-3W-0.3Ti+0.25Y_2O_3 powder as a function

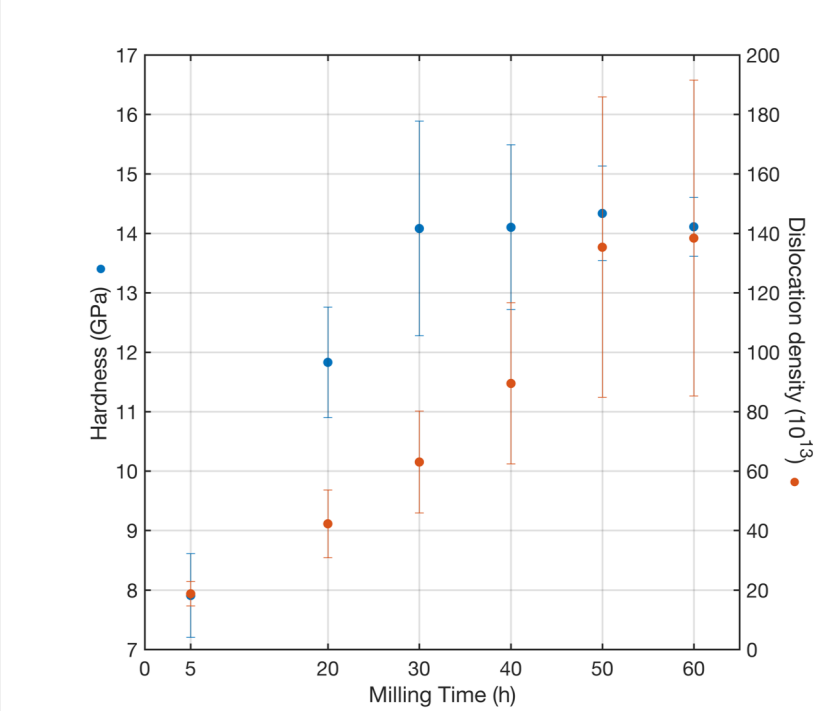


Figure 5.8: Hardness and dislocation density of Fe-14Cr-3W-0.3Ti+0.25Y_2O_3 powder as a function of milling time.

of total milling time. Particle diameter and tap density both reached a plateau by 40 h at $\sim$ 15 μm and $\sim$ 3.75 g/cm^3 respectively, in the range expected from literature [154] and seen previously after 60 h in the mill:pause study. Sintered hardness reached a plateau of $\sim$7 GPa by 40 h, but sintered density continued to fluctuate. This was most likely due to inherent inaccuracies and difficulties in the measurement and run-to-run variations in these early not-yet-optimised FAST experiments. Only relative changes were of interest at this stage.

The distribution of Y was investigated using EPMA as shown in Figure 5.10. Here, at the scale achievable by EPMA and drawing on similar images in the literature, the distribution of Y (on the micron scale) at all milling times was judged 'acceptable'. However, given a starting Y_2O_3 powder diameter on the nm scale and limitation of the EPMA instrument, a robust view on whether sufficient distribution / dissolution of the Y_2O_3 had occured was not possible by EPMA alone. No robust definition of the acceptable distribution of Y or Y_2O_3 for high quality ODS alloys has been suggested in the literature, although it often makes reference to

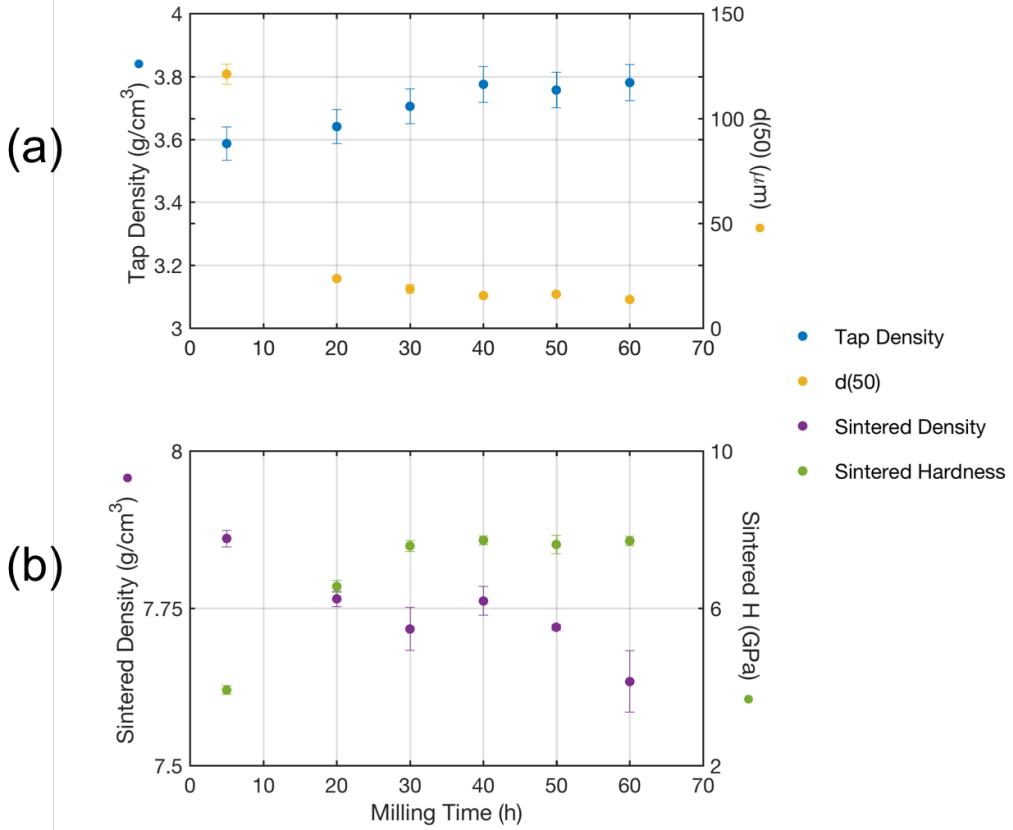
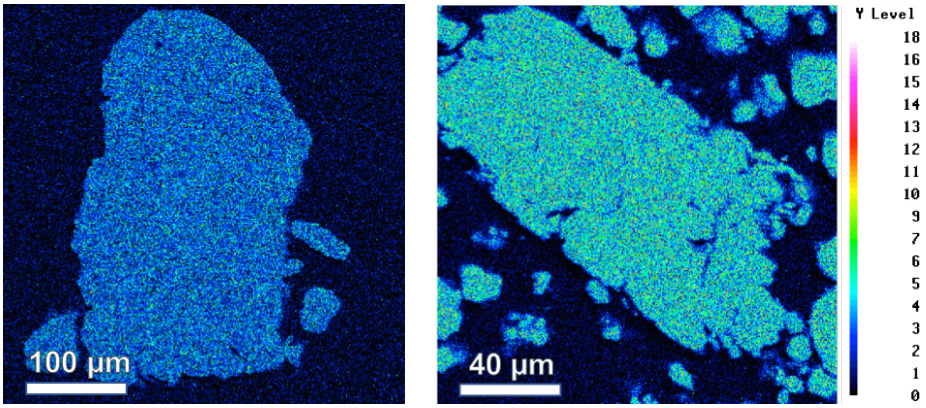


Figure 5.9: (a) Particle diameter and tap density of Fe-14Cr-3W-0.3Ti+0.25Y_2O_3 milled using a pause ratio of 20:40 as a function of total milling time and (b) sintered density and hardness of 20 mm diameter 10 mm thick FAST consolidated compacts using the Fe-14Cr-3W-0.3Ti+0.25Y_2O_3 powder as a function of total milling time.

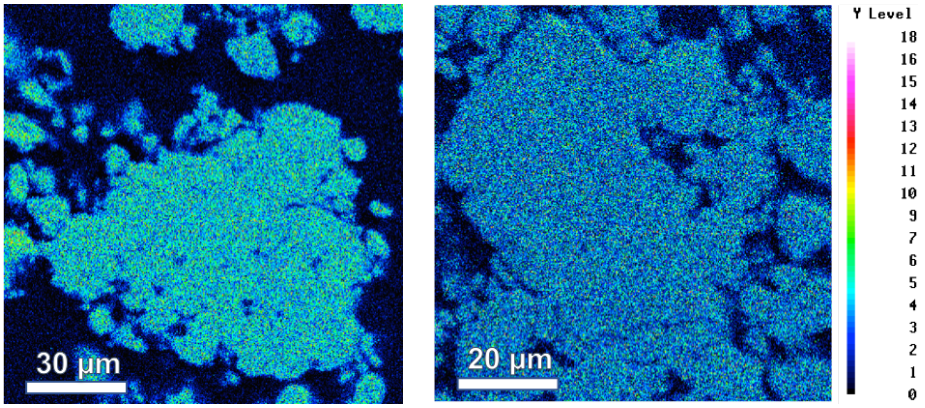
'homogeneous' or 'uniform', without any quantification. Ultimately if high enough resolution is used, the Y / Y_2O_3 distribution will always be 'inhomogeneous'.

5.2.2 Final milling parameters

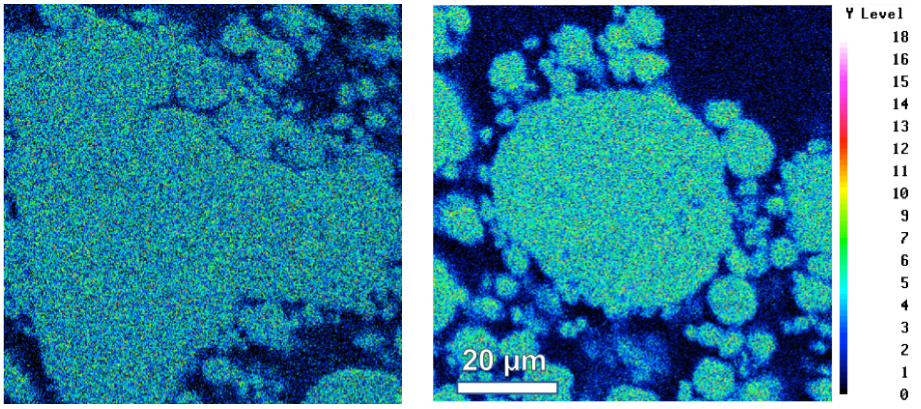
At a mill:pause ratio of 20:40 minutes, and all other milling parameters set as described in [39], there was an approximate steadying of the powder diameter, hardness and microstrain after 40 h. Although microstrain continued to increase slightly and domain size decreased until 50 h (due to a further build up in dislocation density), these made no difference to the properties of the sintered material, and simply risked further contamination of the powder. Therefore the parameters



(a) 5 h (b) 20 h



(c) 30 h (d) 40 h



(e) 50 h (f) 60 h

Figure 5.10: Typical EPMA maps showing the distribution of Y in Fe-14Cr-3W-0.3Ti+0.25Y_2O_3 after milling for a total time of (a) 5 h (b) 20 h (c) 30 h (d) 40 h (e) 50 h and (f) 60 h.

summarised in Table 5.1 were used for all milled powder in the remainder of this work, and represent a time saving of 33% over previous work.

Parameter	
Powder	Fe-14Cr-3W-0.3Ti + $0.25Y_2O_3$
Total milling time	40h
Milling ratio	20:40 minutes
Milling atmosphere	Ar
Ball:powder weight ratio	10:1
Mill RPM	250 rpm

Table 5.1: Final milling parameters for production of Fe-14Cr-3W-0.3Ti+$0.25Y_2O_3$ powder.

5.2.3 Strengthening mechanisms in Fe-14Cr-3W-0.3Ti+$0.25Y_2O_3$

As suggested in Section 2.3.1, at room temperature, the tensile yield strength of powders has been assumed to approximately follow a simple addition of strengthening effects, combining intrinsic strength, Hall-Petch strengthening, dislocation densities due to cold work (work hardening) and Orowan (precipitate / dispersion) particle strengthening.

$$\sigma_y = \sigma_{SS} + \sigma_{BH} + \sigma_0 + \sigma_D + \sigma_K \tag{5.3}$$

where σ_y is yield strength, σ_{SS} is solid solution strengthening, σ_{BH} is Bailey-Hirsch strengthening due to dislocations, σ_{HP} is Hall-Petch strengthening from grain size contributions and is made up of σ_0 from lattice friction and σ_D from grain strengthening and σ_K is Orowan strengthening from particle interactions with dislocations and the strain fields surrounding incoherent particles.

As yield strength can also be approximated by the relationship $\sigma_y = 1/3\times$ H [156] where H is measured hardness, which is justified for cold-worked powders, Equation 5.3 can be rearranged to give an approximation for the strength contribution of Y, both dissolved in the matrix and due to Y-based particles termed $\sigma_{Yadditions}$:

$$\sigma_y - (\sigma_{SS} + \sigma_{BH} + \sigma_0 + \sigma_D) = \sigma_{Yadditions} \tag{5.4}$$

An approximation for the intrinsic strength ($\sigma_{SS} + \sigma_0$) can be found using the pre-alloyed Fe-14Cr-3W-0.3Ti in its relaxed (fully annealed) state. Assuming the

measured crystallite size is equivalent to the grain size in the worked powder, the contribution of grains and sub-grains to overall strengthening can be estimated using the Hall-Petch relationship [157] ($k \times d^{-1/2}$ where k is the strengthening coefficient of the material and d is approximated as the crystallite size from XRD data). The strength contribution of work-hardening can be estimated using estimated dislocation densities calculated from XRD data, shown previously in Figure 5.8.

The terms in Equation 5.4, alongside equations and any necessary input values can be seen in Table 5.2. Using these, an estimation for the Y strengthening contribution, by difference, using Equation 5.4 was estimated as 860 MPa. This value will be compared to the Fe-14Cr-3W-0.3Ti-0.4Y+Fe_3O_4 powder later.

Term	Equation	Strength (MPa)
σ_y	1/3× H	4700
$\sigma_{SS} + \sigma_0$	H of FeCrWTi	1060
σ_D	$k \times d^{-1/2}$	2390
σ_{BH}	$\sigma_{BH} = M\alpha G\beta\rho^{1/2}$	388
$\sigma_{Yadditions}$	$\sigma_y - (\sigma_{SS} + \sigma_{BH} + \sigma_0 + \sigma_D)$	860

Table 5.2: Estimation of strengthening mechanism contributions in Fe-14Cr-3W-0.3Ti+0.25Y_2O_3 powder milled for 40 h at a pause ratio of 20:40, H(Fe-14Cr-3W-0.3Ti+0.25Y_2O_3) = 14 GPa, H(FeCrWTi) = 1060 MPa, k = 0.22 MPam$^{1/2}$ [158], d = 7 nm, M = 2.9 [159], α = 0.24 [159], G = 81.5 [25] b = 0.25 nm*, $\rho = 75\times10^{13}$. *assuming all dislocations have a Burgers vector of type $\frac{1}{2}(111)$

5.3 Y-containing pre-alloyed powder

In order to investigate if a dispersion of Y-containing oxides might be obtained other than by prolonged milling of Y_2O_3, a pre-alloyed inert gas atomised powder was obtained from Sandvik-Osprey (UK) of composition Fe-14Cr-3W-0.3Ti-0.4Y (wt%) as described in Section 3.2.1. Because all powders tend to suffer from O contamination, and further O pick-up is likely in processing, e.g. during transport to the FAST chamber, this study aimed to identify whether this accidental O pick-up might lead to a localised reaction with super-saturated yttrium during Y precipitation in the FAST process or in subsequent heat treatments.

Additions were also made intentionally prior to sintering to act as an O source. Initially, a very fine Fe_3O_4 powder was simply stirred into the Y-containing powder (0.27 g to 79.73 g of Fe-14Cr-3W-0.3Ti-0.4Y) prior to FAST. Although the desire was to minimise / eliminate any milling, it was then considered necessary to work harden the powder to some extent as it has been suggested and generally accepted that the exceptionally high dislocation density of MA powders helps to provide a very high number density of likely nucleation sites for Y_2O_3 precipitation. To investigate if pre-milling the powder slightly was effective, powder was also milled without an O source, and behaviour compared with the O source containing material.

Table 5.3 shows the full matrix of experiments.

Powder	Description
As-received (AR)	Pre-alloyed Fe-14Cr-3W-0.3Ti-0.4Y
Stirred (S)	AR with Fe_3O_4 stirred in with a spatula
Mixed (Mx)	AR with Fe_3O_4 + planetary mill (100 rpm 30 mins)
Milled 0.5 h (M0.5)	AR with Fe_3O_4 + planetary mill (250 rpm 30 mins)
Milled 10 h (M10)	AR with Fe_3O_4 planetary mill (250 rpm 10 h)
Milled no O (M-O)	AR + planetary mill (250 rpm 10 h)

Table 5.3: Powders prepared without / with various additions to the pre-alloyed Fe-14Cr-3W-0.3Ti-0.4Y powder.

Figure 5.11 (a) shows the AR powder was spherical, as expected from the inert gas atomisation, with a median diameter of ~ 25 μm (measured by laser scattering)

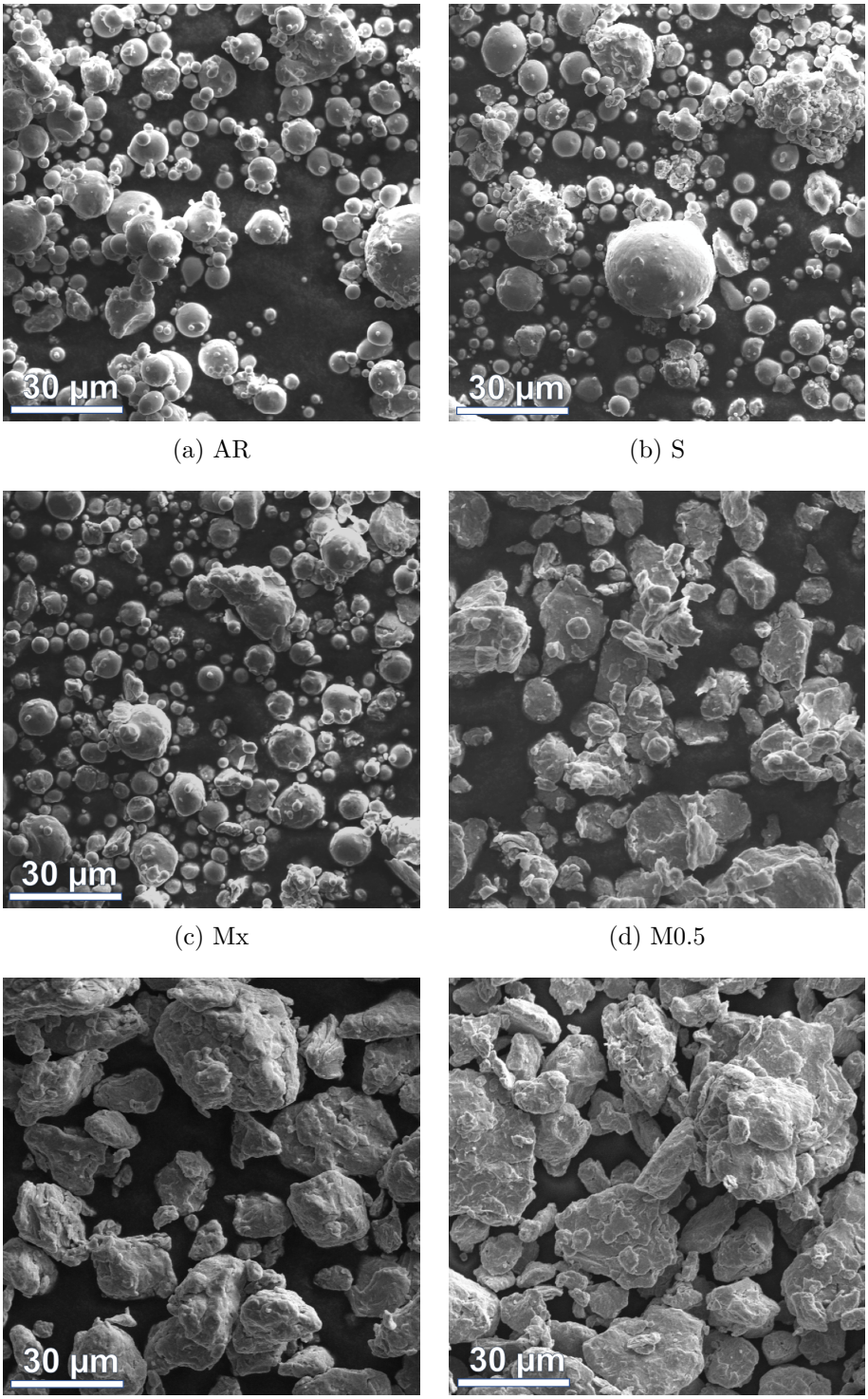
and typical large spread of diameters. Figure 5.11 (b) shows the S powder i.e. AR stirred with Fe_3O_4 and is essentially indistinguishable from the AR powder. Mixing the Fe_3O_4 at low speed is shown in Figure 5.11 (c) and had little effect. Once the mill speed was increased, work hardening and fracture occured and more plate-like powders were formed. Figure 5.11 (d) shows the powder milled for 0.5 h (M0.5) and Figure 5.11 (e) milled for 10 h (M10), both irregular and plate-like. Milling without Fe_3O_4 (M-O) is shown in Figure 5.11 (f) also led to work hardening, fracture, and a more plate-like powder, similar to M10.

To estimate the work hardening, XRD followed by the separation of microstrain and crystallite size contributions was performed as previously described and shown in Figure 5.12. Microstrain started below 0.05 in the AR powder and reached $\sim$ 0.35 in the milled powders (M10 and M-O), similar to Fe-14Cr-3W-0.3Ti+0.25Y_2O_3 powder after 10-20 h. Crystallite sizes started at $\sim$ 45 nm in the AR powder, decreasing to $\sim$ 25 nm in milled powders M10 and M-O, larger than 7 nm in the 40 h milled FeCrWTi+Y_2O_3 powder.

Figure 5.13 shows the estimated dislocation densities and microhardnesses. Dislocation density and microhardness again were correlated, with the milled powders (M10 and M-0) having dislocation densities of $\sim 20\times10^{23}\mathrm{m}^{-3}$ and corresponding microhardness $\sim$ 12 GPa. Overall, milled hardnesses were quite similar to Fe-14Cr-3W-0.3Ti+0.25Y_2O_3 powder milled for 40 h, despite a 75% reduction in total milling time and the breakdown of contributions will be compared later.

Figure 5.14 (a) shows the (number) average powder diameter and packing density for AR, S and Mx powders, each with an average diameter of $\sim$ 25 μm, and relatively high packing density (>3.8 g/cm^3 seen in the Fe-14Cr-3W-0.3Ti+0.25Y_2O_3). Plate-like milled powders did not pack closely and tap density reduced to 3.4-3.7 g/cm^3 that were comparable with Fe-14Cr-3W-0.3Ti+0.25Y_2O_3 powder.

All powders were sintered into 20 mm diameter, 10 mm high compacts using FAST and their sintered density and hardness are shown in Figure 5.14 (b). Sintered density variations were again likely due to the difficulties and inaccuracies in the measurement of sintered density, (with the standard deviation of 5 measurements



(a) AR (b) S

(c) Mx (d) M0.5

(e) M10 (f) M-O

Figure 5.11: SEM images of the powder size and morphology of Fe-14Cr-3W-0.3Ti-0.4Y+Fe_3O_4 powder (a) A-R (b) S (c) Mx (d) M0.5 (e) M10 and (f) M-O as defined in Table 5.3.

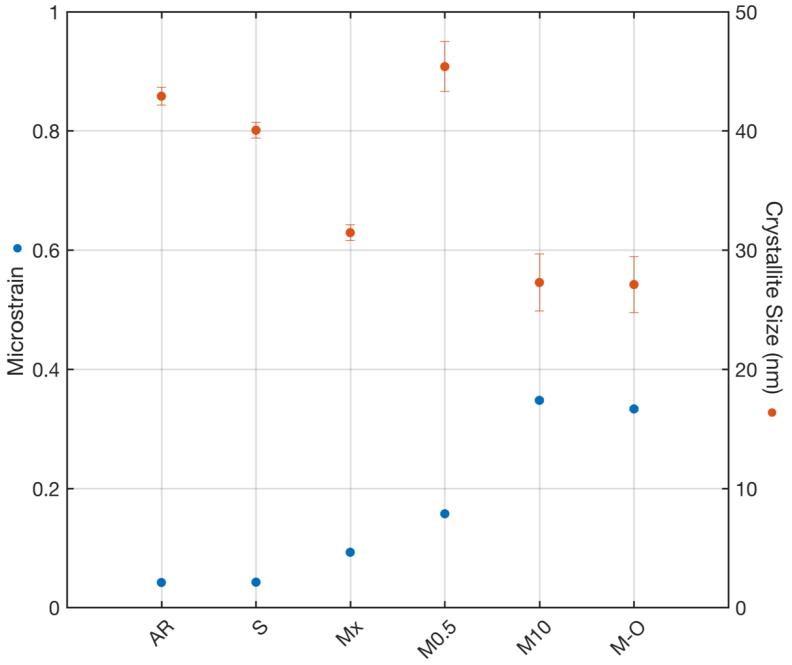


Figure 5.12: Microstrain and domain size contributions to peak broadening for the powders listed in Table 5.3.

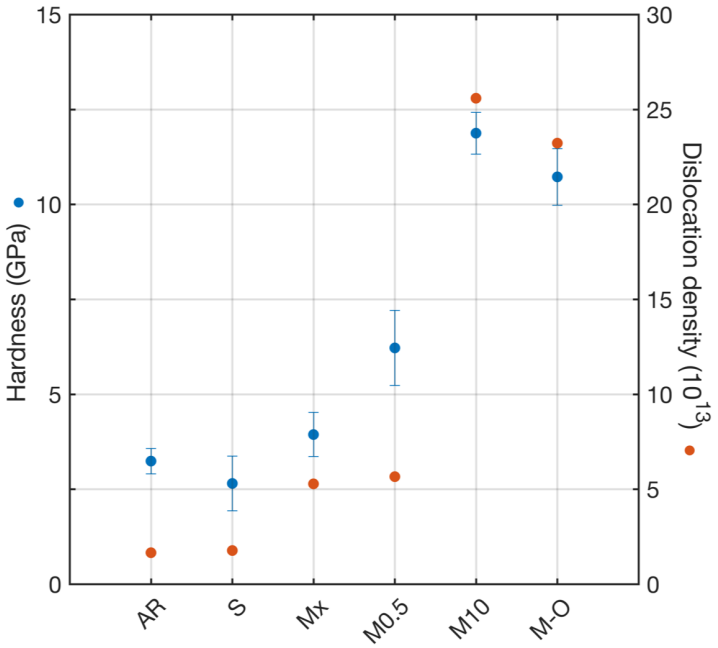


Figure 5.13: Powder hardness and estimated dislocation densities for the powders listed in Table 5.3.

plotted as error bars) and run-to-run variations in these early FAST experiments. Sintered hardness was greatest for M10 at ∼ 5.5 GPa, corresponding to the most highly worked powder, but M-O was only ∼1 GPa softer, and both were softer than Fe-14Cr-3W-0.3Ti+0.25Y_2O_3 (∼8 GPa).

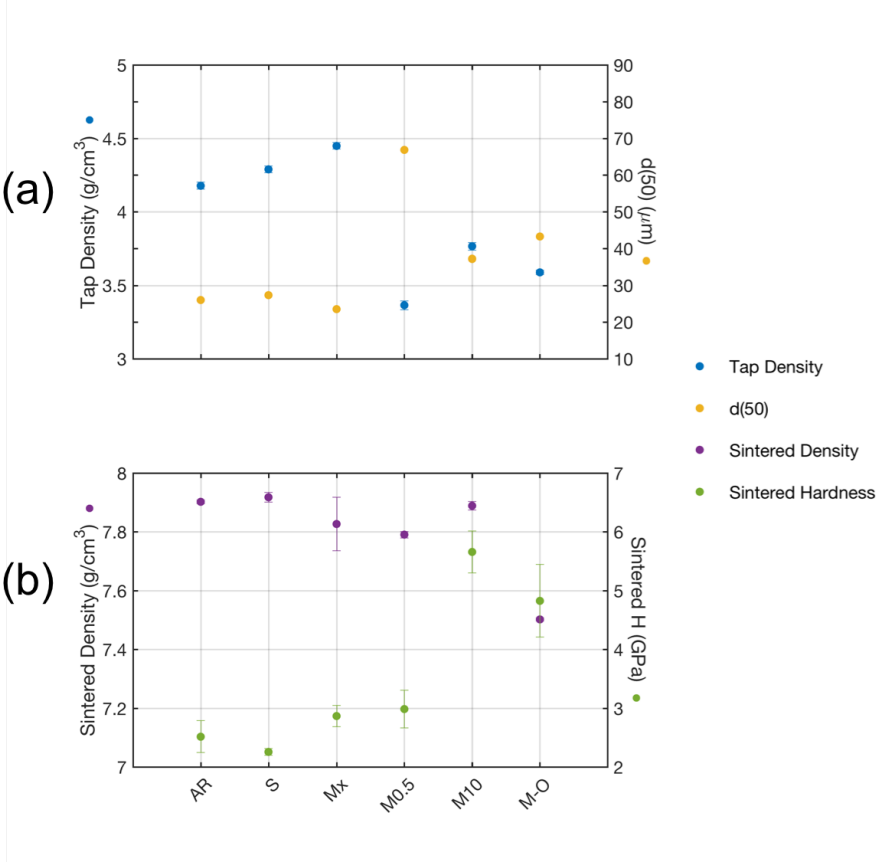


Figure 5.14: (a) powder diameter and tap density for all powders listed in Table 5.3 and (b) sintered density and hardness for 20 mm diameter, 10 mm height sintered compacts from all powders listed in Table 5.3

To ascertain whether hardness differences were due to less residual mechanical work or changes in other strengthening mechanisms, a heat treatment was applied to sintered compacts (750°C for 1 h) to encourage relaxation of residual cold work by recovery or possibly recrystallisation (noting the resistance to recrystallisation seen in Chapter 4). The pre- and post- HT hardness is shown in Figure 5.15, with no more than 200 MPa hardness change following heat treatment, suggesting work hardening effects were broadly similar. Comparing the as-sintered hardness

of M10 and M-O (from Fe-14Cr-3W-0.3Ti-0.4Y+Fe_3O_4 powder) and Fe-14Cr-3W-0.3Ti+0.25Y_2O_3, Fe-14Cr-3W-0.3Ti+0.25Y_2O_3 was ~3.5 GPa harder, but after heat treatment, all had about the same hardness.

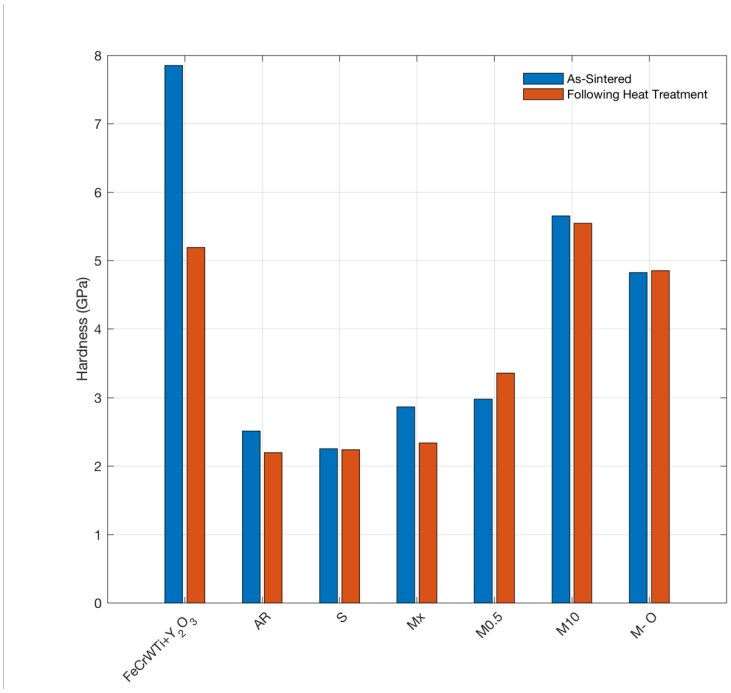


Figure 5.15: Sintered hardness and following a 750°C 1 hr heat treatment, for 20 mm diameter, 10 mm height, sintered compacts from all powders listed in Table 5.3 with FeCrWTi+Y_2O_3 sintered in the same way shown for reference.

The difference in sintered hardness between M10 and M-O (1 GPa) closely matched the difference in powder hardness. To confirm that this difference arose from differences in the extent of work hardening, approximate contributions of the various strengthening mechanisms, as shown earlier in Table 5.2, were estimated. The Y contribution to strengthening was estimated to be 1.36 GPa in M10 and 1.05 GPa in M-O, implying that the addition of Fe_3O_4 contributed an extra 300 MPa powder yield strength. It was unclear if the higher strengthening contribution was simply due to a dispersion of the hard fine-scale ceramic, or whether some Y-containing oxides had started to form (unlikely prior to sintering or heat treatments) or O pick-up was occurring.

Further work used M10 powders in an attempt to ensure necessary O to generate Y-oxides from the supersaturated Fe(Cr,Y) solution. EPMA was again used to

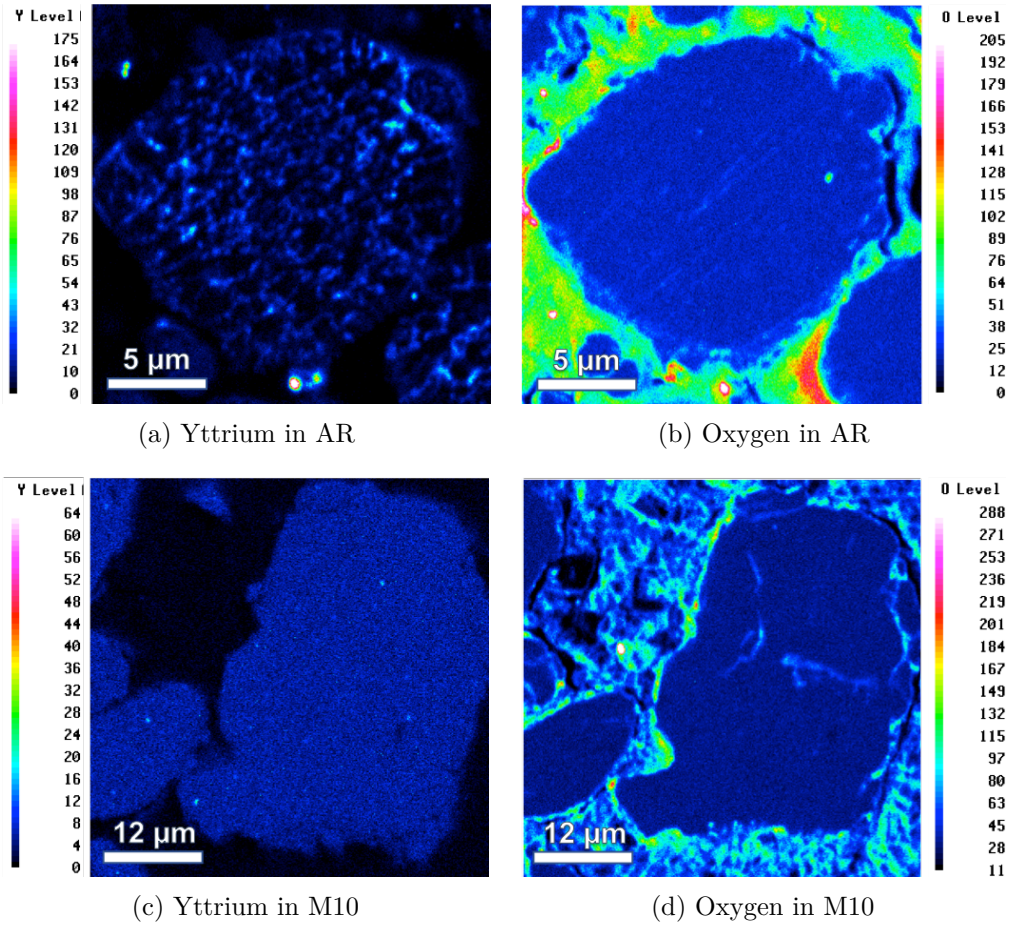
Term	Equation	M10 (MPa)	M-O (MPa)
σ_y	1/3× H	3955	3570
$\sigma_{SS} + \sigma_0$	H of Fe-14Cr-3W-0.3Ti	1060	1060
σ_D	$k \times d^{-1/2}$	1330	1265
σ_{BH}	$\sigma_{BH} = M\alpha G\beta\rho^{1/2}$	205	195
$\sigma_{Yadditions}$	$\sigma_y - (\sigma_{SS} + \sigma_{BH} + \sigma_0 + \sigma_D)$	1360	1050

Table 5.4: Estimation of strengthening mechanism contributions in M10 and M-O powders, values used in calculations: H(M10) = 11.8 GPa, H(M-0) = 10.7 GPa, H(Fe-14Cr-3W-0.3Ti) = 1060 MPa, $k = 0.22$ MPam$^{1/2}$ [158], $d = 7$ nm, $M = 2.9$ [159], $\alpha = 0.24$ [159], $G = 81.5$ [25] $b = 0.25$ nm*, $\rho = 75{\times}10^{13}$. *assuming all dislocations have a Burgers vector of type $\frac{1}{2}111$

characterise Y distributions, in this case, alongside O signals to identify any micro-scale oxide clustering. Figure 5.16 shows EPMA scans of (a) Y distribution in AR, (b) O distribution in AR, (c) Y distribution in M10 and (d) O distribution in M10 powder. Figure 5.16(a) shows localised enrichment of Y along grain boundaries, which has been seen in other studies using gas atomised, Y-containing powder [120, 160]. Unlike other studies, however, there was no localisation of O at these points indicating that Y was likely still in solution and not already in Y-O particles. This showed promise for further oxidation treament and the generation of Y-O based particles. The O enrichment surrounding the powder particle in Figure 5.16 (d) is likely to be due to the mounting resin used rather than a thick surface oxide layer.

Following the introduction of Fe_3O_4 and 10 h of milling, the Y was much more uniformly distributed as can be seen in Figure 5.16(c). The corresponding O distribution in Figure 5.16(d) suggested weak elongated regions of O concentration within the particles that were likely external oxide shells folded into the particle during milling. Avoiding large Y-O particles prior to sintering, and maximising Y in solid solution is essential for the internal oxidation technique. The lack of Fe_3O_4 distribution by EPMA, which can be up to 25 μm upon addition, indicates suitable break up and distribution of the oxide source. Again the surface enrichment of O was due to the resin binder.

Similar studies of GARS and STARS powders showed local enrichment of Y on the surface of particles and Y-O particles along grain boundaries. surface grain



(a) Yttrium in AR (b) Oxygen in AR

(c) Yttrium in M10 (d) Oxygen in M10

Figure 5.16: EPMA maps showing the distribution of (a) Y in AR, (b) O in AR, (c) Y in M10 and (d) O in M10.

boundaries with yttrium oxides. In contrast, no strong surface segregation of Y was detected in the current work.

5.4 Comparison Between Powders

Table 5.5 shows a comparison of powder properties for the Fe-14Cr-3W-0.3Ti powder, Fe-14Cr-3W-0.3Ti+0.25Y_2O_3 powder milled for 40 h using 20:40, AR (Fe-14Cr-3W-0.3Ti-0.4Y) and M10.

Property	FeCrWTi	FeCrWTi+Y_2O_3	FeCrWTiY	FrCrWTiY+Fe_3O_4
Size d(0.5) (μm)	41	15	23	43
Morphology	Spherical	Rounded	Spherical	Blocky
Hardness (GPa)	3.18 ± 0.53	13.73 ± 1.5	3.24 ± 0.33	11.87 ± 0.52
Microstrain (%)	0.03 ± 0.003	0.62 ± 0.009	0.04 ± 0.003	0.34 ± 0.003
Crystallite Size (nm)	42.12 ± 0.60	7.62 ± 0.56	43.61 ± 0.68	22.65 ± 1.47
Surface Area (m^2/g)	0.03	0.25	0.09	0.17
Tap Density (g/cm^3)	4.84 ± 0.02	3.77 ± 0.06	4.18 ± 0.23	3.76 ± 0.03
Hausner Ratio	1.08	1.18	1.15	1.13

Table 5.5: Comparison between final powder properties.

5.4.1 Powder Size and Morphology

The gas atomised powders with / without Y were similar in appearance, both spherical, and with relatively low surface area.

Comparing the milled powders, M10 was larger and more blocky than the Fe-14Cr-3W-0.3Ti+0.25Y_2O_3 powder due to the shorter milling time (10 h compared to 40 h). These blocky particles had faceted surfaces from particle fracture and thus a specific surface area similar to that of the finer Fe-14Cr-3W-0.3Ti+0.25Y_2O_3.

5.4.2 Powder Hardening Mechanisms

The hardness of all powders was within the expected range (∼10 GPa for milled powder) but Fe-14Cr-3W-0.3Ti+0.25Y_2O_3 was especially hard (mainly due to Hall-Petch contributions from the finest grain size). Microstrain and crystallite size values were within expected levels.

5.4.3 Powder Packing Properties

Despite differences in the size and morphology of the milled powders, packing density was almost identical (at 3.77 g/cm^3) which at ∼50% of the theoretical density prior to cold pressing indicates good promise for sintering and densification.

All Hausner ratio values (that of tap to pour density) were less than 1.25, which indicates good powder flowability and pressability i.e. all would be suitable for consolidation.

5.4.4 Powder Chemistry

Table 5.6 shows the nominal composition of the Fe-14Cr-3W-0.3Ti powder according to Sandvik-Osprey (SO), alongside that independently measured by AMG Superalloys (AMG), and after 40 h of milling with 0.25 wt% Y_2O_3. The concentrations from SO and AMG matched closely. Mn concentration was higher than targeted, but accepted, most likely due to pickup from the crucible. Following milling, the major alloying elements remained at similar concentraion, but Y uptake was much lower than expected, and O and N levels much higher than expected. O and N levels were likely due to leakage into the milling pots. Difficulties in maintaining and measuring Y concentrations have been reported elsewhere [39]. As already shown by EPMA, Y dispersion, albeit weakly with low counts, was detected in the milled powders.

Table 5.7 shows the composition of the Fe-14Cr-3W-0.3Ti-0.4Y base powder as measured by Sandvik-Osprey (SO), by AMG Superalloys (AMG) and as measured by AMG following 10 h of milling with Fe_3O_4. Most alloying concentrations were similar between SO and AMG, however Mn concentrations were higher by AMG, almost double that in the FeCrWTi powder. Of greater concern was the decrease in concentration of Y, again reaction with O during transport, or again issues with detecting the low Y concentrations using the Inductively Coupled Plasma Optical Emission Spectroscopy (ICP-OES) technique used by AMG. However, other studies have resolved sensible Y concentrations [98] and low Y concentrations here most likely result from reaction with O during transport and segregation within the batch.

Element	FeCrWTi (SO)	FeCrWTi (AMG)	FeCrWTi+0.25Y_2O_3
Fe	81.73	81.35	80.67
Cr	14.5	14.79	13.84
W	3.1	2.96	3.03
Ti	0.3	0.32	0.30
Y			0.005
Mn	0.26	0.25	0.27
Ni		0.18	0.11
Si	0.1		<0.05
O		0.065	0.609
N		0.18	0.842
All other elements		<0.05	<0.05

Table 5.6: Chemical composition of prealloyed Fe-14Cr-3W-0.3Ti base powder as measured by Sandvik-Osprey (SO), as measured in chemical analysis by AMG Superalloys, and following 40 h of milling with Y_2O_3 (wt%).

Element	FeCrWTiY (SO)	FeCrWTiY (AMG)	FeCrWTiY + Fe_3O_4
Fe	81.48	81.32	81.49
Cr	14.0	13.76	13.53
W	3.1	3.49	3.18
Ti	0.5	0.48	0.46
Y	0.4	0.008	0.006
Mn	0.3	0.48	0.30
Ni		0.08	0.08
Si	0.2	0.21	0.22
O		0.157	0.392
N		0.02	0.140
All other elements		<0.05	<0.05

Table 5.7: Chemical composition of prealloyed Fe-14Cr-3W-0.3Ti-0.4Y base powders as measured by Sandvik-Osprey (SO), as measured in chemical analysis by AMG Superalloys, and following 10 h of milling with Fe_3O_4 (wt%).

5.5 Summary

Two ferritic powders without and with a small addition of Y, were investigated for the production of ODS steels, using gas atomisation and mechanical alloying. It was found that:

- Compared with previous work, optimised milling times could be reduced from 60 h to 40 h total time while still providing a quasi-equilibium state between

the rate of dislocation accumulation (work hardening) and thermally induced recovery, indicated by plateau powder diameter, hardness, crystallite size and dislocation density.

• A prealloyed Fe-14Cr-3W-0.3Ti-0.4Y powder was mixed using a planetary mill with Fe_3O_4 sacrificial O source with the aim of generating a powder with theoretical composition Fe-14Cr-3W-0.3Ti-0.47Y_2O_3, following precipitation of Y from supersaturated solid solution and internal oxidation.

• EPMA elemental maps suggested encouraging Y and O distributions (on the sub-micron scale) following 10 h of high energy mixing, and offered an overall 75% reduction in milling time compared with the optimised conventional route.

• After FAST consolidation, and heat treatment, the hardness of sintered compacts from the two powders was comparable.

• When comparing elemental distributions on the micro-scale to GARS or STARS, using sacrificial Fe_3O_4 a more uniform distribution of Y and O in the powder suggested retention in solid solution. This might indicate Y-O cluster precipititation during subsequent sintering.

• Y concentrations, when measured after transport and after milling, were lower than expected in the Fe-14Cr-3W-0.3Ti-0.4Y powder for reasons that were not clear.

6

Fabrication of ODS Steels: Powder Consolidation

Contents

6.1 Introduction 117
6.2 Experimental Parameters 118
6.3 Chemical Composition 125
6.4 Microstructure 128
6.5 Thermal Stability 157
6.6 Microstructural Summary 169

6.1 Introduction

Consolidation is the process through which a powder mass is transformed into bulk solid material. Many consolidation methods are available, but this study focuses on hot isostatic pressing (HIP) and field assisted sintering (FAST) [161]. Note however, Chapter 4 also showed the efficacy of the direct extrusion of MA powders.

HIP has become the predominant method of pressurised sintering for ODS alloy production, but as discussed in the literature review, the alternate use of FAST may offer potential benefits in terms of reduced sintering time and therefore perhaps better control of grain structure i.e. the avoidance of excessive or abnormal

grain growth. Understanding any differences in grain growth / morphology in HIP and FAST is a principal aim of this chapter, alongside any difference in the evolution of oxide-based dispersions and any contamination. Important temperatures in high Cr ODS steels are the recovery temperature which various studies have suggested lies in the region of 650°C [161], and the recrystallisation temperature >950°C [161]. In ferritic steels, >12 wt% Cr (or Cr equivalent) is usually preferred so that the 'gamma loop' is avoided and the steel remains ferritic throughout high temperature consolidation. Thus introduction of Ni and C - both strong austenite stablisers - is generally avoided. By controlling the temperature-time profile, the amount of residual work and/or the recrystallised grain size and grain growth may be tailored, depending also on the efficacy of grain boundary pinning by any oxide-based dispersoids.

Although FAST appears attractive, it is immature compared with HIP, and is more restricted in pressable geometries. Other aspects identified in the literature review were the inhomogeneous distribution of current, pressure and temperature across samples during FAST consolidation that may lead to an unacceptably inhomogeneous microstructure.

6.2 Experimental Parameters

6.2.1 Hot Isostatic Pressing

Parameters used for HIP sintering at the University of Birmingham were optimised by Gorley in [39] for an alloy of the same composition and are reproduced in Table 6.1. Temperature and pressure as a function of time are shown schematically in Figure 6.1.

Figure 6.2(a) shows the stages of production of the mild steel HIP cans, produced by welding an inner powder filling tube into a wider deformable can tube to create the characteristic HIP can shape (Figure 6.2(a) (1) and (2)). The cans were then filled with the powder using ultrasonic shaking and then attached to the vacuum sealing rig, as seen in Figure 6.2(b). A vacuum of $< 2.5 \times 10^{-4}$ mbar was applied while heating to 500°C for 4 h for degassing. The cans were then heated to > 1000°C and crimped three times along the filler tube using a hydraulic press. The

Parameter	Value
Can	Mild steel
Die size (mm)	$\varnothing$ 10 $\times$ 60
Heating rate (°C/min)	10
Hold temperature (°C)	1150
Hold pressure (MPa)	150
Hold time (Mins)	240
Vacuum (mbar)	$< 5 \times 10^{-2}$
Cooling rate (°C/min)	furnace cool ($\sim$10)

Table 6.1: Sintering parameters for HIP consolidation of Fe-14Cr-3W-0.3Ti+0.25Y_2O_3 and Fe-14Cr-3W-0.3Ti-0.4Y+Fe_3O_4 powders.

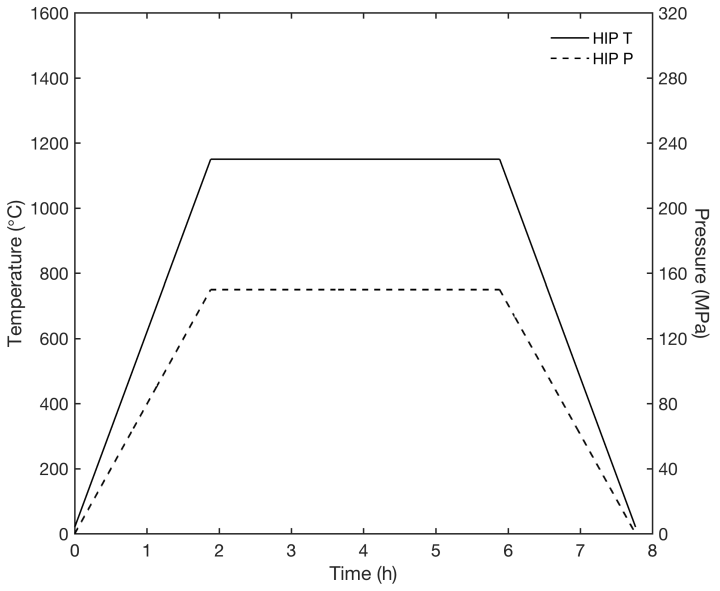
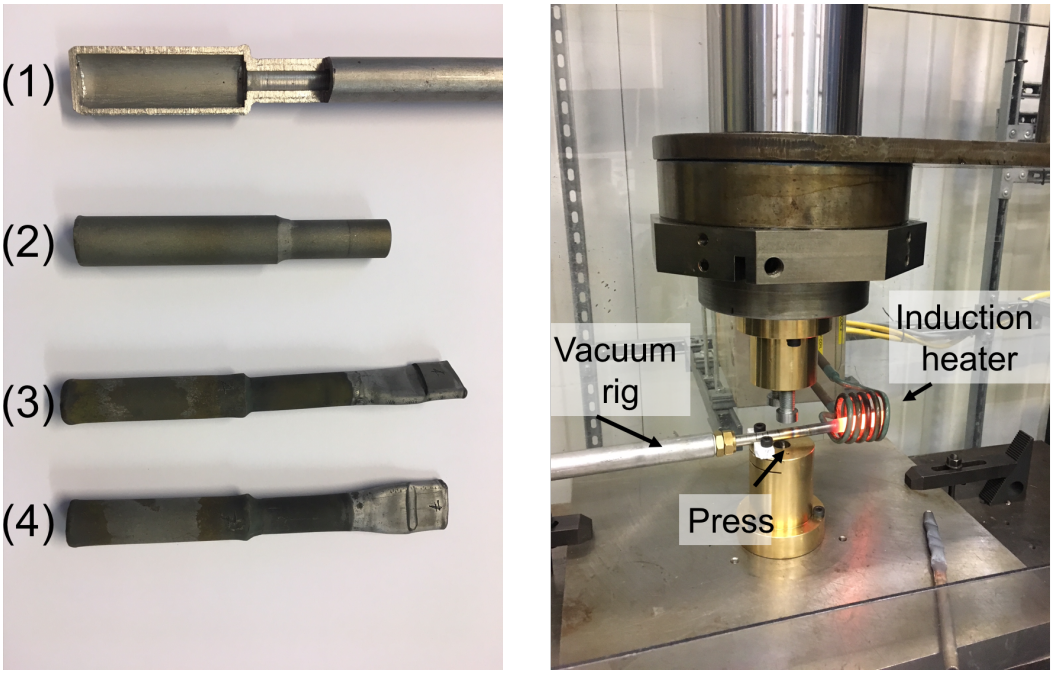


Figure 6.1: Temperature and pressure profiles during consolidation by HIP.

furthest crimp from the HIP can was then sectioned and welded shut. The cans after HIPing are shown in Figure 6.2(a) (3) & (4).

Following HIPing, the can was removed using a lathe and sintered material measured using the Archemedes method. All HIPed samples reached 100% density to within an error estimated as $\pm$1%.



(a) HIP procedure (1) internal of a reinforced can (2) empty mild steel can (3) & (4) filled HIPed can.

(b) HIP can sealing rig.

Figure 6.2: Photographs of the HIP can and sealing process.

6.2.2 Field Assisted Sintering

The powder was cold pressed at 15 MPa in a circular graphite die under Ar atmosphere and assembled with the upper and lower punch in a glovebox. The graphite die and punch set can be seen in Figure 6.3 alongside a final compact. The assembly was placed in a sealed plastic bag and then transferred to the FAST chamber.

Some indication of suitable FAST parameters for ODS steels were given by Zhang *et al.* [97] for Fe-14Cr-0.4Ti-0.25Y_2O_3 that is similar to the Fe-14Cr-3W-0.3Ti-0.25Y_2O_3 described in this thesis. However Zhang *et al.* used an FCT FAST at Queen Mary University London that has significantly different current and voltage characteristics to the FAST used here.

Although temperatures within the die set / compact are known to vary spatially [162], an indication of temperature during FAST was measured by a thermocouple placed in a channel within the graphite die, with the tip 5 mm from the

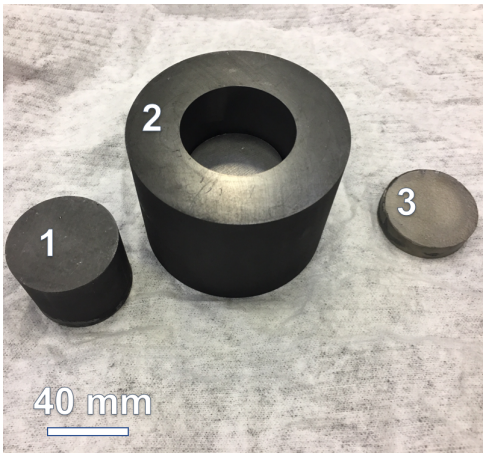


Figure 6.3: Photograph of the [1] graphite punch, [2] graphite die set and [3] sintered 40 mm disc.

inner die wall in contact with the powder. This was used routinely to assess die temperature. In addition, in an early experiment, a sacrificial thermocouple[1] was inserted through the punch and directly into the powder. The typical difference between the die and powder temperature was significant at ~ 100°C within the range of interest, consistent with other studies from literature [163, 164]. Subsequently, consolidation temperatures in this thesis are those of the die, not the powder, and therefore typically underestimate the temperature of the centre of the compact.

By varying the target temperature in the FAST and maintaining a constant die size of ⌀ 20 mm compact height of 10 mm and hold time of 30 minutes, the relationship between sintering temperature and sintered density was investigated. Figure 6.4 shows the density of Fe-14Cr-3W-0.3Ti and Fe-14Cr-3W-0.3Ti-0.25Y_2O_3 compacts using powders milled for 60 h. The theoretical density was assumed to be 7.891 g/cm^3 for Fe-14Cr-3W-0.3Ti and 7.880 g/cm^3 for Fe-14Cr-3W-0.3Ti-0.25Y_2O_3.

Fe-14Cr-3W-0.3Ti sintered relatively easily, reaching full density at 1000°C. Fe-14Cr-3W-0.3Ti-0.25Y_2O_3 powder densified less rapidly, requiring temperatures as high as 1150°C, similar to Zhang *et al.* [97]. The lower deformability of the Y-containing powder ($>$ 3 times harder seen in Chapter 5) may contribute to the

[1]Powder bonded to the thermocouple during sintering meaning it became unusable. This did not affect the temperature measurement or local chemistry, simply is not sustainable for multiple tests as the thermocouple is unrecoverable

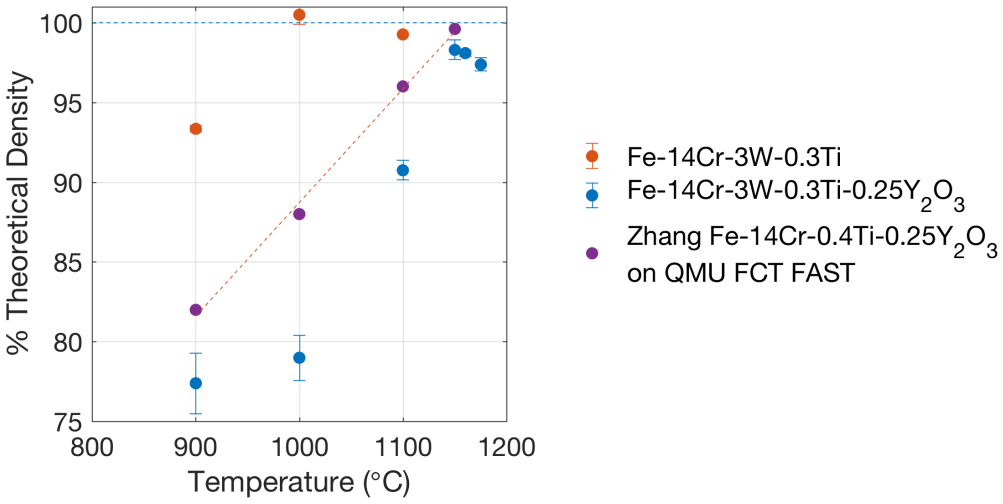


Figure 6.4: Density of Fe-14Cr-3W-0.3Ti and Fe-14Cr-3W-0.3Ti-0.25Y_2O_3 after 60 h of milling as a function of FAST temperature, with results for Fe-14Cr-0.4Ti-0.25Y_2O_3 from Zhang *et al.* [97] for comparison.

higher required FAST temperature, as has been seen in other ODS studies [39, 98]. The temperature-dependent resistance characteristics of powders may also differ.

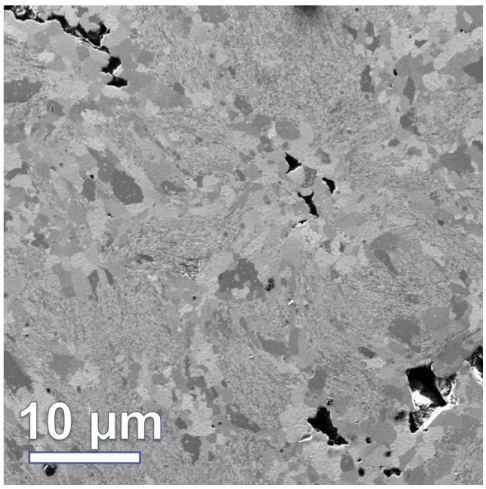


Figure 6.5: Macro-scale porosity in ⌀ 20 mm Fe-14Cr-3W-0.3Ti-0.25Y_2O_3 milled powder sintered at 1150°C and pressure of 50 MPa.

Even at 1150°C, the SEM image in Figure 6.5 shows that occasional local pores could endure. Temperatures above 1150°C led to localised or occasionally widescale melting, likely in the earliest part of conslidation when temperature anisotropy was at its greatest [165]. Higher pressures were also investigated but were limited to not much more than 50 MPa by the strength of the graphite dies. Figure 6.6 shows the sintered density as a function of applied pressures for ⌀ 20 mm, 10 mm height compacts produced from Fe-14Cr-3W-0.3Ti-0.25Y_2O_3 powder milled for 60 h. At 75 MPa, there was an increase in density, but at small diameters and such high pressures any punch misalignment led to die cracking. A ⌀ 40 mm die was less sensitive to mis-alignment and full densification was achieved.

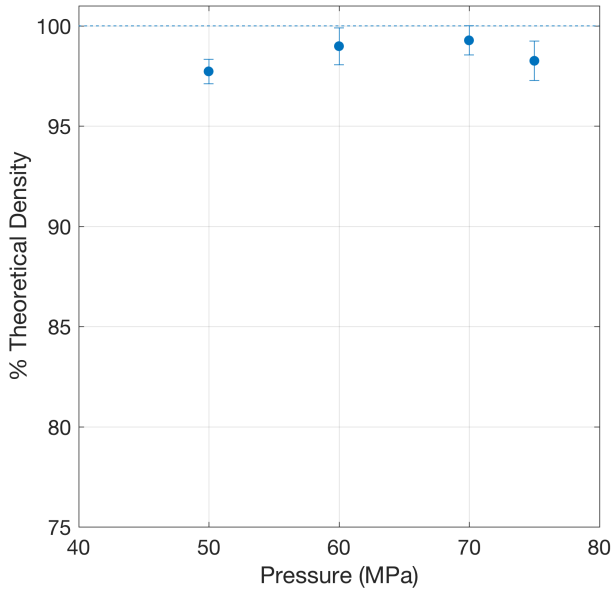


Figure 6.6: Sintered density of ⌀ 20 mm, 10 mm height Fe-14Cr-3W-0.3Ti-0.25Y_2O_3 milled powder compacts as a function of applied pressure during FAST.

The effect of the isothermal hold time during FAST was also investigated, again using ⌀ 20 mm dies. Figure 6.7 shows that final density was surprisingly independent of isothermal peak temperature hold time (as usually a parabolic relationship is seen [166]), and that much of the powder consolidation likely took place during the heating up to peak temperature. Subsequently and unless otherwise stated, an isothermal hold time of 5 min was used.

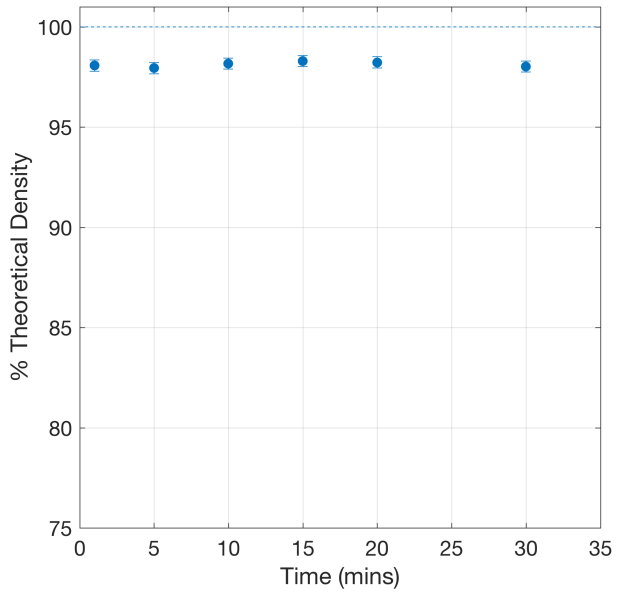


Figure 6.7: Sintered density of ⌀ 20 mm Fe-14Cr-3W-0.3Ti-0.25Y_2O_3 milled powder compacts as a function of isothermal hold time during FAST.

The final chosen sintering parameters are given in Table 6.2, and are shown schematically in Figure 6.8, where they are also compared with the HIP parameters.

Parameter	HIP	FAST
Die material	Mild steel can	Graphite
Die size (mm)	⌀ 10 × 60	⌀ 40 × 10
Heating rate (°C/min)	10	200
Hold temperature (°C)	1150	1150
Hold pressure (MPa)	150	75
Hold time (Mins)	240	5
Vacuum (mbar)	$< 5 \times 10^{-2}$	$< 5 \times 10^{-1}$
Cooling rate (°C/min)	furnace cool (∼10)	100

Table 6.2: Sintering parameters for HIP and FAST consolidation of Fe-14Cr-3W-0.3Ti-0.25Y_2O_3 and Fe-14Cr-3W-0.3Ti-0.47Y_2O_3 powders.

As the sintering time was so short, a post-FAST heat treatment of 750°C for 1 h under vacuum was applied to promote any unfinished microstructural recovery / relaxation, and the precipitation of any oxide-based dispersions or other second phases.

For simplicity, all samples are given abbreviated names, as given in Table 6.3.

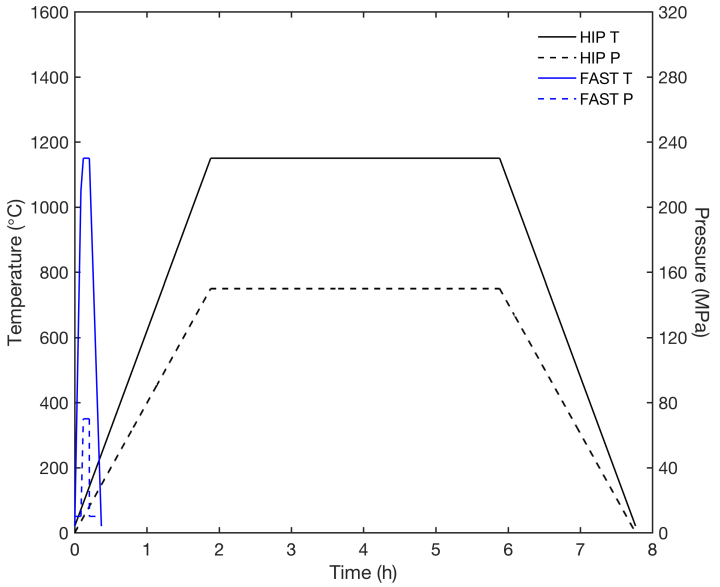


Figure 6.8: FAST and HIP profiles as a function of time for temperature and pressure, used for the consolidation of Fe-14Cr-3W-0.3Ti-0.25Y_2O_3 and Fe-14Cr-3W-0.3Ti-0.47Y_2O_3 powders.

6.3 Chemical Composition

Chemical analysis of sintered samples was undertaken by AMG Superalloys, as shown for Fe-14Cr-3W-0.3Ti+0.25Y_2O_3 in Table 6.4 and Fe-14Cr-3W-0.3Ti-0.4Y+0.27Fe_3O_4 in Table 6.5. Concentrations of particular interest are highlighted in red.

The major alloying element concentrations in Fe-14Cr-3W-0.3Ti-0.25Y_2O_3 remained acceptably stable throughout processing, with the exception of Ti, that reduced after FAST. N levels were elevated in the FAST materials. Y concentrations were lower than expected in the powder and after sintering. The high concentrations of O, alongside the reduced concentration of oxide forming elements could indicate that oxide particles were not being correctly characterised. Chemical characterisation utilised inductively coupled plasma optical emission spectrometry (ICP-OES), which is often requires acid dissolution to aid in detecting oxides [167], not used during analysis. It is also anomalous that O levels reduced between the milled powder and HIPed material, which suggests either the measurement on the milled powder wasn't that reliable or another factor such as oxygen adsorption or entrapments. In this

Sample designation	Processing method
HIP Y_2O_3	Fe-14Cr-3W-0.3Ti + Y_2O_3 powder milled for 40 h consolidated using HIP
FAST Y_2O_3	Fe-14Cr-3W-0.3Ti + Y_2O_3 powder milled for 40 h consolidated using FAST
HIP Fe_3O_4	Fe-14Cr-3W-0.3Ti-0.4Y + Fe_3O_4 powder milled for 10 h consolidated using HIP
FAST Fe_3O_4	Fe-14Cr-3W-0.3Ti-0.4Y + Fe_3O_4 powder milled for 10 h consolidated using FAST

Table 6.3: Sample designations.

respect, HIP offers an advantage since the powder can be degassed and back-filled with Ar in a glovebox. The Y_2O_3 HIP compact in Table 6.4 was consolidated in this way and had the lowest oxygen concentration of all alloys produced.

Element	Powder (SO)	Milled Powder	HIP Y_2O_3	FAST Y_2O_3
Fe	81.73	80.67	82.06	80.40
Cr	14.5	13.84	13.47	13.48
W	3.10	3.03	3.17	3.15
Ti	0.30	0.30	0.31	0.02
Y		<0.005	<0.005	<0.005
Mn	0.26	0.27	0.27	0.27
Ni		0.11	0.10	0.14
Si	0.10	0.08	0.11	0.10
O		0.609	0.219	0.840
N		<0.005	0.219	0.859
All other elements	<0.05			

Table 6.4: Chemical composition of base powder (measured by Sandvik-Osprey (SO), Fe-14Cr-3W-0.4Ti+0.25Y_2O_3 milled powder, FeCrWTi+Y_2O_3 milled powder consolidated by HIP, and by FAST (wt%), measured by AMG Superalloys with compositions of concern highlighted in red.

The major alloying element concentrations in Fe-14Cr-3W-0.3Ti-0.4Y+Fe_3O_4 also remained acceptably constant through processing. Y concentrations were again lower than expected, and O and N levels higher than hoped, emphasising the difficulties in avoiding ambient contamination of reactive metallic powders, even in glovebox handling. Here, the O content increased with both sintering methods, so suggestion that O entrapment within the powder and release during degassing prior to HIPing are less likely, but given the in-house setup of this HIP run, a conclusion can not be fully drawn.

In practice, it was almost impossible to prevent some interaction of atmospheric O with the powder, especially in the FAST that involved an unavoidable step in air when the cold pressed die set is introduced into the FAST chamber. Future work should develop new hardware and protocols to allow reactive powders to be transferred from cold pressing to the FAST chamber without contamination. At this stage, it was not clear if the elevated O was due to the successful 'internal oxidation' of dissolved Y to an oxide dispersion, or more likely a more general contamination of particle surfaces prior to consolidation.

Element	Powder (SO)	Milled Powder	HIP Fe_3O_4	FAST Fe_3O_4
Fe	81.48	81.49	80.44	80.71
Cr	14.00	13.53	13.92	13.73
W	3.10	3.18	3.46	3.31
Ti	0.5	0.46	0.45	0.46
Y	0.4	0.006	0.005	0.006
Mn	0.30	0.30	0.31	0.31
Ni		0.08	0.011	0.09
Si	0.20	0.22	0.21	0.22
O		0.392	0.703	0.586
N		0.14	0.204	0.154
All other elements	<0.05			

Table 6.5: Chemical composition of base powder (measured by Sandvik-Osprey (SO), Fe-14Cr-3W-0.3Ti-0.4Y+Fe_3O_4 milled powder, Fe-14Cr-3W-0.3Ti-0.4Y+Fe_3O_4 milled powder consolidated by HIP, and by FAST (wt%) with compositions of concern highlighted in red.

6.4 Microstructure

Microstructural analysis of the consolidated samples focused on any differences in grain structure and any indication for the formation of oxide-based dispersoids.

6.4.1 HIP Consolidated Fe-14Cr-3W-0.3Ti+0.25Y_2O_3

Figure 6.9 shows the Fe-14Cr-3W-0.3Ti-0.25Y_2O_3 microstructure by HIP consolidation in a BSE image, and 6.10 (a) and (b) show false coloured EBSD orientation maps at low and high magnification respectively, with (c) showing the grain size distribution and (d) the grain area distribution. There was a bimodal grain diameter distribution (seen more clearly in the grain area distribution) with a primary peak at 0.1 μm and a secondary peak at 3 μm and a number average grain size of 0.9 μm. The large grains had qualitative character of abnormal grain growth when a few grains rapidly consume their smaller neighbours and typical of dispersoid stabilised grain structures; as described in the literature review, such bimodality after HIP is common (see Section 2.3.2).

Figure 6.10(b) shows evidence of some residual misorientation within grains, suggesting some residual strain may be present. Grain boundaries were wavy, in a

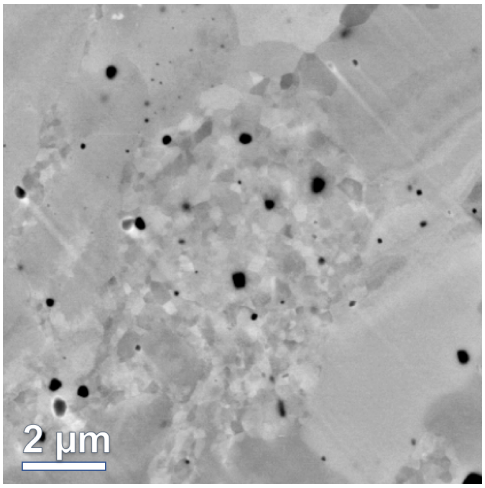


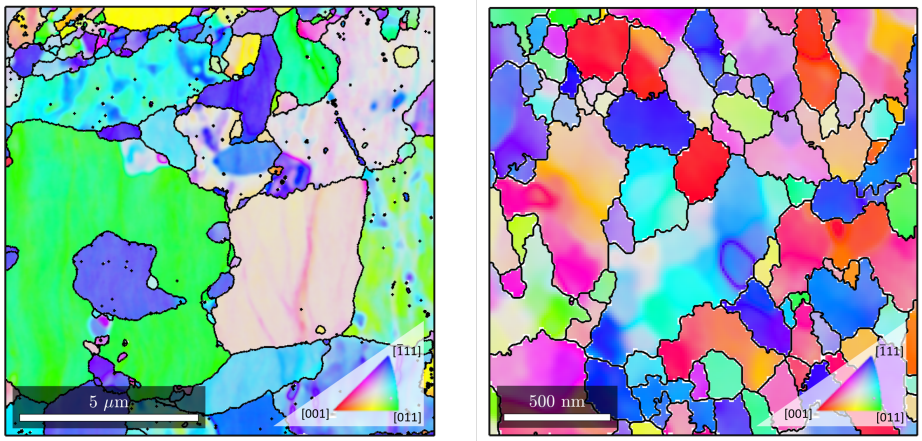
Figure 6.9: SEM back-scattered electron (BSE) image of milled Fe-14Cr-3W-0.3Ti+0.25Y_2O_3 powder consolidated by HIP.

relatively high energy state, typical of dispersoid pinning (not resolved).

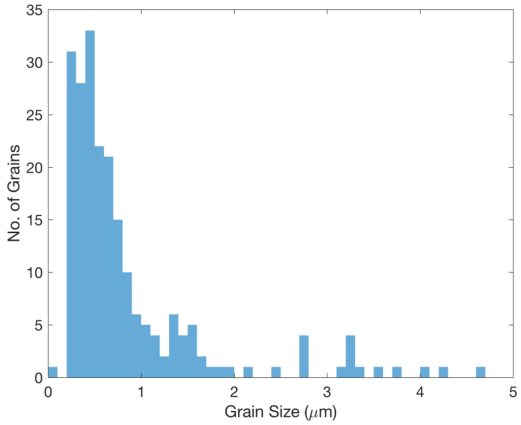
Figure 6.11 (a) shows a higher magnification view of some of the dark particles seen in Figure 6.9 scattered through the microstructure. The inset EDS maps in (b) suggested some of these may be WC, $W_{23}C_6$, etc and were angular, faceted, $\sim$ 0.5 μm, while the SE micrograph in (c) and EDS maps in (d) suggested smaller Ti-rich oxide particles (spherical, $\sim$ 0.2 μm).

In collaboration with Robert Abernethy, attempts were made by TEM to identify the smaller particles that could not be satisfactorily resolved by SEM. Figure 6.12 shows 5 - 40 nm particles and the suggestion of a further population of smaller 3 - 5 nm particles. These particles were located both within the grains and along grain boundaries.

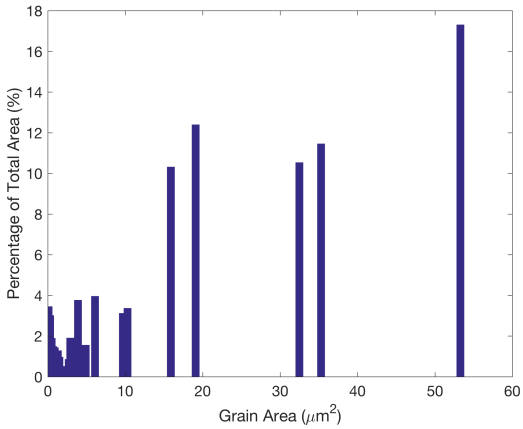
The grain size distributions by EBSD were consistent with those in literature (sub nm and micron sized grains in a bimodal distribution), as were the size of particles by TEM. As this combination of powder and sintering method has been well-studied, they were not analysed in any further detail as sufficient evidence that a 'typical' MA / HIP ODS steel microstructure had been achieved for comparative purposes.



(a) Low magnification (b) High magnification

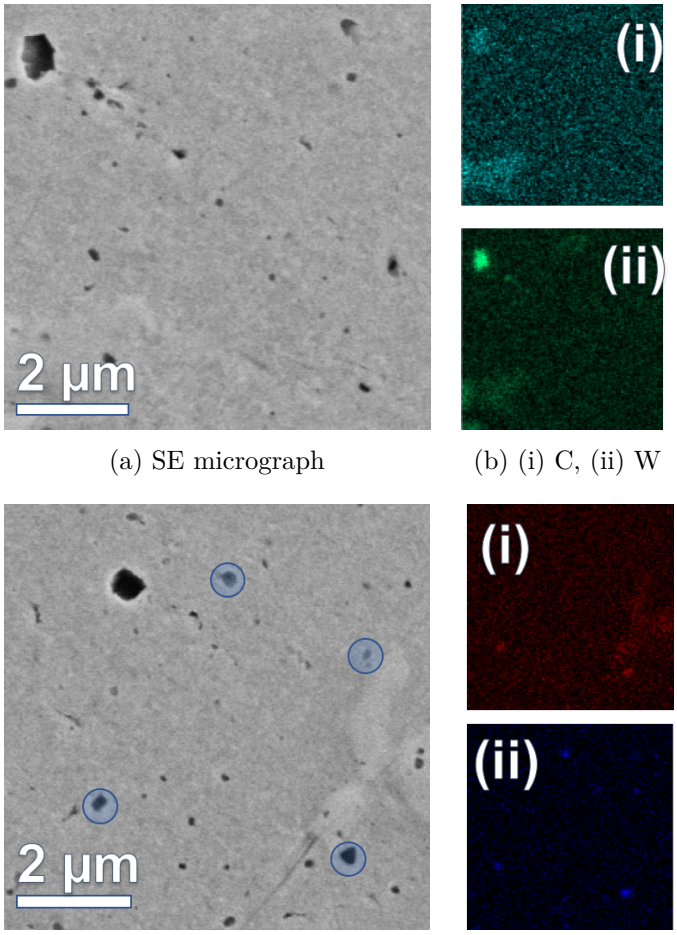


(c) Grain diameter distribution



(d) Grain area distribution

Figure 6.10: EBSD false coloured orientation maps of milled Fe-14Cr-3W-0.3Ti+0.25Y_2O_3 powder consolidated by HIP (a) low magnification, (b) high magnification (c) histogram of grain size distribution and (d) histogram of grain area distribution.



(a) SE micrograph (b) (i) C, (ii) W

(c) SE micrograph (d) (i) Ti, (ii) O

Figure 6.11: SE micrographs and EDS maps of (a) and (b) W- and C-rich particles and (c) and (d) Ti- and O-rich particles in HIP consolidated Fe-14Cr-3W-0.3Ti+0.25Y_2O_3 milled powder.

6.4.2 HIP Consolidated Fe-14Cr-3W-0.3Ti-0.4Y+Fe_3O_4

Figure 6.13 shows the Fe-14Cr-3W-0.3Ti-0.4Y+Fe_3O_4 microstructure consolidated by HIP in a BSE image and Figures 6.14 (a) and (b) show false coloured EBSD orientation maps at low and high magnification respectively, with (c) showing the grain size distribution and (d) the grain area distribution. Both the SEM images and EBSD scans show the grain size distribution again to be bimodal and consistent with a dispersoid stabilised grain structure held at elevated temperatures for extended time, but the grain area distribution shows this to be less pronounced than the Fe-14Cr-3W-0.3Ti+0.25Y_2O_3 material. The grain size distribution showed

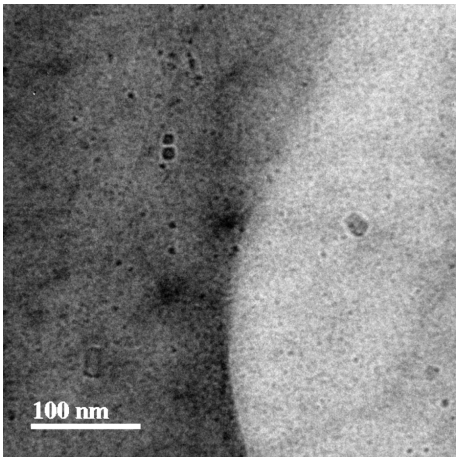


Figure 6.12: BF TEM micrograph of particles seen in Fe-14Cr-3W-0.3Ti+Y_2O_3 milled powder consolidated by HIP.

a primary peak at 1.5 μm and secondary peak at 0.4 μm with an average grain size of 0.6 $\pm$ 0.5 μm; the high variability of the grains was broadly similar to the Fe-14Cr-3W-0.3Ti+0.25Y_2O_3 HIP consolidated compact. Again, residual misorientation within larger grains in Figure 6.14 was suggestive of residual strain. The 'wavy' grain boundaries again implicated, indirectly, the presence of pinning dispersoids.

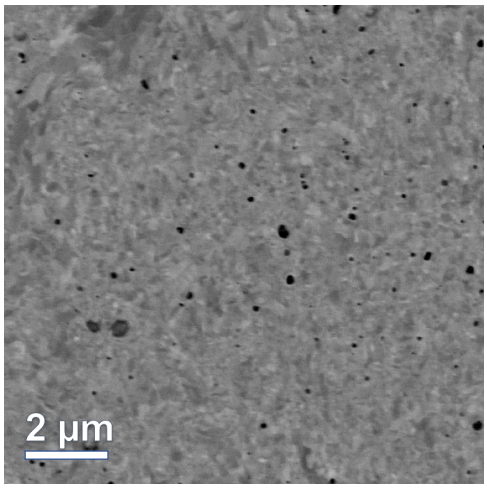
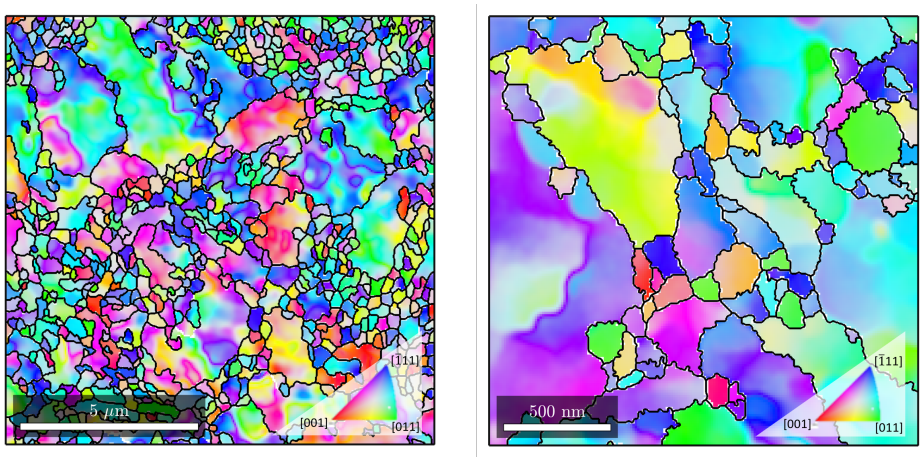
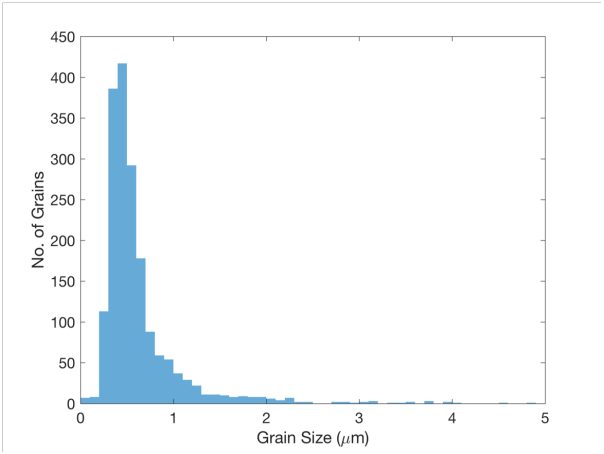


Figure 6.13: SEM micrograph of Fe-14Cr-3W-0.3Ti-0.4Y+Fe_3O_4 milled powder consolidated by HIP.

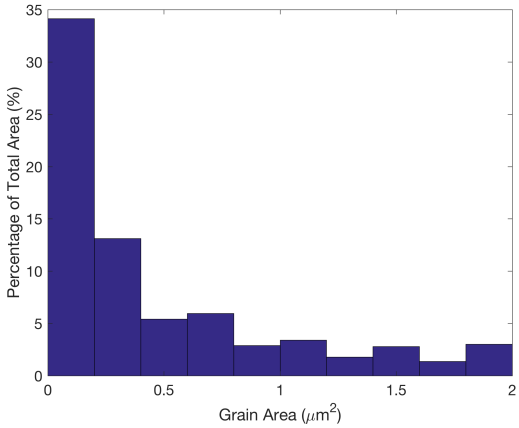
Figure 6.15 (a) shows a SE micrograph and the corresponding EDS maps in Figure 6.15(b) for (i) Ti and (ii) O (weakly). One particle (highlighted on the SE image) suggested a Ti-based oxide, but other particles were too small to be resolved by EDS with confidence. There was no evidence of WC or other particulate,



(a) Low magnification (b) High magnification



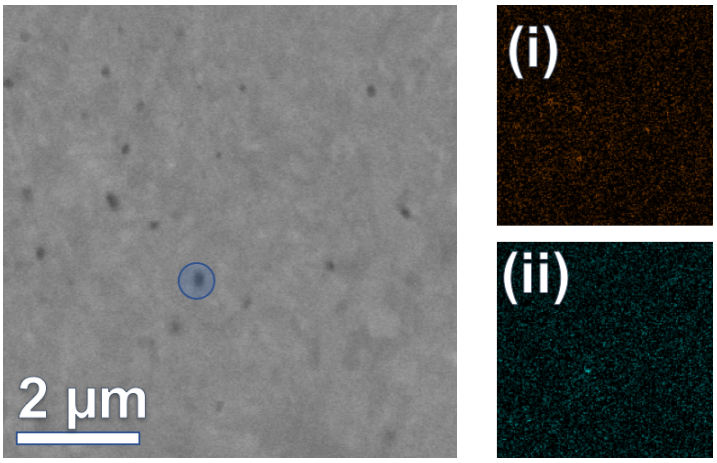
(c) Grain size distribution



(d) Grain area distribution

Figure 6.14: EBSD maps of Fe-14Cr-3W-0.3Ti-0.4Y+Fe_3O_4 milled powder consolidated by HIP (a) low magnification, (b) high magnification (c) histogram of grain size distribution and (d) histogram of grain area distribution.

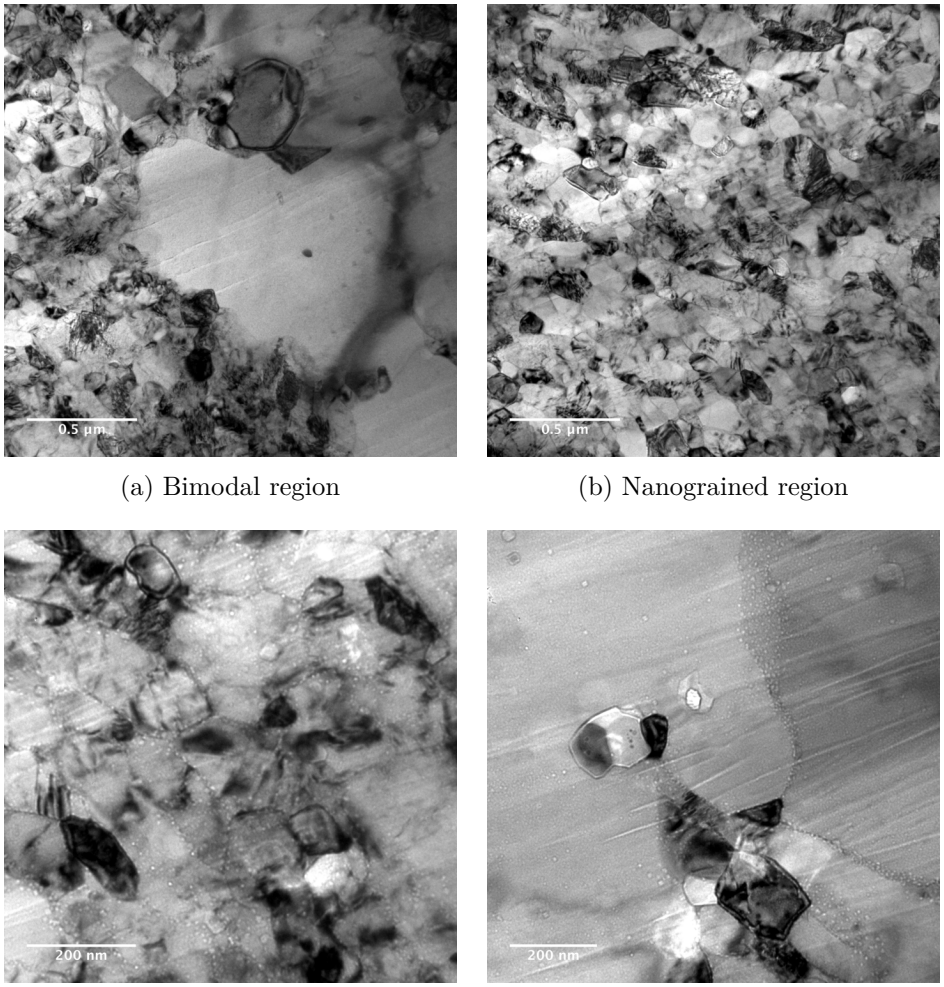
including remnants of the Fe_3O_4 additions. The Fe_3O_4 powder was 20-40 nm, although initially agglomerated to $\sim$ 25 μm during storage. Milling broke up the weakly bound agglomerates and no evidence of Fe_3O_4 was found following milling, although detection of fine-scale Fe_3O_4 against a Fe-rich and O containing matrix might be at the limit of the technique.



(a) SE micrograph (b) (i) Ti, (ii) O

Figure 6.15: SE micrographs and EDS maps of larger particles in HIP consolidated Fe-14Cr-3W-0.3Ti-0.4Y+Fe_3O_4 milled powder.

Figure 6.16(a) shows a bright field TEM image of the bimodal grain structure, confirming the mixture of $\sim$ 1 μm and $\sim$ 100 nm grains. Figure 6.16(b) shows a bright field image of a region populated solely with $\sim$ 100 nm grains. Figures 6.16(c) and (d) show both types of grain structure (nm and microns in size respectively) with very fine particles decorating the grain boundaries and within grains. These particles were estimated to have an average size of 6 $\pm$ 2 nm. These were too small to be the Fe_3O_4 powder added prior to milling, but identification of the chemistry of the particles was not possible and the particles were too small to give analysable diffraction patterns. With further effort in TEM, such information may be available but as TEM was pursued only by collaboration, additional collaborative effort was unavailable.



(a) Bimodal region (b) Nanograined region

(c) Particles in nanograined region (d) Particles in bimodal region

Figure 6.16: TEM bright field micrographs of the microstructure and particles seen in Fe-14Cr-3W-0.3Ti-0.4Y+Fe_3O_4 milled powder consolidated by HIP.

6.4.3 FAST Consolidated Fe-14Cr-3W-0.3Ti+0.25Y_2O_3

Figures 6.17 (a) and (b) show low and high magnification false coloured EBSD orientation maps of Fe-14Cr-3W-0.3Ti+0.25Y_2O_3 consolidated by FAST, with (c) showing the grain size distribution and (d) the grain area distribution. Compared with the same powder consolidated by HIP, the grain structure was finer, with less bimodality. Although hard to quantify, the qualitative impression was that regions of the smallest ferritic grains were more evenly dispersed around the larger grains when compared with the pronounced clustering in the HIP equivalents (seen in Figure 6.10(a)).

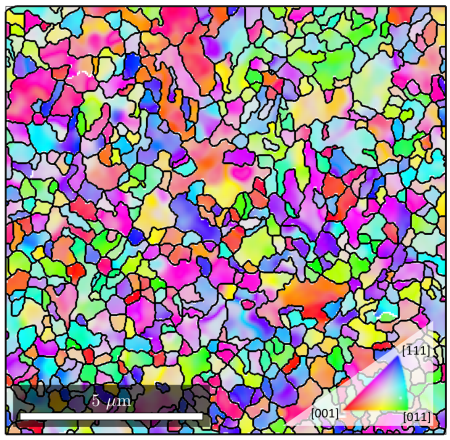
The average grain size was 0.6 ± 0.3 μm, similar to HIPed material with the same starting powder, but with a slightly narrower spread. As in the HIPed material, there was some residual misorientation in larger grains, but despite the much shorter time at the elevated sintering temperature, the microstructural differences were not marked.

Following heat treatment at 750°C, shown in the SEM micrograph in Figure 6.18, and false coloured EBSD orientation maps in Figure 6.19 (a) and (b), recovery of the residual cold work (the coalescence of regions of high crystal misorientation into cell walls dividing smaller grains with much lower misorientation, eventually separated by distinct grain boundaries) had occured. The microstructure was now more regular with a mean diameter reduced to 0.3 ± 0.18 μm, as shown by the change in grain size and area distributions, with no strong evidence of the bimodal grain size distribution reported by Zhang *et al.* [97] for FAST ODS steel. However, the similar composition powder used by Zhang was more highly worked (60 h vs 40 h milling) and no post sintering heat treatment was applied.

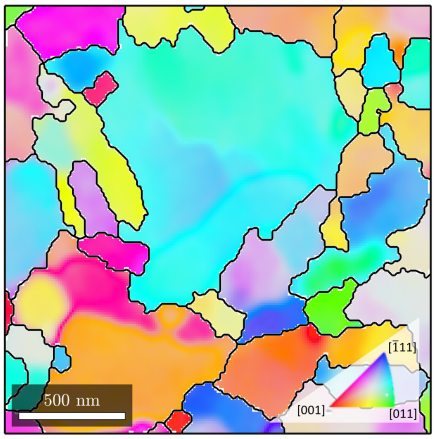
Again there were many particles in the SEM image (Figure 6.18) that were then investigated using EDS in Figure 6.20(a). Larger particles highlighted in blue were rich in Cr, Ti and O. Smaller particles highlighted in green were rich in Y and O. Other particles were likely to be Ti-based oxides but the Ti signal was not localised sufficiently for positive identification. Unlike the HIPed material, no significant population of W or C rich precipitates were identified.

Figure 6.21(a) shows a bright field TEM micrograph of the Fe-14Cr-3W-0.3Ti+0.25Y_2O_3 milled powder consolidated using FAST after heat treatment, which confirmed the relatively refined grain size. Figure 6.21(a) (b) shows small ($\sim$ 10 nm) particles lying both on grain boundaries and within grains. From a sample of 20 particles, an average diameter of 7 ± 4 nm was estimated.

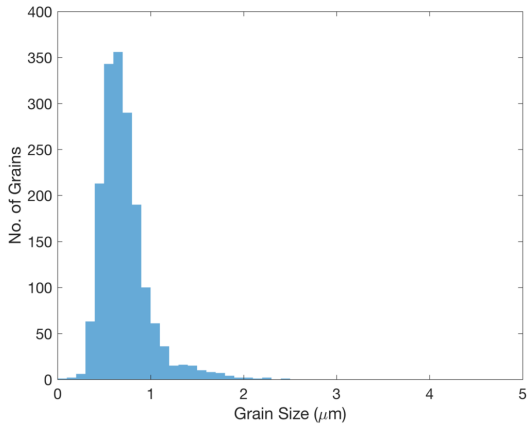
Electron energy loss spectroscopy (EELS) analysis was used to investigate the chemistry of the small particles. Figure 6.22 shows an annular dark field (ADF) image, along with the corresponding EELS spectra for Fe, Cr, Ti and O. The mean particle diameter was 5 ± 2 nm, and were identified to be predominantly



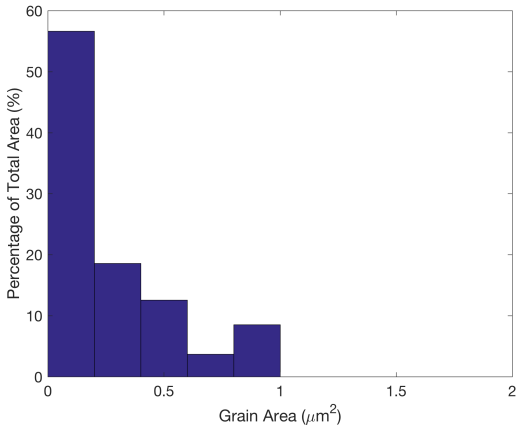
(a) Low magnification



(b) High magnification



(c) Grain Distributions



(d) Grain Distributions

Figure 6.17: EBSD maps of the microstructure of Fe-14Cr-3W-0.3Ti+0.25Y_2O_3 milled powder consolidated by FAST (a) low magnification (b) high magnification (c) histogram of grain size distribution.

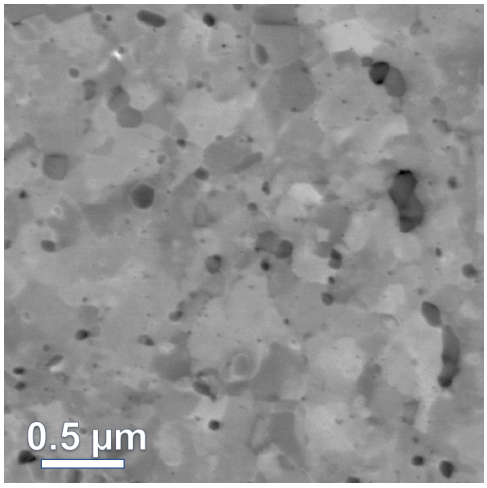
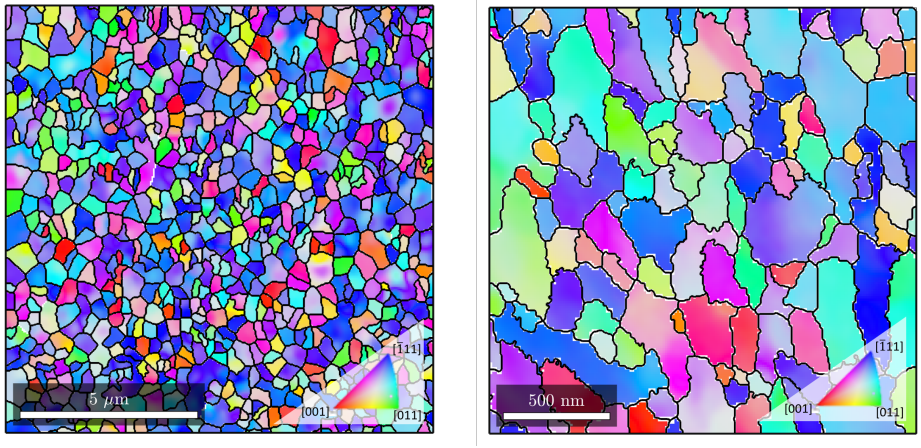


Figure 6.18: SEM micrograph of Fe-14Cr-3W-0.3Ti+0.25Y_2O_3 milled powder consolidated by FAST then heat treated at 750°C for 1 h.

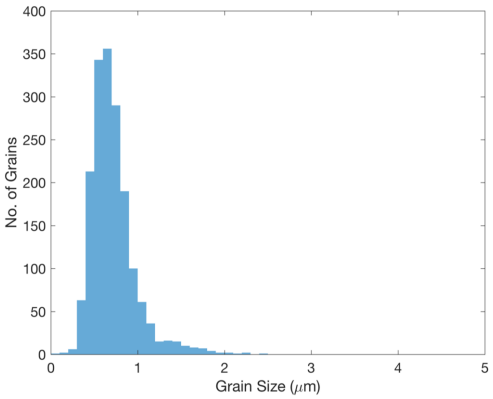
Ti-based oxides, with a Cr-rich outer shell. The Y signal in this area was too weak to be resolved.

In another area, shown in Figure 6.23, the Y signal was weakly resolved (the contrast in the Y map was normalised by the minimum intensity so the apparent strength of the Y signal is somewhat misleading). Comparing the EELS signal to the ADF image, Y enrichment occurred in the lighter contrast areas (the boundary of which is highlighted by the dotted line on the Y map). The edge of the Y-enriched region was also enriched in Cr, suggesting the possibility of a grain boundary (as seen in other ferritic ODS studies [168]), meaning this region could be a grain relatively enriched in Y (although still low absolute Y concentration).

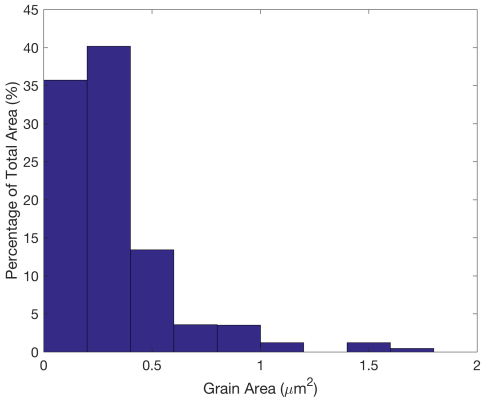
Atom probe tomography (APT) was explored as an alternative route to investigate the chemistry of the finest particles. Experiments were completed by Thomas Davis (Oxford University) as part of a collaborative project and atom reconstruction maps for Fe-14Cr-3W-0.3Ti+0.25Y_2O_3 are shown in Figure 6.24 for (a) Fe, Cr, W and Ti and (b) Y, CrO, TiO and YO. The APT needle sample size was approximately 40 × 40 × 270 nm. As expected, Fe and Cr concentrations were relatively uniform throughout the needle. There was a slight increase in Cr and W concentrations near the base that may suggest W enrichment at a grain boundary-like or dislocation-like feature. Elemental Ti (i.e. not associated with



(a) Low magnification (b) High magnification

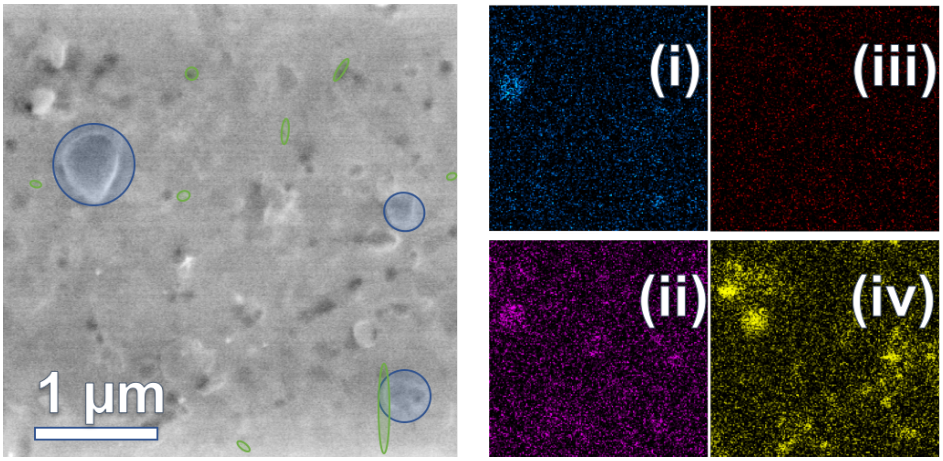


(c) Grain size distribution



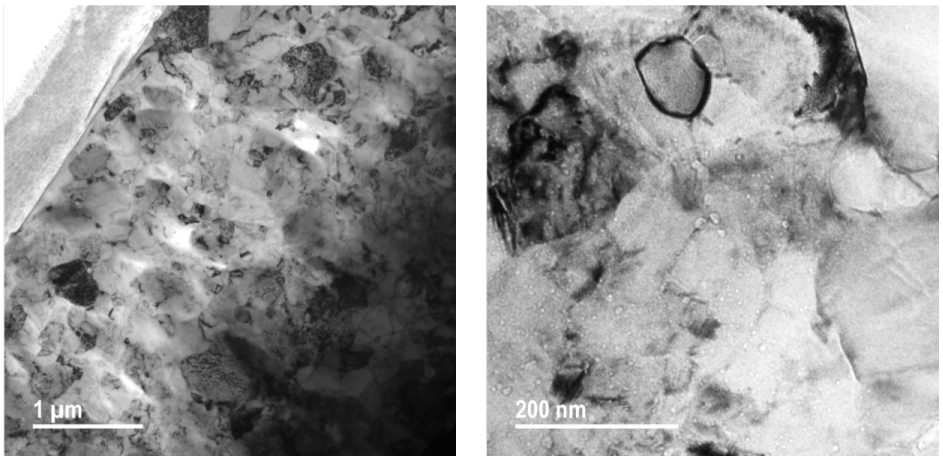
(d) Grain area distribution

Figure 6.19: False coloured EBSD orientation maps of Fe-14Cr-3W-0.3Ti+0.25Y_2O_3 milled powder consolidated by FAST then heat treated at 750°C for 1 h (a) low magnification (b) high magnification (c) histogram of grain size distribution and (d) histogram of grain area distribution.



(a) SE micrograph (b) (i) Ti, (ii) Cr, (iii) Y, (iv) O

Figure 6.20: SE micrographs and EDS maps of larger particles in FAST consolidated Fe-14Cr-3W-0.3Ti+0.25Y_2O_3 milled powder following heat treatment at 750°C for 1 h.



(a) Overview of sample (b) Particles on grain boundaries and within grains

Figure 6.21: Bright field TEM micrographs of (a) the microstructure and (b) the particles seen in Fe-14Cr-3W-0.3Ti+0.25Y_2O_3 milled powder consolidated by FAST and heat treated at 750°C for 1 h.

oxygen) tended to be more clustered than the other alloying elements, showing a large 30 nm area heavily enriched in Ti and much smaller clusters distributed through the needle. The 30 nm enrichment area also showed high concentrations of TiO, and some localisation of CrO. Elsewhere in the needle, overlap in enrichment of Y, YO_2, TiO and CrO indicated the presence of complex oxides.

Using the maximum separation method described in Section 3.5.3, cluster

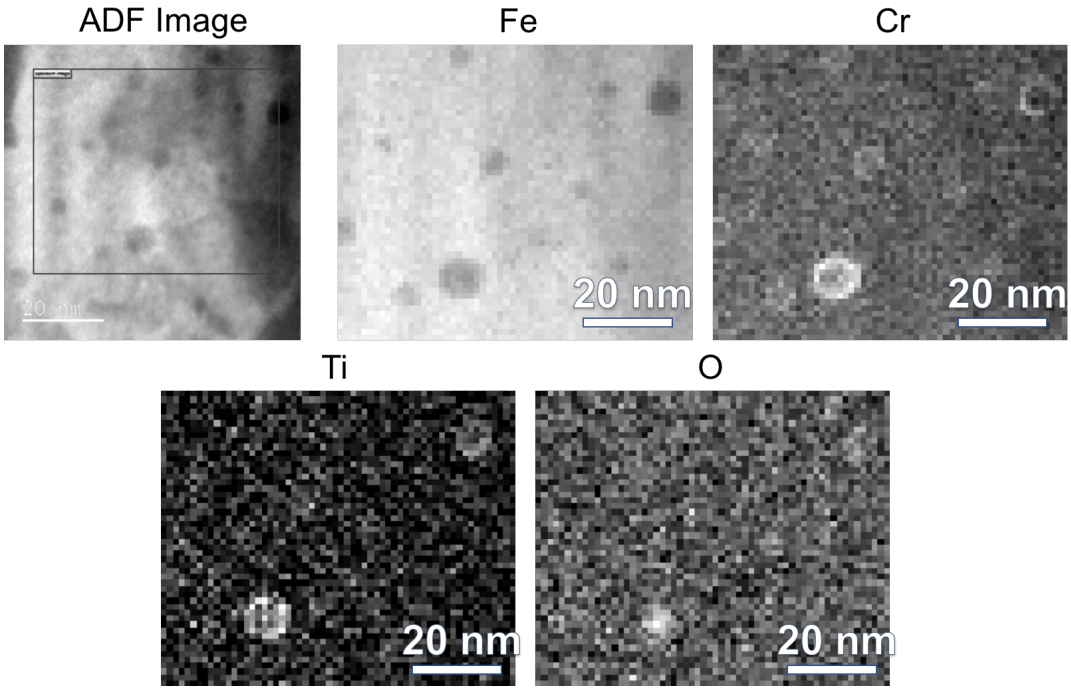


Figure 6.22: An ADF image of Fe-14Cr-3W-0.3Ti+0.25Y_2O_3 consolidated by FAST and corresponding EELS spectra (from the area highlighed in the ADF image) suggesting Ti-rich oxides with a Cr-rich shell.

analysis was performed showing a mean cluster diameter of 1 ± 0.4 nm. The elements making up these clusters are shown in Figure 6.25 (a), namely Ti, Y, TiO and YO, with the clusters isolated in (b) and an enlargement of the region of interest highlighted in (b), shown in (c). The approximate number density of clusters was 1.7×10^{24} m^{-3}. The average size was below that expected from literature (3-5 nm) for ferritic ODS steel produced via powder processing followed by field assisted sintering [97, 122].

Considering the cluster highlighted in Figure 6.25 (c), green atoms are from TiO, dark grey from Ti signal, blue from Y and purple from YO_2. Most of this cluster, and typical of most of the clusters, was suggested to comprise TiO. A proxigram concentration profile was taken over the cluster showing decomposed atomic concentrations of all of the elements in Figure 6.25 and is shown in Figure 6.26. The profiles were taken parallel to the z-axis in Figure 6.25 (c), from the origin of the x- and y-axes (positive z to negative z).

The cluster was predominantly Ti-O and elemental Y, with greater Y enrichment

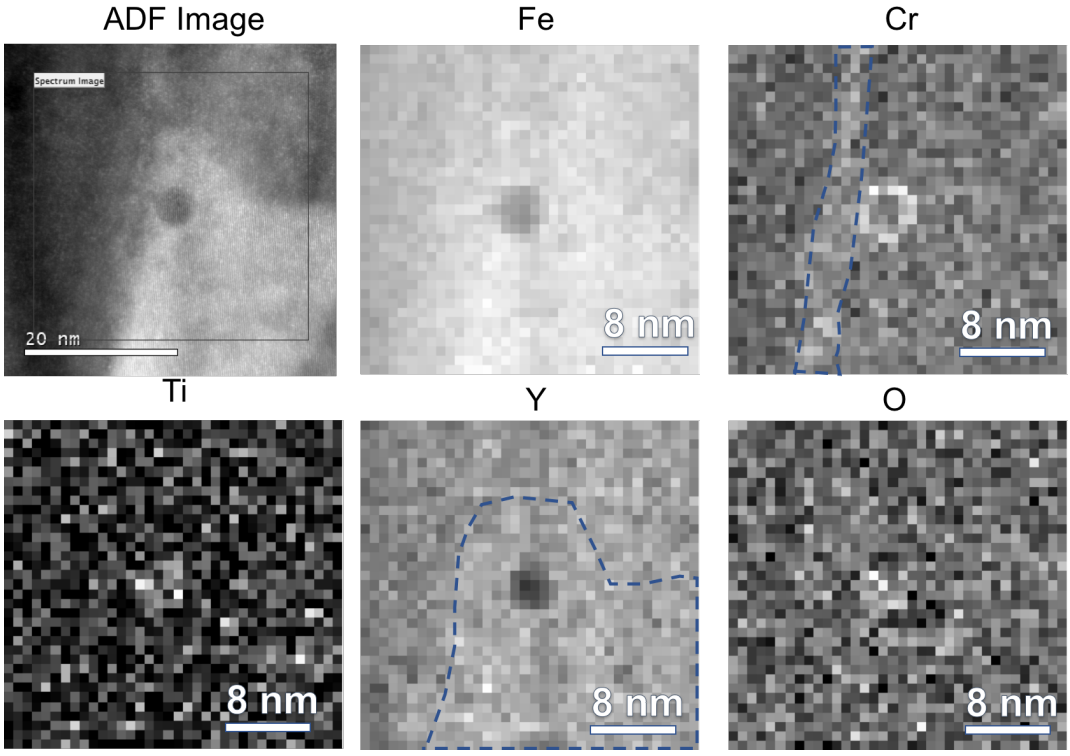


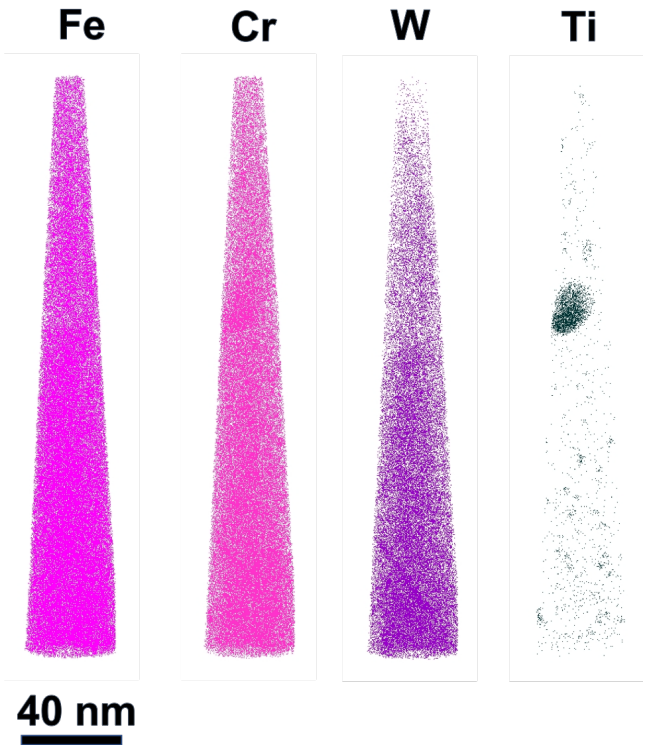
Figure 6.23: An ADF image of Fe-14Cr-3W-0.3Ti+0.25Y_2O_3 consolidated by FAST and corresponding EELS spectra (from the area highlighed in the ADF image) suggesting a Ti-Cr-rich shell, and local matrix enrichment of Y.

on the surface. This is unlike other studies where core / shell behaviour was shown by APT to have an Y-rich centre, and a Cr- or Ti- rich shell [169, 170]. The stoichiometry was estimated to be $Y_2Ti_2O_4$, which could suggest either the commonly reported $Y_2Ti_2O_5$ or elemental Y intermixed with a TiO_2 particle.

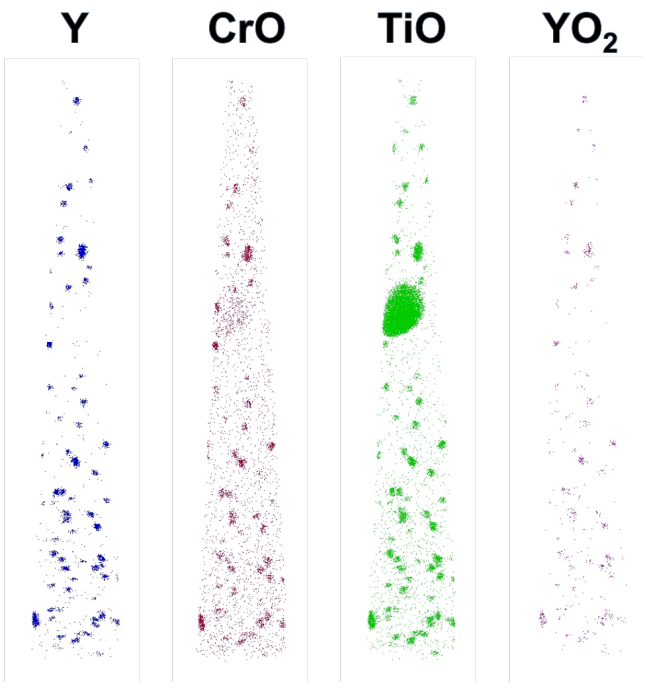
Due to the small size of the particles, it is likely that the latter is true, and these are in the early stages of particle development due to the short sintering time, and that the post-sintering heat treatment was not at a high enough temperature for further particle development.

6.4.4 FAST Consolidated Fe-14Cr-3W-0.3Ti-0.4Y+Fe_3O_4

Figure 6.27 shows an SEM image of Fe-14Cr-3W-0.3Ti-0.4Y+Fe_3O_4 consolidated by FAST and Figures 6.28 (a) and (b) show low and high magnification false coloured EBSD orientation maps respectively, with (c) showing the grain size distribution and (d) the grain area distribution. Compared to the Fe_3O_4 milled powder consolidated



(a)



(b)

Figure 6.24: APT reconstructions from a Fe-14Cr-3W-0.3Ti-0.25Y_2O_3 FAST needle approximate dimensions 40 × 40 × 270 nm showing the main alloying elements.

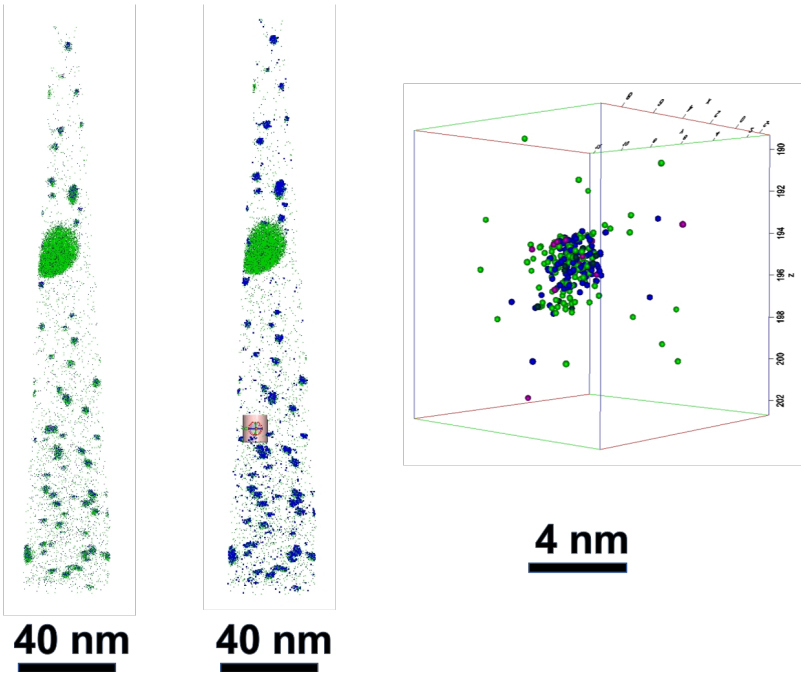


Figure 6.25: APT reconstructions from (a) Ti, Y, TiO and YO (b) isolated clusters (c) enlarged image of cluster from region of interest in (b).

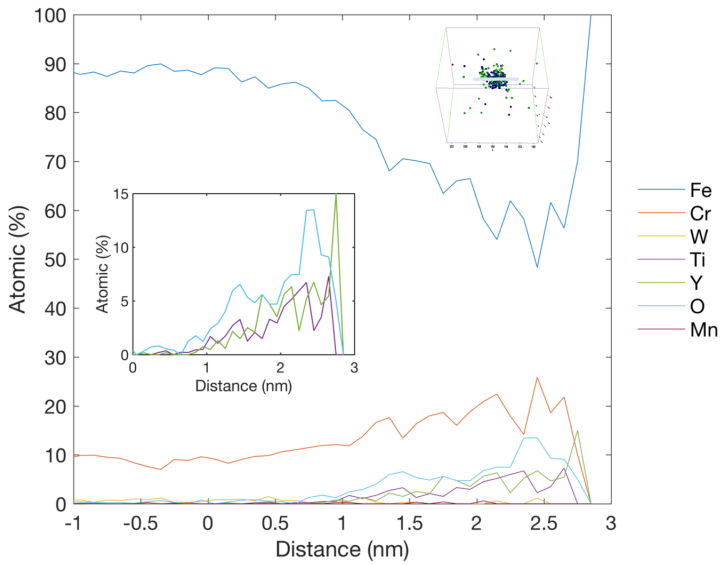


Figure 6.26: Proxigram concentration profile over the cluster seen in Figure 6.25 (c) showing decomposed atomic concentrations of Fe, Cr, W, Ti, Y, O and Mn and inset enlarged view of Ti, Y and O concentrations.

by HIP, the grain structure was similar, with larger (1-2 μm) grains decorated by smaller grains (mean $\sim$ 0.2 μm). The overall average grain size was 0.73 $\pm$ 0.7 μm, with the large variation reflecting the bimodality, also confirmed in the

grain area distribution. As in the same powder consolidated by HIP, (Figure 6.14), EBSD orientation maps showed evidence of residual misorientation within the larger grains, indicative of residual strain.

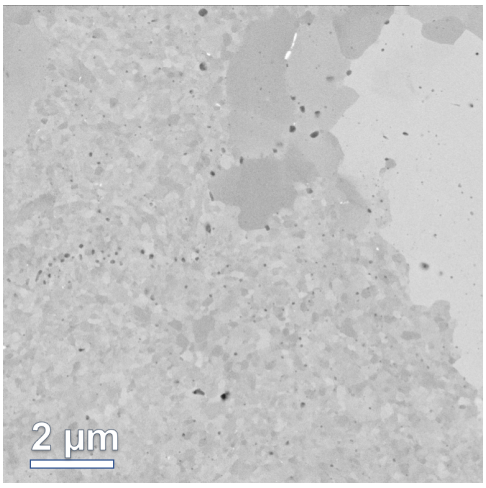
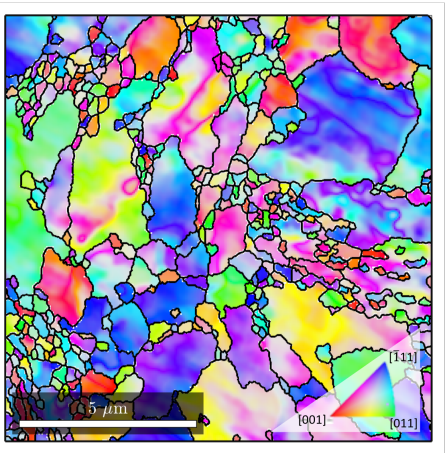


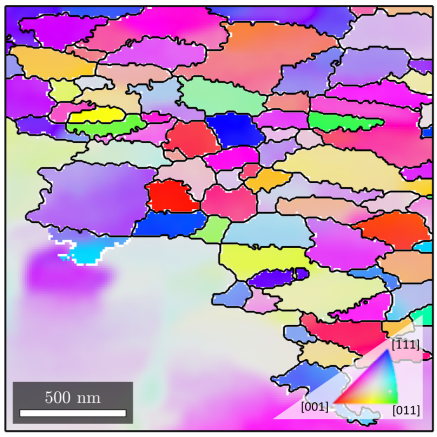
Figure 6.27: SEM micrograph of the bimodal grain size distribution in Fe-14Cr-3W-0.3Ti-0.4Y+Fe_3O_4 milled powder consolidated by FAST.

To relieve some of this work, and allow any further development of the oxide particles not complete during the short sintering time, a 750°C 1 h heat treatment was applied. Figures 6.29, 6.30 (a) and (b) show an SEM micrograph, low and high magnification EBSD orientation maps respectively of the microstructure following this heat treatment. Recovery of residual strain led to a reduction in average grain diameter to 0.54 ± 0.4 μm, with finer grains of 200 nm in average diameter. Compared with the same heat treatment applied to the Fe-14Cr-3W-0.3Ti+Y_2O_3 sintered by FAST, heat treatment had a less dramatic effect on microstructure (∼25% reduction in grain size compared with 50%), most likely due to less mechanical work being present in the powder (shown in Chapter 5) therefore less driving force for sub-grain development.

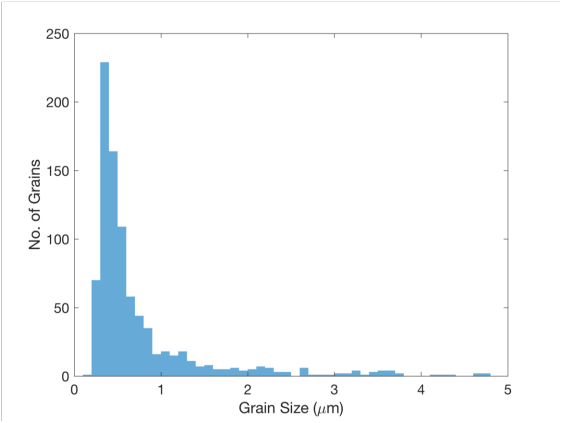
Figure 6.31 (a) shows an SE micrograph with corresponding EDX maps shown in (b) for Fe-14Cr-3W-0.3Ti-0.4Y+Fe_3O_4 milled powder consolidated by FAST then heat treated at 750°C for 1 h. Following the heat treatment, there were both Ti-rich oxides (highlighted in blue) and Y-rich oxides (highlighted in green) not



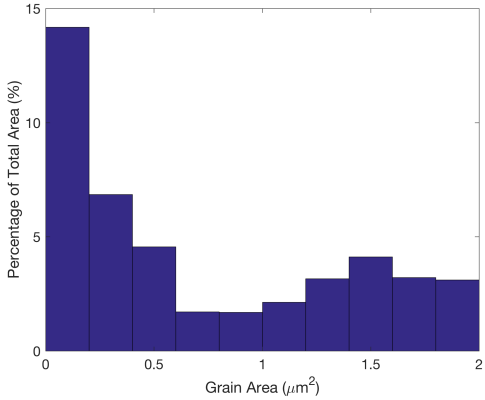
(a) Low magnification



(b) High magnification



(c) Grain size distribution



(d) Grain area distribution

Figure 6.28: False coloured EBSD orientation maps of the microstructure of Fe-14Cr-3W-0.3Ti-0.4Y+Fe_3O_4 milled powder consolidated by FAST (a) low magnification (b) high magnification (c) histogram of grain size distribution and (d) histogram of grain area distribution.

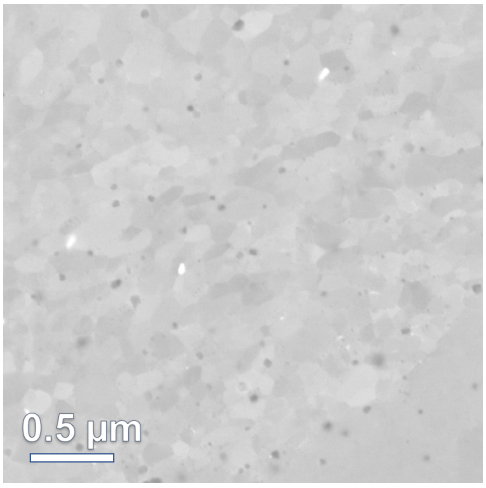


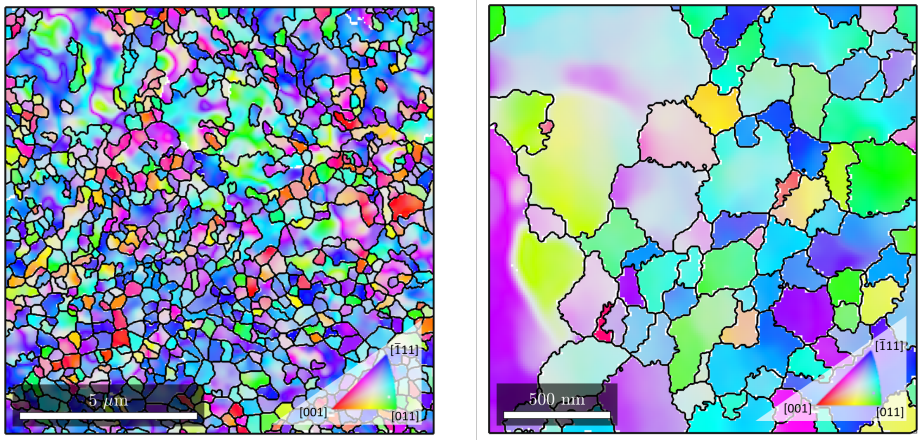
Figure 6.29: SEM micrograph of the microstructure of Fe-14Cr-3W-0.3Ti-0.4Y+Fe_3O_4 milled powder consolidated by FAST and heat treated for 1 h at 750°C.

seen prior to HT. The signal intensity and spatial resolution were not sufficient to identify the stoichiometry of the oxides.

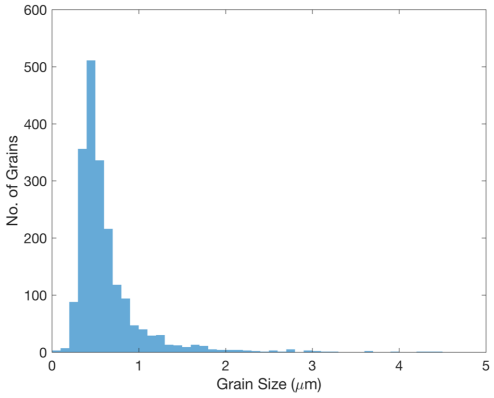
The bright field TEM micrograph in Figure 6.32 (a) shows again the bimodal grain size distribution indicated by EBSD, with a mixture of > 1 μm and ~ 100 nm grains. Figure 6.32(b) shows nanoparticles within grains and decorating grain boundaries with a mean particle size (measured by image analysis) of 8 ± 3 nm.

Due to constraints on the configuration of the microscope, chemical analysis could not be conducted and consequently APT was explored as an alternative route to investigate the chemistry of the finest particles.

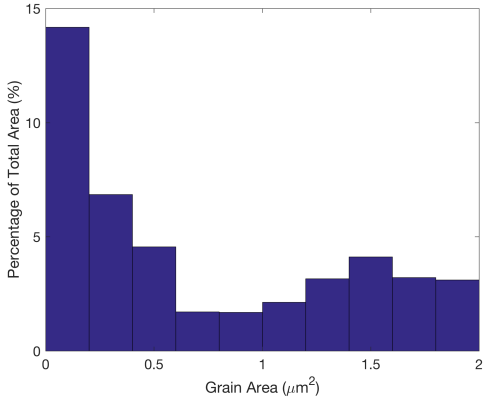
APT was again completed by Thomas Davis and atom reconstruction maps for Fe-14Cr-3W-0.3Ti-0.4Y+Fe_3O_4 are shown in Figure 6.33 for (a) Fe, Cr, W and Ti and (b) Y, CrO, TiO and YO. The APT needle sample size was approximately 40 $\times$ 40 $\times$ 180 nm. As expected, Fe and Cr concentrations were relatively uniform throughout the needle. There was a slight increase in W concentration near the base that may suggest W enrichment at a grain boundary-like or dislocation-like feature, supported by the weak suggestion of a grain triple point in this region. Elemental Ti (i.e. not associated with oxygen) tended to be more clustered than the other alloying elements. The reconstructions in (b) of Y, and the oxides, showed



(a) Low magnification (b) High magnification

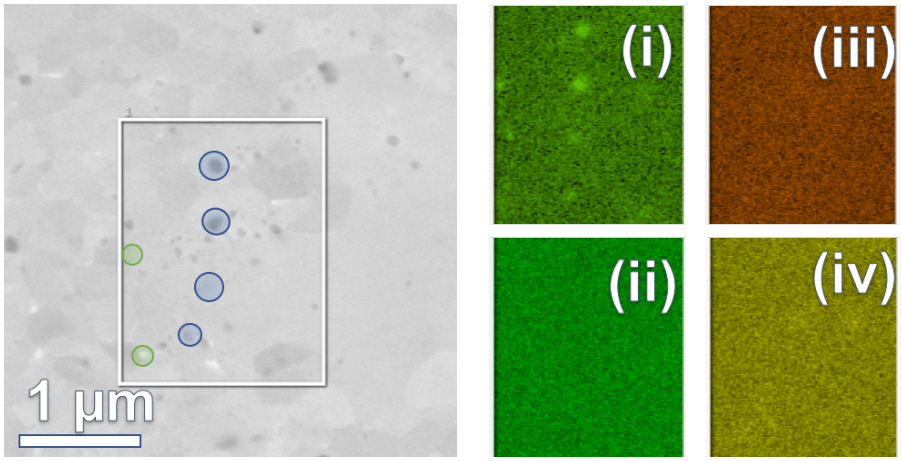


(c) Grain size distribution



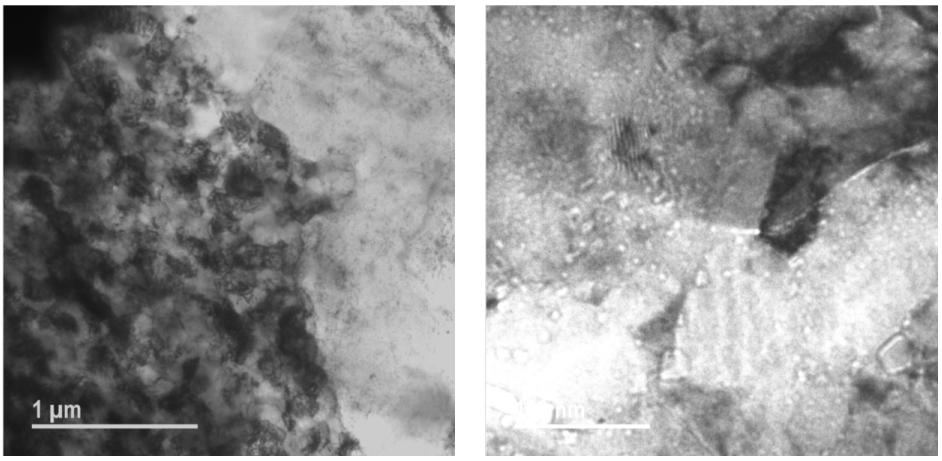
(d) Grain area distribution

Figure 6.30: False coloured EBSD orientation maps of the microstructure of Fe-14Cr-3W-0.3Ti-0.4Y+Fe_3O_4 milled powder consolidated by FAST then heat treated at 750°C for 1 h (a) low magnification (b) high magnification (c) histogram of grain size distribution and (d) grain area distribution.



(a) SE micrograph (b) (i) Ti, (ii) Cr, (iii) Y, (iv) O

Figure 6.31: SE micrographs and EDS maps of larger particles in FAST consolidated Fe-14Cr-3W-0.3Ti-0.4Y+Fe_3O_4 milled powder.

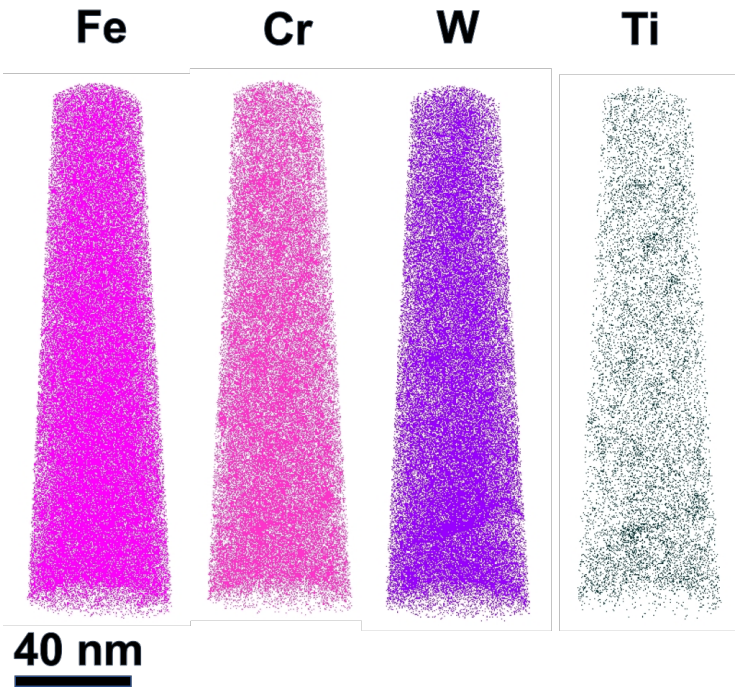


(a) Overview of sample showing bimodal microstructure (b) Particles on grain boundaries and within grains

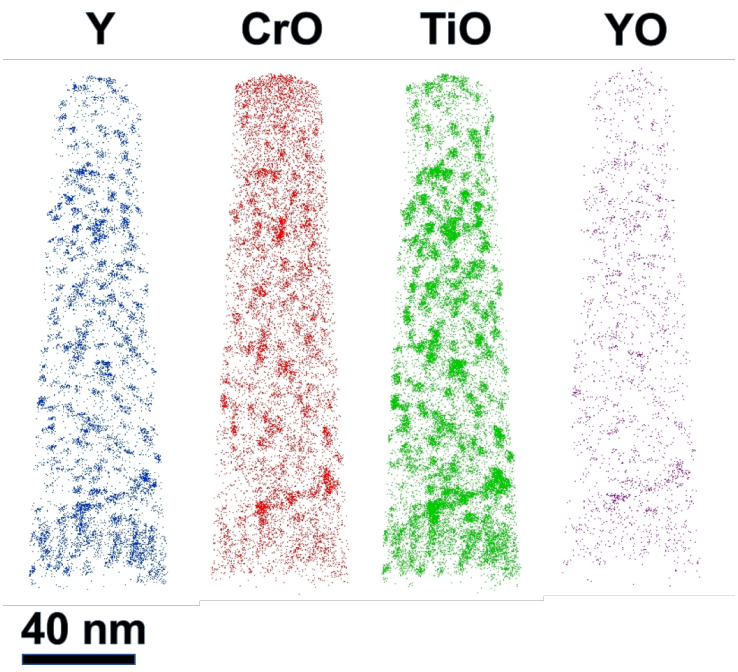
Figure 6.32: Bright field TEM micrographs of the microstructure and particles seen in Fe-14Cr-3W-0.3Ti-0.4Y+Fe_3O_4 milled powder consolidated by FAST.

much clearer evidence of clustering. Many of the clusters comparatively rich in Y were also enriched in TiO, YO and in places, CrO.

Cluster analysis showed an mean cluster diameter of 2.2 ± 0.4 nm. The elements making up these clusters are shown in Figure 6.34 (a), namely Ti, Y, TiO and YO, with the clusters isolated in (b) and an enlargement of the region of interest highlighted in (b), shown in (c). The approximate number density of clusters was 2.2×10^{24} m^{-3}. The average size agreed well with the literature, for ferritic ODS



(a)



(b)

Figure 6.33: APT reconstructions from a Fe-14Cr-3W-0.3Ti-0.4Y+0.27Fe_3O_4 FAST needle approximate dimensions 40 × 40 × 180 nm showing the main alloying elements.

steel produced via powder processing followed by FAST [97, 122].

Considering the cluster highlighted in Figure 6.34 (c), green-labelled atoms are

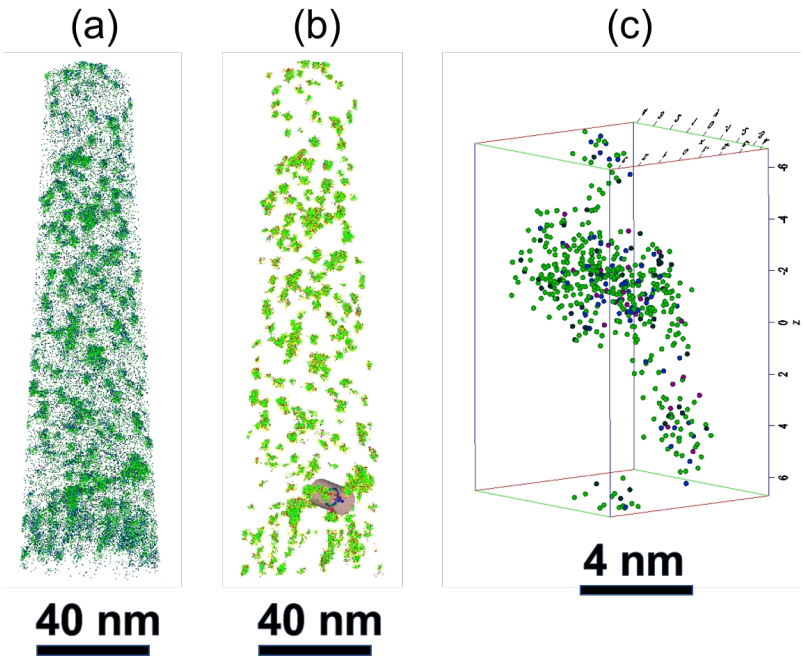


Figure 6.34: APT reconstructions from (a) Ti, Y, TiO and YO (b) isolated clusters (c) enlarged image of cluster from region of interest in (b).

from TiO, dark grey from Ti signal, blue from Y and purple from YO. Most of this cluster, and typical of most of the clusters, was suggested to comprise TiO. A proxigram concentration profile was taken over the cluster showing decomposed atomic concentrations of all of the elements in Figure 6.35. The profiles were taken parallel to the z-axis in Figure 6.34 (c), from the origin of the x- and y-axes (positive z to negative z).

Two distinct clusters lay on this line (at $\sim$ 2 nm and $\sim$ 9 nm), and were predominantly Ti and O with outer "shells" slightly enriched in Y compared with the volumes between the two clusters. This is unlike other studies where core / shell behaviour was shown by APT to have an Y-rich centre, and a Cr- or Ti-rich shell [169, 170]. The second cluster (at $\sim$ 9 nm) may have had this type of Cr-rich outer shell, but due to the small number of points sampled, firm conclusions could not be drawn reliably. The exact stoichiometry of the clusters cannot be determined reliably but were closer to TiO and TiO_2 (i.e. TiO_x) rather than to the more commonly reported Y containing stoichiometries such as $Y_2Ti_2O_5$, Y_2TiO_7

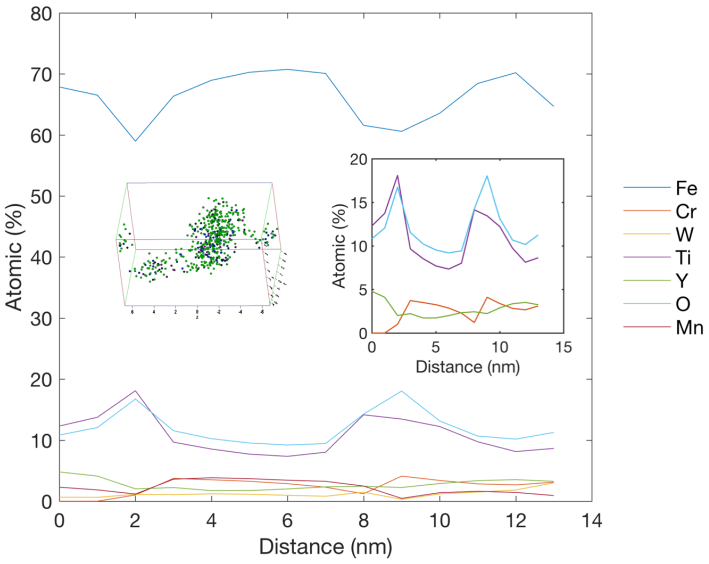


Figure 6.35: Proxigram concentration profile over the cluster seen in Figure 6.34 (c) showing decomposed atomic concentrations of Fe, Cr, W, Ti, Y, O and Mn and inset enlarged view of Cr, Ti, Y and O concentrations.

and Y_2O_3. Mn remained in solid solution surrounding the clusters and was not associated with any Mn-O type oxides.

Kumar *et al.* [171] compared the microstructure and mechanical properties for an austenitic ODS steel milled with Y_2O_3 or with TiO_2. Experiments showed highest density and hardness in the TiO_2 containing material, with TiO_2 particles showing an mean diameter of 20-35 nm, larger than those seen in the current work. Zener pinning effects, however, have been reported identical in both Ti- and Y-based oxides [172].

The Ellingham diagram (seen previously in Figure 2.9) indicating TiO_2 is formed in preference to FeO, Fe_3O_4 or Cr_2O_3, but are not as energetically favourable as Y_2O_3. The predominance of TiO_x supported that either the concentrations of Y were lower than initially intended (Y and Ti were targeted to be approximately equal) so there was not enough Y in solid solution to form oxides on precipitation and consistent with low Y concentrations in Tables 5.7 and 6.5, or the Y was already substantially reacted with O to form Y_2O_3 or similar as larger (> 1 μm) inclusions, at some stage earlier in the sequence of processing steps and such large inclusions were not integrated into the small APT needle.

6.4.5 Microstructural differences and similarities between HIP and FAST

Comparing the various processing methods, a number of different microstructures have been generated with different levels of residual misorientation within grains, different grain size distributions and potentially different particle distributions.

Table 6.6 shows a comparison between key microstructural and particle characteristics seen in Fe-14Cr-3W-0.3Ti+0.25Y_2O_3 powder consolidated by HIP (HIP Y_2O_3) and FAST (FAST Y_2O_3) and Fe-14Cr-3W-0.3Ti-0.4Y+Fe_3O_4 powder consolidated by HIP (Fe_3O_4 HIP) and FAST (Fe_3O_4 FAST). Results for the FAST consolidated materials are shown following heat treatment to make them more comparable with HIP.

Characteristic	HIP Y_2O_3	HIP Fe_3O_4	FAST Y_2O_3	FAST Fe_3O_4
Mean grain size (μm)	0.87	0.62	0.32	0.54
O-based particle diameter (nm)				$\sim$ 2 (TiO_x)
Particle density ($\times$ 10^{24})				$\sim$ 2 (TiO_x)
Microstrain (%)	0.08	0.12	0.12	0.03
Crystallite size (nm)	13.3	33.1	28.9	7.2
Dislocation density ($\times 10^{13}$)	8.8	5.0	5.9	5.1

Table 6.6: Microstructural comparison between final material.

XRD

XRD was used to estimate the microstrain and crystallite size for the sintered, and heat treated materials. Figure 6.36 shows that in the case of the FAST samples, both pre- and post-HT (labelled HT), microstrain was approximately constant at $\sim$ 0.1 except for Fe-14Cr-3W-0.3Ti+0.25Y_2O_3 FAST that retained more strain due to a shorter sintering time, and Fe-14Cr-3W-0.3Ti-0.4Y+Fe_3O_4 FAST HT that showed very low microstrain as there was already little cold work remaining prior to the heat treatment. The Fe-14Cr-3W-0.3Ti-0.4Y+Fe_3O_4 FAST HT sample was quite thin and most likely led to an artifact during XRD measurement, as the errors in the Williamson-Hall plot, and therefore errors in the calculated values were quite large, and results from this measurement should not be overly interpreted.

Estimated crystallite sizes ranged from $\sim$ 7 nm to $\sim$ 35 nm, smaller than the average grain sizes, as shown in Table 6.7. The small crystallite size seen following both HIP and FAST+HT consolidation may imply effective grain and / or sub-grain pinning. Given crystallite, or domain, sizes were so much smaller than grain sizes, this may also imply sub-grain strengthening, which was assumed in the analysis of strengthening contributions in Chapter 5. If domain size was comparable to grain size, this would indicate full recovery or recrystallisation, but there was 1 - 2 orders of magnitude difference. There are inherent inaccuracies and limitations in these estimations, not least from using laboratory XRD kit with its own resolution limits, but the grain / crystallite size difference are nonetheless significant.

(μm)	HIP Y_2O_3	HIP Fe_3O_4	FAST Y_2O_3	FAST Fe_3O_4
Mean grain size pre-HT	0.87	0.62	0.6	0.73
Mean grain size post-HT			0.32	0.54
Mean crystallite site pre-HT	0.009	0.005	0.035	0.009
Mean crystallite size post-HT			0.006	0.005

Table 6.7: Mean grain size and crystallite size pre- and post- HT for all materials.

Comparing Fe-14Cr-3W-0.3Ti+0.25Y_2O_3 alloys, as-FAST was more strained than HIPed, but with a similar domain size. Following heat treatment, the microstrain were reduced similarly to $\sim$ 0.1 and the crystallite size increased to 30 nm.

Comparing Fe-14Cr-3W-0.3Ti-0.4Y+Fe_3O_4 alloys, HIPing led to a larger domain size but the microstrain was the same in both HIP and FAST, since the starting powder had little microstrain initially.

As previously performed for the unconsolidated powders, using the microstrain and crystallite size, the mean dislocation density ρ was estimated using Equation 5.1.

Table 6.8 shows the estimated dislocation densities for each processing method, and in the case of FAST, pre- and post- heat treatment. For Fe-14Cr-3W-0.3Ti+0.25Y_2O_3, as expected, FAST with its shorter sintering time led to a higher residual dislocation density (35 $\times 10^{13}$ m^{-3}) than HIP (8 $\times 10^{13}$ m^{-3}), and similarly for Fe-14Cr-3W-0.3Ti-0.4Y+Fe_3O_4, with FAST leading to a slightly higher dislocation density (9 $\times 10^{13}$ m^{-3}) than HIP (5 $\times 10^{13}$ m^{-3}). Comparing with the

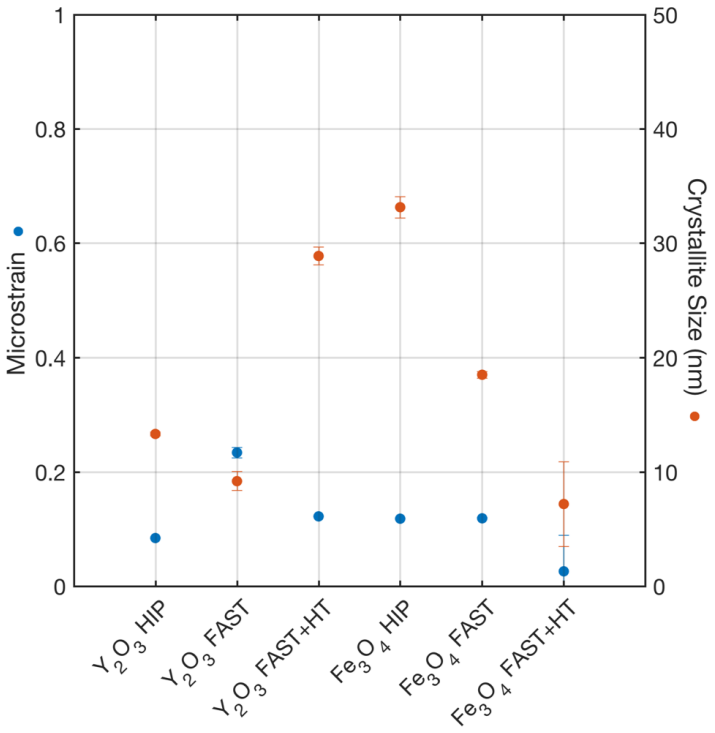


Figure 6.36: Microstrain and crystallite size estimations from XRD data for Fe-14Cr-3W-0.3Ti+0.25Y_2O_3 consolidated by HIP and FAST and Fe-14Cr-3W-0.3Ti-0.4Y+Fe_3O_4.

starting powder, HIP gave a 80-90% reduction in dislocation density, and FAST gave a 50-60% reduction, with post sintering heat treatment leading to an overall reduction of 80-90%, similar to HIP alone.

Dislocation density ($\times 10^{13}$ m^{-3})	HIP Y_2O_3	HIP Fe_3O_4	FAST Y_2O_3	FAST Fe_3O_4
Powder	75	26	75	26
Sintered (pre-HT)	9	5	35	9
Sintered (post-HT)			6	5

Table 6.8: Dislocation density of Fe-14Cr-3W-0.3Ti+0.25Y_2O_3 consolidated by HIP and FAST+HT and Fe-14Cr-3W-0.3Ti-0.4Y+Fe_3O_4 consolidated by HIP and FAST+HT estimated from XRD data.

Grain Structure

Comparing the consolidation methods for MA Fe-14Cr-3W-0.3Ti+0.25Y_2O_3, HIP led to the characteristic bimodal grain diameter distribution typical of ODS steels [12],

with a mean diameter of 0.9 μm. FAST consolidation of the same material led to a slightly more refined grain distribution with mean grain diameter of 0.6 μm which, following heat treatment, became further refined to 0.3 μm with a narrow standard deviation of 0.18 μm. It is assumed that the heat treatment chosen allowed recovery to occur, but prevented recrystallisation, or fast, diffusion-enhanced, grain boundary migration, notwithstanding difficulties in distinguishing recovery from recrystallisation in that complex, ultrafine stabilised microstructures. Other studies on the recrystallisation temperature of Fe-14Cr ODS steels have suggested a range of 750-800°C, most commonly at the upper end of this range [30]. Although abnormal grain growth can occur at any temperature, the thermal contribution to overcoming the pinning energy barrier so that grain boundaries become mobile and grains may coarsen means that abnormal grain growth is normally seen at temperatures above 850-900°C in Fe-14Cr ODS steels [30].

Comparison of the final grain structure with the literature is complicated as most published grain distribution data is from extruded or HIPed material, where extruded materials retain a strong texture following heat treatment (as in Chapter 4). Most data published on FAST material is only in the as-sintered state. Overall, comparing the two consolidation methods when applied to Fe-14Cr-3W-0.3Ti-0.4Y+Fe_3O_4, both HIP and FAST led to a bimodal microstructure, of similar size (0.6-0.7 μm). Following heat treatment of the FAST material, the average grain size decreased slightly to $\sim$ 0.5 μm, but remained bimodal, comparable to the HIP microstructure.

6.5 Thermal Stability

As described in Section 2.5.1, thermal stability, especially grain size, is of particular importance in thin wall fuel cladding applications. Excessive grain growth could lead to a very small number of grains spanning the wall thickness and degrade resistance to pressure and radiation induced swelling. Therefore, the thermal stability of the ODS alloys were investigated at reactor relevant temperatures.

Due to tight time constraints the same area of microstructure was not analysed at each stage, so only general trends can be discussed, not changes to specific grains. Microhardness during thermal ageing was also investigated and is discussed later in Section 7.2.2. The ageing treatment was at 650°C for a range of times up to 675 h under vacuum.

6.5.1 Fe-14Cr-3W-0.3Ti+0.25Y_2O_3 HIP

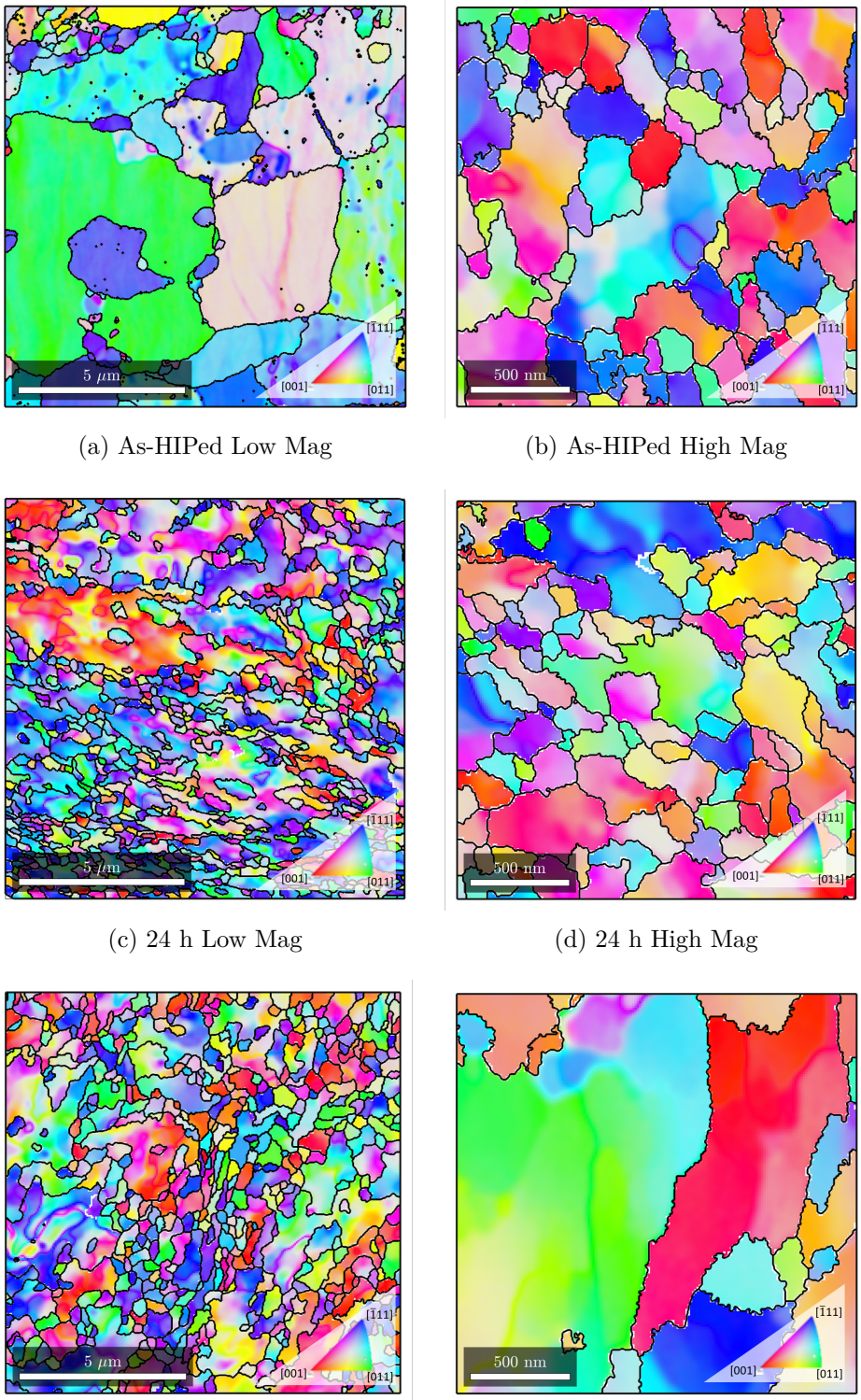
Figure 6.37 shows false coloured EBSD orientation maps at 0 h, 24 h and 675 h at 650°C under vacuum at low and high magnification. Figure 6.38 shows a histogram of the grain size distribution and the grain area distribution for the 24 h and 675 h samples, with average grain sizes shown in Table 6.9 alongside the as-HIPed values. Overall, a decrease of ∼0.1 μm showed the grain structure was essentially unchanged during the thermal ageing process, and some level of bimodality remained as seen in the grain area distribution.

Heat treatment time	Grain size (μm)
0 h	0.87 ± 1.11
24 h	0.74 ± 0.35
675 h	0.76 ± 0.67

Table 6.9: Grain size as a function of ageing time for Fe-14Cr-3W-0.3Ti+0.25Y_2O_3 HIP material.

6.5.2 Fe-14Cr-3W-0.3Ti-0.4Y+Fe_3O_4 HIP

Figure 6.39 shows the false coloured EBSD orientation maps at 0 h, 24 h and 675 h at 650°C under vacuum at low and high magnification. Figure 6.40 shows the histogram



(a) As-HIPed Low Mag

(b) As-HIPed High Mag

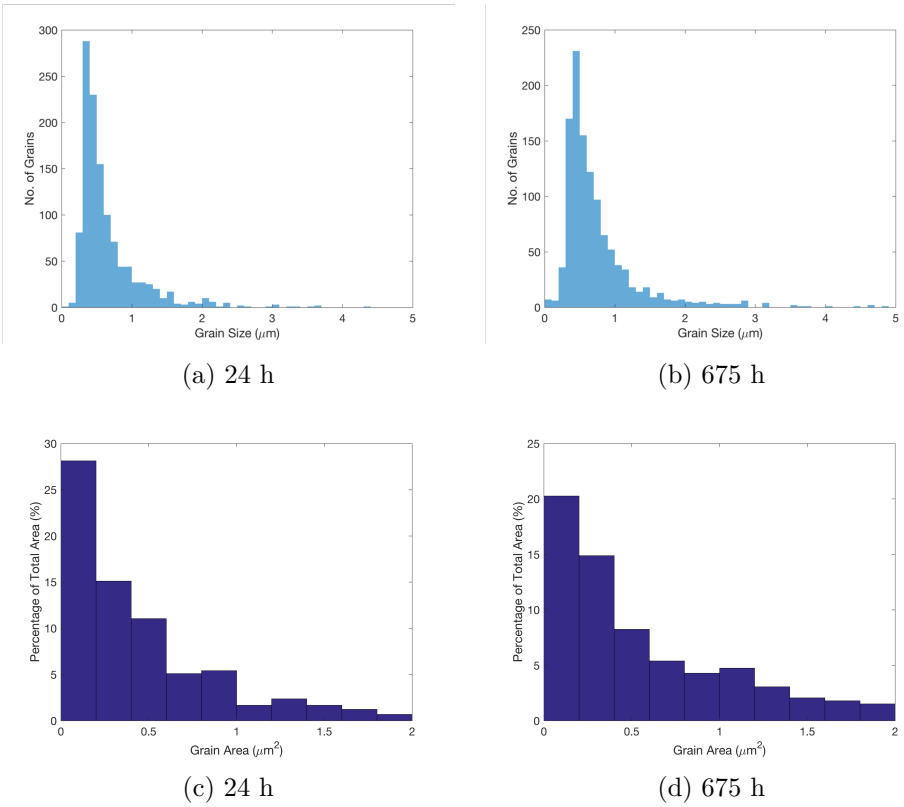
(c) 24 h Low Mag

(d) 24 h High Mag

(e) 675 h Low Mag

(f) 675 h High Mag

Figure 6.37: EBSD maps of Fe-14Cr-3W-0.3Ti+0.25Y_2O_3 HIP following a heat treatment at 650°C for (a), (b) 0 h (c), (d) 24 h (e), (f) 675 h under vacuum.



(a) 24 h (b) 675 h

(c) 24 h (d) 675 h

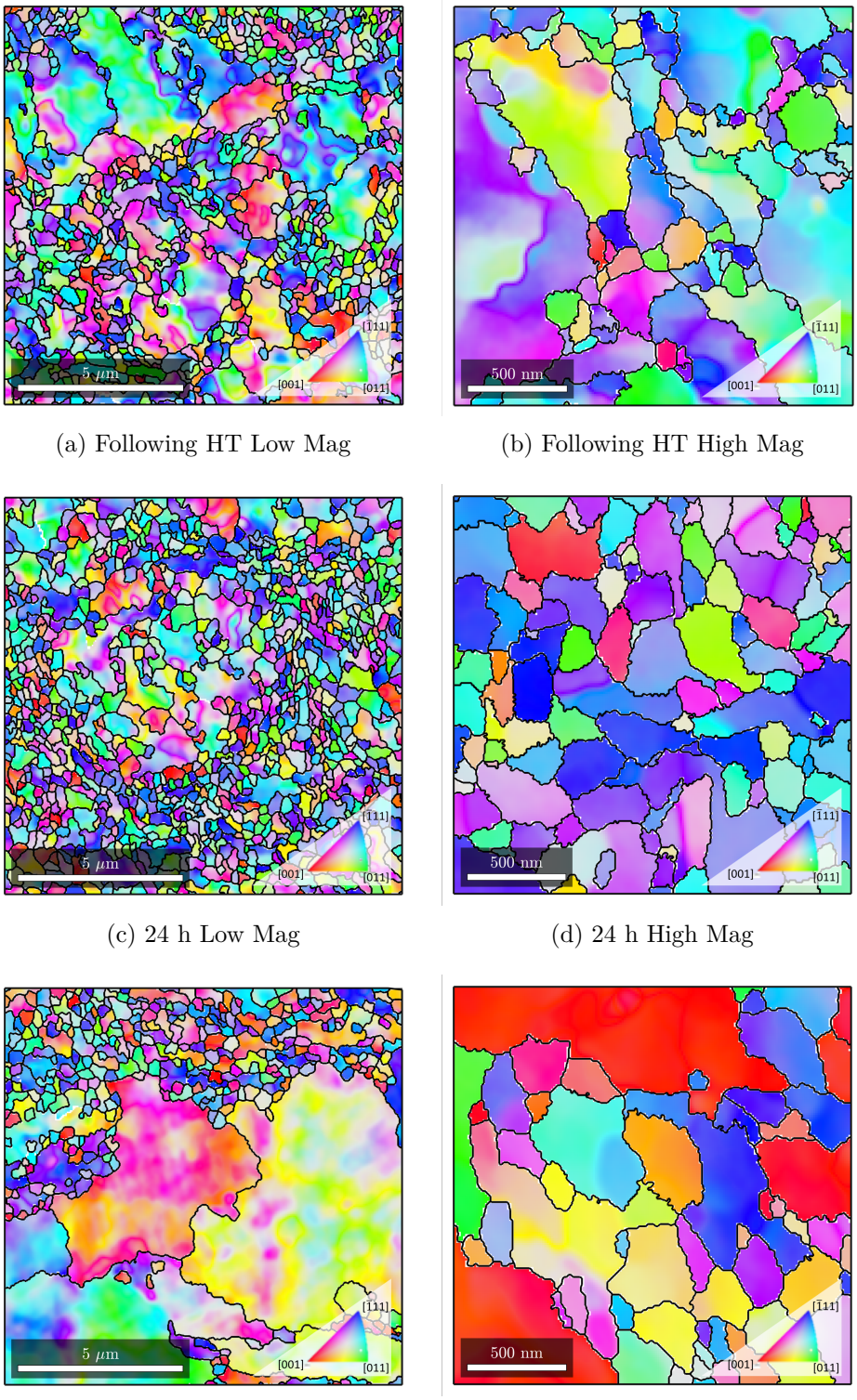
Figure 6.38: Histogram of grain size distributions and grain area distributions from EBSD orientation maps of Fe-14Cr-3W-0.3Ti+0.25Y_2O_3 milled powder consolidated by HIP following a heat treatment at 650°C for (a) and (c) 24 h and (b) and (d) 675 h.

of grain size distributions and Figure 6.40(d) the grain area distributions for the 24 h and 675 h samples. Table 6.10 shows the average grain sizes measured from this data, alongside the as-HIPed value, which remained approximately constant up to 675 h, as did the grain area distributions.

Heat treatment time	Grain size (μm)
0 h	0.62 ± 0.48
24 h	0.64 ± 0.41
675 h	0.62 ± 0.59

Table 6.10: Grain size as a function of ageing time for Fe-14Cr-3W-0.3Ti-0.4+Fe_3O_4 HIP material.

Figure 6.41 shows the microstructure of the Fe-14Cr-3W-0.3Ti-0.4Y+Fe_3O_4 HIP material after 675 h. Before the heat treatment, only fine TiO_x particles were detected (e.g. in Figure 6.15(b)), but a range of particles were detected after 675 h.



(a) Following HT Low Mag

(b) Following HT High Mag

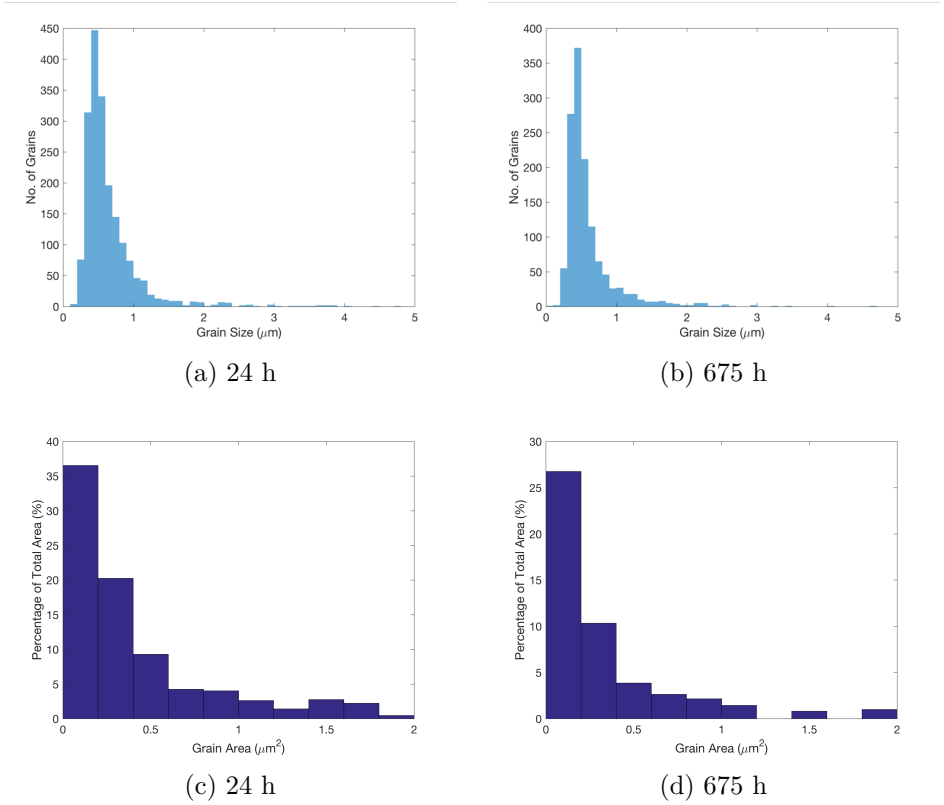
(c) 24 h Low Mag

(d) 24 h High Mag

(e) 675 h Low Mag

(f) 675 h High Mag

Figure 6.39: EBSD maps of Fe-14Cr-3W-0.3Ti-0.4Y+Fe_3O_4 HIP following an isothermal hold at 650°C for (a), (b) 0 h (c), (d) 24 h (e), (f) 675 h.



(a) 24 h (b) 675 h

(c) 24 h (d) 675 h

Figure 6.40: Histogram of grain size distributions and area distributions from EBSD orientation maps of Fe-14Cr-3W-0.3Ti-0.4Y+Fe_3O_4 milled powder consolidated by HIP following a heat treatment at 650°C for (a) and (c) 24 h and (b) and (d) 675 h.

Particles highlighted in blue had elevated concentrations of Y ($\sim$ 9 wt%) and Ti (7 wt%). Particles highlighted in purple showed enrichment in Ti (12 wt%) and some Y (0.5 wt%) and Cr (24 wt%). Particles highlighted in green and showing as light on the BSE image (therefore a heavier atomic weight than the matrix) were enriched in W, but the associated C and O signals could not be resolved with confidence, i.e. micro-segregation of W in solid solution or the formation of second phase particles such as WC. Table 6.11 shows the composition of particles highlighted in Figure 6.41. The electron beam diameter was 10s of nm for EDS, so isolation of elemental signals from particles alone could not be obtained and only particles type was possible. These were suggested as Y+Yi rich oxides, not previously detected.

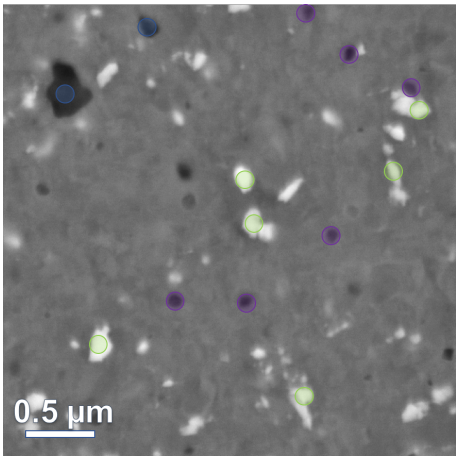


Figure 6.41: BSE micrograph of the Fe-14Cr-3W-0.3Ti+0.25Y_2O_3 HIP microstructure following 675 h at 650°C with Y- and Ti-rich regions higlighted in blue, Ti-, Cr- and Ti-rich regions highlighted in purple and W rich regions in green.

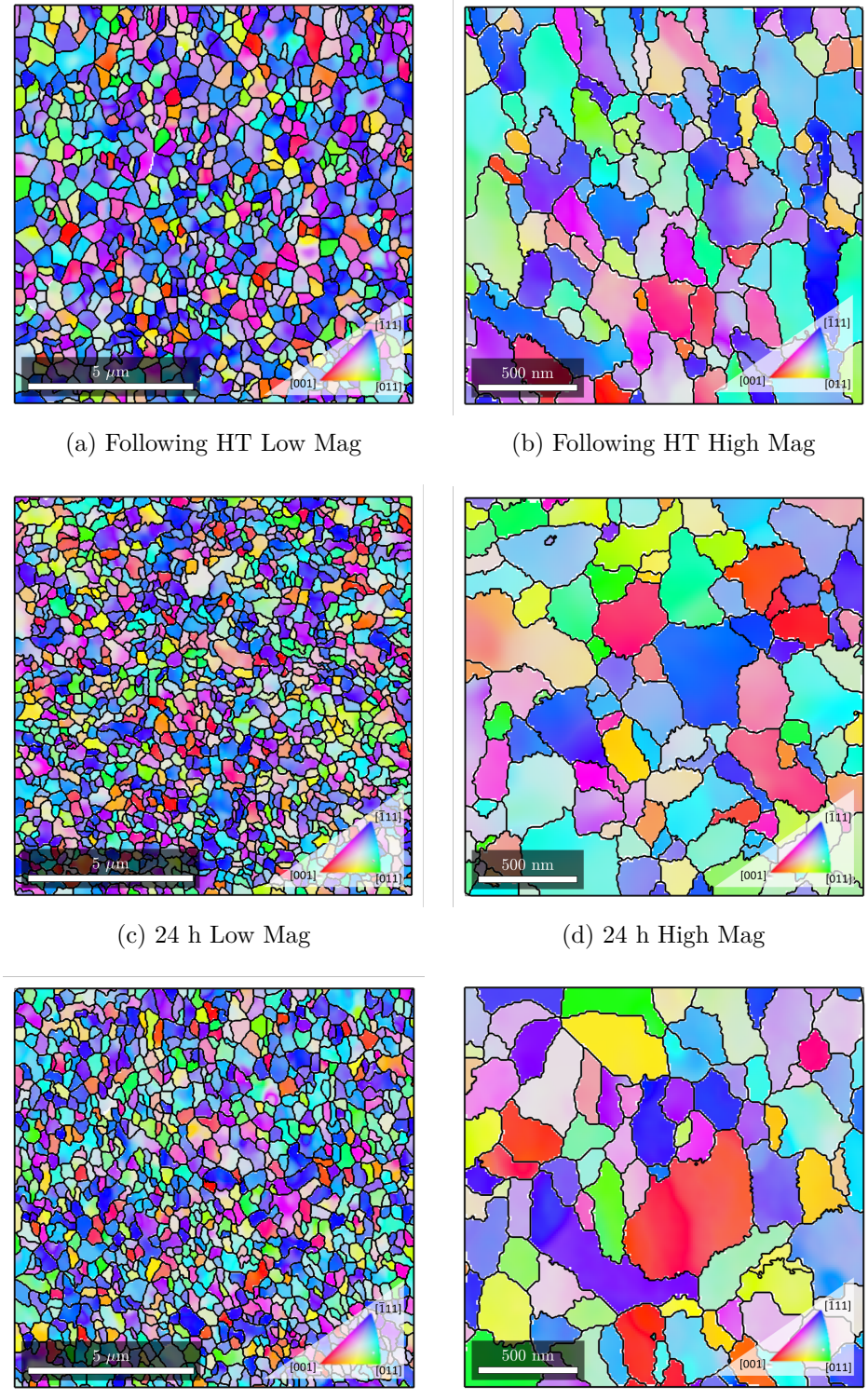
Region	Fe (wt%)	Cr (wt%)	W (wt%)	Ti (wt%)	Y (wt%)
Blue	69	12	4	7	9
Purple	62	24	1	12	0.5
Green	59	16	25	0	0
Matrix	80	16	3	1	0.4

Table 6.11: Approximate chemical composition of particles highlighted in Figure 6.41 measured by EDS.

6.5.3 Fe-14Cr-3W-0.3Ti+0.25Y_2O_3 FAST

Figure 6.42 shows false coloured EBSD orientation maps after 0 h, 24 h and 675 h at 650°C under vacuum at low and high magnifications. The initial microstructure shown here had already received 1 h at 650°C and was thus a very stable microstructure. Figure 6.43 shows histograms of the grain size distribution and the grain area distribution for 24 h and 675 h samples. Average grain sizes are shown in Table 6.12 alongside as-FAST (following the post-sintering heat treatment), where the average grain size remained constant at 0.3 μm, and very little change was seen in the grain size or area distributions following the heat treatments.

Prior to heat treatment, Cr-, Ti- and O- rich particles, and smaller particles rich in Y and O were detected. After 675 h at 650°C, more particles appeared rich in Y ($\sim$ 0.5 wt%) and Ti (1-2 wt%), highlighted in blue in Figure 6.44, and with some

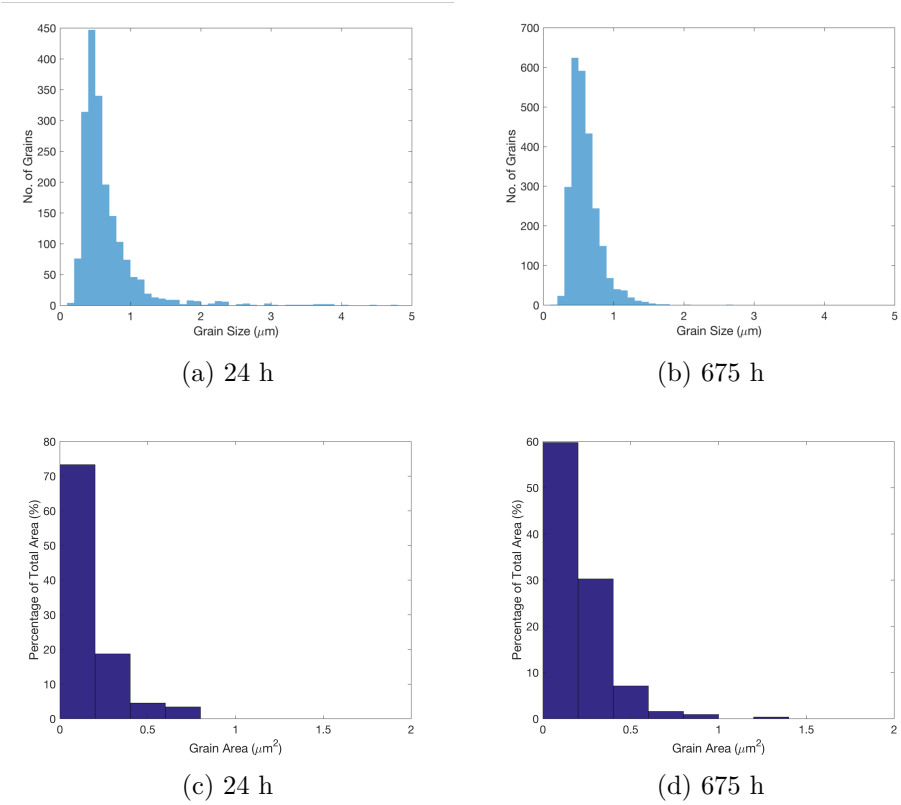


(a) Following HT Low Mag (b) Following HT High Mag

(c) 24 h Low Mag (d) 24 h High Mag

(e) 675 h Low Mag (f) 675 h High Mag

Figure 6.42: EBSD maps of Fe-14Cr-3W-0.3Ti+0.25Y_2O_3 FAST following heat treatment at 650°C for (a), (b) 0 h (c), (d) 24 h (e), (f) 675 h under vacuum.



(a) 24 h (b) 675 h

(c) 24 h (d) 675 h

Figure 6.43: Histogram of grain size distributions from EBSD orientation maps of Fe-14Cr-3W-0.3Ti+0.25Y_2O_3 milled powder consolidated by FAST following a heat treatment at 650°C for (a) 24 h and (b) 675 h.

Heat Treatment Time	Grain Size (μm)
HT	0.3 ± 0.2
24 h	0.3 ± 0.2
675 h	0.3 ± 0.2

Table 6.12: Grain size as a function of ageing time for Fe-14Cr-3W-0.3Ti+0.25Y_2O_3 FAST material.

elevated concentrations of Cr (highlighted in purple). There were Ti- and Cr- rich oxide particles (highlighted in orange), W-rich regions (highlighted in green) and Cr-rich particles (highlighted in red). Compositions from these regions are shown in Table 6.13, again implying the presence of "Y+Ti" rich oxides.

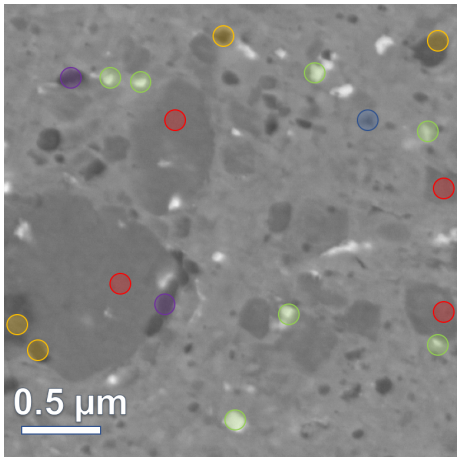


Figure 6.44: BSE micrograph of the Fe-14Cr-3W-0.3Ti+0.25Y_2O_3 FAST microstructure following a 675 h hold at 650°C with Y and Ti rich regions higlighted in blue, Ti- Cr- and Y- rich regions highlighted in purple, Ti- and Cr- rich regions highlighted in orange, W- rich regions in green and CrN in red.

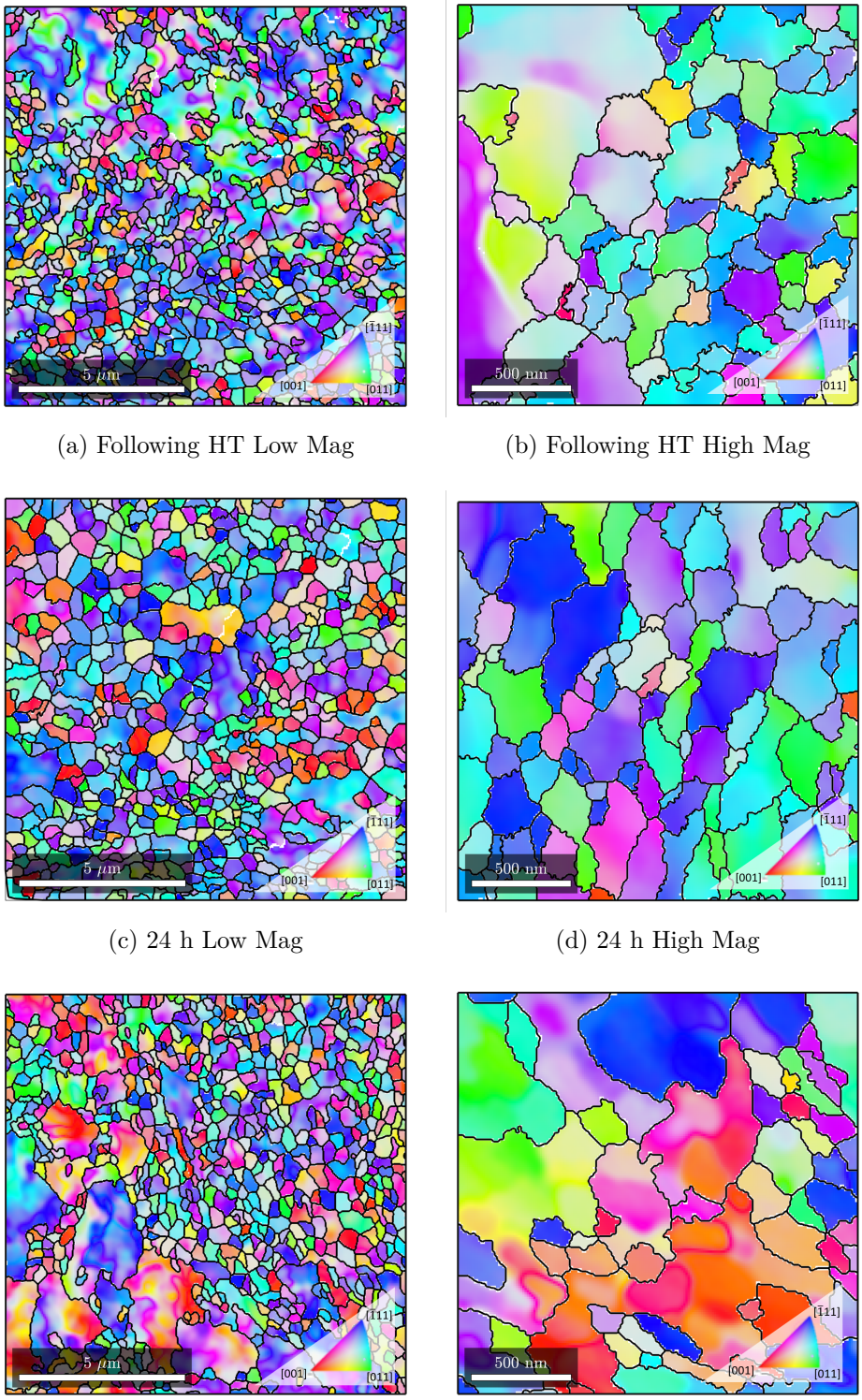
Region	Fe (wt%)	Cr (wt%)	W (wt%)	Ti (wt%)	Y (wt%)
Blue	80	16	2	1	0.5
Purple	71	24	2	3	0.4
Green	71	15	14	0.3	0
Orange	20	66	1	13	0.1
Red	40	56	4	1	0
Matrix	87	11	2	0.3	0.03

Table 6.13: Chemical composition of particles highlighted in Figure 6.44 measured by EDS.

6.5.4 Fe-14Cr-3W-0.3Ti-0.4Y+Fe_3O_4 FAST

Figure 6.45 shows false coloured EBSD orientation maps after 0 h, 24 h and 675 h at 650°C under vacuum. Figure 6.46 shows histograms of the grain size distributions and the grain area distributions for the 24 h and 675 h samples. Table 6.14 shows the average grain size from this data, alongside the as-FAST (following the post-sintering heat treatment), was approximately constant at ~0.5 μm, and very little change in the grain area distributions.

Figure 6.47 shows the microstructure of the Fe_3O_4 FAST material following 675 h at 650°C. As in the Y_2O_3 FAST material, there were a small number of particles: Y- and Ti-rich regions higlighted in blue, Ti- Cr- and Y-rich regions



(a) Following HT Low Mag

(b) Following HT High Mag

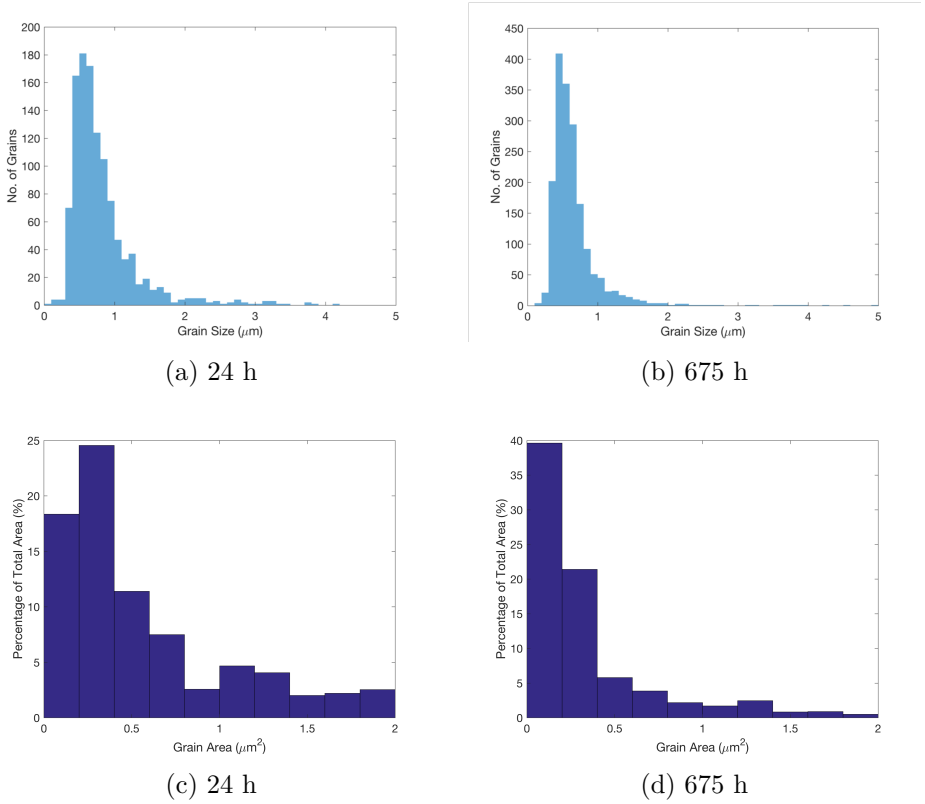
(c) 24 h Low Mag

(d) 24 h High Mag

(e) 675 h Low Mag

(f) 675 h High Mag

Figure 6.45: EBSD maps of Fe-14Cr-3W-0.3Ti-0.4Y+Fe_3O_4 FAST following an heat treatment at 650°C for (a), (b) 0 h (c), (d) 24 h (e), (f) 675 h under vacuum.



(a) 24 h (b) 675 h

(c) 24 h (d) 675 h

Figure 6.46: Histogram of grain size distributions from EBSD orientation maps of Fe-14Cr-3W-0.3Ti-0.4Y+Fe_3O_4 milled powder consolidated by HIP following a heat treatment at 650°C for (a) 24 h and (b) 675 h.

Thermal hold time	Grain size (μm)
HT	0.54 ± 0.41
24 h	0.40 ± 0.30
675 h	0.50 ± 0.35

Table 6.14: Grain size as a function of ageing time for Fe-14Cr-3W-0.3Ti-0.4Y+Fe_3O_4 material.

highlighted in purple, Ti- and Cr-rich regions highlighted in orange, W-rich regions in green and Cr-rich areas in red. Approximate compositions of the particles by EDS is given in Table 6.15.

6.5.5 Thermal Stability Summary

All the processing methods produced ODS-like microstructures with very stable grain sizes up to 675 h at 650°C. It was suggested that all the processing methods

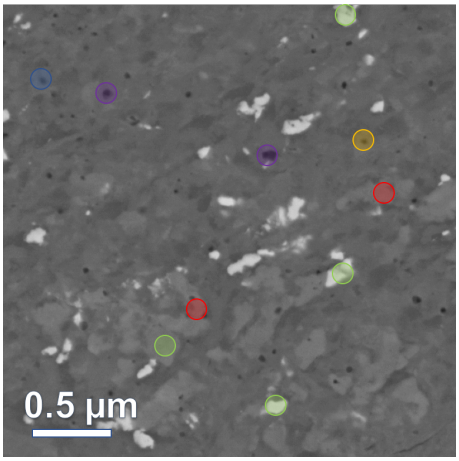


Figure 6.47: BSE micrograph of the Fe-14Cr-3W-0.3Ti+0.25Y_2O_3 microstructure following 675 h at 650°C with Y- and Ti-rich regions higlighted in blue, Ti- Cr- and Y-rich regions highlighted in purple, Ti- and Cr-rich regions highlighted in orange, W-rich regions in green and Cr-rich areas in red.

Region	Fe (wt%)	Cr (wt%)	W (wt%)	Ti (wt%)	Y (wt%)
Blue	73	13	1	6	6.5
Purple	57	22	2	10	8
Green	60	15	24	0.3	0
Orange	72	22	1	5	0
Red	72	24	3	0.4	0.4
Matrix	82	16	2	0.3	0.5

Table 6.15: Chemical composition of particles highlighted in Figure 6.47 measured by EDS.

developed a fine distribution of oxides that were effective in pinning sub and grain boundaries that evolved from initially high dislocation densities, even at elevated temperatures. The next chapter investigates of the resultant mechanical properties.

EBSD maps of the FAST material appears to be the most stable in terms of grain structure. The FAST material was not as bimodal initially, but seems to stay largely unchanged through the thermal exposure. The HIP material was more bimodal initially, but then seems to lose this aspect following the heat treatment so that the microstructure becomes more like the FAST. This gives good indication that FAST is a successful alternative sintering mechanism to HIP.

In terms of the fine-scale second phase particles, these included Y, Ti and Cr rich oxides, some of which coarsened to 75 ± 30 nm according to SEM. Finer oxides,

unresolvable by SEM, were likely present also. Y+Ti rich oxides were visible by SEM EDS, which are usually too fine to be resolved by SEM in other studies using conventional routes. The reason for the relative coarseness of Y+Ti oxides may relate to excess O in the structure, as seen in chemical measurements in Tables 6.4 and 6.5. The small amounts of Y measured by chemical analysis may be below the solubility limit, still in solid solution during sintering and heat treatment, and only with extended amounts of time at high temperatures could complex oxides develop e.g. during long term thermal ageing.

While these Y+Ti particles were not the usual fine distribution associated with ODS steels, they give some encouragement for the in situ internal oxidation route to develop effective pinning oxides, the size and distribution of which might be further advanced in future work.

6.6 Microstructural Summary

The four processing methods produced material similar to state-of-the-art ODS steels reported in literature, with small variations between them. There was encouragement, at least implicitly, that a fine dispersion of oxide pinning particles were developed, although perhaps coarser and with a wider range of chemistries than normally seen.

For the Fe-14Cr-3W-0.3Ti+0.25Y_2O_3 milled powder, both HIP and FAST+HT gave approximately similar final microstructures, with HIP having a slightly larger mean grain size on account of its greater bimodality, and consistent with previous work [76, 97].

In the case of the Fe-14Cr-3W-0.3Ti-0.4Y+Fe_3O_4 milled powder, no residual Fe_3O_4 was evident within the microstructure, indicating internal oxidation was successful in transfering the O from Fe to more reactive elements such as Y, Ti and Cr although confirmation was at a level below the resolution limit of techniques used. Mean grain sizes were similar to materials from powder milled for 4 to 6 times longer, and there were again 'wavy' grain boundaries, suggestive of Zener pinning by fine-scale particulate. Bimodality was perhaps reduced, but it was not

clear whether that is significant. Microstrains were similar or lower to Fe-14Cr-3W-0.3Ti+0.25Y_2O_3 and reasonable given the shorter milling time. Fine domain sizes, especially after FAST processing, suggested efficient grain or sub-grain pinning. TiO_x based particles predominated over the Y-based oxides but consistent with the low concentrations of Y according to chemical analysis in Table 6.5.

The formation of predominantly TiO_x could be interpreted as the first stage of the usual Y+Ti based oxides in these compositions i.e. Ti reacts first with O to form a TiO_x particle which then later reacts with Y to form the 'usual' Y-Ti-O particles. However, here there is little free Y so the majority of particles remain as TiO_x that slowly coarsens. Following long term thermal ageing, eventually the free Y has time to 'find' and react with some of the TiO_x to form Y-Ti-O. This idea is also consistent with the experimental observation that Ti refines oxides in ODS alloys, i.e. has a critical role in the early formation of the oxides. However other studies on ferritic ODS steels have suggested that Y is involved in the earliest steps of nucleation [69, 173].

Thermal ageing was induced the growth of Y-Ti-rich oxides to sizes detectable even using SEM EDS and at least confirmed that Y was present despite the low concentrations.

Despite difficulty in retaining bulk Y concentrations at the target level, and some ambiguity in the role of Y, good direct and indirect evidence was presented for dispersoids forming in Fe-14Cr-3W-0.3Ti-0.4Y+Fe_3O_4 without the need for the 40 h milling process by an in situ oxidation reaction.

7 Mechanical Properties

Contents

7.1 Introduction 171
7.2 Microhardness 173
7.3 Electrothermal Mechanical Testing 175
7.4 Small Punch Testing 203
7.5 Summary of Mechanical Behaviour 215

7.1 Introduction

This Chapter investigates the mechanical properties of the Fe-14Cr-3W-0.3Ti based alloys produced by the four processing routes, as described in Chapter 6. Mechanical testing was completed at three temperatures: room temperature, 350°C and 650°C, spanning the three different deformation regimes described in Section 2.6 and corresponding to the operating temperatures of pressurised water reactors (∼350°C) and fast reactors (∼ 650°C) [174]. Microhardness of the sintered materials, both prior to and post heat treatment is investigated. Because powder consolidated materials may have tensile properties dominated by a small fraction of persistent porosity, tensile property data was correlated with microhardness testing which is generally considered less sensitive to a small fraction of residual porosity. Finally,

small punch isothermal indentation testing was used to simulate creep resistance testing, an important property in potential cladding materials, and to then rank the materials in terms of their high temperature creep resistance.

As described in the literature review in Section 2.3.1, the yield strength of an ODS steel has been assumed to be given by a simple sum of the different strengthening mechanisms:

$$\sigma_y = \sigma_{SS} + \sigma_{BH} + \sigma_0 + \sigma_D + \sigma_K \tag{7.1}$$

where σ_y is yield strength, σ_{SS} is solid solution strengthening, σ_{BH} is Bailey-Hirsch strengthening due to dislocation interactions (work-hardening), σ_{HP} is Hall-Petch strengthening from grain size contributions and is made up of σ_0 from lattice friction and σ_D from grain size strengthening, σ_K is Orowan strengthening from particles interacting with dislocations. Although this is an oversimplified calculation, and the sum of all the terms duplicates strength factors which should be considered over different length scales, an experimentally calculated correction factor of 0.7 was found by Schneibel *et al.* [175] to correct for this. While the use of this factor further questions the validity of the simple model, the calculations are used mainly as a discussion point for the mechanisms active at each testing temperature.

Equation 7.1 considered only room temperature properties, but as temperature increases, some of the strengthening contributions will change due to thermally induced microstructural changes and the activation of other deformation mechanisms. σ_D will reduce as grains may coarsen but also Coble creep (σ_{CC}) becomes active as grain boundaries no longer provide obstacles for dislocations (and now provide fast diffusion paths) and σ_K may also lose its efficiency and can (it is assumed) be replaced by σ_{ARW}, the Arzt-Rösler-Wilkinson stress from interfacial pinning and dislocation climb at elevated temperatures [27]. Dislocation densities will reduce so σ_{BH} becomes smaller and solid solutions may break down via precipitation, reducing σ_{SS} but potentially increasing σ_{ARW}. In an attempt at approximate quantification, at high temperature therefore, the strength of an ODS steel is assumed to follow:

$$\sigma_y = \sigma_{SS} + \sigma_{BH} + \sigma_0 + \sigma_{ARW} + \sigma_{CC} \quad (7.2)$$

where one or more of the terms on the right hand side are now explicitly recognised as being temperature-related.

Equations 7.1 and 7.2 are used in considering the mechanical response of each of the alloys. The use of these equations is not intended to be predictive, but to provide a simple framework for approximate estimation of the sensible, or relative, contribution to yield strength of various strength-related phenomena.

7.2 Microhardness

Figure 7.1 shows the microhardness of all the materials described in Chapter 6, with both pre- and post- heat treatment measurements for the FAST material, and all measurements taken at room temperature.

Comparing Fe-14Cr-3W-0.3Ti+0.25Y_2O_3 samples, the HIPed material was softer than as-FAST (4.5 GPa compared with 8 GPa), but following heat treatment of the FAST material, there was only $\sim$ 1 GPa difference, supporting the suggestions in Section 6.4.3 of a $\sim$ 80% reduction in the work-hardening dislocation density during heat treatment. The similar hardnesses may indicate that FAST+HT could be a faster processing alternative method for the production of ODS steels, approximately comparable with MA ODS steels.

Comparing the different Fe-14Cr-3W-0.3Ti-0.4Y+Fe_3O_4 materials, hardnesses were similar, and with little difference after sintering. This again corresponded with the prior microstructural investigations (seen in Section 6.4.5) that suggested only small changes in dislocation density, and stable particles and grain structure.

Comparing with the literature, hot extrusion ODS ferritic steels have a hardness of $\sim$ 4.5 GPa, MA/HIP $\sim$ 3.5 GPa, MA/FAST $\sim$ 4 GPa, and novel methods such as GARS and STARS $\sim$ 1.8 GPa i.e. materials in this chapter had a similar or higher hardness.

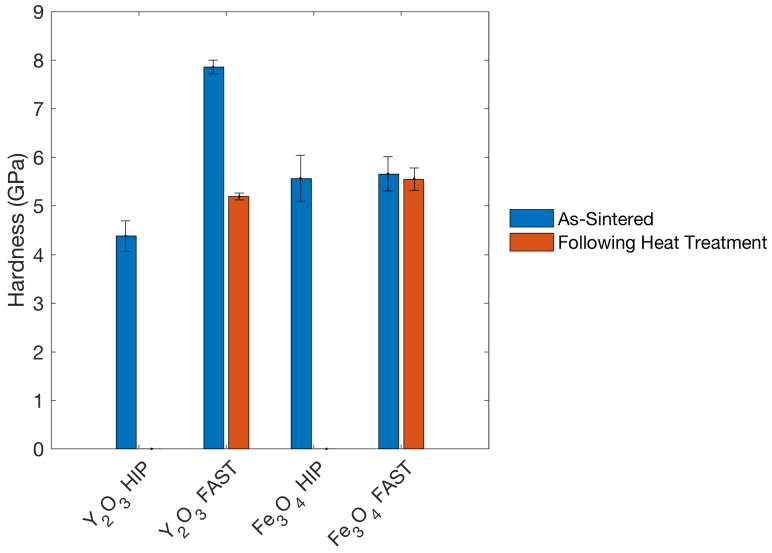


Figure 7.1: Microhardness of MA Fe-14Cr-3W-0.3Ti+0.25Y_2O_3 HIP and FAST, Fe-14Cr-3W-0.3Ti-0.4Y+Fe_3O_4 HIP and FAST, with FAST data both pre- and post- heat treatment.

7.2.1 Hot Microhardness

Figure 7.2 shows the Fe-14Cr-3W-0.3Ti+0.25Y_2O_3 HIP hardness as a function of temperature, with a marked drop-off in hardness above 300-400°C (for reasons described in Section 2.6), and becoming very soft by 800°C (0.8 GPa).

Unfortunately the machine suffered irrepairable problems at this point when only the Fe-14Cr-3W-0.3Ti+0.25Y_2O_3 HIP material had been investigated, and no further data could be collected.

7.2.2 Thermal Stability

As seen in Section 6.5, the alloys had excellent thermal stability in terms of microstructure at 650°C and supported the consistent and stable hardnesses shown in Figure 7.3, with hardnesses following 24 h and 675 h heat treatments at 650°C maintained.

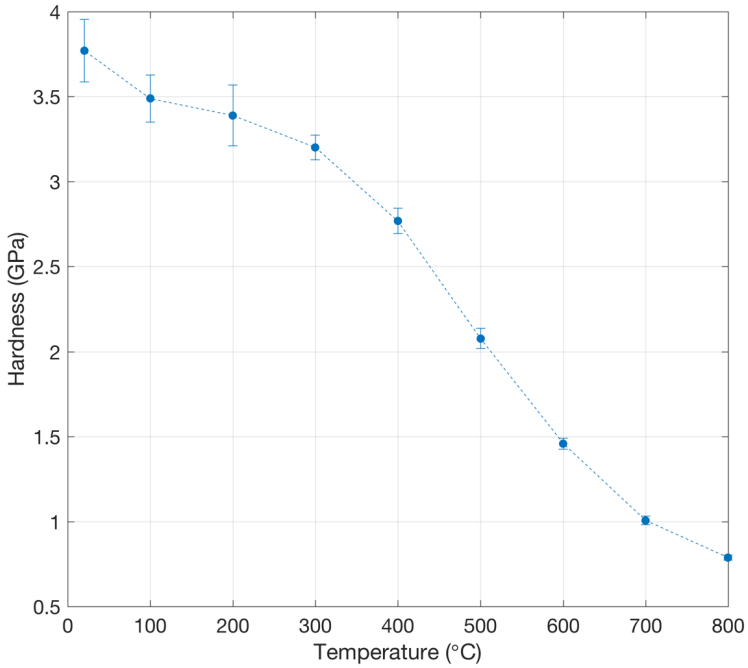


Figure 7.2: Microhardness as a function of testing temperature for Fe-14Cr-3W-0.3Ti+0.25Y_2O_3 HIP.

7.3 Electrothermal Mechanical Testing

The four alloys were investigated by electro-thermal mechanical testing (ETMT) at room temperature, 350°C and 650°C and a constant strain rate of $1\times10^{-4}s^{-1}$. From the raw data, stress-strain curves were generated, allowing yield strengths, ultimate tensile strengths and ultimate tensile strains to be estimated.

7.3.1 Fe-14Cr-3W-0.3Ti+0.25Y_2O_3 Alloys

Figures 7.4 (a) and (b) show the stress-strain curves for the alloys at all three temperatures for HIP and FAST respectively. As temperature increased, there was an expected decrease in ultimate tensile strength (from $\sim$ 1200 MPa at room temperature to $\sim$ 400 MPa at 650°C) and increase in ductility (from $\sim$ 4-5% strain for HIP and $\sim$ 2% for FAST below 400°C to $\sim$ 10% at 650°C for both), supporting the change in deformation mechanisms described in Section 2.6. At temperatures approaching 500°C, an increase in ductility is seen as a result of high temperature mobility, dislocation glide, weakening of grain boundaries and intergranular crack

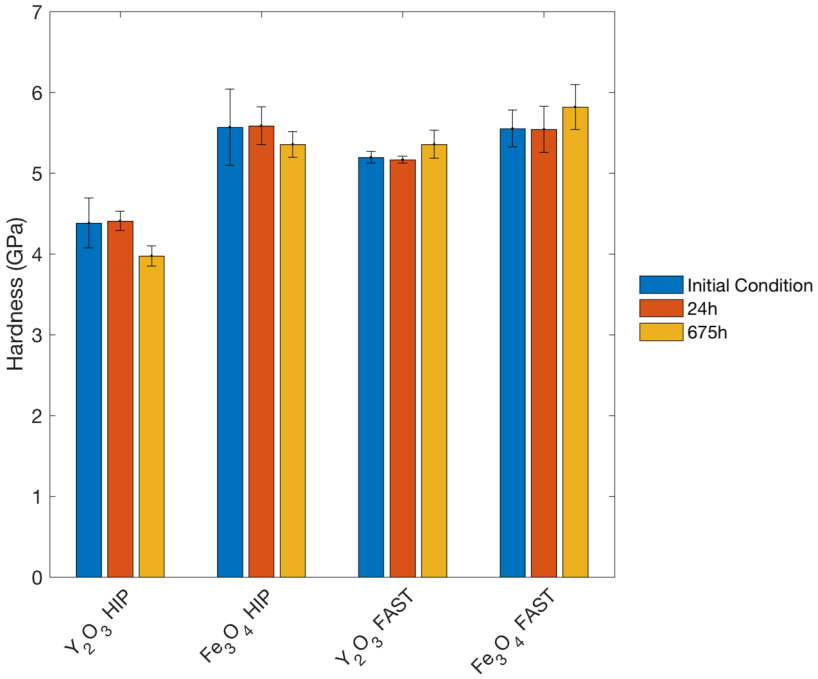


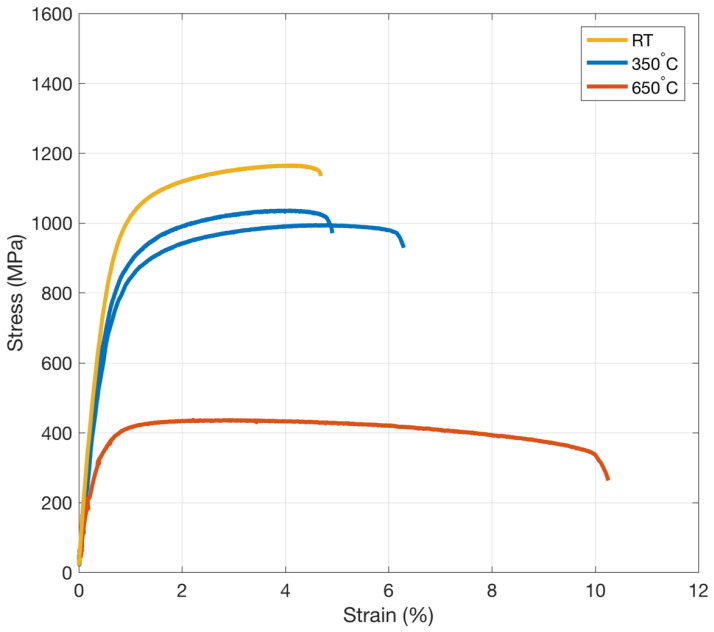
Figure 7.3: Microhardness of MA Fe-14Cr-3W-0.3Ti+0.25Y_2O_3 HIP and FAST and Fe-14Cr-3W-0.3Ti-0.4Y+Fe_3O_4 HIP and FAST following an isothermal hold at 650°C for 24 and 675 h.

propogation. Figures 7.5 and 7.6 show the fracture surfaces for HIP and FAST samples respectively, where the fracture behaviour was qualitatively similar. At room temperature in (a), fracture surfaces were relatively flat with a number of facetted cleavage planes, which are enlarged in (b) (from the area highlighted by the red box in (a)). The flat regions were $\sim$ 10-20 μm in size (much larger than the average grain size, and $\sim$ 2-5 times the size of the larger grains), and suggested to be formed through intragranular crack propogation and brittle failure. During testing at 350°C, (c) showed evidence of surface dimpling as well as some cleavage planes (again 10-20 μm). This dimpling is enlarged in (d), from regions highlighted by the red box in (c), with a dimple size to be 0.5-3 μm, closely correlating to the grain sizes described in Section 6.4.1. This suggested the onset of intergranular cracking and a more tortuous crack path along grain boundaries. There was also a mixture of cleavage planes and a dimpled surface at 650°C in (e), but the dimples (from within the red box in (e)) shown in (f) were smaller and deeper, with some evidence

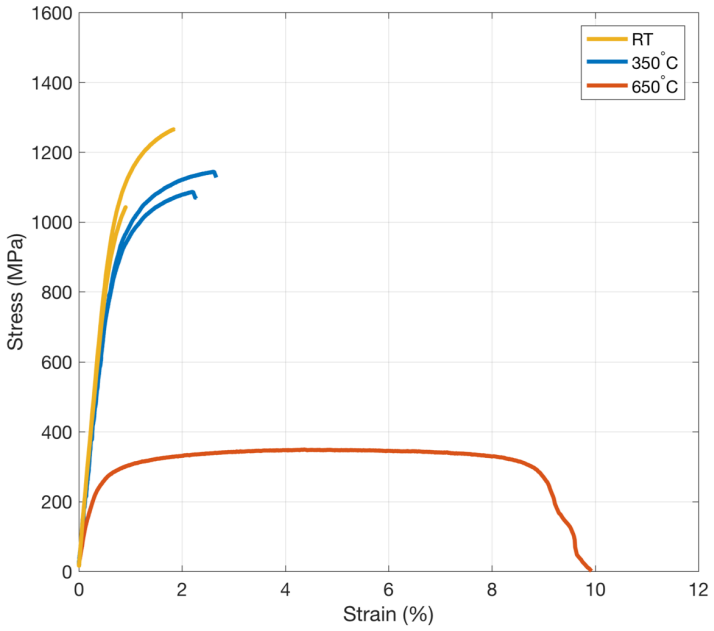
of particle pullout, consistent with the larger amount of ductility in the stress-strain plots, but due to the high temperatures and testing in air, the fracture surface was too heavily oxidised for analysis by EDS. This type of qualitative change in the fracture mechanism in Fe-14Cr-0.16W-0.4Ti-0.18Y_2O_3 was also seen by Stoica et al. [176] from low temperature strain hardening to high temperature strain softening with a cross-over temperature between 400-600°C. Below the transition temperature, intragranular dislocation slip caused cleavage to dominate, whereas intergranular grain boundary activity was predominant at higher temperatures. As no tests were completed between room temperature and 400°C, it is likely that the mixed fracture surface seen in the current work when testing at 350°C was an early indication of this transition behaviour.

7.3.2 Fe-14Cr-3W-0.3Ti-0.4Y+Fe_3O_4 Alloys

Figures 7.7 (a) and (b) show the stress-strain curves for alloys tested at all three temperatures for HIP and FAST consolidation respectively. As temperature increased, there was again a typical decrease in ultimate tensile strength (from $\sim$ 1400 MPa at room temperature to $\sim$ 500-600 MPa at 650°C), but ductility was always low, with no samples reaching 4% strain. This lack of ductility is reflected in Figures 7.8 and 7.9 that show the fracture surfaces for HIP and FAST samples respectively, which were qualitatively similar. For both, as for Fe-14Cr-3W-0.3Ti+0.25Y_2O_3, at room temperature in (a), fracture surfaces were relatively flat and consisted of a number of facetted cleavage planes, which are enlarged in (b) (from the area highlighted by the red box in (a)), again 10-20 μm in size, again larger than the average grain size, and $\sim$ 2-5 times the size of the larger grains. During testing at 350°C in (c), there was some surface dimpling as well as cleavage planes (again $\sim$ 10-20 μm in size). This dimpling is enlarged in (d), from regions highlighted by the red box in (c), with a dimple size of $\sim$ 1 μm, correlating to the grain sizes described in Section 6.4.2. There was again a mixture of cleavage planes and dimples at 650°C in (e), but unlike forthe Fe-14Cr-3W-0.3Ti+0.25Y_2O_3



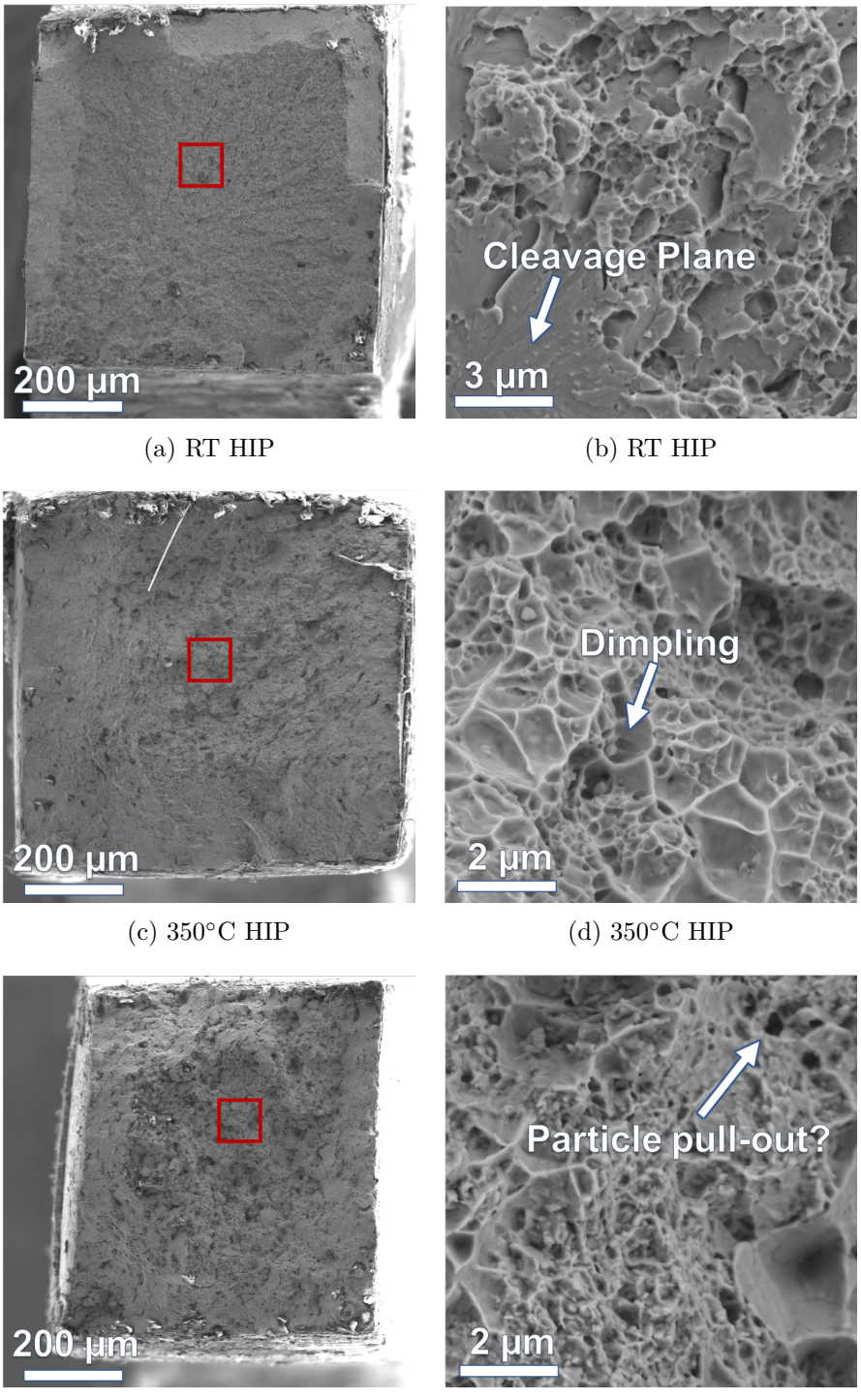
(a) HIP



(b) FAST

Figure 7.4: Stress-strain curves for Fe-14Cr-3W-0.3Ti+0.25Y_2O_3 HIP and FAST ETMT samples.

alloy, the dimples (from within the red box in (e)) shown in (f) remained relatively shallow, consistent with the more limited ductility.

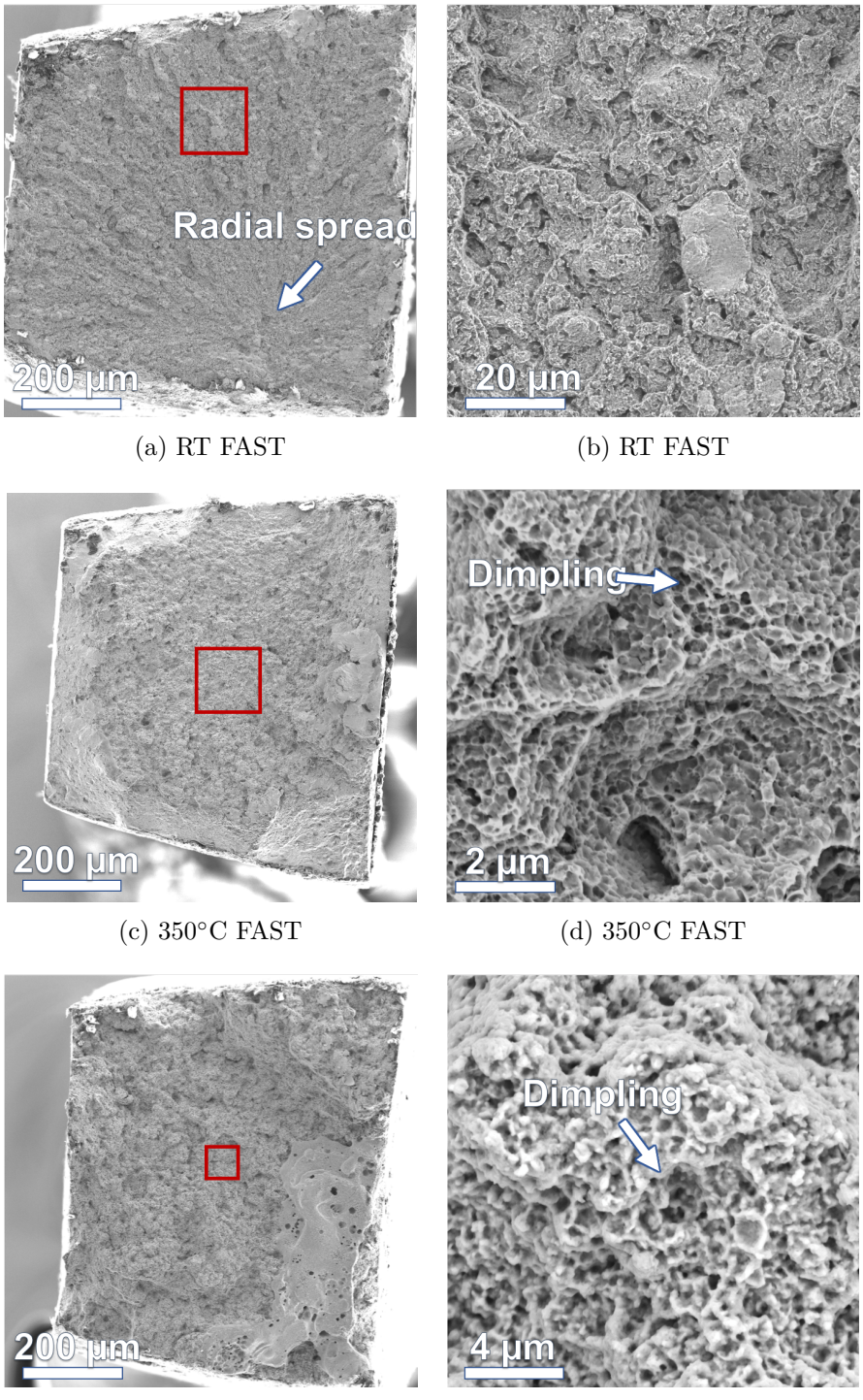


(a) RT HIP (b) RT HIP

(c) 350°C HIP (d) 350°C HIP

(e) 650°C HIP (f) 650°C HIP

Figure 7.5: SEM images of the fracture surface of a Fe-14Cr-3W-0.3Ti+0.25Y_2O_3 HIP ETMT specimen tested at (a) room temperature and a cleavage plane (enlarged from the red box) highlighted in (b), (c) 350°C and surface dimpling (enlarged from the red box) highlighted in (d), and (e) 650°C and dimpling with possible particle pull out (from the red box) highlighted in (f).

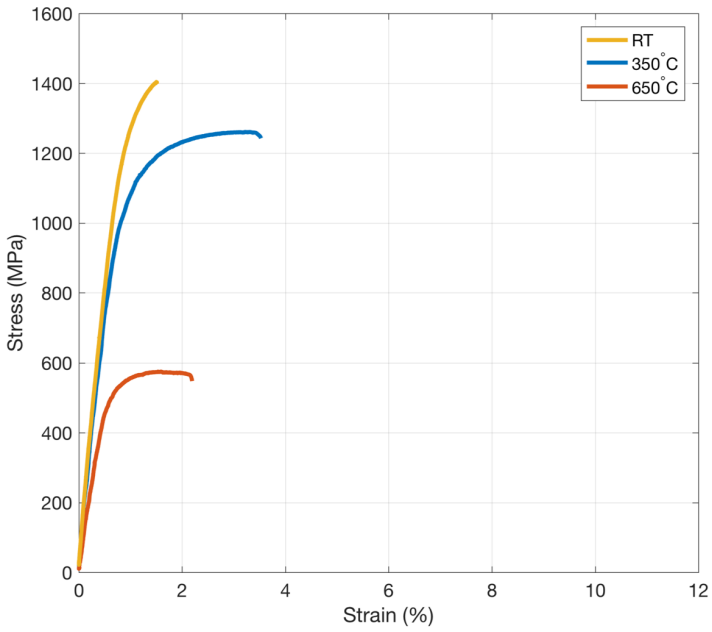


(a) RT FAST (b) RT FAST

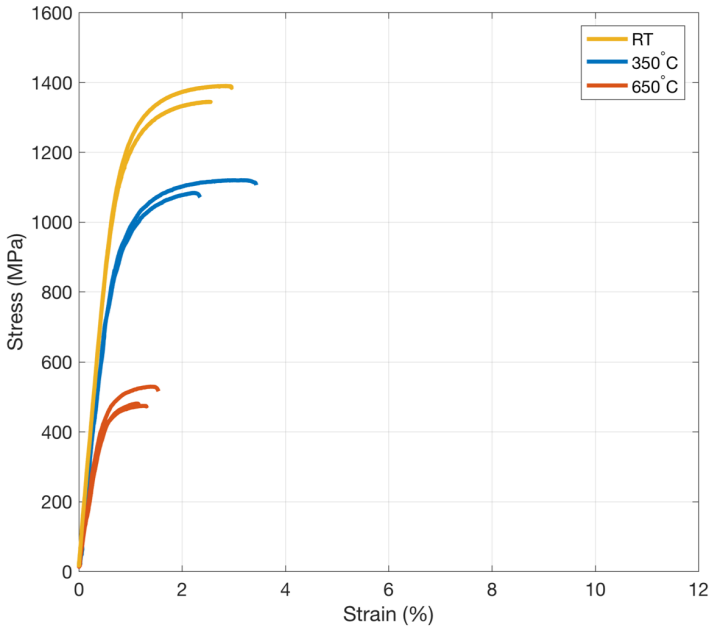
(c) 350°C FAST (d) 350°C FAST

(e) 650°C FAST (f) 650°C FAST

Figure 7.6: SEM images of the fracture surface of a Fe-14Cr-3W-0.3Ti+0.25Y_2O_3 FAST ETMT specimen tested at (a) room temperature and cleavage planes (enlarged from the red box) highlighted in (b), (c) 350°C and surface dimpling (enlarged from the red box) highlighted in (d), and (e) 650°C and dimpling with possible particle pull out (from the red box) highlighted in (f).

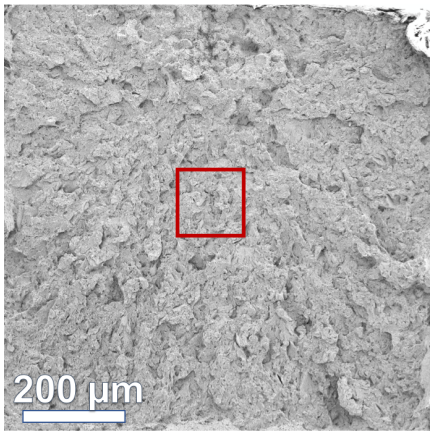


(a) HIP

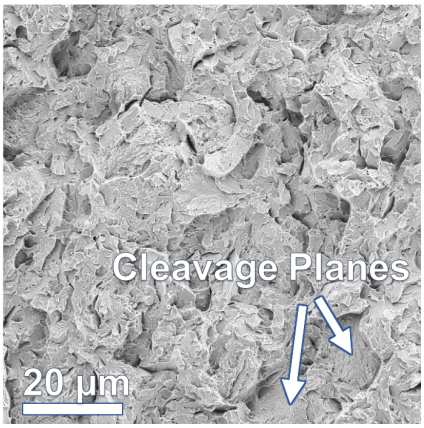


(b) FAST

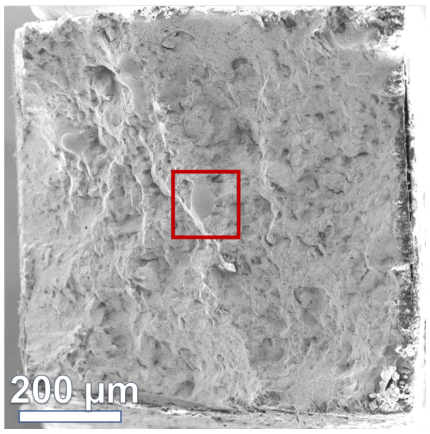
Figure 7.7: Stress-strain ETMT curves for Fe-14Cr-3W-0.3Ti-0.4Y+Fe_3O_4 consolidated by HIP and FAST.



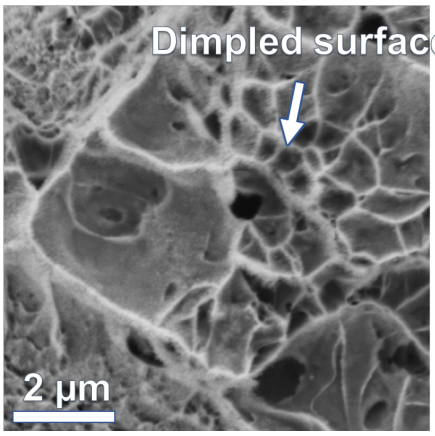
(a) RT HIP



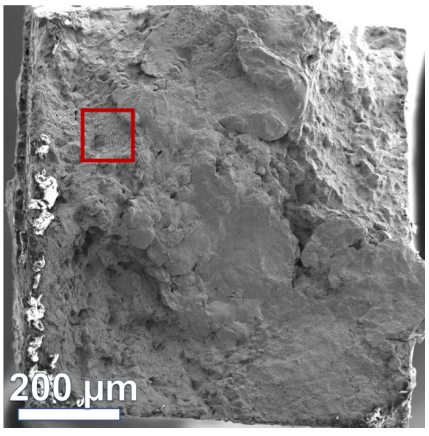
(b) RT HIP



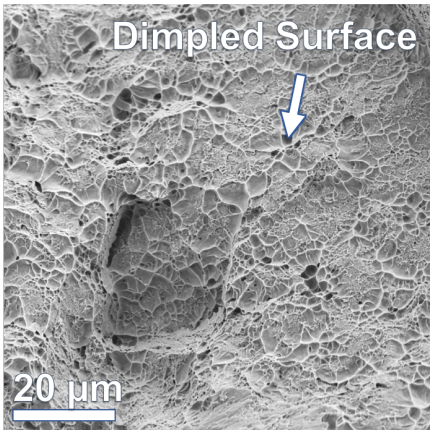
(c) 350°C HIP



(d) 350°C HIP

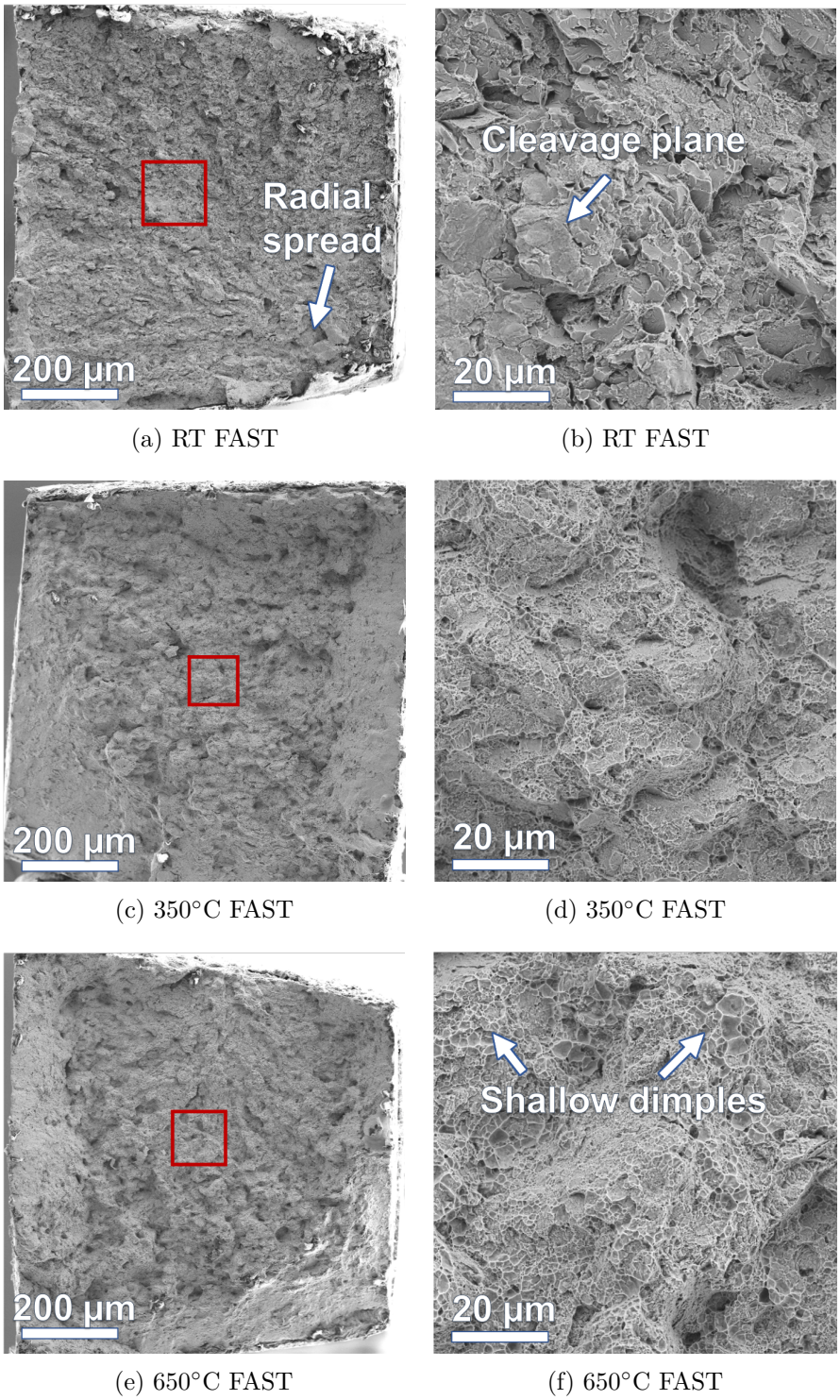


(e) 650°C HIP



(f) 650°C HIP

Figure 7.8: SEM images of the fracture surface of a Fe-14Cr-3W-0.3Ti-0.4Y+Fe_3O_4 HIP ETMT specimen tested at (a) room temperature and a cleavage plane (enlarged from the red box) highlighted in (b), (c) 350°C and surface dimpling (enlarged from the red box) highlighted in (d), and (e) 650°C and dimpling (from the red box) highlighted in (f).



(a) RT FAST (b) RT FAST

(c) 350°C FAST (d) 350°C FAST

(e) 650°C FAST (f) 650°C FAST

Figure 7.9: SEM images of the fracture surface of a Fe-14Cr-3W-0.3Ti-0.4Y+Fe_3O_4 FAST ETMT specimen tested at (a) room temperature and a cleavage plane (enlarged from the red box) highlighted in (b), (c) 350°C and surface dimpling (enlarged from the red box) highlighted in (d), and (e) 650°C and dimpling (from the red box) highlighted in (f).

7.3.2.1 Summary of Tensile Properties from ETMT

From the ETMT curves, key materials properties (yield strength (YS), ultimate tensile strength (UTS) and total elongation) were estimated for each processing method, as shown in Table 7.1[1]:

Material	YS (MPa)	UTS (MPa)	Total Elong (%)
Room Temperature			
Y_2O_3 HIP	894	1165	4.5
Fe_3O_4 HIP	1206	1405	1.4
Y_2O_3 FAST	1081	1266	1.3
Fe_3O_4 FAST	1148	1350	2.7
350°C			
Y_2O_3 HIP	782	1015	5
Fe_3O_4 HIP	1048	1260	3
Y_2O_3 FAST	945	1115	2.45
Fe_3O_4 FAST	941	1100	2.5
650°C			
Y_2O_3 HIP	383	437	9.5
Fe_3O_4 HIP	528	575	1.24
Y_2O_3 FAST	277	350	9
Fe_3O_4 FAST	459	495	1.2

Table 7.1: Tensile properties for all four alloys tested by ETMT.

[1]Fe-14Cr-3W-0.3Ti+0.25Y_2O_3 is referred to as Y_2O_3 HIP, Fe-14Cr-3W-0.3Ti-0.4Y+Fe_3O_4 HIP as Fe_3O_4 HIP, Fe-14Cr-3W-0.3Ti+0.25Y_2O_3 FAST as Y_2O_3 FAST and Fe-14Cr-3W-0.3Ti-0.4Y+Fe_3O_4 FAST as Fe_3O_4 FAST

7.3.3 Validation of Experimental Results Against Estimations

First considering the microhardness, the following relationships are often used in metals to estimate yield strength (YS) and ultimate tensile strength (UTS) [177]:

$$YS = \frac{H}{3}(0.1)^n \tag{7.3}$$

where n is the strain-hardening exponent. The strain hardening exponent is a measure of the ease of dislocation motion that in the presence of a grain boundary, sub-grain boundary or second phase particle. n also decreases as the volume fraction of a second phase increases for a given particle size and decreases with decreasing particle size for a given volume fraction and particle size. A lower n therefore indicates means a higher strain hardening effect. It has been shown that strain-dependent properties, such as the strain-hardening exponent, cannot be reliably obtained solely using Vickers hardness tests (a spherical indenter is required) and therefore an approximation is required to instead retrieve a value of n from the ETMT data, using [178]:

$$\sigma = K\epsilon^n \tag{7.4}$$

where K is the shear modulus, σ is stress and ϵ is strain.

By plotting a log-log plot of stress and strain from the ETMT tests, a best-fit to the gradient of the plot in the plastic region, n can be estimated, while the y-intercept estimates the shear modulus, as shown in Table 7.2, the shear modulus calculated alongside the R^2 degree of fit[2].

HIP Fe_3O_4, FAST Y_2O_3 and FAST Fe_3O_4 showed similar strain-hardening exponents of ~ 0.16, primarily due to their similar grain sizes and particle distributions. The HIP Y_2O_3 alloy had lower n and K values likely due to the higher strain

[2]Fe-14Cr-3W-0.3Ti+0.25Y_2O_3 is referred to as Y_2O_3 HIP, Fe-14Cr-3W-0.3Ti-0.4Y+Fe_3O_4 HIP as Fe_3O_4 HIP, Fe-14Cr-3W-0.3Ti+0.25Y_2O_3 FAST as Y_2O_3 FAST and Fe-14Cr-3W-0.3Ti-0.4Y+Fe_3O_4 FAST as Fe_3O_4 FAST

Material	n	K (GPa)	R^2
HIP Y_2O_3	0.11	102	0.95
HIP Fe_3O_4	0.17	131	0.99
FAST Y_2O_3	0.16	115	0.99
FAST Fe_3O_4	0.16	125	0.98

Table 7.2: Strain hardening coefficient n and bulk modulus K estimated from a best fit to the ETMT stress-strain plots.

hardening effect possible in larger grained materials. Due to the slightly flawed method of using an ETMT parameter to compare hardness, values were compared to the standard approximation of $H/3$. These are shown alongside estimations using Equation 7.3.3, in Table 7.3, alongside experimental values from ETMT[3].

Material	n	$\frac{H}{3}(0.1)^n$ (MPa)	$H/3$	Yield Strength (MPa)
HIP Y_2O_3	0.11	1120	1460	894
HIP Fe_3O_4	0.17	1260	1855	1206
FAST Y_2O_3	0.16	1190	1730	1081
FAST Fe_3O_4	0.16	1280	1850	1148

Table 7.3: Strain hardening coefficients n for the four alloys, the corresponding yield strength estimated and measured by ETMT at room temperature.

Comparing the values estimated by the two methods to the yield strength found experimentally using ETMT, both overpredict but the method utilising a value for n was a closer approximation. Although not ideal, this method was used for all further comparisons between yield strength and microhardness based predictions. The overestimation between hardness-based predictions and yield strength was suggested by Zhang et al. [179] to be indicative of dominant cleavage cracking and brittle failure. ETMT calculations were based solely on tensile behaviour, wheras hardness testing creates a complex stress state with the surface in tension and the bulk in compression. This is likely the difference between the predicted and experimental values as cleavage cracking and brittle failure is less likely to occur in hardness testing.

[3]Fe-14Cr-3W-0.3Ti+0.25Y_2O_3 is referred to as Y_2O_3 HIP, Fe-14Cr-3W-0.3Ti-0.4Y+Fe_3O_4 HIP as Fe_3O_4 HIP, Fe-14Cr-3W-0.3Ti+0.25Y_2O_3 FAST as Y_2O_3 FAST and Fe-14Cr-3W-0.3Ti-0.4Y+Fe_3O_4 FAST as Fe_3O_4 FAST

7.3.3.1 Summation Strengthening Mechanism Model at Room Temperature

As described previously, Equation 7.1 is used as a simple summation model of strengthening terms active at room temperature to form an approximate estimation of the sensible contribution to yield strength [25].

Solid Solution Strengthening

In Fe-14Cr-3W-0.3Ti, solid solution strengthening (σ_{SS}) is provided primarily by Cr and W, estimated from:

$$\sigma_{SS} = 0.00689kC^n \tag{7.5}$$

where C is the atomic concentration of elements, n is 0.75, and the coefficient k is 1400 for Cr and 11,000 for W [25]. Using the chemical compositions of the alloys (from chemical analysis by AMG) in Section 6.3, Table 7.4 shows the contribution of solid solutioning to yield stress for the four alloys[4].

Contribution	Y_2O_3 HIP	Fe_3O_4 HIP	Y_2O_3 FAST	Fe_3O_4 FAST
σ_{SSCr}	72.3	73.7	72.2	73.1
σ_{SSW}	74.7	79.2	74.1	76.9
$\sigma_{SStotal}$	147.0	152.8	146.3	150.0

Table 7.4: Solid solution strengthening contributions for the four Fe-14Cr-3W-0.3Ti-based alloys.

Assuming Cr and W remained in solid solution, they contributed $\sim$ 150 MPa towards the yield stress. Note that previous results suggested that WC and possibly CrN may form in some alloys after heat treatment, but their volume fraction was extremely low.

[4]Fe-14Cr-3W-0.3Ti+0.25Y_2O_3 is referred to as Y_2O_3 HIP, Fe-14Cr-3W-0.3Ti-0.4Y+Fe_3O_4 HIP as Fe_3O_4 HIP, Fe-14Cr-3W-0.3Ti+0.25Y_2O_3 FAST as Y_2O_3 FAST and Fe-14Cr-3W-0.3Ti-0.4Y+Fe_3O_4 FAST as Fe_3O_4 FAST

Bailey-Hirsch Strengthening

The Bailey-Hirsch stress (σ_{BH}) is the contribution of dislocation forests to the yield stress and can be estimated from:

$$\sigma_{BH} = M\alpha Gb\rho^{1/2} \tag{7.6}$$

where $M = 2.9$, α is the Taylor factor for bcc metals = 0.24 [159], $b = 0.25$ nm, the modulus of Burgers vector (assuming all dislocations have a Burgers vector of type $\frac{1}{2}111$), ρ is the dislocation density and G is the shear modulus [25].

Dislocation densities for the alloys were estimated using XRD data, as given in Section 6.4.5. Table 7.5 shows the estimated values[5].

Contribution	Y_2O_3 HIP	Fe_3O_4 HIP	Y_2O_3 FAST	Fe_3O_4 FAST
$\rho_{dislocation}$ (10^{13})	8.8	5.0	5.9	5.1
σ_{BH} (MPa)	133	100	109	101

Table 7.5: Bailey Hirsch contributions for the four Fe-14Cr-3W-0.3Ti-based alloys at room temperature.

Sanctis *et al.* [25] gave σ_{BH} in the range 21-28 MPa for a Fe-14Cr-1W-0.4Ti-0.3Y_2O_3 alloy prepared by MA, hot extrusion and heat treatment, and lower than those in Table 7.5 due to a higher dislocation density in the current work (5-10 $\times 10^{13}$ compared to 4 $\times 10^{12}$). However Chauhan *et al.* [27] presented σ_{BH} in the range 75-150 MPa for ferritic ODS alloys prepared by MA and HE, and more consistent with the estimated Bailey-Hirsch contribution here.

Hall-Petch Strengthening

Hall-Petch strengthening (σ_{HP}) is due to the contributions from inherent lattice friction, combined with strengthening due to grain boundary barriers.

$$\sigma_{HP} = \sigma_0 + \sigma D \tag{7.7}$$

[5]Fe-14Cr-3W-0.3Ti+0.25Y_2O_3 is referred to as Y_2O_3 HIP, Fe-14Cr-3W-0.3Ti-0.4Y+Fe_3O_4 HIP as Fe_3O_4 HIP, Fe-14Cr-3W-0.3Ti+0.25Y_2O_3 FAST as Y_2O_3 FAST and Fe-14Cr-3W-0.3Ti-0.4Y+Fe_3O_4 FAST as Fe_3O_4 FAST

$$\sigma_D = G^{1/2} k d^{-1/2} \tag{7.8}$$

Addressing the two terms seperately, σ_0 is the matrix yield stress for a grain of theoretically infinite size and given as 50 ± 10 MPa in pure iron by Takaki *et al.* [180], G is the shear stress, $k_p = 0.22$ MPam$^{1/2}$ is the Hall-Petch coefficient for Fe-14Cr steels [158] and d is the average grain size as calculated previously for the four processing methods and shown in Table 7.6[6].

Contribution	Y_2O_3 HIP	Fe_3O_4 HIP	Y_2O_3 FAST	Fe_3O_4 FAST
Mean grain size (μm)	0.87	0.62	0.32	0.54
σ_D (MPa)	240	284	395	304

Table 7.6: Hall-Petch strengthening for the four Fe-14Cr-3W-0.3Ti-based alloys at room temperature.

Table 7.6 shows that grain size contributions to yield strength were estimated to be the largest contributing factor of those examined at room temperature. Compared with values from literature, Sanctis *et al.* [25] presented σ_D in the range 260-285 MPa for a Fe-14Cr-1W-0.4Ti-0.3Y_2O_3 alloy prepared by MA, HE and heat treatment, comparable with σ_D for Fe-14Cr-3W-0.3Ti+0.25Y_2O_3 HIP and FAST in Table 7.5, although σ_D for Fe-14Cr-3W-0.3Ti-0.4Y+Fe_3O_4 HIP and FAST were higher due to the more refined grain structure within the range reported by Chauhan *et al.* [27] for ferritic ODS alloys prepared by MA and HE (150-500 MPa). Thus the estimated Hall-Petch contribution here is judged to be reasonable.

Orowan Strengthening

Orowan strengthening σ_K relates to the particle strengthening due to a dispersion of hard, fine-scale non-shearable particles that impede dislocation motion by [175]:

$$\sigma_K = M\Big(\frac{6f}{\pi}\Big)^{1/2} \frac{Gb}{d_p} \tag{7.9}$$

[6]Fe-14Cr-3W-0.3Ti+0.25Y_2O_3 is referred to as Y_2O_3 HIP, Fe-14Cr-3W-0.3Ti-0.4Y+Fe_3O_4 HIP as Fe_3O_4 HIP, Fe-14Cr-3W-0.3Ti+0.25Y_2O_3 FAST as Y_2O_3 FAST and Fe-14Cr-3W-0.3Ti-0.4Y+Fe_3O_4 FAST as Fe_3O_4 FAST

where M is the Taylor factor = 2.9, f is the volume fraction of disperse, non-shearable particles, G is the shear modulus which varies with temperature as previously shown, b = 0.25 nm is the modulus of Burgers vector (assuming all dislocations have a Burgers vector of type $\frac{1}{2}111$) and d_p is the average particle diameter. The particle information for Fe-14Cr-3W-0.3Ti+0.25Y_2O_3 was taken from the estimates based on atom probe data for the FAST material given in Section 6.5.3 and particle information for the Fe-14Cr-3W-0.3Ti-0.4Y+Fe_3O_4 samples was taken from the estimates based on atom probe data for the FAST material given in Section 6.4.4. For the purposes of estimation, it was assumed identical to that in the HIP processed material of the same composition. This is likely a relatively unsafe assumption, but the only one available[7].

Contribution	Y_2O_3 HIP	Fe_3O_4 HIP	Y_2O_3 FAST	Fe_3O_4 FAST
f	0.00031	0.00081	0.00031	0.00081
d_p (m)	1.8×10^{-9}	2.18×10^{-9}	1.8×10^{-9}	2.18×10^{-9}
σ_K (MPa)	836	1113	836	1113

Table 7.7: Orowan strengthening for the four Fe-14Cr-3W-0.3Ti-based alloys at room temperature.

Table 7.7 shows the estimated non-shearable particle contribution to strengthening for the four Fe-14Cr-3W-0.3Ti-based alloys. The relatively high particle density from the atom probe data for Fe-14Cr-3W-0.3Ti-0.4Y+Fe_3O_4 FAST compared with the literature lead to a pronounced Orowan particle strengthening effect. The APT data samples from only a very small volume and has not yet been cross-validated by TEM, and thus could contain significant inaccuracy.

Summation of Contributions at Room Temperature

Figure 7.10 shows all of the estimated contributions graphically as a stacked bar chart, with the final summed yield strength compared with experiment in Table 7.8. Estimates for HIP Y_2O_3 and FAST Fe_3O_4 overpredicted by 100 and

[7]Fe-14Cr-3W-0.3Ti+0.25Y_2O_3 is referred to as Y_2O_3 HIP, Fe-14Cr-3W-0.3Ti-0.4Y+Fe_3O_4 HIP as Fe_3O_4 HIP, Fe-14Cr-3W-0.3Ti+0.25Y_2O_3 FAST as Y_2O_3 FAST and Fe-14Cr-3W-0.3Ti-0.4Y+Fe_3O_4 FAST as Fe_3O_4 FAST

60 MPa respectively, but HIP Fe_3O_4 and FAST Y_2O_3 matched more closely. The interpretation of this reasonable agreement should be done with care, but may, for example suggest that at room temperature, there was relatively little particle decohesion or shearing and that the critical strengthening due to fine scale particles was present[8].

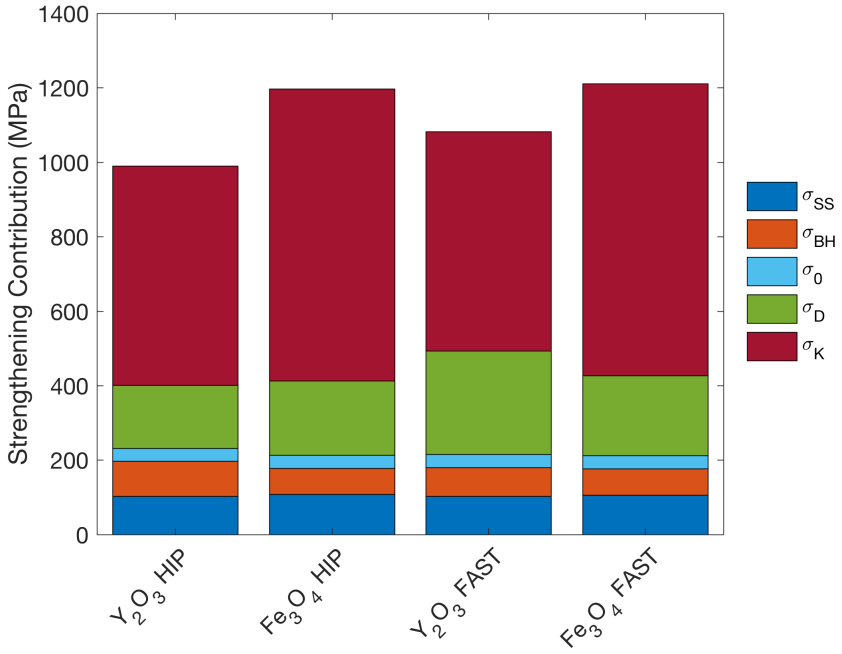


Figure 7.10: Stacked bar chart of the contributions of the summation model to yield stress for each of the four Fe-14Cr-3W-0.3Ti-based alloys at room temperature.

Material	Model Output (MPa)	Yield Strength (MPa)
HIP Y_2O_3	990	894
HIP Fe_3O_4	1197	1206
FAST Y_2O_3	1082	1081
FAST Fe_3O_4	1210	1148

Table 7.8: Comparison between output from the summation model for yield stress and experimental values.

[8]Fe-14Cr-3W-0.3Ti+0.25Y_2O_3 is referred to as Y_2O_3 HIP, Fe-14Cr-3W-0.3Ti-0.4Y+Fe_3O_4 HIP as Fe_3O_4 HIP, Fe-14Cr-3W-0.3Ti+0.25Y_2O_3 FAST as Y_2O_3 FAST and Fe-14Cr-3W-0.3Ti-0.4Y+Fe_3O_4 FAST as Fe_3O_4 FAST

7.3.3.2 Effect of Temperature

As temperature increases, dislocation densities can be expected to decrease, reducing the σ_{BH} contribution, and solid solutions may break down via precipitation, reducing σ_{SS}.

At further elevated temperatures (>400-500°C), as previously described, grain size strengthening effects (σ_D) may reduce, if grains coarsen (which they do not $<$ 650°C) and Coble creep (σ_{CC}) may become active, so that dislocations are able to climb around obstacles so σ_K strengthening might be better represented by σ_{ARW}, the Arzt-Rösler-Wilkinson stress due to residual interfacial pinning and dislocation climb.

For simplicity of the model, a number of contributions were assumed to be constant over the low-mid temperature regime, based on observations of the alloys' good thermal stability in this regime.

Solid Solution Strengthening

It was assumed that any changes in solid solution strengthening effects up to 650°C were negligibly small as there was no evidence of significant precipitation or other changes in phase equilibrium.

Bailey-Hirsch Strengthening

M, α and b were assumed to be constant over the temperature range of interest. The dislocation density was likely to vary over the temperature range, but due to a lack of high temperature XRD equipment, and the relaxation treatment applied to all materials at a temperature higher (750°C) than the highest testing temperature (650°C), was assumed constant. G was assumed to vary with temperature according to Figure 7.11 for Fe-14Cr-1W-0.4Ti-0.3Y_2O_3.

Using this approach, Table 7.9 estimates the Bailey-Hirsch contribution at the different temperatures for each alloy[9].

[9]Fe-14Cr-3W-0.3Ti+0.25Y_2O_3 is referred to as Y_2O_3 HIP, Fe-14Cr-3W-0.3Ti-0.4Y+Fe_3O_4 HIP as Fe_3O_4 HIP, Fe-14Cr-3W-0.3Ti+0.25Y_2O_3 FAST as Y_2O_3 FAST and Fe-14Cr-3W-0.3Ti-0.4Y+Fe_3O_4 FAST as Fe_3O_4 FAST

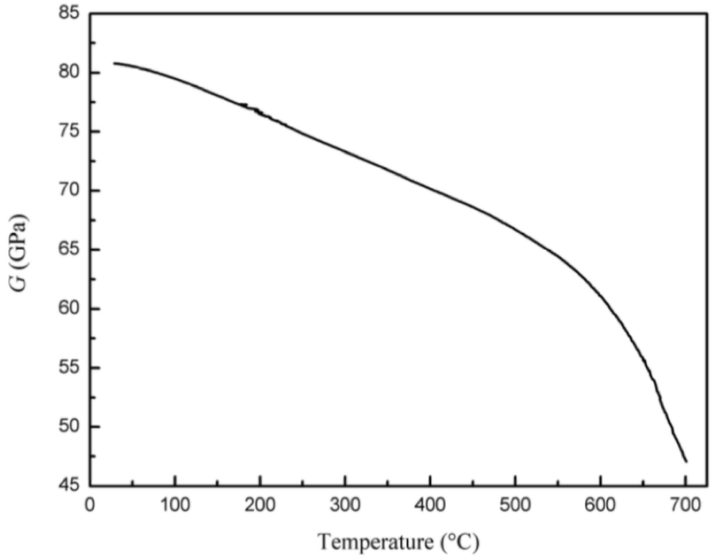


Figure 7.11: Shear modulus, G, of Fe-14Cr-1W-0.4Ti-0.3Y_2O_3 as a function of temperature [25].

Contribution	Y_2O_3 HIP	Fe_3O_4 HIP	Y_2O_3 FAST	Fe_3O_4 FAST
$\rho_{dislocation}$ (10^{13})	9	5	6	5
σ_{BH} 20°C (MPa)	133	100	109	101
σ_{BH} 350°C (MPa)	118	88	96	89
σ_{BH} 650°C (MPa)	91	69	75	69

Table 7.9: Estimated Bailey-Hirsch contributions for the four Fe-14Cr-3W-0.3Ti-based alloys at room temperature, 350°C and 650°C.

Hall-Petch Strengthening

Matrix yield strength (σ_0) was assumed to be constant over the temperature range. σ_D varied with G at 350°C, but k was assumed constant, because there was almost no change in the grain size in the thermal stability study, d was also assumed to be constant. At 650°C σ_D was substituted for σ_{CC}, as the creep becomes the dominant strengthening mechanism over grain boundary strengthening. The resulting estimates are shown in Table 7.10, indicating a reduction in yield strength contribution of $\sim$ 10% at 350°C[10].

[10]Fe-14Cr-3W-0.3Ti+0.25Y_2O_3 is referred to as Y_2O_3 HIP, Fe-14Cr-3W-0.3Ti-0.4Y+Fe_3O_4 HIP as Fe_3O_4 HIP, Fe-14Cr-3W-0.3Ti+0.25Y_2O_3 FAST as Y_2O_3 FAST and Fe-14Cr-3W-0.3Ti-0.4Y+Fe_3O_4 FAST as Fe_3O_4 FAST

Contribution	Y_2O_3 HIP	Fe_3O_4 HIP	Y_2O_3 FAST	Fe_3O_4 FAST
Mean grain size (μm)	0.87	0.62	0.32	0.54
σ_D 20°C (MPa)	240	284	395	304
σ_D 350°C (MPa)	225	267	371	286

Table 7.10: Estimated Hall-Petch strengthening for the four Fe-14Cr-3W-0.3Ti-based alloys at room temperature and 350°C.

Orowan Strengthening

Assuming the particles remained stable at 350°C, the only temperature dependent term considered was G, as previously described. Above 600°C Orowan strengthening was replaced by σ_{ARW} at temperatures above 500-600°C. Table 7.11 shows the resulting estimates, indicating a similar reduction of $\sim 10\%$ at 350°C[11].

Contribution	Y_2O_3 HIP	Fe_3O_4 HIP	Y_2O_3 FAST	Fe_3O_4 FAST
f	0.00031	0.00081	0.00031	0.00081
d_p	1.8×10^{-9}	2.18×10^{-9}	1.8×10^{-9}	2.18×10^{-9}
σ_K 20°C (MPa)	836	1113	836	1113
σ_K 350°C (MPa)	739	983	739	983

Table 7.11: Orowan strengthening for the four Fe-14Cr-3W-0.3Ti-based alloys at room temperature and 350°C.

Coble Creep

Coble creep becomes predominant at temperatures at which Hall-Petch breaks down when $\sigma_{CC} < \sigma_{HP}$. The undermining effect on strength due to Coble creep has been given as [25]:

$$\sigma_{CC} = \frac{k_B T d^3 \dot{\epsilon}}{47\Omega\delta_B D_{B0}} exp(\frac{Q_B}{RT}) \tag{7.10}$$

where k_B is Boltzmann's constant (1.38×10^{-23}), T is temperature, d is grain size, $\dot{\epsilon}$ is the steady state creep rate ($10^{-3}s^{-1}$ [25]), Ω is the atomic volume

[11] Fe-14Cr-3W-0.3Ti+0.25Y_2O_3 is referred to as Y_2O_3 HIP, Fe-14Cr-3W-0.3Ti-0.4Y+Fe_3O_4 HIP as Fe_3O_4 HIP, Fe-14Cr-3W-0.3Ti+0.25Y_2O_3 FAST as Y_2O_3 FAST and Fe-14Cr-3W-0.3Ti-0.4Y+Fe_3O_4 FAST as Fe_3O_4 FAST

($1.18 \times 10^{-29} m^3$ [25]), $\delta_B D_{B0}$ is the product of grain boundary width and the pre-exponential factor of grain boundary diffusion ($1.1 \times 10^{-12} m^3 s^{-1}$ [25]), Q_B is the activation energy for grain boundary diffusion (174 kJ/mol [25]) and R is the gas constant (8.31 J/molK).

Using Equation 7.3.3.2, Table 7.12 shows very high estimated values of σ_{CC} (10^{21}-10^{22}) at room temperature, and at 350°C (10^6), but at 650°C $\sigma_{CC} << \sigma_D$ and Coble creep becomes predominant. Values in Table 7.12 were comparable to those suggested by Sanctis *et al.* for similar material of 16 MPa at 600°C [25][12].

Contribution	Y_2O_3 HIP	Fe_3O_4 HIP	Y_2O_3 FAST	Fe_3O_4 FAST
Grain Size (μm)	0.87	0.62	0.32	0.54
σ_{CC} 20°C (MPa)	4.7×10^{22}	1.4×10^{22}	1.5×10^{21}	5.6×10^{21}
σ_{CC} 350°C (MPa)	3.7×10^{6}	1.3×10^{6}	0.16×10^{6}	0.75×10^{6}
σ_{CC} 650°C (MPa)	98	35	4.6	22

Table 7.12: Estimated Coble-creep contributions for the four Fe-14Cr-3W-0.3Ti-based alloys at room temperature, 350°C and 650°C.

Arzt-Rösler-Wilkinson Strengthening

The Arzt-Rösler-Wilkinson stress is related to the process of dislocation climb over hard particles, and becomes effective at temperatures above ∼500°C where Orowan strengthening loses its efficiency, and was estimated using [25]:

$$\sigma_{ARW} = 0.9M \frac{R^{3/2}}{2\sqrt{2} + R^{3/2}} \frac{Gb}{L} \tag{7.11}$$

where R is the decrease of line tension of a pinned dislocation segment (0.77), G is the shear modulus which varies with temperature as shown previously, $b = 0.25$ nm, the modulus of Burgers vector (assuming all dislocations have a Burgers vector of type $\frac{1}{2}111$) and L is the mean spacing between particles. L is related to the particle size and number density through the equation [158]:

[12] Fe-14Cr-3W-0.3Ti+0.25Y_2O_3 is referred to as Y_2O_3 HIP, Fe-14Cr-3W-0.3Ti-0.4Y+Fe_3O_4 HIP as Fe_3O_4 HIP, Fe-14Cr-3W-0.3Ti+0.25Y_2O_3 FAST as Y_2O_3 FAST and Fe-14Cr-3W-0.3Ti-0.4Y+Fe_3O_4 FAST as Fe_3O_4 FAST

$$L = d[\left(\frac{\pi}{4f}\right)^{1/2} - 1] \tag{7.12}$$

Using Equations 7.3.3.2 and 7.3.3.2, Table 7.13 shows the estimated values of σ_{ARW} at 650°C[13]. The higher barrier to climb in the Fe-14Cr-3W-0.3Ti-0.4Y+Fe_3O_4 alloys was due to their finer particle distribution. Comparing values with the literature, σ_{ARW} contributions were similar to those reported by Sanctis *et al.* for a similar alloy.

Contribution	Y_2O_3 HIP and FAST	Fe_3O_4 HIP and FAST
σ_{ARW} 650°C (MPa)	79	107

Table 7.13: Estimated Arzt-Rösler-Wilkinson contributions for the samples at each of the testing temperatures.

Estimates at Intermediate and High Temperatures

Following the method described by Sanctis *et al.* [25] and Schneibel *et al.* [175], summing the contributions from all of the strengthening mechanisms, Figures 7.12 and 7.13 show the estimated yield strengths alongside experimental data, with the low/mid temperature regime shown in red, high temperature regime in yellow, and experimental data over-laid.

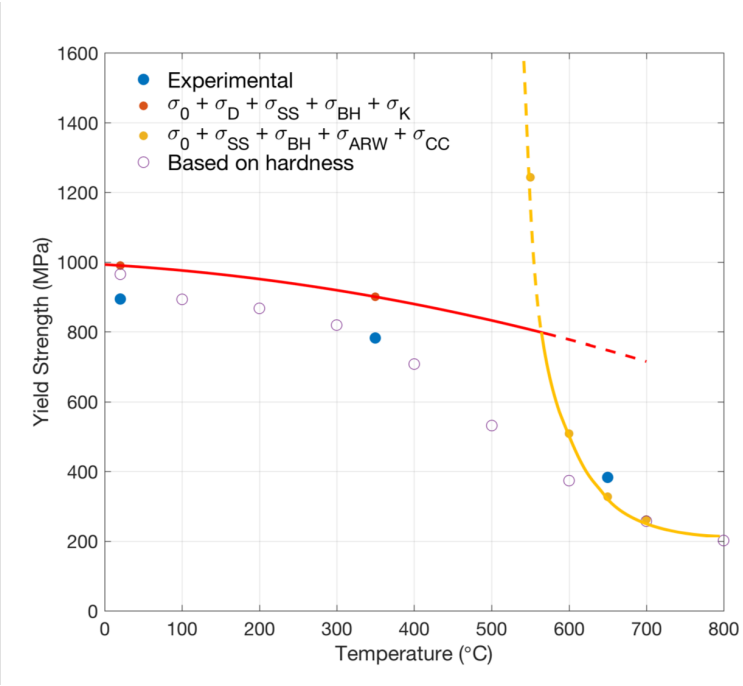
Figure 7.12(a) for Fe-14Cr-3W-0.3Ti-Y_2O_3 powder processed by (a) HIP and (b) FAST. The HIP plot also shows the predictions of yield stress from hot microhardness values calculated from Equation 7.3.3. For Fe-14Cr-3W-0.3Ti-Y_2O_3 HIP in Figure 7.12 (a), the 'model' overpredicts yield strength in the low temperature regime, but agrees more closely with predictions from hardness at room temperature, as previously discussed. As temperature increases, strength decreases with temperature more quickly than the model suggests, indicating that

[13]Fe-14Cr-3W-0.3Ti+0.25Y_2O_3 is referred to as Y_2O_3 HIP, Fe-14Cr-3W-0.3Ti-0.4Y+Fe_3O_4 HIP as Fe_3O_4 HIP, Fe-14Cr-3W-0.3Ti+0.25Y_2O_3 FAST as Y_2O_3 FAST and Fe-14Cr-3W-0.3Ti-0.4Y+Fe_3O_4 FAST as Fe_3O_4 FAST

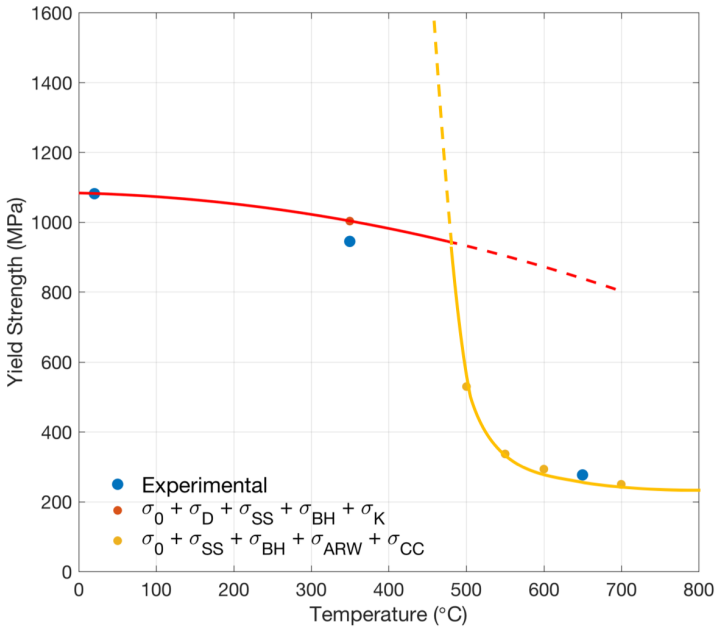
assumptions of unchanging dislocation density, grain size, or particles being non-shearable at 350°C reduce in validity. A transition temperature between the two regimes of $\sim$ 565°C may be inferred between the low and high temperature regimes, which is within the range expected from literature [25] for the onset of creep and dislocation climb: in reality changes between regimes will be more gradual, more of a sigmoid function shape, as captured in the hot hardness data but further testing temperatures would be required to isolate this transition shape.

For Fe-14Cr-3W-0.3Ti-0.25Y_2O_3 FAST in Figure 7.12 (b), the model fits more closely to experiment, save a slight overprediction at 350°C. The transition was reduced to $\sim$ 475°C, lower than expected from literature [25], and perhaps due to the particularly refined grain size causing 'early' onset of diffusion based processes such as creep / climb. Unfortunately without further hot microhardness or further ETMT data, the detailed shape of transitions could not be further resolved.

Figure 7.13 shows the comparison for Fe-14Cr-3W-0.3Ti-0.4Y+Fe_3O_4 material consolidated by (a) HIP and (b) FAST. For Fe-14Cr-3W-0.3Ti-0.4Y+Fe_3O_4 HIP, the model predicts properties in the lower temperature regime reasonably well, but under-estimates the yield strength at 650°C. The model in Figure 7.13 (b) for Fe-14Cr-3W-0.3Ti-0.4Y+Fe_3O_4 FAST overpredicts in the lower temperature regime, likely for the same reasons as Fe-14Cr-3W-0.3Ti+0.25Y_2O_3. In both cases, the high temperature tensile properties are significantly under-estimated. This may be due to: σ_D does not reduce as grain coarsening is negligible, Coble creep is more restricted than assumed and has a higher energy barrier, shifting the curve to the right, or σ_K maintains efficiency in interfacial pinning and dislocation climb (σ_{ARW}) is prevented. Other studies, however, have shown a high dislocation of oxides in ferritic ODS steels, suppressing dislocation glide meaning σ_K remains relatively large and reductions in σ_{ARW} contributions do not occur until higher temperatures. If in the high temperature regime, σ_K is used instead of σ_{ARW}, the estimates from the model can be seen as purple crosses in Figures 7.13 (a) and (b). In both cases, mechanical properties are now over-estimated, but this does give an indication that particle pinning is still active in the Fe-14Cr-3W-0.3Ti-0.4Y+Fe_3O_4 materials



(a) Fe-14Cr-3W-0.3Ti-0.25Y_2O_3 HIP



(b) Fe-14Cr-3W-0.3Ti-0.25Y_2O_3 FAST

Figure 7.12: Comparison between the strengthening model and experimental yield strength values for (a) Fe-14Cr-3W-0.3Ti-0.25Y_2O_3 HIP showing both experiment and hardness predictions and (b) Fe-14Cr-3W-0.3Ti-0.25Y_2O_3 FAST.

at 650°C, giving explanation to both the maintained yield and ultimate tensile strengths, and the lack of ductility. The transition temperature for both the Fe_3O_4 HIP and FAST models was 520°C, within the expected range from literature [25].

7.3.3.3 Comparison with the literature values

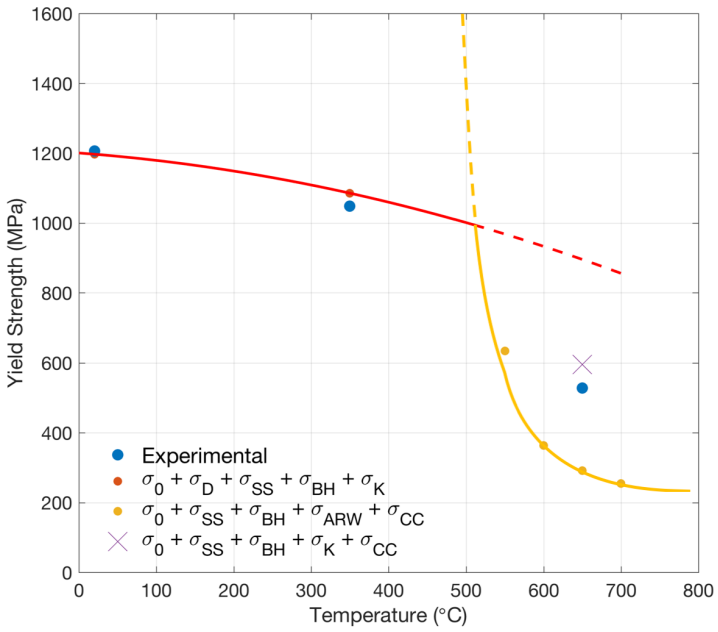
Figure 7.14 shows the measured of yield strength for all materials alongside values from literature of Fe-14Cr based ODS alloys processed through different methods.

The alloys were broadly within the range of previous work despite the different process routes, with Fe-14Cr-3W-0.3Ti-0.4Y+Fe_3O_4 having the highest yield strength.

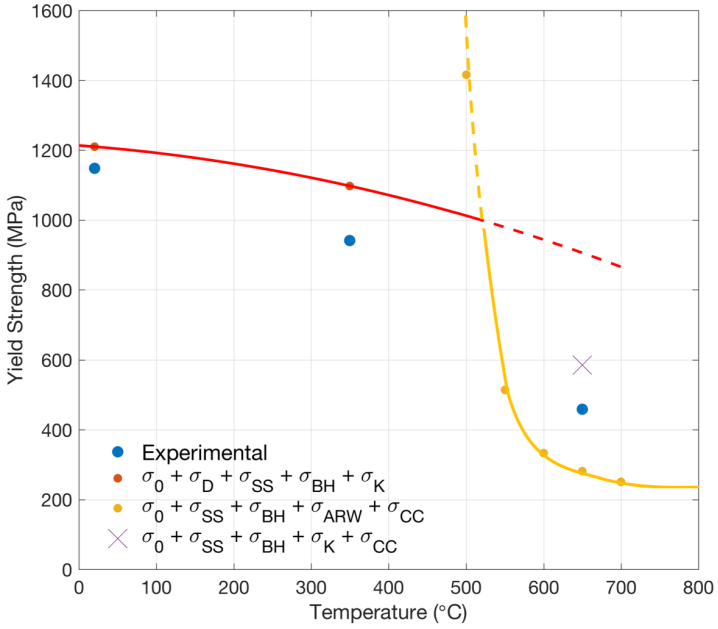
Figure 7.15 shows the measured ultimate tensile strength for all materials alongside typical results from literature on the same alloy processed through different methods. Again, Fe-14Cr-3W-0.3Ti-0.4Y+Fe_3O_4 alloys showed the highest strength across the temperature testing range, with all alloys being within the expected range from literature.

A reduction in yield or ultimate strength with elevated temperature is usually accompanied by an increase in ductility, and tensile elongation to failure is compared with the literature in Figure 7.16. Fe-14Cr-3W-0.3Ti+0.25Y_2O_3 HIP showed similar ductility at room temperature to the material produced previously using the same procedure by Gorley [39], and performed better at elevated temperatures ($\sim$ 10% strain compared with $\sim$ 4%). However these are both comparatively low as most reports are >10% strain across the temperature range. Despite Fe-14Cr-3W-0.3Ti+0.25Y_2O_3 FAST showing very low ductility in the low temperature regime, at 650°C ductility was closer to the literature. Over the whole temperature range, Fe-14Cr-3W-0.3Ti-0.4Y+Fe_3O_4 showed the lowest levels of ductility, consistent with its higher strength.

A requirement for most structural components is that the material is both strong and tough in order to be damage tolerant, and a minimum of 2% total circumferential elongation is required at the end of service life for cladding tubes [181], including any allowance for any reduction in elongation due to irradiation. Safety requirements



(a) Fe-14Cr-3W-0.3Ti-0.4Y+Fe_3O_4 HIP



(b) Fe-14Cr-3W-0.3Ti-0.4Y+Fe_3O_4 FAST

Figure 7.13: Comparison between the strengthening model and experiment yield strength for (a) Fe-14Cr-3W-0.3Ti-0.4Y+Fe_3O_4 HIP and (b) Fe-14Cr-3W-0.3Ti-0.4Y+Fe_3O_4 FAST.

also require justification that within predicted operating conditions, the cladding should not strain by more than 1% over the lifetime of the fuel [182], meaning a

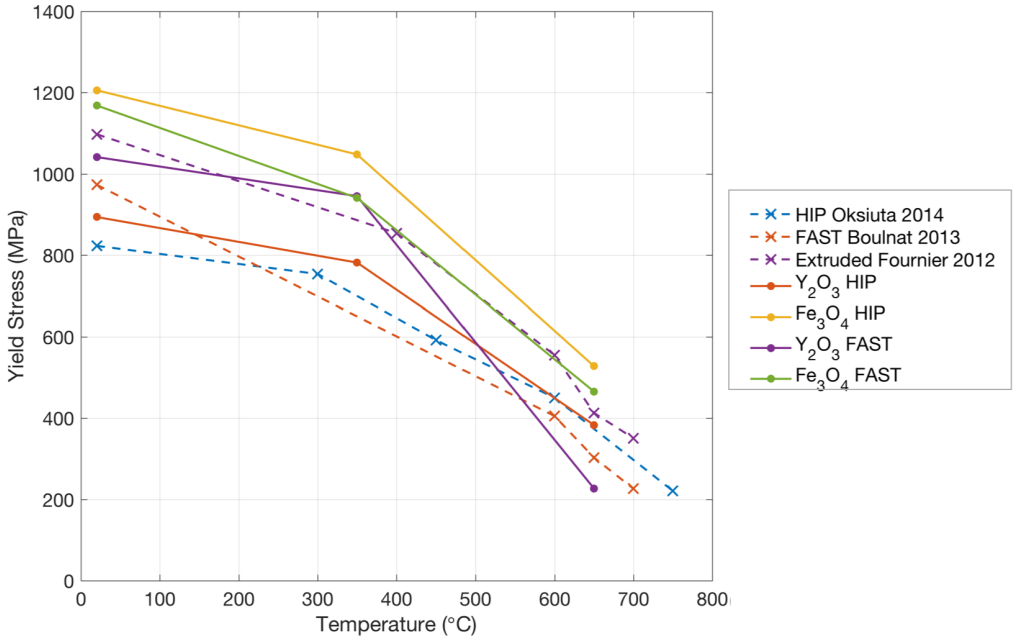


Figure 7.14: Yield strength as a function of temperature for Fe-14Cr-3W-0.3Ti+0.25Y_2O_3 HIP (Y_2O_3 HIP), Fe-14Cr-3W-0.3Ti+0.25Y_2O_3 FAST (Y_2O_3 FAST) and Fe-14Cr-3W-0.3Ti-0.4Y+Fe_3O_4 FAST (Fe_3O_4 FAST) compared with similar alloys.

stronger tube would be of benefit. As previously mentioned, 15:15Ti austenitic steel is the main competitor for use in cladding applications in SFR and shows a strain to failure of 5% at 300°C and 7% at 500°C [132]. Tensile strength is maintained up to 500°C at $\sim$ 800 MPa across this temperature range. The operational conditions for SFRs are reasonably well established, but how this translates into required material property behaviour for ODS (or an austenitic steel) to survive these conditions is the current issue and requires further research and guidance from industry. Given that the embrittlement of ferritic ODS steel is not fully understood, and SFR operating conditions not fully set, industry must set targets for R&D as to acceptable levels of ductility for unirradiated material at reactor operating temperatures before uptake of an ODS steel will be considered. The ductility at room temperature of the alloys in this thesis is unsufficient, but some encouragement is provided in the balance of elevated temperature properties.

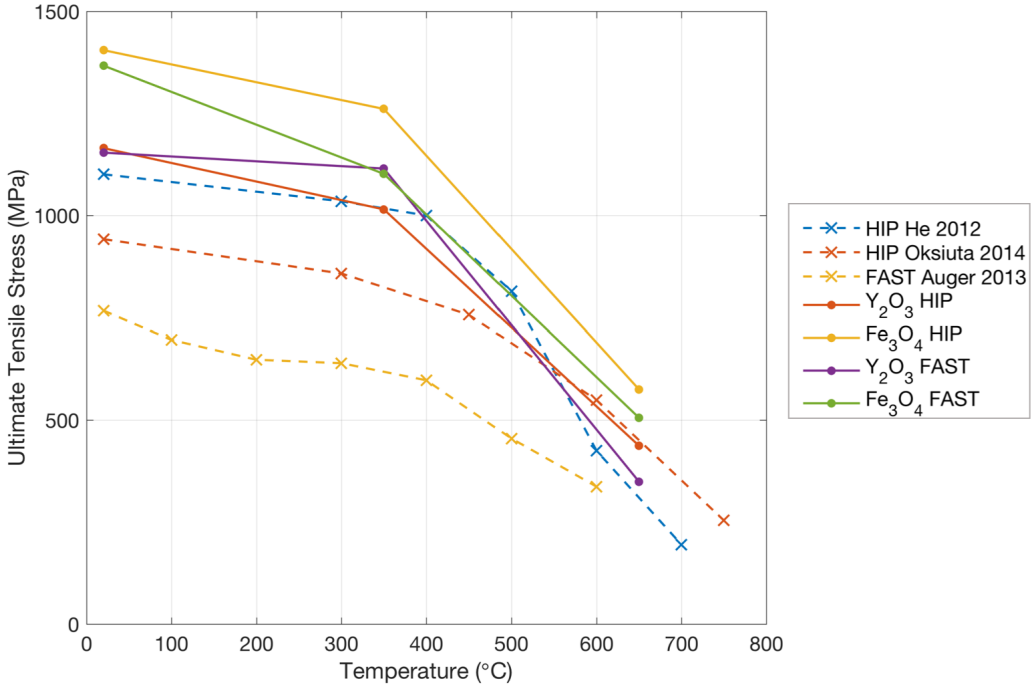


Figure 7.15: Ultimate tensile strength as a function of temperature for Fe-14Cr-3W-0.3Ti+0.25Y_2O_3 HIP (Y_2O_3 HIP), Fe-14Cr-3W-0.3Ti+0.25Y_2O_3 FAST (Y_2O_3 FAST) and Fe-14Cr-3W-0.3Ti-0.4Y+Fe_3O_4 FAST (Fe_3O_4 FAST) compared with similar allloys.

7.3.4 ETMT Summary

All processing methods demonstrate good and typical high temperature strength when compared with data in the literature. At elevated temperatures, Fe-14Cr-3W-0.3Ti+0.25Y_2O_3 alloys show good promise for both strength and ductility, showing positive indications for FAST as a consolidation method. Fe-14Cr-3W-0.3Ti-0.4Y+Fe_3O_4 alloys show good promise in terms of yield strength and ultimate tensile strength but were potentially over strengthened, and fail with very little elongation across the whole temperature range examined. Guidance must be sought from industry as to targets for properties in terms of acceptable high temperature yield strength and total elongation to understand what compromises may be possible. Further thermal treatment of the Fe-14Cr-3W-0.3Ti-0.4Y+Fe_3O_4 alloys could lead to the generation of a larger, lower density distribution of particles which give better compromise between strength and ductility and should be examined further. Residual porosity must be removed by further improved processing.

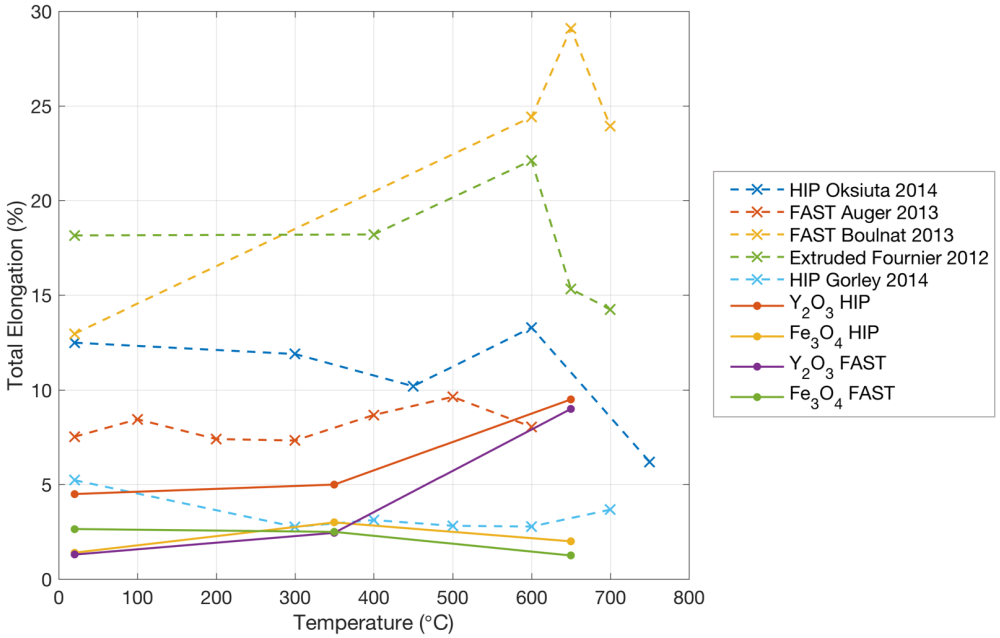


Figure 7.16: Total elongation as a function of temperature for Fe-14Cr-3W-0.3Ti+0.25Y_2O_3 HIP (Y_2O_3 HIP), Fe-14Cr-3W-0.3Ti+0.25Y_2O_3 FAST (Y_2O_3 FAST) and Fe-14Cr-3W-0.3Ti-0.4Y+Fe_3O_4 FAST (Fe_3O_4 FAST) compared with similar allloys.

7.4 Small Punch Testing

It has already been seen that the two different powders and two different sintering methods generate subtly different microstructures with some effect on corresponding tensile mechanical properties. However, tensile creep resistance is critical in cladding applications, and may not be readily inferred from simple tensile tests.

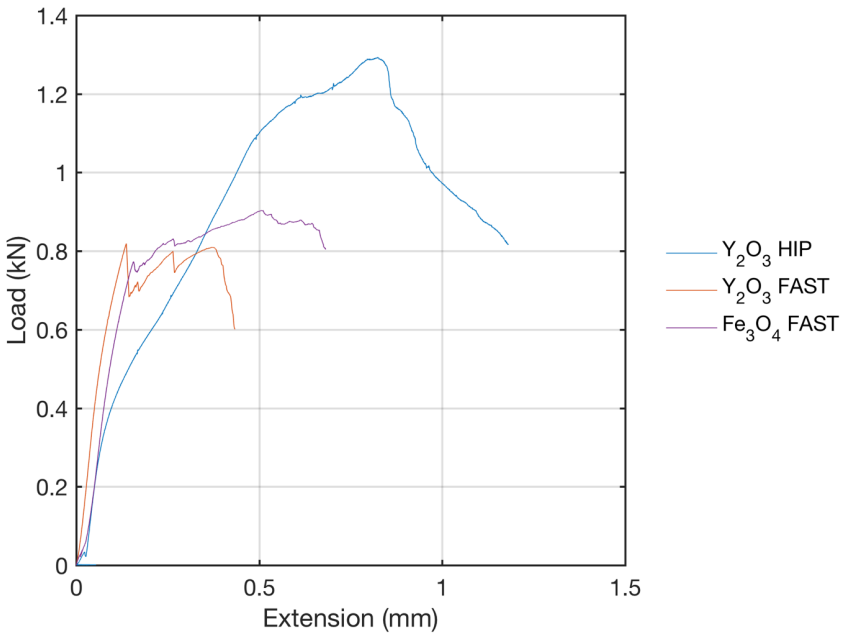
Using small punch testing, creep behaviour may be studied using constant load, as shown in Section 3.7.3. This technique is still in development, but standard procedures are beginning to be set up (e.g. European standard for small punch testing of metallic materials [183]). Modelling is still required to fully understand the relatively complex deformation process which has some similarity to indentation creep testing (which is also very difficult to interpret). Because of the constantly changing deformation behaviour and contact area with the punch as it moves, it is not yet possible to determine the stress state, convert displacement into strain or to compare data with constant load tensile tests. Due to the shorter testing

times of small punch testing, microstructural changes in long term creep do not occur, although extrapolation of SPT data has shown good correlation with long term conventional creep test results [184]. Here, SPT is used only as a comparative technique for creep resistance and therefore no significant discussion of quantitative results in terms of other creep data in the literature is included.

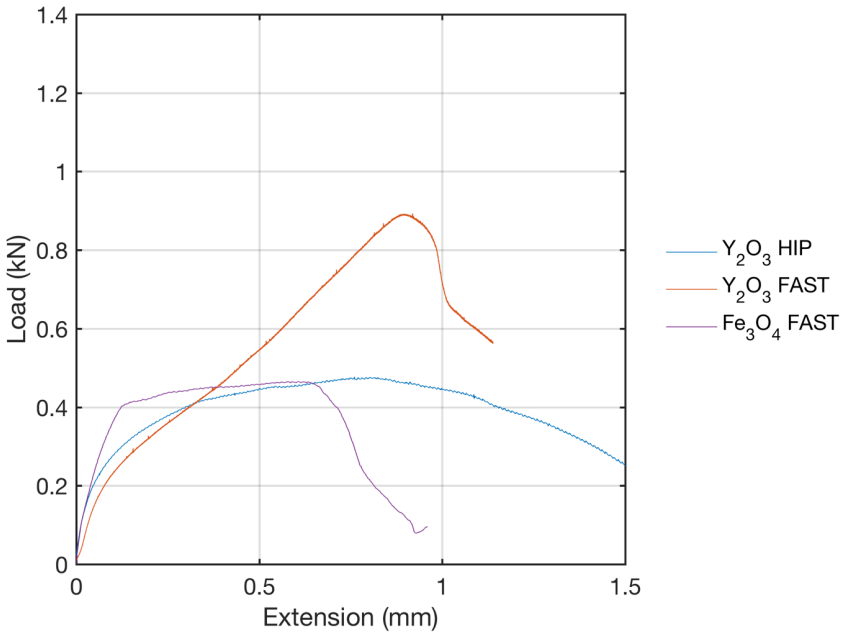
Testing was only completed on three of the processing methods due to lack of available time on the equipment at UKAEA. These were selected to be Fe-14Cr-3W-0.3Ti+0.25Y_2O_3 HIP as a baseline more easily compared with the literature, Fe-14Cr-3W-0.3Ti+0.25Y_2O_3 FAST, to assess HIP versus FAST, and Fe-14Cr-3W-0.3Ti-0.4Y+Fe_3O_4 FAST to assess the in-situ oxidation route.

7.4.1 Constant Displacement Rate Tests

Figure 7.17 shows the load-displacement curves for room temperature tests conducted using a constant displacement mode of 0.2 mm/min. In Figure 7.17(a) at room temperature, Fe-14Cr-3W-0.3Ti+0.25Y_2O_3 HIP withstood the highest load prior to fracture (1.3kN) at room temperature and failed after 1 mm of displacement (failure is commonly classed as a 20% load drop). In Figure 7.17(b), however, this material withstood only 0.5 kN at 650°C, failing at a similar displacement of $\sim$ 1.2 mm. The two FAST alloys behaved similarly at room temperature, both showing 'pop-in' type fractures (showing discontinuities in the force-displacement curves), which are a likely sign of crack initiation and arrest or formation of cleavage planes perpendicular to the loading plane, at $\sim$ 0.8 kN, and following a series of further pop-ins led to failure at 0.45 mm and 0.7 mm for Fe-14Cr-3W-0.3Ti+0.25Y_2O_3 FAST and Fe-14Cr-3W-0.3Ti-0.4Y+Fe_3O_4 FAST respectively. At high temperature, Fe-14Cr-3W-0.3Ti+0.25Y_2O_3 FAST withstood a similar load of $\sim$ 0.9 kN, failing at $\sim$ 1 mm, but Fe-14Cr-3W-0.3Ti-0.4Y+Fe_3O_4 FAST yielded after only 0.4 kN, again failing at $\sim$ 0.7 mm. Comparing with the literature, Hernandez-Mayoral [122] reported a maximum load of 1.5-1.8 kN in the longitudinal direction, slightly higher than here for Y_2O_3 HIP.



(a) RT



(b) 650°C

Figure 7.17: Load-displacement curves for constant displacement tests at 0.2 mm/min tested at (a) room temperature and (b) 650°C using small punch testing for Fe-14Cr-3W-0.3Ti+0.25Y_2O_3 HIP (Y_2O_3 HIP), Fe-14Cr-3W-0.3Ti+0.25Y_2O_3 FAST (Y_2O_3 FAST) and Fe-14Cr-3W-0.3Ti-0.4Y+Fe_3O_4 FAST (Fe_3O_4 FAST).

The corresponding fracture surfaces are shown in Figure 7.18 (a) for Fe-14Cr-3W-0.3Ti+0.25Y_2O_3 HIP at room temperature, (b) at 650°C, (c) for Fe-14Cr-3W-0.3Ti+0.25Y_2O_3 FAST at room temperature (d) at 650°C (e) for Fe-14Cr-3W-0.3Ti-0.4Y+Fe_3O_4 FAST at room temperature and (f) at 650°C. All fracture surfaces showed brittle behaviour indicated by long, relatively straight cracks either in a star or cross shape below the indenter, with no evidence of necking.

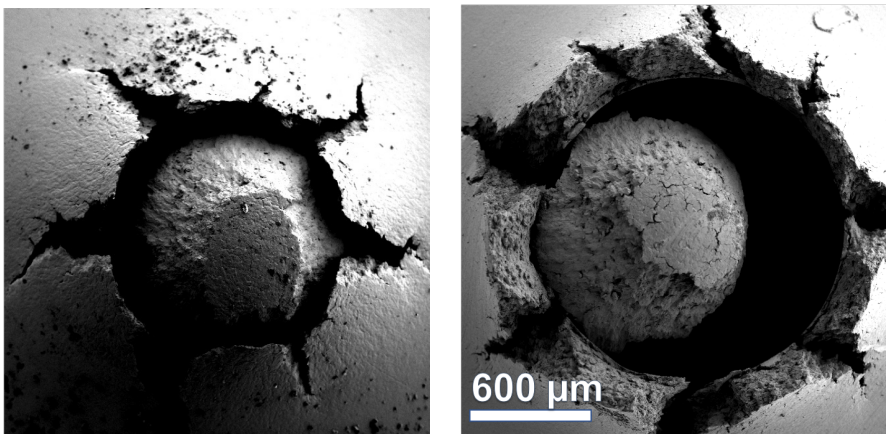
7.4.2 Creep Tests

Using the failure loads during constant displacement tests as a guide, a series of constant loads from 250 to 375 N were investigated using Fe-14Cr-3W-0.3Ti+0.25Y_2O_3 HIP alloy with the aim to give a range of practical failure times, which are shown in Figure 7.19(a). The applied loads gave to a good spread of failure times from 1 h (for 375 N) to $\sim$ 30 h (for 255 N). Creep behaviour of Fe-14Cr-3W-0.3Ti+0.25Y_2O_3 HIP (Y_2O_3 HIP), Fe-14Cr-3W-0.3Ti+0.25Y_2O_3 FAST (Y_2O_3 FAST) and Fe-14Cr-3W-0.3Ti-0.4Y+Fe_3O_4 FAST (Fe_3O_4 FAST) at the highest load of 375 N was investigated, and is shown in Figure 7.19(b), with failure times of $\sim$ 1 h, 6 h and 11 h respectively. Similar displacement prior to failure was shown by both the Fe-14Cr-3W-0.3Ti+0.25Y_2O_3 alloys ($\sim$ 0.9 mm), but only 0.4 mm in the Fe-14Cr-3W-0.3Ti-0.4Y+Fe_3O_4 alloy.

Failure times spanning the approximate range 1 h, 10 h and 100 h to give good confidence in the load / failure time plot. Unfortunately due to working in an impure Ar atmosphere, the WC punch head slowly diffusion bonded to the die set during prolonged times at elevated temperatures. It was therefore difficult to specify a single load at which the minimum creep rate caused a creep failure at times greater than 30 h but did not lead to the sticking. A number of samples failed to reach failure after 100 to 150 h due to punch sticking.

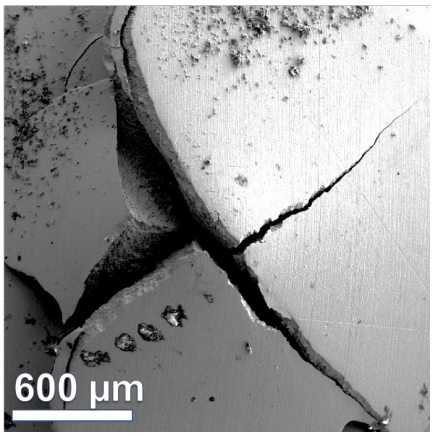
A typical creep curve consists of three regimes:

- Primary creep loading regime where deformation is quite rapid, but decreases with time as dislocation densities increase and a sub-grain structure develops meaning strain rate diminishes.

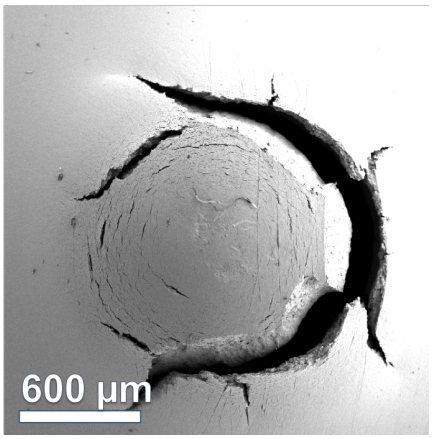


(a) Y_2O_3 HIP RT

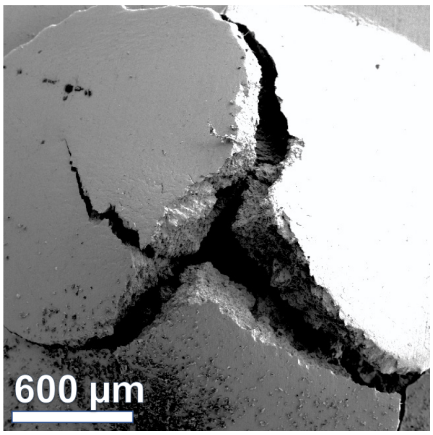
(b) Y_2O_3 HIP 650°C



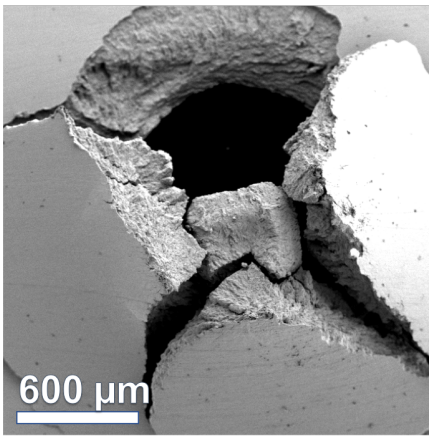
(c) Y_2O_3 FAST RT



(d) Y_2O_3 FAST 650°C

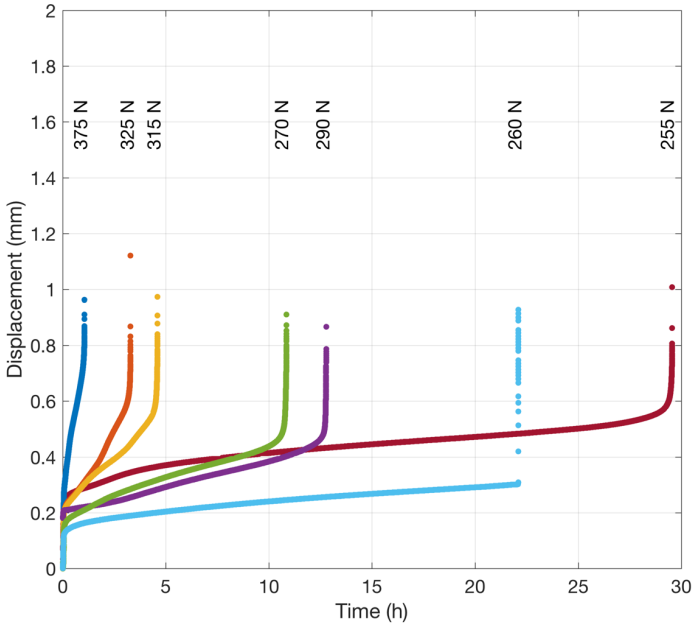


(e) Fe_3O_4 FAST RT

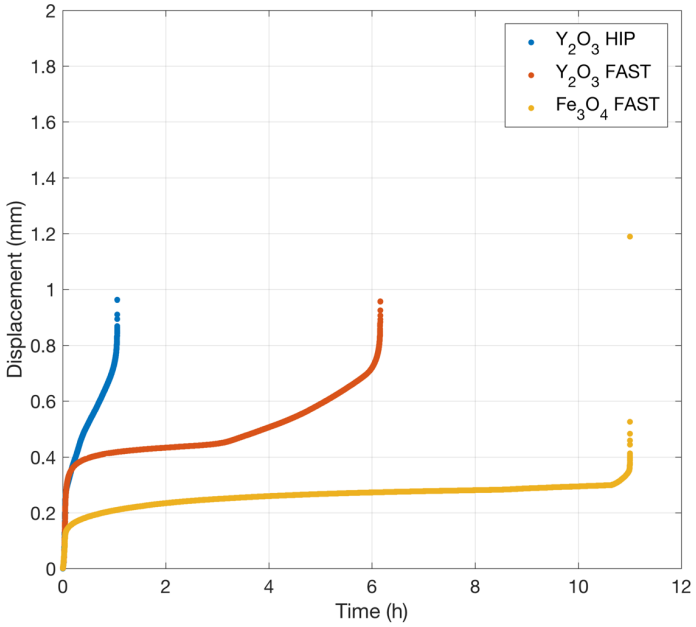


(f) Fe_3O_4 FAST 650°C

Figure 7.18: SEM micrographs of the fracture surface of (a) Fe-14Cr-3W-0.3Ti+0.25Y_2O_3 HIP at room temperature (b) at 650°C (c) Fe-14Cr-3W-0.3Ti+0.25Y_2O_3 FAST at room temperature (d) at 650°C (e) Fe-14Cr-3W-0.3Ti-0.4Y+Fe_3O_4 FAST at room temperature and (f) at 650°C.



(a) Failure times for a series of constant loads for Fe-14Cr-3W-0.3Ti+0.25Y_2O_3 HIP alloy.



(b) Creep failure times for Fe-14Cr-3W-0.3Ti+0.25Y_2O_3 HIP (Y_2O_3 HIP), Fe-14Cr-3W-0.3Ti+0.25Y_2O_3 FAST (Y_2O_3 FAST) and Fe-14Cr-3W-0.3Ti-0.4Y+Fe_3O_4 FAST (Fe_3O_4 FAST) at 650°C and 375 N.

Figure 7.19: SPT calibration tests.

- Secondary regime during which changes in displacement are slow and recovery is concurrent with deformation. Creep rate is characterised by the strain rate during this period.

- Tertiary creep where the strain rate increases exponentially due to necking, internal cracks or void formation which all decrease the effective area of the sample. Strength is quickly lost and the shape is permanently changed leading to rupture.

A difference in creep resistance changes the minimum strain rate during secondary creep and therefore extends the time to failure.

Without further information on the stress state and microstructure within the samples, clear identification of the creep regimes cannot be made but general trends were identified.

Comparatively, Fe-14Cr-3W-0.3Ti-0.4Y+Fe_3O_4 FAST showed the best creep resistance, failing after $\sim$ 11 h, followed by Fe-14Cr-3W-0.3Ti+0.25Y_2O_3 FAST after $\sim$ 6 h and Fe-14Cr-3W-0.3Ti+0.25Y_2O_3 after only $\sim$ 1 h.

The standard comparison for small punch test creep tests is rupture time as a function of hold force, which can is shown in Figure 7.20 alongside data from literature [134].

Comparing with HE ODS Fe-14Cr, Fe-14Cr-3W-0.3Ti-0.4Y+Fe_3O_4 FAST showed the closest similarity in gradient, an indication of similar creep resistance [184], maintained over the (relatively narrow) testing range, and at higher force. Fe-14Cr-3W-0.3Ti+0.25Y_2O_3 HIP showed similar creep resistance over short times but the load that it could withstand reduced relatively quickly in the longer term tests. The gradient of the plots was steeper than those in literature indicating a lack of long term creep resistance on the scale of 1000s of hours which is obviously a concern for cladding applications. Fe-14Cr-3W-0.3Ti+0.25Y_2O_3 FAST showed the largest deviation from the literature trend, and showed the best creep resistance. It is hypothesised that, due to the differences in yield strength at 650°C (383 MPa for Fe-14Cr-3W-0.3Ti+0.25Y_2O_3 HIP, 277 for Fe-14Cr-3W-0.3Ti+0.25Y_2O_3 FAST and

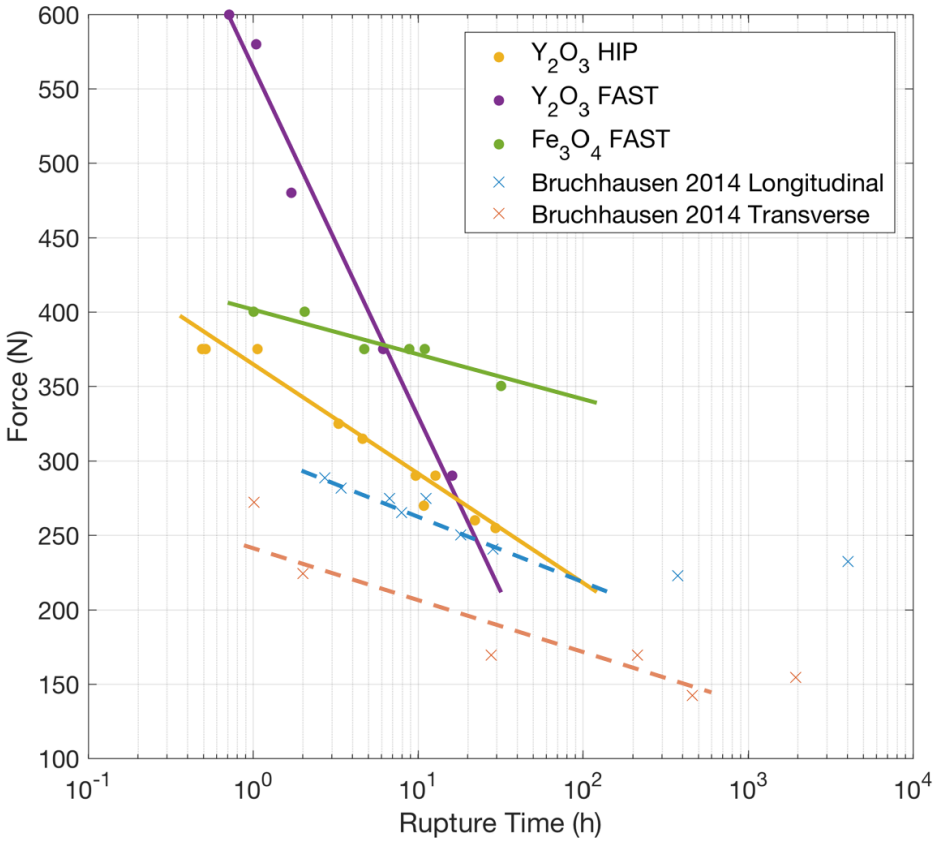


Figure 7.20: Stress-rupture plots for all SPT samples and literature values.

459 for Fe-14Cr-3W-0.3Ti-0.4Y+Fe_3O_4 FAST from ETMT), that the equivalent applied stress in a solely tensile creep test would be proportionally different to the yield strength of each alloy and that a different deformation mechanism could be active and a difference in the stability of crack propogation. It should be noted that the increase in creep resistance, as with high temperature strength, came at the expense of ductility but that properties could potentially be tailored with further heat treatment as discussed previously in Section 7.3.4.

In order to determine the stress imposed during the secondary regime, an analysis method shown in the European standard for small punch testing of metallic materials was employed [183]. Although the method is empirically based, it has been validated from a large pool of public-domain data, in-house and round robin studies. The method aims to identify an equivalent stress that would give the

same stress rupture time as in a uniaxial test conducted at the same stress. By identifying the point of minimum deflection rate ($\dot{u}$) (averaged over an hour to allow for insensitivities recorded data below 1 nm/s), the following expression can be used to determine the 'force-to-stress' conversion [183]:

$$\frac{F}{\sigma} = 1.916\dot{u}^{0.6579} \tag{7.13}$$

where F is the force applied in N and σ is the equivalent stress in a uniaxial test.

Applying Equation 7.13 during the secondary regime, the results of the maximum, mean and standard deviation for the equivalent uniaxial stress applied during creep testing of each material type, along with the yield stress from uniaxial testing (σ_{UAY}) for comparison, is shown in Table 7.14.

(MPa)	Y_2O_3 HIP	Y_2O_3 FAST	Fe_3O_4 FAST
σ_{max}	306	345	456
σ_{mean}	275	334	449
σ_{StDev}	31.7	7.5	8.5
σ_{UAY}	383	277	459

Table 7.14: Estimated stress during the secondary creep regime during SPT creep tests (maximum, mean and standard deviation of applied stress) compared with the yield strength from ETMT (σ_{UAY}) at room temperature.

These stresses were averages based on the applied force. Some regions, especially in the region that stretches at great curvature in the region between the grips and the punch head, will experience much higher local stresses that lead to local crack initiation that weakens the material. Due to the fact that the samples all failed, it would be contradictory to describe the failure stress as below the yield stress, but these estimations do indicate that unstable crack propogation was likely in the Fe-14Cr-3W-0.3Ti+0.25Y_2O_3 FAST alloy, and it is more likely that crack opening resistance was being tested than creep properties as the average stress was just below the UTS for that alloy (349 MPa). As a point of reference, the 290 N load achieved a very similar creep lifetime for both Fe-14Cr-3W-0.3Ti+0.25Y_2O_3 HIP and FAST, so in future lower loads should be applied to better simulate creep in all alloys.

As a second comparison, the average extension prior to failure is shown in Table 7.15. Fe-14Cr-3W-0.3Ti+0.25Y_2O_3 HIP samples had an almost consistent failure displacement $\sim$ 0.9 mm, seemingly independent of load. Fe-14Cr-3W-0.3Ti+0.25Y_2O_3 FAST failed on average at 1.2 mm, slightly more than HIP equivalents. Finally, the Fe-14Cr-3W-0.3Ti-0.4Y+Fe_3O_4 FAST alloy, despite seeming to perform best on the stress-rupture plot, failed at only $\sim$ 0.5 mm, and further analysis of fracture mechanisms is required to increase ductility.

(mm)	Y_2O_3 HIP	Y_2O_3 FAST	Fe_3O_4 FAST
mean d_f	0.91	1.22	0.46
StDev d_f	0.08	0.15	0.13

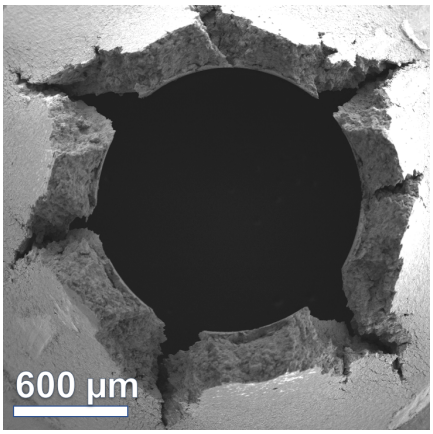
Table 7.15: Average extension before failure for the three alloys.

Typical SPT fracture surfaces close to 10 h for each processing method are shown in Figures 7.21 (a) (c) and (e). All demonstrate the star-shaped failure associated with brittle failure rather than more cup-and-cone, ductile behaviour. The enlarged images seen in (b), (d) and (f) show the edges of the deformed region in contact with the clamped die set, where it is predicted that the highest local stress is seen, as previously described. Fe-14Cr-3W-0.3Ti+0.25Y_2O_3 FAST shows the most ductile bending of the material around the clamp. Fe-14Cr-3W-0.3Ti+0.25Y_2O_3 HIP shows some evidence of ductility, while Fe-14Cr-3W-0.3Ti-0.4Y+Fe_3O_4 shows a large crack running along the boundary as the material failed in a brittle fashion around the circumference.

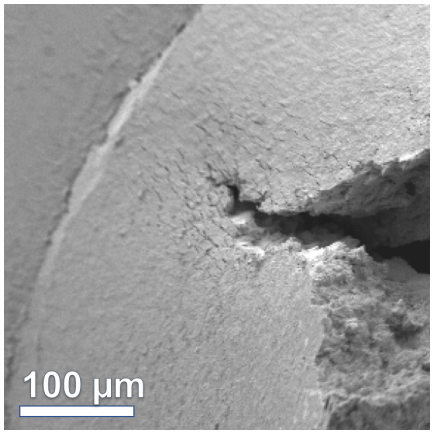
In future, all samples could be pre-stressed to the materials yield stress prior to creep testing, in a method shown by Cortellino et al. [185], to control the loading of the sample and generate an initial dislocation density that estimates the variability of the transition from primary to secondary creep and improves the reproducability of SPT creep life evaluation.

7.4.3 SPT Summary

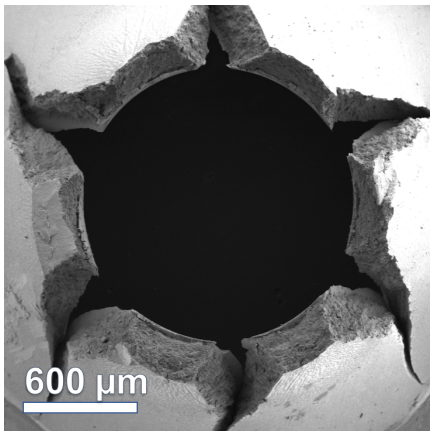
The results of SPT creep tests can not be considered in isolation, for example while the standard plot of load against time to failure might indicate excellent creep



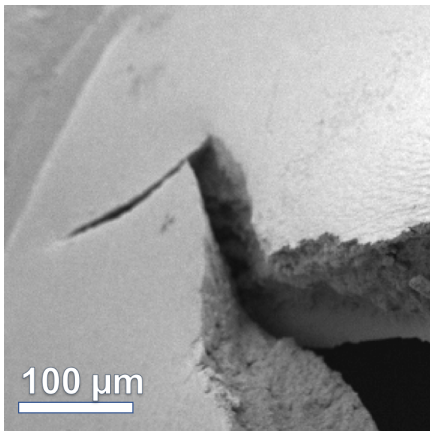
(a) Y_2O_3 HIP



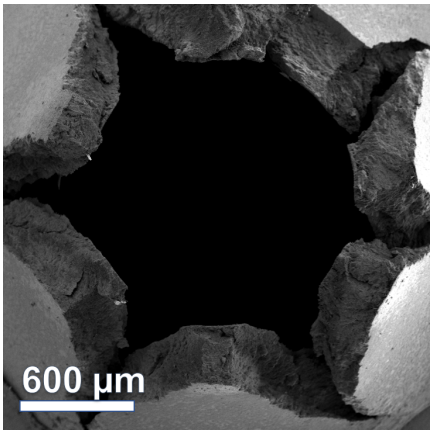
(b) Y_2O_3 HIP Edge



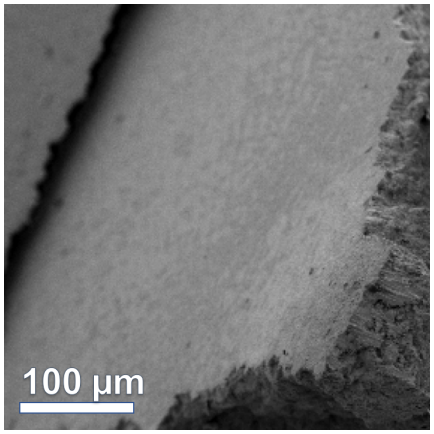
(c) Y_2O_3 FAST



(d) Y_2O_3 FAST Edge



(e) Fe_3O_4 FAST



(f) Fe_3O_4 FAST Edge

Figure 7.21: SEM images of the fracture surface of 10 h SPT creep tests (a) Fe-14Cr-3W-0.3Ti+0.25Y_2O_3 HIP (b) edge of deformed region (c) Fe-14Cr-3W-0.3Ti+0.25Y_2O_3 FAST (d) edge of deformed region (e) Fe-14Cr-3W-0.3Ti-0.4Y+Fe_3O_4 FAST (f) edge of deformed region.

resistance at high loads for Fe-14Cr-3W-0.3Ti-0.4Y+Fe_3O_4 FAST, brittle failure was typical on all fracture surfaces and its likely there would be a comparatively wide spread of failure times across multiple samples. The Fe-14Cr-3W-0.3Ti+0.25Y_2O_3 HIP alloy behaved closest to similar alloys in the literature, but it was not possible to assess long term performance due to punch sticking at low secondary creep rates. Finally, the Fe-14Cr-3W-0.3Ti+0.25Y_2O_3 FAST material demonstrated the worst creep resistance from the stress rupture plot, however the stress applied during secondary creep, in this case was only slightly below its ultimate tensile strength (as found by ETMT), promoting crack opening displacement resistance rather than creep resistance. Further work would involve lower loads to examine longer term exposure and mitigation of sticking / diffusion bonding issues.

7.5 Summary of Mechanical Behaviour

At room temperature, the ODS material developed through all processing methods had comparable or higher hardness, yield strength and ultimate tensile strength when compared to similar alloys from literature. All material, however, demonstrated brittle failure at low and intermediate temperatures, with fracture surfaces showing intragranular crack propogation and cleavage planes. At elevated temperatures, the Fe-14Cr-3W-0.3Ti+0.25Y_2O_3 alloy strength decreased and there was an increase in ductility, reaching around 10% elongation, double that of previous work using the same processing method. The Fe-14Cr-3W-0.3Ti-0.4Y+Fe_3O_4 alloy best maintained strength at elevated temperatures, likely due to the prevention of dislocation climb around particles, but with the price of relatively low levels of tensile elongation.

The low ductilities most probably arose from a minority of hard-to-close, residual porosity by either HIP or FAST, which may account for commercial interest in the hot extrusion route that applies very high levels of deformation unachievable by HIP or FAST. HE is however very expensive and comparatively hard to assess.

Overall, it is perhaps surprising that the differences between Y_2O_3 or Fe_3O_4, or HIP or FAST, were not greater than explored here, with in general rather similar microstructures, hardnesses, stability and preliminary microstrucural propertties, all of which lie in the range of similar alloys from the literature. Accepting required improvements in ductility, this can be seen as a positive outcome for the alternative approaches taken, particularly the more radical use of Fe_3O_4 to promote Y-O particles by internal oxidation, which offers encouragement for the further pursuit of this and related approaches to circumvent the long MA-based approach. One obvious avenue would be a Y-containing powder + Fe_3O_4 and direct hot extrusion to marry the avoidance of MA with high deformation consolidation of HE.

8 Conclusions and Further Work

8.1 Conclusions

The thesis has investigated the manufacture, microstructure and mechanical properties of ODS steels for possible cladding applications in Gen IV nuclear fission reactors. Work has focused on the development of novel processing methods that aim to reduce production complexity and time, allowing greater possibility for industrial uptake in the future. Key validations of success were high temperature stability and mechanical properties in comparison with alloy behaviour in the literature, and these were examined fully.

Objective 1

To assess the thermal stability at reactor relevant temperatures of the current "state-of-the-art" material as part of the European collaborative project, MatISSE, to act as a baseline for comparisons with novel processing methods.

SEM EBSD imaging was used to analyse the thermal stability of extruded ODS material after thermal ageing at 750°C for up to 675 h. The grain structure remained stable over the whole ageing period, with slight recovery during initially, followed by very little change. Hardness reduced slightly initially, indicative of

recovery, but quickly returned to hardnesses consistent with prior work. Extrusion texture was preserved under all conditions studied.

This study confirmed that the current preferred industrial processing method, of mechanical alloying followed by hot extrusion formed a stable ODS microstructure at reactor relevant temperatures.

Objective 2

To investigate any possible reductions in powder production time using tailored working parameters and advanced techniques and compare key parameters to current powder.

First, using the conventional route to introduce a fine Y_2O_3 powder into the pre-alloyed powder (Fe-14Cr-3W-0.3Ti), optimised parameters enabled use of a 40 h total mill time that represented a 33% reduction on previous work, identified by the quasi-equilibrium state between the rate of dislocation accumulation (hardening) and thermally induced recovery (softening), and comparable powder properties within the accuracy of the techniques employed.

A more novel route used planetary milling to introduce work hardening into an Y-containing pre-alloyed supplied by Sandvik-Osprey, while also mixing in a sacrificial Fe_3O_4 oxygen source. This provided a decrease in milling time of 83%.

Analysis of both MA Fe-14Cr-3W-0.3Ti+0.25Y_2O_3 and MA Fe-14Cr-3W-0.3Ti-0.4Y+Fe_3O_4 powders suggested an even oxygen distribution. When comparing to other novel powder production routes, such as GARS or STARS, a more homogeneous oxygen/oxide distribution was obtained, with no evidence of grain boundary particle enrichment (typical of GARS/STARS) of either Y or O. A concentration of Y in the powder by chemical analysis was suggested and this was monitored through further processing.

Objective 3

To investigate the effect of novel sintering techniques in the consolidation of these powders and the effect on microstructure and mechanical properties.

Two sintering methods were applied to the two powders: the more commonly used HIP and the newer FAST process.

FAST allowed a reduction of sintering time from 4 h in HIPing to 5 mins. The microstructure was found to be more dependent on the starting powder than the sintering method, giving strong promise for FAST as an alternative to HIP.

The Fe-14Cr-3W-0.3Ti+0.25Y_2O_3 powder, when sintered by HIP, led to the usual bimodal microstructure, wheras when sintered by FAST, there was a relatively refined microstructure. Extended sintering times at high temperature during HIP encouraged grain growth, but during FAST, hold times at these temperatures were minimised and excessive grain growth was avoided. Consequently, post-sinter, the dislocation density and levels of strain were comparatively high in FAST alloys, and a heat treatment at 750°C for 1 h allowed recovery, but was below the recrystallisation temperature. Oxide particles were strongly implicated in preventing grain boundary migration (Zener pinning). Instead, sub-grains formed, refining the microstructure and promoting an equiaxed grain structure.

The less highly worked Fe-14Cr-3W-0.3Ti-0.4Y+Fe_3O_4 powder showed a similar microstructure following both sintering methods, with large grains decorated with finer grains, somewhat different to the clusters of large and clusters of small grains in Fe-14Cr-3W-0.3Ti+0.25Y_2O_3 HIP. The post-FAST heat treatment reduced residual microstrain and the domain size, with a less marked effect than in Fe-14Cr-3W-0.3Ti+0.25Y_2O_3 FAST.

Fine-scale particles were identified by TEM and APT studies to be Y and/or Ti rich, but further work is required to fully characterise their distributions and stoichiometries.

All processing methods led to high room temperature hardness and strength, but low ductility which resulted in brittle failure. Fracture surfaces showed intragranular deformation and cleavage planes. At elevated temperatures, ductility in the Fe-14Cr-3W-0.3Ti+0.25Y_2O_3 alloys improved to $\sim$ 10%, with the onset of intergranular deformation and grain boundary deformation, but ductility remained low in the Fe-14Cr-3W-0.3Ti-0.4Y+Fe_3O_4 alloys. The generation of fine oxide particles that

retain microstructural stability and strength showed strong promise for the more novel Fe_3O_4 addition route, but encouraging some limited plastic deformation at elevated temperatures requires optimisation.

Objective 4

To assess the success of novel processing methods on the basis of microstructural stability and mechanical properties as an indicator for in-reactor performance and further development.

A 650°C thermal age was chosen to assess the stability of the grain structure from each of the processing routes. HIPed alloys had a slight reduction in grain size during the first 24 h. This was due to a lack of post HIP heat treatment and the elimination of some limited residual work by recovery. Over the following 650 h, the microstructure was stable in all cases, with little change in average grain size. This was strongly indicative that a fine distribution of particles were pinning grain boundaries and preventing their migration.

High temperature tensile properties showed promise in strength for each of the four alloys, and good high temperature ductility in the Fe-14Cr-3W-0.3Ti+$0.25Y_2O_3$ alloys. Ductility in Fe-14Cr-3W-0.3Ti-0.4Y+Fe_3O_4 was too low to be considered viable for cladding applications and further work should investigate the effects of further particle growth (and associated decrease in number density) with longer sintering times or alternative methods to increase ductility.

SPT was used to rapidly simulate creep resistance behaviour and was shown to be a convenient but a relatively primitive technique with further understanding required to calibrate it to unixial creep test results. In particular, the heterogeneity of stress/strain conditions across SPT samples makes interpretation hard; stiction was also problematic at long times. Comparatively, the Fe-14Cr-3W-0.3Ti-0.4Y+Fe_3O_4 FAST alloys withstood the highest load for creep resistance, slightly outperforming Fe-14Cr-3W-0.3Ti+$0.25Y_2O_3$ HIP. From post testing calculations of equivalent

uniaxial stress, the retained high temperature strength of the Fe-14Cr-3W-0.3Ti-0.4Y+Fe_3O_4 FAST was because it was tested well below its yield strength, while Fe-14Cr-3W-0.3Ti+0.25Y_2O_3 FAST was tested just below its UTS.

Fe-14Cr-3W-0.3Ti+0.25Y_2O_3 alloys performed according to the literature in terms of their high temperature tensile properties, with a reduction in yield strength at high temperatures giving better elongation values. The Fe-14Cr-3W-0.3Ti-0.4Y+Fe_3O_4 alloys, whilst offering even larger reductions in processing time, retained their strength across this whole temperature range, but suffered from brittle failure at high temperatures with little elongation. Attempts made to rationalise the relative contributions of various strength mechanisms to the strength using a simple summation approach of well-known analytical expressions requiring many assumptions and simplifications, was helpful in understanding relative contributions, with grain size and precipitate particle effects shown as the most important to tensile yield strength.

Three new processing routes were developed providing a reduction in processing time of between 33 and 83% respectively. Although high resolution analysis of the critical ODS particles developed in the novel routes could not confirm the exact stoichiometry of these Y-Ti containing oxides, the resulting strength at room temperature and stability at reactor relevant temperatures was encouraging in terms of prior work. The microstructures all consisted of fine ferrite grains on the sub-micron scale, which were stable at reactor relevant temperatures following exposure for up to 675 h, consistent with the 'state-of-the-art' material, also supplied by industry and tested in the current work. It is hypothesised that a high density of very fine particles may in some cases 'over-strengthen' the material, and a further thermal treatment to allow growth of the oxide particles and further ensure Y diffusion to these sites may be necessary, residual porosity was suggested to be problematic for tensile properties.

8.2 Further Work

Milling

Despite the desire to scale up the milling process to an industrial level, milling here was limited to planetary mills and therefore a maximum powder mass of 320 g per run. Use of a large scale attritor mill with a greater energy could significantly reduce milling time and make this method more attractive to industry. Detailed comparison between the powder produced by attritor mill and planetary mill can be seen in the report to NNL [186].

Further work should also consider the M-O (milled to induce mechanical work but absence of a sacrificial oxide source such as Fe_3O_4) powder to examine whether simply the addition of mechanical work would be enough to induce a fine scale distribution of oxide particles during sintering, as initial studies gave promising results.

Consolidation

One large concern with the consolidation route currently is the contamination between powder and milling media. In future, a better sealing and transport system should be installed to prevent contamination with air. This was a particular issue for the FAST and a glovebox loading system should be considered.

Although the novel consolidation method utilised in this work (FAST) gave a reduction in sintering time the industrial material supported the assumption that by direct, hot extrusion is superior. Despite the directionality of resulting properties (texture), HE induces large amounts of mechanical work, shearing powders (and rupturing any surface oxide layers) during consolidation. It is likely that this abrasive process could be enough to work the Fe-14Cr-3W-0.3Ti-0.4Y powder and that simply stirring in the sacrificial Fe_3O_4 powder prior to canning could be enough to produce a strong ODS steel. This has huge potential to reduce the processing time by eliminating milling entirely, creating a one-step production process.

Characterisation

Through the limited high resolution characterisation possible within this project it was discovered that in the Fe_3O_4 FAST sample, and potentially the Y_2O_3 FAST sample, the nanooxides were predominantly Ti-rich rather than the typical Ti-Y-O. Further characterisation is required to gain the statistics to draw a conclusion on the particle chemistry with confidence, and perhaps that TiO_x particles are the early stage versions of the more common Y-Ti-O, because of the relatively low Y concentrations that were retained in the powders here.

Mechanical Properties

The main limitation of the alloys was the lack of ductility. Once a target has been set by industry for the minimal acceptable ductility, further development should be completed to encourage ductility to the required level. This is likely to be in combination with tailoring sintering or heat treatment parameters.

Irradiation Damage

A subsequent project within The University of Oxford, being completed by Thomas Davis, will examine the irradiation damage response of Fe-14Cr-3W-0.3Ti+$0.25Y_2O_3$ FAST material, the best understood processing method at the time of beginning his project, alongside legacy Fe-14Cr-3W-0.3Ti+$0.25Y_2O_3$ HIP material, to assess the difference in behaviours based on grain size and potential differences in particle distributions.

Corrosion Studies

Due to the severe environment of SFRs, the stability of ODS materials under a liquid sodium environment should be examined to ensure any differences in microstructure do not lead to a difference in stability, and this exposure does not degrade high temperature properties.

ODS FeCrAl

ODS FeCrAl alloys are now also being investigated extensively for application as accident tolerant fuel (ATF) cladding in current LWRs. This is due to their potentially enhanced corrosion resistance to water at high temperatures, compared to currently used zirconium alloys. Further work could look to apply the knowledge gained this project regarding the advancement of ODS steel manufacturing techniques to FeCrAl variants in support of this nearer term application.

Spray Casting

As described in [187], spray casting was investigated early in this work as a potential method for 'trapping' Y within a bulk ($\sim$ 30 kg) ferritic steel. As with the Sandvik-Osprey powder, retaining Y in the melt and sprayed billet was problematic, as well as dispersing Y in the melt initially. This work is not described in the thesis but, based on subsequent developments described in this thesis, it is likely that a high level of mechanical work is always required to encourage fine-scale of oxides on dislocation forests, implying expensive forging of large spray cast billets before heat treatment would be required - a significant technological challenge. Futher, modelling may be useful to optimise the work required and the optimum temperature for internal oxidation, allowing inward travel of O without losing Y in the opposite direction to form a thick oxide scale.

Bibliography

[1] IAEA. *Energy, Electricity and Nuclear Power Estimates for the Period up to 2050*. Tech. rep. 2014. URL: http://www-pub.iaea.org/MTCD/Publications/PDF/rds-1-34-web-57882020.pdf.

[2] U.S. DOE. *A Technology Roadmap for Generation IV Nuclear Energy Systems*. 2002. URL: https://www.gen-4.org/gif/upload/docs/application/pdf/2013-09/genivroadmap2002.pdf (visited on 05/27/2015).

[3] CEA. *4th Generation Sodium Cooled Fast Reactors*. Tech. rep. December. 2012.

[4] Vienna: International Atomic Energy Agency. *Structural Materials for Liquid Metal Cooled Fast Reactor Fuel Assemblies - Operational Behaviour*. IAEA, 2012.

[5] D. Shepherd. "Technology readiness level (TRL) assessment of cladding for advanced nuclear fuels". In: *Structural Materials for Innovative Nuclear Systems (SMINS-3)*. 2013, pp. 108–116. URL: https://www.oecd-nea.org/science/docs/2015/nsc-wpfc-doc2015-9.pdf.

[6] B. Van Der Schaaf et al. "Progress and critical issues of reduced activation ferritic/martensitic steel development". In: *Journal of Nuclear Materials* 283-287 (2000), pp. 52–59. ISSN: 00223115. DOI: 10.1016/S0022-3115(00)00220-8.

[7] M. Inoue, T. Kaito, and S. Ohtsuka. "Research and development of oxide dispersion strengthened ferritic steels for sodium cooled fast breeder reactor fuels". In: *Materials for Generation IV Nuclear Reactors*. 2007.

[8] P. He. *On the structure-property correlation and the evolution of Nanofeatures in 12-13.5% Cr oxide dispersion strengthened ferritic steels*. 2013. ISBN: 9783731501411.

[9] M. K. Miller et al. "Vacancies as a constitutive element for the design of nanocluster-strengthened ferritic steels". In: *Front. Mater. Sci. China* 3.1 (2009), pp. 9–14. ISSN: 03029743. URL: http://download.springer.com/static/pdf/518/art%7B%5C%%7D3A10.1007%7B%5C%%7D2Fs11706-009-0001-8.pdf?auth66=1419847005%7B%5C_%7D%7B%5C&%7Dext=.pdf.

[10] A. Katoh, H. Hayafune, and S. Kotake. "Design features and cost reduction potential of JSFR". In: *Nuclear Engineering and Design* 280 (Dec. 2014), pp. 586–597. ISSN: 00295493. DOI: 10.1016/j.nucengdes.2014.08.031. URL: http://www.sciencedirect.com/science/article/pii/S0029549314005354.

[11] K. Aoto et al. "Design Study and R&D Progress on Japan Sodium-Cooled Fast Reactor". en. In: *Journal of Nuclear Science and Technology* (Jan. 2012). URL: http://www.tandfonline.com/doi/abs/10.1080/18811248.2011.9711720%7B%5C#%7D.VdHb1ot8Pww.

[12] G. R. Odette, M. J. Alinger, and B. D. Wirth. "Recent Developments in Irradiation-Resistant Steels". In: *Annual Review of Materials Research* 38.1 (Aug. 2008), pp. 471–503. ISSN: 1531-7331. DOI: 10.1146/annurev.matsci.38.060407.130315. URL: http://www.annualreviews.org/doi/abs/10.1146/annurev.matsci.38.060407.130315.

[13] A. De Bremaecker. "Past research and fabrication conducted at SCK CEN on ferritic ODS alloys used as cladding for FBR's fuel pins". In: *Journal of Nuclear Materials* 428.1-3 (Sept. 2012), pp. 13–30. ISSN: 00223115. DOI: 10.1016/j.jnucmat.2011.11.060. URL: http://www.sciencedirect.com/science/article/pii/S0022311511010166.

[14] M. B. Toloczko et al. "Irradiation creep and swelling from 400 to 600 °C of the oxide dispersion strengthened ferritic alloy MA957". In: *Journal of Nuclear Materials*. Vol. 329-333. 2004, pp. 352–355. ISBN: 0022-3115. DOI: 10.1016/j.jnucmat.2004.04.296.

[15] P. Dubuisson et al. "ODS Ferritic/martensitic alloys for Sodium Fast Reactor fuel pin cladding". In: *Journal of Nuclear Materials* 428.1-3 (Sept. 2012), pp. 6–12. ISSN: 00223115. DOI: 10.1016/j.jnucmat.2011.10.037. URL: http://www.sciencedirect.com/science/article/pii/S0022311511009317.

[16] M. L. Hamilton et al. "Fabrication Technological Development of the Oxide Dispersion Strengthened Alloy MA957 for Fast Reactor Applications". In: *Pacific Northwest National Laboratory Publications* (2000).

[17] K. Asano et al. "Microstructural evolution of an oxide dispersion strengthened steel under charged particle irradiation". In: *Journal of Nuclear Materials* 155-157 (July 1988), pp. 928–934. ISSN: 00223115. DOI: 10.1016/0022-3115(88)90443-6. URL: http://www.sciencedirect.com/science/article/pii/0022311588904436.

[18] S. Yamashita et al. "Effect of mechanical alloying parameters on irradiation damage in oxide dispersion strengthened ferritic steels". In: *Journal of Nuclear Materials* 283-287 (Dec. 2000), pp. 647–651. ISSN: 00223115. DOI: 10.1016/S0022-3115(00)00111-2. URL: ftp://ftp.stormchild.name/books/physics,%20math/%D0%96%D1%83%D1%80%D0%BD%D0%B0%D0%BB%D1%8B/Journal%20of%20Nuclear%20Materials%20(1997-2011)/2000%20Volume%20282/2-3/647-651.pdf%20http://www.sciencedirect.com/science/article/pii/S0022311500001112.

[19] Yingye Gan et al. "Energetic Study of Helium Cluster Nucleation and Growth in 14YWT through First Principles". In: *Materials* 9.1 (Jan. 2016), p. 17. ISSN: 1996-1944. DOI: 10.3390/ma9010017. URL: http://www.mdpi.com/1996-1944/9/1/17.

[20] P.D. Edmondson et al. "Helium bubble distributions in a nanostructured ferritic alloy". In: *Journal of Nuclear Materials* 434.1-3 (Mar. 2013), pp. 210–216. ISSN: 00223115. DOI: 10.1016/j.jnucmat.2012.11.049. URL: http://linkinghub.elsevier.com/retrieve/pii/S0022311512006447.

[21] P. Pareige et al. "Stability of nanometer-sized oxide clusters in mechanically-alloyed steel under ion-induced displacement cascade damage conditions". In: *Journal of Nuclear Materials* 360.2 (2007), pp. 136–142. ISSN: 00223115. DOI: 10.1016/j.jnucmat.2006.09.011.

[22] J. Saito et al. "Void formation and microstructural development in oxide dispersion strengthened ferritic steels during electron-irradiation". In: *Journal of Nuclear Materials* 258-263 (Oct. 1998), pp. 1264–1268. ISSN: 00223115. DOI: 10.1016/S0022-3115(98)00140-8. URL: http://www.sciencedirect.com/science/article/pii/S0022311598001408.

[23] H. Kinoshita et al. "Microstructural change on electron irradiated oxide dispersion strengthened ferritic steels". In: *Journal of Nuclear Materials* 191-194 (Sept. 1992), pp. 874–878. ISSN: 00223115. DOI: 10.1016/0022-3115(92)90598-F. URL: http://www.sciencedirect.com/science/article/pii/002231159290598F.

[24] N. Akasaka et al. "Microstructural changes of neutron irradiated ODS ferritic and martensitic steels". In: *Journal of Nuclear Materials* 329-333 (Aug. 2004), pp. 1053–1056. ISSN: 00223115. DOI: 10.1016/j.jnucmat.2004.04.133. URL: http://www.sciencedirect.com/science/article/pii/S0022311504002983.

[25] Massimo Sanctis et al. "Mechanical Characterization of a Nano-ODS Steel Prepared by Low-Energy Mechanical Alloying". In: *Metals* 7.8 (July 2017), p. 283. ISSN: 2075-4701. DOI: 10.3390/met7080283. URL: http://www.mdpi.com/2075-4701/7/8/283.

[26] M. J. Alinger. "On the formation and stability of nanometer scale precipitates in ferritic alloys during processing and high temperature service". PhD thesis. University of California, Santa Barbara, 2004, p. 341. URL: http://search.proquest.com/docview/305201099/abstract?accountid=13042.

[27] A. Chauhan et al. "Microstructure characterization and strengthening mechanisms of oxide dispersion strengthened (ODS) Fe-9%Cr and Fe-14%Cr extruded bars". In: *Journal of Nuclear Materials* 495 (Nov. 2017), pp. 6–19. ISSN: 0022-3115. DOI: 10.1016/J.JNUCMAT.2017.07.060. URL: https://www.sciencedirect.com/science/article/pii/S002231151730750X.

[28] S. V. Rogozhkin et al. "Effect of alloying with titanium on the microstructure of an oxide dispersion strengthened 13.5% Cr steel". In: *The Physics of Metals and Metallography* 115 (2014), pp. 1259–1266. ISSN: 0031-918X. DOI: 10.1134/S0031918X14120060. URL: http://download.springer.com/static/pdf/177/art:10.1134/S0031918X14120060.pdf?originUrl=http://link.springer.com/article/10.1134/S0031918X14120060%7B%

5C&%7Dtoken2=exp=1438075625%7B~%7Dacl=/static/pdf/177/art%7B%5C%7D3A10.1134%7B%5C%7D2FS0031918X14120.

[29] S. Terahsima and H. K. D. H. Bhadeshia. *Grain Growth: Zener Pinning of Grain Boundaries by Oxide Particles*. URL: http://www.phase-trans.msm.cam.ac.uk/2005/Zener/.

[30] N. Sallez. "Recrystallization, abnormal grain growth and ultrafine microstructure of ODS ferritic steels". PhD thesis. 2015.

[31] M. Mujahid and J. W. Martin. "The effect of oxide particle coherency on Zener pinning in ODS superalloys". In: *Journal of Materials Science Letters* 13 (1994), pp. 153–155.

[32] T. Gladman. "Second phase particle distribution and secondary recrystallisation". In: *Scripta Metallurgica et Materialia* 27.11 (Dec. 1992), pp. 1569–1573. ISSN: 0956716X. DOI: 10.1016/0956-716X(92)90146-6. URL: http://www.sciencedirect.com/science/article/pii/0956716X92901466.

[33] M. Hillert. "On the theory of normal and abnormal grain growth". In: *Acta Metallurgica* 13.3 (Mar. 1965), pp. 227–238. ISSN: 00016160. DOI: 10.1016/0001-6160(65)90200-2. URL: http://www.sciencedirect.com/science/article/pii/0001616065902002.

[34] Y. Brechet and M. Militzer. "A note on grain size dependent pinning". In: *Scripta Materialia* 52.12 (June 2005), pp. 1299–1303. ISSN: 13596462. DOI: 10.1016/j.scriptamat.2005.02.021. URL: http://www.sciencedirect.com/science/article/pii/S1359646205001144.

[35] V. Y. Novikov. "Grain growth and disperse particles: Impact of triple junctions". In: *Materials Letters* 84 (Oct. 2012), pp. 136–138. ISSN: 0167577X. DOI: 10.1016/j.matlet.2012.06.056. URL: http://www.sciencedirect.com/science/article/pii/S0167577X12008920.

[36] M. Perez et al. "In situ characterization of microstructural instabilities : Recovery , recrystallization and abnormal growth in nanoreinforced steel powder". In: 87 (2015), pp. 377–389. DOI: 10.1016/j.actamat.2014.11.051.

[37] N. Sallez et al. "On ball-milled ODS ferritic steel recrystallization: From as-milled powder particles to consolidated state". In: *Journal of Materials Science* 50.5 (Dec. 2014), pp. 2202–2217. ISSN: 0022-2461. DOI: 10.1007/s10853-014-8783-1. URL: http://link.springer.com/10.1007/s10853-014-8783-1.

[38] M. A. Auger et al. "Microstructure and mechanical properties of ultrafine-grained Fe-14Cr and ODS Fe-14Cr model alloys". In: *Journal of Nuclear Materials*. Vol. 417. 1-3. 2011, pp. 213–216. DOI: 10.1016/j.jnucmat.2010.12.060.

[39] M. J. Gorley. "Powder processing of oxide dispersion strengthened alloys for nuclear applications". PhD thesis. University of Oxford, 2014.

[40] S. Ukai et al. "Tube manufacturing and mechanical properties of oxide dispersion strengthened ferritic steel". In: *Journal of Nuclear Materials* 204 (Sept. 1993), pp. 74–80. ISSN: 00223115. DOI: 10.1016/0022-3115(93)90201-9. URL: http://www.sciencedirect.com/science/article/pii/0022311593902019.

[41] T. Liu et al. "Structure evolution of Y2O3 nanoparticle/Fe composite during mechanical milling and annealing". In: *Progress in Natural Science: Materials International* 23.4 (Aug. 2013), pp. 434–439. ISSN: 10020071. DOI: 10.1016/j.pnsc.2013.06.009. URL: http://www.sciencedirect.com/science/article/pii/S1002007113001093.

[42] T. Okuda and M. Fujiwara. "Dispersion behaviour of oxide particles in mechanically alloyed ODS steel". In: *Journal of Materials Science Letters* 14 (1995), pp. 1600–1603. ISSN: 02618028. DOI: 10.1007/BF00455428.

[43] A. Kimura et al. "Development of Al added high-Cr ODS steels for fuel cladding of next generation nuclear systems". In: *Journal of Nuclear Materials*. Vol. 417. 2011, pp. 176–179. ISBN: 9781617386084. DOI: 10.1016/j.jnucmat.2010.12.300.

[44] D.R. Gaskell. *Introduction to Metallurgical Thermodynamics*. 1973, pp. 226–227.

[45] M. K. Miller et al. "Atom probe tomography of nanoscale particles in ODS ferritic alloys". In: *Materials Science and Engineering: A* 353.1-2 (July 2003), pp. 140–145. ISSN: 09215093. DOI: 10.1016/S0921-5093(02)00680-9. URL: http://www.sciencedirect.com/science/article/pii/S0921509302006809.

[46] S. Ukai and M. Fujiwara. *Perspective of ODS alloys application in nuclear environments*. 2002. DOI: 10.1016/S0022-3115(02)01043-7.

[47] R. L. Klueh et al. "Oxide dispersion-strengthened steels: A comparison of some commercial and experimental alloys". In: *Journal of Nuclear Materials* 341 (2005), pp. 103–114. ISSN: 00223115. DOI: 10.1016/j.jnucmat.2005.01.017.

[48] S. Ukai. *Comprehensive Nuclear Materials*. Elsevier, 2012, pp. 241–271. ISBN: 9780080560335. DOI: 10.1016/B978-0-08-056033-5.00069-0. URL: http://www.sciencedirect.com/science/article/pii/B9780080560335000690.

[49] J. S. Cheon et al. "Sodium fast reactor evaluation: Core materials". In: *Journal of Nuclear Materials* 392.2 (July 2009), pp. 324–330. ISSN: 00223115. DOI: 10.1016/j.jnucmat.2009.03.021. URL: http://www.researchgate.net/publication/232370539%7B%5C_%7DSodium%7B%5C_%7Dfast%7B%5C_%7Dreactor%7B%5C_%7Devaluation%7B%5C_%7DCore%7B%5C_%7Dmaterials.

[50] S. Ohtsuka et al. "Nano-structure control in ODS martensitic steels by means of selecting titanium and oxygen contents". In: *Journal of Physics and Chemistry of Solids*. Vol. 66. 2005, pp. 571–575. ISBN: 0022-3697. DOI: 10.1016/j.jpcs.2004.06.033.

[51] S. Ohtsuka et al. "Improvement of 9Cr-ODS martensitic steel properties by controlling excess oxygen and titanium contents". In: *Journal of Nuclear Materials*. Vol. 329-333. 2004, pp. 372–376. DOI: 10.1016/j.jnucmat.2004.04.043.

[52] Frank Bergner et al. "Alternative Fabrication Routes toward Oxide- Dispersion-Strengthened Steels and Model Alloys". In: *Metallurgical and Materials Transactions A* 47 (2016). DOI: 10.1007/s11661-016-3616-2. URL: https://link.springer.com/content/pdf/10.1007%7B%5C%%7D2Fs11661-016-3616-2.pdf.

[53] C. Suryanarayana. "Mechanical alloying and milling". In: *Progress in Materials Science* 46.1-2 (Jan. 2001), pp. 1–184. ISSN: 00796425. DOI: 10.1016/S0079-6425(99)00010-9. URL: http://www.sciencedirect.com/science/article/pii/S0079642599000109.

[54] J. Hoffmann et al. "TEM study of mechanically alloyed ODS steel powder". In: *Journal of Nuclear Materials*. Vol. 428. 1-3. Sept. 2012, pp. 165–169. DOI: 10.1016/j.jnucmat.2011.09.034. URL: http://www.sciencedirect.com/science/article/pii/S0022311511008841.

[55] N. Iwata et al. "Characterization of Mechanically Alloyed Powders for High-Cr Oxide Dispersion Strengthened Ferritic Steel". In: *ISIJ International* 49.12 (Dec. 2009), pp. 1914–1919. ISSN: 0915-1559. DOI: 10.2355/isijinternational.49.1914. URL: https://www.jstage.jst.go.jp/article/isijinternational/49/12/49%7B%5C_%7D12%7B%5C_%7D1914/%7B%5C_%7Darticle.

[56] C. Cayron et al. "Microstructural evolution of Y2O3 and MgAl 2O4 ODS EUROFER steels during their elaboration by mechanical milling and hot isostatic pressing". In: *Journal of Nuclear Materials* 335.1 (2004), pp. 83–102. ISSN: 00223115. DOI: 10.1016/j.jnucmat.2004.06.010.

[57] J. J. Sunol and L. Escoda. "SEM and TEM studies in alloys developed by mechanical alloying". In: *Modern Research and Educational Topics in Microscopy*. 2007. URL: http://www.formatex.org/microscopy3/pdf/pp666-670.pdf.

[58] Y. Kimura et al. "Ultra Grain Refining and Decomposition of Oxide during Super-heavy Deformation in Oxide Dispersion Ferritic Stainless Steel Powder." In: *ISIJ International* 39.1 999 (1999), pp. 176–182. ISSN: 0915-1559. DOI: 10.2355/isijinternational.39.176.

[59] L. Toualbi et al. "Use of neutron and X-ray diffraction to study the precipitation mechanisms of oxides in ODS materials". In: *Journal of Nuclear Materials*. Vol. 417. 1-3. 2011, pp. 225–228. ISBN: 00223115. DOI: 10.1016/j.jnucmat.2010.12.071.

[60] M. Yamamoto et al. "Formation of residual ferrite in 9Cr-ODS ferritic steels". In: *Materials Science and Engineering A* 527.16-17 (2010), pp. 4418–4423. ISSN: 09215093. DOI: 10.1016/j.msea.2010.03.079.

[61] M. P. Phaniraj et al. "Microstructure development in mechanically alloyed yttria dispersed austenitic steels". In: *Acta Materialia* 57.6 (2009), pp. 1856–1864. ISSN: 13596454. DOI: 10.1016/j.actamat.2008.12.026.

[62] A. Ramar et al. "Effect of mechanical alloying on the mechanical and microstructural properties of ODS EUROFER 97". In: *Fusion Engineering and Design* 82.15-24 (2007), pp. 2543–2549. ISSN: 09203796. DOI: 10.1016/j.fusengdes.2007.05.048.

[63] Zbigniew Oksiuta. "Microstructural Changes of Ods Ferritic Steel Powders During Mechanical Alloying". In: ().

[64] H. Zhang et al. "An in situ powder neutron diffraction study of nano-precipitate formation during processing of oxide-dispersion-strengthened ferritic steels". In: *Journal of Alloys and Compounds* 582 (Jan. 2014), pp. 769–773. ISSN: 09258388. DOI: 10.1016/j.jallcom.2013.08.069. URL: http://linkinghub.elsevier.com/retrieve/pii/S0925838813019294.

[65] L. L. Hsiung et al. "Formation mechanism and the role of nanoparticles in Fe-Cr ODS steels developed for radiation tolerance". In: *Physical Review B - Condensed Matter and Materials Physics* 82 (2010). ISSN: 10980121. DOI: 10.1103/PhysRevB.82.184103.

[66] X. Boulnat et al. "Influence of oxide volume fraction on abnormal grain growth of nanostructured ferritic steels during non-isothermal treatments: An in situ study". In: *Acta Materialia* 97 (2015), pp. 124–130.

[67] M. J. Alinger, G. R. Odette, and D. T. Hoelzer. "On the role of alloy composition and processing parameters in nanocluster formation and dispersion strengthening in nanostuctured ferritic alloys". In: *Acta Materialia* 57 (2009), pp. 392–406. ISSN: 13596454. DOI: 10.1016/j.actamat.2008.09.025.

[68] D. T. Hoelzer et al. "Development of High-Strength ODS Steels for Nuclear Energy Applications". In: *ODS 2010 Materials Workshop*. 2010. URL: https://www.netl.doe.gov/File%20Library/Events/2010/ods/HoelzerDT.pdf.

[69] C. A. Williams et al. "Nanoscale characterisation of ODS-Eurofer 97 steel: An atom-probe tomography study". In: *Journal of Nuclear Materials* 400.1 (2010), pp. 37–45. ISSN: 00223115. DOI: 10.1016/j.jnucmat.2010.02.007.

[70] C. A. Williams et al. "The formation and evolution of oxide particles in oxide-dispersion-strengthened ferritic steels during processing". In: *Acta materialia* 61 (2013), pp. 2219–2235. ISSN: 13596454. DOI: 10.1016/j.actamat.2012.12.042.

[71] J. L. Bechade et al. “Application of synchrotron radiation to analyze the precipitation in ODS materials before irradiation in Fe-9%Cr single grain of powder and consolidated Fe-18%Cr”. In: *Journal of Nuclear Materials*. Vol. 428. 1-3. Sept. 2012, pp. 183–191. DOI: 10.1016/j.jnucmat.2011.08.025. URL: http://www.sciencedirect.com/science/article/pii/S0022311511008014.

[72] Lei Dai, Yongchang Liu, and Zhizhong Dong. “Size and structure evolution of yttria in ODS ferritic alloy powder during mechanical milling and subsequent annealing”. In: *Powder Technology* 217 (Feb. 2012), pp. 281–287. ISSN: 0032-5910. DOI: 10.1016/J.POWTEC.2011.10.039. URL: https://www.sciencedirect.com/science/article/pii/S0032591011005821?via%7B%5C%%7D3Dihub.

[73] Z. Z. Fang. *Sintering of Advanced Materials*. Elsevier Science, 2010, p. 500. ISBN: 1845699947. URL: https://books.google.com/books?id=NYpwAgAAQBAJ%7B%5C&%7Dpgis=1.

[74] P. Miao et al. “Effects of consolidation temperature, strength and microstructure on fracture toughness of nanostructured ferritic alloys”. In: *Journal of Nuclear Materials* 367-370 A (2007), pp. 208–212. ISSN: 00223115. DOI: 10.1016/j.jnucmat.2007.03.144.

[75] P. He et al. “Characterization of precipitates in nano structured 14% Cr ODS alloys for fusion application”. In: *Journal of Nuclear Materials*. Vol. 428. 2012, pp. 131–138. DOI: 10.1016/j.jnucmat.2011.08.026.

[76] J. Macías-Delgado et al. “Microstructure and tensile properties of ODS ferritic steels mechanically alloyed with Fe2Y”. In: *Nuclear Materials and Energy* 9 (Dec. 2016), pp. 372–377. ISSN: 2352-1791. DOI: 10.1016/J.NME.2016.09.019. URL: https://www.sciencedirect.com/science/article/pii/S2352179115300661.

[77] D. J. Larson et al. “Three-dimensional atom probe observation of nanoscale titanium-oxygen clustering in an oxide-dispersion-strengthened Fe-12Cr-3W-0.4Ti+Y2O3 ferritic alloy”. In: *Scripta Materialia* 44.2 (2001), pp. 359–364. ISSN: 13596462. DOI: 10.1016/S1359-6462(00)00593-5.

[78] C. H. Zhang et al. “Characterization of the oxide particles in Al-added high-Cr ODS ferritic steels”. In: *Journal of Nuclear Materials* 417.1-3 (Oct. 2011), pp. 221–224. ISSN: 00223115. DOI: 10.1016/j.jnucmat.2010.12.063. URL: http://www.sciencedirect.com/science/article/pii/S0022311510008858.

[79] B. Fournier et al. “Mechanical behaviour of ferritic ODS steels – Temperature dependancy and anisotropy”. In: *Journal of Nuclear Materials* 430.1-3 (Nov. 2012), pp. 142–149. ISSN: 00223115. DOI: 10.1016/j.jnucmat.2012.05.048. URL: http://www.sciencedirect.com/science/article/pii/S0022311512002826.

[80] R. L. Klueh et al. "Tensile and creep properties of an oxide dispersion-strengthened ferritic steel". In: *Journal of Nuclear Materials* 311.2002 (2002), pp. 773–777. ISSN: 00223115. DOI: 10.1016/S0022-3115(02)01046-2.

[81] D. T. Hoelzer et al. "Influence of particle dispersions on the high-temperature strength of ferritic alloys". In: *Journal of Nuclear Materials* 367-370 (Aug. 2007), pp. 166–172. ISSN: 00223115. DOI: 10.1016/j.jnucmat.2007.03.151. URL: http://www.sciencedirect.com/science/article/pii/S0022311507003583.

[82] M. Couvrat et al. "Microstructure Evolution of Mechanically Alloyed ODS Ferritic Steels during Hot Extrusion". In: *Solid State Phenomena* 172-174 (June 2011), pp. 721–726. ISSN: 1662-9779. DOI: 10.4028/www.scientific.net/SSP.172-174.721. URL: http://www.researchgate.net/publication/272617318%7B%5C_%7DMicrostructure%7B%5C_%7DEvolution%7B%5C_%7Dof%7B%5C_%7DMechanically%7B%5C_%7DAlloyed%7B%5C_%7DODS%7B%5C_%7DFerritic%7B%5C_%7DSteels%7B%5C_%7Dduring%7B%5C_%7DHot%7B%5C_%7DExtrusion.

[83] Z Špirit, M Chocholoušek, and M Šíma. "Mechanical testing of anisotropy in ODS steel tubes". In: 755 (2016). DOI: 10.1088/1742-6596/755/1/011001. URL: http://iopscience.iop.org/article/10.1088/1757-899X/179/1/012065/pdf.

[84] Marta Serrano, Mercedes Hernández-Mayoral, and Andrea García-Junceda. "Microstructural anisotropy effect on the mechanical properties of a 14Cr ODS steel". In: *Journal of Nuclear Materials* 428.1-3 (Sept. 2012), pp. 103–109. ISSN: 0022-3115. DOI: 10.1016/J.JNUCMAT.2011.08.016. URL: https://www.sciencedirect.com/science/article/pii/S0022311511007926.

[85] A Hobt et al. "Report on creep and LCF-Data on ODS-Materials for GEN IV-Reactors". In: (). URL: https://www.oecd-nea.org/science/smins4/documents/IIIa-3%7B%5C_%7DGenIV%7B%5C_%7DReactors%7B%5C_%7DMPA%7B%5C_%7DCIEMAT%7B%5C_%7Dcomplete.pdf.

[86] M. Suarez et al. "Challenges and Opportunities for Spark Plasma Sintering: A Key Technology for a Generation of New Materials". In: *Sintering Applications*. Ed. by Burcu Ertug. InTech, Feb. 2013. ISBN: 978-953-51-0974-7. DOI: 10.5772/56064. URL: http://dx.doi.org/10.5772/53706%20http://www.intechopen.com/books/sintering-applications.

[87] B. McWilliams and A. Zavaliangos. "Multi-phenomena simulation of electric field assisted sintering". In: *Journal of Materials Science* 43.14 (June 2008), pp. 5031–5035. ISSN: 0022-2461. DOI: 10.1007/s10853-008-2744-5. URL: http://link.springer.com/10.1007/s10853-008-2744-5.

[88] O. Yanagisawa, T. Hatayama, and K. Matsugi. "Recent research on spark plasma sintering". In: *Materials Japan* 33.12 (Aug. 1994), pp. 1489–1496. ISSN: 1340-2625. DOI: 10.2320/materia.33.1489. URL: https://www.jstage.jst.go.jp/article/materia1994/33/12/33%7B%5C_%7D12%7B%5C_%7D1489/%7B%5C_%7Darticle/-char/ja/.

[89] M Tokita. "Trends in advanced SPS spark plasma sintering systems and technology". In: *Journal of the Japan Society of Powder and Powder Metallurgy* 30 (1993), pp. 790–804.

[90] Joanna R. Groza et al. "Surface oxide debonding in field assisted powder sintering". In: *Materials Science and Engineering: A* 270.2 (1999), pp. 278–282.

[91] M Tokita. "Mechanism of spark plasma sintering". In: *Proceeding of NEDO International Symposium on ...* (1999). URL: http://d.yimg.com/kq/groups/3862917/2054596553/name/SUMITOMO%20REVIEW-Spark-Plasma-Sintering.pdf.

[92] D. M. Hulbert et al. "The absence of plasma in "spark plasma sintering"". In: *Journal of Applied Physics* 104.3 (Aug. 2008), p. 033305. ISSN: 00218979. DOI: 10.1063/1.2963701. URL: http://scitation.aip.org/content/aip/journal/jap/104/3/10.1063/1.2963701.

[93] A. I. Raicheko. "Fundamental Processes in Powder Sintering". In: *Metalurgiya* (1987).

[94] H. Conrad. "Thermally activated plastic flow of metals and ceramics with an electric field or current". In: *Materials Science and Engineering A* 322 (2002), pp. 100–107. ISSN: 09215093. DOI: 10.1016/S0921-5093(01)01122-4.

[95] J. Räthel, M. Herrmann, and W. Beckert. "Temperature distribution for electrically conductive and non-conductive materials during Field Assisted Sintering (FAST)". In: *Journal of the European Ceramic Society* 29.8 (May 2009), pp. 1419–1425. ISSN: 09552219. DOI: 10.1016/j.jeurceramsoc.2008.09.015. URL: http://www.sciencedirect.com/science/article/pii/S0955221908005074.

[96] H. Tomino, H. Watanabe, and Y. Kondo. "Electric Current Path and Temperature Distribution for Spark Sintering". In: *Journal of the Japan Society of Powder and Powder Metallurgy* 44.10 (1997), pp. 974–979.

[97] Hongtao Zhang et al. "Processing and microstructure characterisation of oxide dispersion strengthened Fe–14Cr–0.4Ti–0.25Y 2 O 3 ferritic steels fabricated by spark plasma sintering". In: *Journal of Nuclear Materials* 464 (Sept. 2015), pp. 61–68. ISSN: 00223115. DOI: 10.1016/j.jnucmat.2015.04.029. URL: http://repository.liv.ac.uk/2003761/%20http://linkinghub.elsevier.com/retrieve/pii/S0022311515002391.

[98] A. P. C. Morrison. "Powder Based Processing of Novel Dispersion Strengthened Copper Alloys for Fusion Applications". PhD thesis. Oxford, 2018.

[99] M. A. Yar. "Development of Nanostructured Tungsten Based Composites for Energy Applications". PhD thesis. 2012. URL: http://www.diva-portal.org/smash/get/diva2:547136/FULLTEXT01.pdf.

[100] M. A. Auger et al. "Microstructure and mechanical behavior of ODS and non-ODS Fe–14Cr model alloys produced by spark plasma sintering". In: *Journal of Nuclear Materials* 436.1-3 (May 2013), pp. 68–75. ISSN: 00223115. DOI: 10.1016/j.jnucmat.2013.01.331. URL: http://linkinghub.elsevier.com/retrieve/pii/S0022311513003747.

[101] X. Boulnat et al. "High-Temperature Tensile Properties of Nano-Oxide Dispersion Strengthened Ferritic Steels Produced by Mechanical Alloying and Spark Plasma Sintering". en. In: *Metallurgical and Materials Transactions A* 44.6 (Apr. 2013), pp. 2461–2465. ISSN: 1073-5623. DOI: 10.1007/s11661-013-1719-6. URL: http://ezproxy-prd.bodleian.ox.ac.uk:2142/article/10.1007/s11661-013-1719-6/fulltext.html.

[102] K. Verhiest et al. "Experimental study on the contact angle formation of solidified iron–chromium droplets onto yttria ceramic substrates for the yttria/ferrous alloy system with variable chromium content". In: *Ceramics International* 40.1 (Jan. 2014), pp. 2187–2200. ISSN: 0272-8842. DOI: 10.1016/J.CERAMINT.2013.07.137. URL: https://www.sciencedirect.com/science/article/pii/S0272884213009310.

[103] K. Verhiest et al. "Advances in the development of corrosion and creep resistant nano-yttria dispersed ferritic/martensitic alloys using the rapid solidification processing technique". In: *Ceramics International* 40.9 (Nov. 2014), pp. 14319–14334. ISSN: 0272-8842. DOI: 10.1016/J.CERAMINT.2014.06.023. URL: https://www.sciencedirect.com/science/article/pii/S0272884214008955.

[104] P. Franke, S. Miran, and H.S. Seifert. "Preparation of Stainless ODS Steels by Internal Oxidation". In: *ODISSEUS*. 2017.

[105] J.R. Rieken et al. "Reactive gas atomization processing for Fe-based ODS alloys". In: *Journal of Nuclear Materials* 428.1-3 (Sept. 2012), pp. 65–75. ISSN: 00223115. DOI: 10.1016/j.jnucmat.2011.08.015. URL: https://doi.org/10.1016/j.jnucmat.2011.08.015%20http://linkinghub.elsevier.com/retrieve/pii/S0022311511007914.

[106] H. H. Liebermann. "Rapidly solidified alloys made by chill block melt-spinning processes". In: *Journal of Crystal Growth* 70.1-2 (Dec. 1984), pp. 497–506. ISSN: 00220248. DOI: 10.1016/0022-0248(84)90308-7. URL: http://www.sciencedirect.com/science/article/pii/0022024884903087.

[107] Zuliang Hong et al. "Development of a Novel Melt Spinning-Based Processing Route for Oxide Dispersion-Strengthened Steels". In: *Metallurgical and Materials Transactions A* 49.2 (Feb. 2018), pp. 604–612. ISSN: 1073-5623. DOI: 10.1007/s11661-017-4398-x. URL: http://link.springer.com/10.1007/s11661-017-4398-x.

[108] F.N. Rhines, W.A. Johnson, and W.A Anderson. "No T". In: *AIME, Trans.* 147 (1942), pp. 205–21.

[109] P. S. Grant. "Spray forming". In: *Progress in Materials Science* 39.4-5 (Jan. 1995), pp. 497–545. ISSN: 00796425. DOI: 10.1016/0079-6425(95)00004-6. URL: http://www.sciencedirect.com/science/article/pii/0079642595000046.

[110] M. Hasegawa and M. Osawa. "Oxide dispersion strengthened nickel-base heat resistant alloys by means of the spray-dispersion method". In: *Metallurgical Transactions A* 16.6 (June 1985), pp. 1043–1048. ISSN: 0360-2133. DOI: 10.1007/BF02811674. URL: http://link.springer.com/10.1007/BF02811674.

[111] Z. Li et al. "A high strength and high conductivity copper alloy prepared by spray forming". In: *Journal of Materials Processing Technology* 137 (2003), pp. 60–64.

[112] Hye Jung Chang, Hye Young Cho, and Jeoung Han Kim. "Stability of Y–Ti–O nanoparticles during laser melting of advanced oxide dispersion-strengthened steel powder". In: *Journal of Alloys and Compounds* 653 (Dec. 2015), pp. 528–533. ISSN: 09258388. DOI: 10.1016/j.jallcom.2015.08.273. URL: http://linkinghub.elsevier.com/retrieve/pii/S0925838815309695.

[113] Thomas Boegelein et al. "Mechanical response and deformation mechanisms of ferritic oxide dispersion strengthened steel structures produced by selective laser melting". In: *Acta Materialia* 87 (Apr. 2015), pp. 201–215. ISSN: 1359-6454. DOI: 10.1016/J.ACTAMAT.2014.12.047. URL: https://www.sciencedirect.com/science/article/pii/S1359645414009732.

[114] John C. Walker et al. "Fabrication of Fe-Cr-Al Oxide Dispersion Strengthened PM2000 Alloy Using Selective Laser Melting". In: *Advanced Engineering Materials* 11.7 (July 2009), pp. 541–546. ISSN: 14381656. DOI: 10.1002/adem.200800407. URL: http://doi.wiley.com/10.1002/adem.200800407.

[115] H. Springer et al. "Efficient additive manufacturing production of oxide- and nitride-dispersion-strengthened materials through atmospheric reactions in liquid metal deposition". In: *Materials & Design* 111 (Dec. 2016), pp. 60–69. ISSN: 02641275. DOI: 10.1016/j.matdes.2016.08.084. URL: http://linkinghub.elsevier.com/retrieve/pii/S0264127516311479.

[116] C. Y. Yap et al. "Review of selective laser melting: Materials and applications". In: *Applied Physics Reviews* 2.4 (Dec. 2015), p. 041101. ISSN: 1931-9401. DOI: 10.1063/1.4935926. URL: http://aip.scitation.org/doi/10.1063/1.4935926.

[117] Tiberiu Stan et al. "Fabrication and Characterization of Naturally Selected Epitaxial Fe-{111} Y2Ti2O7 Mesoscopic Interfaces: Some Potential Implications to Nano-Oxide Dispersion-Strengthened Steels". In: *Metallurgical and Materials Transactions A* 44.10 (Oct. 2013), pp. 4505–4512. ISSN: 1073-5623. DOI: 10.1007/s11661-013-1827-3. URL: http://link.springer.com/10.1007/s11661-013-1827-3.

[118] T.C. Kaspar et al. "Epitaxial Fe/Y 2 O 3 interfaces as a model system for oxide-dispersion-strengthened ferritic alloys". In: *Journal of Nuclear Materials* 457 (Feb. 2015), pp. 352–361. ISSN: 00223115. DOI: 10.1016/j.jnucmat.2014.11.046. URL: http://linkinghub.elsevier.com/retrieve/pii/S002231151400837X.

[119] Iver E Anderson, Joel E Rieken, and David J Byrd. "ATOMIZATION AND POWDER PROCESSING OF HIGH TEMPERATURE FERRITIC STAINLESS STEEL". In: (). URL: https://pdfs.semanticscholar.org/de12/d1323cbdee7a0206a79a7e6b74bf40ebd403.pdf.

[120] J. R. Rieken et al. "Reactive gas atomization processing for Fe-based ODS alloys". In: *Journal of Nuclear Materials* 428.1-3 (Sept. 2012), pp. 65–75. ISSN: 00223115. DOI: 10.1016/j.jnucmat.2011.08.015. URL: http://www.sciencedirect.com/science/article/pii/S0022311511007914.

[121] E. Gil et al. "ODS ferritic steels produced by an alternative route (STARS): microstructural characterisation after atomisation, HIPping and heat treatments". In: *Powder Metallurgy* 59.5 (Oct. 2016), pp. 359–369. ISSN: 0032-5899. DOI: 10.1080/00325899.2016.1254894. URL: https://www.tandfonline.com/doi/full/10.1080/00325899.2016.1254894%20http://www.eurofusionscipub.org/wp-content/uploads/eurofusion/WPMATPR16%7B%5C_%7D15309%7B%5C_%7Dsubmitted.pdf.

[122] M. Hernández-Mayoral et al. "Microstructural and mechanical characterisation of ODS ferritic alloys produced by mechanical alloying and spark plasma sintering". In: *Materials Science and Technology* 30.13 (Nov. 2014), pp. 1669–1675. ISSN: 0267-0836. DOI: 10.1179/1743284714Y.0000000555. URL: http://www.tandfonline.com/doi/full/10.1179/1743284714Y.0000000555.

[123] Y. Li et al. "Grain structural characterization of 9Cr–ODS steel aged at 973K up to 10,000h by electron backscatter diffraction". In: *Journal of Nuclear Materials* 455.1-3 (Dec. 2014), pp. 568–572. ISSN: 00223115. DOI: 10.1016/j.jnucmat.2014.08.047. URL: http://linkinghub.elsevier.com/retrieve/pii/S0022311514005753.

[124] M. K. Miller, K. F. Russell, and D. T. Hoelzer. "Characterization of precipitates in MA/ODS ferritic alloys". In: *Journal of Nuclear Materials* 351.1-3 (June 2006), pp. 261–268. ISSN: 00223115. DOI: 10.1016/j.jnucmat.2006.02.004. URL: http://www.sciencedirect.com/science/article/pii/S0022311506000894.

[125] S. Y. Zhong et al. "Influence of nano-particle coherency degree on the coarsening resistivity of the nano-oxide particles of Fe–14Cr–1W ODS alloys". In: *Journal of Nuclear Materials* 455.1-3 (Dec. 2014), pp. 618–623. ISSN: 00223115. DOI: 10.1016/j.jnucmat.2014.08.045. URL: http://linkinghub.elsevier.com/retrieve/pii/S002231151400573X.

[126] Ankur Chauhan, Dimitri Litvinov, and Jarir Aktaa. "High temperature tensile properties and fracture characteristics of bimodal 12Cr-ODS steel". In: *Journal of Nuclear Materials* 468 (Jan. 2016), pp. 1–8. ISSN: 00223115. DOI: 10.1016/j.jnucmat.2015.11.013. URL: http://linkinghub.elsevier.com/retrieve/pii/S0022311515303214.

[127] J. H. Ahn, S. H. Lee, and J. S. Jang. "Mechanical Alloying and Properties of ODS Ferritic Steels". EN. In: *Advanced Materials Research* 15-17 (Feb. 2007), pp. 696–701. ISSN: 1662-8985. DOI: 10.4028/www.scientific.net/AMR.15-17.696. URL: http://zh.scientific.net/AMR.15-17.696.

[128] Z. Oksiuta et al. "Influence of HIP pressure on tensile properties of a 14Cr ODS ferritic steel". In: *Fusion Engineering and Design* 89.2 (Feb. 2014), pp. 137–141. ISSN: 09203796. DOI: 10.1016/j.fusengdes.2014.01.052. URL: http://linkinghub.elsevier.com/retrieve/pii/S0920379614000532.

[129] K. N. Allahar et al. "Ferritic oxide dispersion strengthened alloys by spark plasma sintering". In: *Journal of Nuclear Materials* 443.1-3 (Nov. 2013), pp. 256–265. ISSN: 00223115. DOI: 10.1016/j.jnucmat.2013.07.019. URL: http://linkinghub.elsevier.com/retrieve/pii/S0022311513009070%20http://www.sciencedirect.com/science/article/pii/S0022311513009070.

[130] Q. X. Sun et al. "Microstructure and mechanical properties of oxide dispersion strengthened ferritic steel prepared by a novel route". In: *Journal of Nuclear Materials* 424 (2012), pp. 279–284. ISSN: 00223115. DOI: 10.1016/j.jnucmat.2011.12.020.

[131] A. García-Junceda, M. Hernández-Mayoral, and M. Serrano. "Influence of the microstructure on the tensile and impact properties of a 14Cr ODS steel bar". In: *Materials Science and Engineering: A* 556 (Oct. 2012), pp. 696–703. ISSN: 09215093. DOI: 10.1016/j.msea.2012.07.051. URL: http://linkinghub.elsevier.com/retrieve/pii/S0921509312010131.

[132] S. Holmstrom et al. *Determination of high temperature material properties of 15-15Ti steel by small specimen techniques*. Tech. rep. EERA JPNM Pilot Project TASTE, 2017. DOI: 10.2760/49859.

[133] M. Richardson and M. J. Gorley. *Realisation of Small Punch Testing to Accelerate Materials Qualification for Fusion Applications*. Tech. rep. CCFE, 2016.

[134] M. Bruchhausen et al. "Characterization of a 14Cr ODS steel by means of small punch and uniaxial testing with regard to creep and fatigue at elevated temperatures". In: *Journal of Nuclear Materials* 444.1-3 (Jan. 2014), pp. 283–291. ISSN: 00223115. DOI: 10.1016/j.jnucmat.2013.09.059. URL: http://linkinghub.elsevier.com/retrieve/pii/S0022311513011367.

[135] Z. Oksiuta et al. "Development and characterisation of a new ODS ferritic steel for fusion reactor application". In: *Journal of Nuclear Materials* 393 (2009), pp. 114–119. ISSN: 00223115. DOI: 10.1016/j.jnucmat.2009.05.013. URL: http://ac.els-cdn.com/S0022311509006369/1-s2.0-S0022311509006369-main.pdf?%7B%5C_%7Dtid=dfad8a40-35db-11e5-9db2-00000aacb360%7B%5C&%7Dacdnat=1438165597%7B%5C_%7D.

[136] Nguyen Tien. "Particle-Particle Interaction in Dry Powder Blending: Applying theoretical concepts to practical systems". PhD thesis. 2014. URL: https://www.tipharma.com/fileadmin/user%7B%5C_%7Dupload/Theses/PDF/Nguyen%7B%5C_%7DTien%7B%5C_%7DThanh%7B%5C_%7DD6-203.pdf.

[137] R E Logé et al. "Optimisation of the fabrication route of ferritic / martensitic ODS cladding tubes: metallurgical approach and pilgering numerical modeling CEA-EdF-AREVA collaboration ANR-Stratotube project (CEA-CEMEF-VN) New fast-neutron sodium-cooled GEN IV reactors Fo". In: (2013). URL: http://www.iaea.org/inis/collection/NCLCollectionStore/%7B%5C_%7DPublic/45/089/45089556.pdf?r=1.

[138] Malvern Instruments. *Malvern Mastersizer 2000 User Manual*. 2012. URL: http://www.malvern.com/en/support/product-support/mastersizer-range/mastersizer-2000/.

[139] T Wriedt. "Mie theory: a review". In: *The Mie Theory* (2012). URL: http://link.springer.com/chapter/10.1007/978-3-642-28738-1%7B%5C_%7D2.

[140] B. R. Jennings and K. Parslow. "Particle Size Measurement: The Equivalent Spherical Diameter". In: *Proceedings of the Royal Society A: Mathematical, Physical and Engineering Sciences* 419.1856 (Sept. 1988), pp. 137–149. ISSN: 1364-5021. DOI: 10.1098/rspa.1988.0100. URL: http://rspa.royalsocietypublishing.org/cgi/doi/10.1098/rspa.1988.0100.

[141] World Health Organization. *Bulk Density and Tapped Density if Powders*. Tech. rep. 2012.

[142] B. Yao et al. "Multislice simulation of transmission electron microscopy imaging of helium bubbles in Fe". In: *Journal of Electron Microscopy* 61.6 (Dec. 2012), pp. 393–400. ISSN: 0022-0744. DOI: 10.1093/jmicro/dfs065. URL: https://academic.oup.com/jmicro/article-lookup/doi/10.1093/jmicro/dfs065.

[143] C. C. Ahn and O. L. Krivanek. *EELS Atlas: A reference for collection of electron energy loss spectra covering all stable elements*. 1983.

[144] A.A.N. Németh et al. "Environmentally-assisted grain boundary attack as a mechanism of embrittlement in a nickel-based superalloy". In: *Acta Materialia* 126 (Mar. 2017), pp. 361–371. ISSN: 13596454. DOI: 10.1016/j.actamat.2016.12.039. URL: http://linkinghub.elsevier.com/retrieve/pii/S1359645416309752.

[145] Xavier Boulnat et al. "Microstructure Evolution in Nano-reinforced Ferritic Steel Processed By Mechanical Alloying and Spark Plasma Sintering". In: (). DOI: 10.1007/s11661-013-2107-y.

[146] R. E. Loge et al. "Optimization of the fabrication route of ferritic/martensitic ODS cladding tubes: metallurgical approach and pilgering numerical modeling". In: *IAEA International Conference on Fast Reactors and Related Fuel Cycles: Safe Technologies and Sustainable Scenarios*. 2013.

[147] Dierk Raabe and K. Lücke. "Rolling and Annealing Textures of BCC Metals". In: *Materials Science Forum* 157-162 (1994), pp. 597–610. ISSN: 1662-9752. DOI: 10.4028/www.scientific.net/MSF.157-162.597. URL: http://www.scientific.net/MSF.157-162.597.

[148] Sanghoon Noh et al. "Effects of heat treatments on microstructures and mechanical properties of dual phase ODS steels for high temperature strength". In: *Nuclear Engineering and Technology* 45.6 (Nov. 2013), pp. 821–826. ISSN: 17385733. DOI: 10.5516/NET.02.2013.529. URL: http://linkinghub.elsevier.com/retrieve/pii/S1738573315301844.

[149] U. Ehrnstén et al. *Assessment of the effect of anisotropy on the mechanical properties of ODS steel tube*. Tech. rep. 2017.

[150] NPL. *FeY phase diagram*.

[151] P. Le Brun, L. Froyen, and L. Delaey. "The modelling of the mechanical alloying process in a planetary ball mill: comparison between theory and in-situ observations". In: *Materials Science and Engineering A* 161.75-82 (1993).

[152] C. D. Hartley. *Laboratory scale mill: powder location tests*. Tech. rep. NNL (11) 11764 Issue 2, 2017.

[153] P. Franke et al. "Mechanical Properties of Spark Plasma Sintered Fe-Cr Compacts Strengthened by Nanodispersed Yttria Particles". In: *Materials Testing* 52.3 (Mar. 2010), pp. 133–138. ISSN: 0025-5300. DOI: 10.3139/120.110115. URL: http://www.researchgate.net/publication/279757238%7B%5C_%7DMechanical%7B%5C_%7DProperties%7B%5C_%7Dof%7B%5C_%7DSpark%7B%5C_%7DPlasma%7B%5C_%7DSintered%7B%5C_%7DFe-Cr%7B%5C_%7DCompacts%7B%5C_%7DStrengthened%7B%5C_%7Dby%7B%5C_%7DNanodispersed%7B%5C_%7DYttria%7B%5C_%7DParticles.

[154] Haijian Xu et al. "Microstructural evolution in a new Fe based ODS alloy processed by mechanical alloying". In: *Nuclear Materials and Energy* 7 (May 2016), pp. 1–4. ISSN: 2352-1791. DOI: 10.1016/J.NME.2016.04.006. URL: https://www.sciencedirect.com/science/article/pii/S2352179116300011.

[155] F. Qiang et al. *X-ray Diffraction Rietveld Analysis of Shot-peened Duplex Stainless Steel during Isothermal Annealing*. Tech. rep. URL: https://www.shotpeener.com/library/pdf/2014089.pdf.

[156] Wang Xingqing et al. "Formation of Intermetallic Compound in Iron-Aluminum Alloys". In: *JOURNAl. OF SHANGHAI UNIVERSITY* 2.4 (1998). URL: https://link.springer.com/content/pdf/10.1007%7B%5C%%7D2Fs11741-998-0045-5.pdf.

[157] J. R. Cahoon, W. H. Broughton, and A. R. Kutzak. "The determination of yield strength from hardness measurements". In: *Metallurgical Transactions* 2.7 (), pp. 1979–1983. ISSN: 0360-2133. DOI: 10.1007/bf02913433. URL: https://link.springer.com/article/10.1007/BF02913433.

[158] Lulu Li et al. "Long-term stability of 14YT-4Sc alloy at high temperature". In: *Materials Science and Engineering A* (2015).

[159] U.F. Kocks and H. Mecking. "Physics and phenomenology of strain hardening: the FCC case". In: *Progress in Materials Science* 48.3 (Jan. 2003), pp. 171–273. ISSN: 00796425. DOI: 10.1016/S0079-6425(02)00003-8. URL: http://linkinghub.elsevier.com/retrieve/pii/S0079642502000038.

[160] E Gil et al. "XPS and SEM analysis of the surface of gas atomized powder precursor of ODS ferritic steels obtained through the STARS route". In: *Applied Surface Science* 427 (2018), pp. 182–191. DOI: 10.1016/j.apsusc.2017.07.205. URL: https://ezproxy-prd.bodleian.ox.ac.uk:6335/S0169433217322055/1-s2.0-S0169433217322055-main.pdf?%7B%5C_%7Dtid=cf924ac0-a770-11e7-ae87-00000aacb35f%7B%5C&%7Dacdnat=1506949042%7B%5C_%7D.

[161] K Dawson et al. "Recovery and recrystallisation in mechanically alloyed and annealed, legacy, FeCrAlY ODS alloy precursor powders". In: *IOP Conference Series: Materials Science and Engineering* 89 (Aug. 2015), p. 012020. ISSN: 1757-8981. DOI: 10.1088/1757-899X/89/1/012020. URL: http://iopscience.iop.org/article/10.1088/1757-899X/89/1/012020/pdf%20http://stacks.iop.org/1757-899X/89/i=1/a=012020?key=crossref.7a5583a33bde5779a2e21446b674844d.

[162] J. B. Allen and C. Walter. "Numerical Simulation of the Temperature and Stress Field Evolution Applied to the Field Assisted Sintering Technique". In: *ISRN Materials Science* 2012 (May 2012), pp. 1–9. ISSN: 2090-6099. DOI: 10.5402/2012/698158. URL: https://www.hindawi.com/archive/2012/698158/.

[163] K Vanmeensel et al. "Modelling of the temperature distribution during field assisted sintering". In: *Acta Materialia* 53 (2005), pp. 4379–4388. DOI: 10.1016/j.actamat.2005.05.042. URL: http://citeseerx.ist.psu.edu/viewdoc/download?doi=10.1.1.505.2414%7B%5C&%7Drep=rep1%7B%5C&%7Dtype=pdf.

[164] Heinz Kessel et al. *"FAST" field assisted sintering technology-a new process for the production of metallic and ceramic sintering materials*. Tech. rep. 2015.

[165] Olivier Guillon et al. "Field-Assisted Sintering Technology/Spark Plasma Sintering: Mechanisms, Materials, and Technology Developments". In: *Advanced Engineering Materials* 16.7 (July 2014), pp. 830–849. ISSN: 14381656. DOI: 10.1002/adem.201300409. URL: http://doi.wiley.com/10.1002/adem.201300409.

[166] Muhammad Dilawer Hayat, Erik Adolfsson, and Elis Carlstrom. "Electric Field Assisted Sintering of Metal Oxides". PhD thesis. 2011.

[167] Brian Alexander. "Element Compatability and Stability of Tough Samples and Problem Elements". In: *3rd Annual ICP Conference. Getting back to basics: Drilling down*. 2017.

[168] S. Rogozhkin et al. "Nanostructure evolution in ODS steels under ion irradiation". In: *Nuclear Materials and Energy* 9 (Dec. 2016), pp. 66–74. ISSN: 23521791. DOI: 10.1016/j.nme.2016.06.011. URL: http://linkinghub.elsevier.com/retrieve/pii/S2352179116300035.

[169] A J London et al. "Comparison of atom probe tomography and transmission electron microscopy analysis of oxide dispersion strengthened steels". In: *Journal of Physics: Conference Series* 522 (June 2014), p. 012028. ISSN: 1742-6588. DOI: 10.1088/1742-6596/522/1/012028. URL: http://stacks.iop.org/1742-6596/522/i=1/a=012028?key=crossref.339acca06043bbbb39ae8963b7379148.

[170] Jae-Bok Seol and Jeoung-Han Kim. "Grain Boundary Segregation and Core/Shell Structured Nanofeatures in Oxide-Dispersion Strengthened Fe-Cr Alloys". In: *Microscopy and Microanalysis* 22.S3 (July 2016), pp. 674–675. ISSN: 1431-9276. DOI: 10.1017/S1431927616004220. URL: http://www.journals.cambridge.org/abstract%7B%5C_%7DS1431927616004220.

[171] Sambaraj Sravan Kumar et al. "Development of nano-oxide dispersed 304L steels by mechanical milling and conventional sintering". In: *Materials Research* 19.1 (Feb. 2016), pp. 175–182. ISSN: 1980-5373. DOI: 10.1590/1980-5373-MR-2015-0593. URL: http://www.scielo.br/scielo.php?script=sci%7B%5C_%7Darttext%7B%5C&%7Dpid=S1516-14392016000100175%7B%5C&%7Dlng=en%7B%5C&%7Dtlng=en.

[172] D. L. Sornin, A. Karch, and R. E. Logé. "Competition between intragranular and intergranular deformation mechanisms in ODS ferritic steels during hot deformation at high strain rate". In: *Journal of Materials Science* 53.4 (Feb. 2018), pp. 2965–2975. ISSN: 0022-2461. DOI: 10.1007/s10853-017-1730-1. URL: http://link.springer.com/10.1007/s10853-017-1730-1.

[173] M. P. Higgins et al. "Crossover from disordered to core-shell structures of nano-oxide Y2O3 dispersed particles in Fe". In: *Applies Physics Letters* 109.3 (2016). DOI: 10.10163/1.4959776.

[174] A. Steckmeyer et al. "Tensile properties and deformation mechanisms of a 14Cr ODS ferritic steel". In: *Journal of Nuclear Materials* 405.2 (Oct. 2010), pp. 95–100. ISSN: 00223115. DOI: 10.1016/j.jnucmat.2010.07.027. URL: http://linkinghub.elsevier.com/retrieve/pii/S0022311510003259.

[175] Joachim H. Schneibel and Martin Heilmaier. "Hall-Petch Breakdown at Elevated Temperatures". In: *MATERIALS TRANSACTIONS* 55.1 (2014), pp. 44–51. ISSN: 1345-9678. DOI: 10.2320/matertrans.MA201309. URL: https://www.jstage.jst.go.jp/article/matertrans/55/1/55%7B%5C_%7DMA201309/%7B%5C_%7Darticle.

[176] G.M. Stoica et al. "Temperature-dependent elastic anisotropy and mesoscale deformation in a nanostructured ferritic alloy". In: *Nature Communications* 5.1 (Dec. 2014), p. 5178. ISSN: 2041-1723. DOI: 10.1038/ncomms6178. URL: http://www.nature.com/articles/ncomms6178.

[177] E.J. Pavlina and C.J. Van Tyne. "Correlation of Yield Strength and Tensile Strength with Hardness for Steels". In: *Journal of Materials Engineering and Performance* 17.6 (Dec. 2008), pp. 888–893. ISSN: 1059-9495. DOI: 10.1007/s11665-008-9225-5. URL: http://link.springer.com/10.1007/s11665-008-9225-5.

[178] J. R. Cahoon. "An Improved Equation Relating Hardness to Ultimate Tensile Strength". In: *Metallurgical Transactions* 3 (1972), p. 3040. DOI: 10.1007/BF02913433.

[179] P. Zhang, S.X. Li, and Z.F. Zhang. "General relationship between strength and hardness". In: *Materials Science and Engineering: A* 529 (Nov. 2011), pp. 62–73. ISSN: 09215093. DOI: 10.1016/j.msea.2011.08.061. URL: http://linkinghub.elsevier.com/retrieve/pii/S0921509311009555.

[180] Setsuo Takaki et al. "Effect of Grain Boundary Segregation of Interstitial Elements on Hall-Petch Coefficient in Steels". In: *MATERIALS TRANSACTIONS* 55.1 (2014), pp. 28–34. ISSN: 1345-9678. DOI: 10.2320/matertrans.MA201314. URL: https://www.jstage.jst.go.jp/article/matertrans/55/1/55%7B%5C_%7DMA201314/%7B%5C_%7Darticle.

[181] R. Chidambaram and S. Banerjee. *Materials Research: Current Scenario and Future Projections*. Allied Publishers, 2003, pp. 195–97. ISBN: 81-7764-450-5. URL: https://books.google.co.uk/books?id=a3EWH%7B%5C_%7DvGQp0C%7B%5C&%7Dprintsec=frontcover%7B%5C#%7Dv=onepage%7B%5C&%7Dq%7B%5C&%7Df=false.

[182] ONR. *Generic Design Assessment - New Civil Reactor Build*. Tech. rep. 2011.

[183] Matthias Bruchhausen et al. "European Standard on Small Punch Testing of Metallic Materials". In: *Volume 1A: Codes and Standards*. ASME, July 2017, V01AT01A065. ISBN: 978-0-7918-5790-8. DOI: 10.1115/PVP2017-65396. URL: http://proceedings.asmedigitalcollection.asme.org/proceeding.aspx?doi=10.1115/PVP2017-65396.

[184] H. Weekes. *Use of the Small Punch (Creep) Test to Measure Mechanical Properties NNL 14348 Issue 1*. Tech. rep. NNL, 2017, pp. 1–111.

[185] F. Cortellino. "Experimental and numerical investigation of small punch creep test". PhD thesis. University of Nottingham, 2015. URL: http://eprints.nottingham.ac.uk/28954/1/PhD%7B%5C_%7DThesis%7B%5C_%7DCortellino.pdf.

[186] S. Connolly and P. Grant. *Comparison between powder produced by attritor mill and planetary mill, Report to NNL*. Tech. rep. 2018.

[187] S. Connolly and P. S. Grant. *Spray Casting as a Novel Production Method for ODS Steel, Report to NNL*. Tech. rep. 2018.